STUDYING MILLISECOND PULSARS AND PULSAR TAILS IN THE VERY-HIGH-ENERGY GAMMA-RAY REGIME WITH VERITAS

A Dissertation
Presented to
The Academic Faculty

By

Alasdair E. Gent

In Partial Fulfillment
of the Requirements for the Degree
Doctor of Philosophy in the
School of Physics

Georgia Institute of Technology

August 2022

STUDYING MILLISECOND PULSARS AND PULSAR TAILS IN THE VERY-HIGH-ENERGY GAMMA-RAY REGIME WITH VERITAS

Approved by:

Dr. A. Nepomuk Otte, Advisor
School of Physics
Georgia Institute of Technology

Dr. Ignacio Taboada
School of Physics
Georgia Institute of Technology

Dr. Sven Simon
School of Earth and Atmospheric Science
Georgia Institute of Technology

Dr. Gongjie Li
School of Physics
Georgia Institute of Technology

Dr. John Wise
School of Physics
Georgia Institute of Technology

Date Approved: June 27, 2022

ACKNOWLEDGEMENTS

Firstly, I wish to thank my family for their unwavering support and confidence in me. I surely would not have succeeded in this endeavor without you all.

I also owe a great debt of gratitude to my secondary school science teacher, Mr. Brooks, whose engaging teaching, passion for science and keen sense of humor captured my interest and set me on the path to further pursue physics in academia.

My sincere thanks also goes to all those involved in the Robert T. Jones, Jr. Fellowship program, both at the University of St Andrews and Georgia Tech, the trust members and, in particular, Ashlee Toomey-Flinn, for her support and friendship over the years. The Bobby Jones Fellowship has offered an incredible opportunity to many students and provides an essential link between the 'Auld Grey Toon' and Atlanta.

The steep learning curve of starting doctoral research in astrophysics was greatly eased by insight and advice from Greg, Chris and James. Numerous stimulating, and often humorous, conversations about physics and everything else relating to being a graduate student provided much needed grounding and direction.

I also wish to thank everyone I've worked with in the VERITAS collaboration; a group of dedicated, kind, and highly intelligent scientists that welcomed me to their ranks and provided encouragement in the field, and in my studies. Any large undertaking is better made in good company; all the friends I've had the honor of knowing, both before and those made during this degree, have provided, equally important, encouragement and distraction, when called for.

I must also express my deepest gratitude, of course, to my advisor, Nepomuk: for guidance, patience, many illuminating discussions about astrophysics in general and, of course, an endless enthusiasm for wee chats about golf.

Finally, my heartfelt thanks to Julianne; without her care, support, hilarity and love, I would not be the person I am today.

All of the above individuals, and many more besides, have helped me along the journey of this degree that not only produced this thesis, but also, hopefully, a better scientist and human being.

TABLE OF CONTENTS

LIST OF TABLES

LIST OF FIGURES

SUMMARY

Years have passed since the first detection of pulsed very-high-energy (VHE; E >100 GeV) gamma-rays from the Crab pulsar with VERITAS, yet much is still unresolved in relation to the nature of pulsar emission mechanisms (see [1]) and how they interact with the surrounding medium.

No completely satisfactory model has been produced that can accurately describe all aspects of the pulsed gamma-ray emission observed from the Crab and other pulsars. Understanding the properties of VHE emission detected in observations made by many different experiments still poses a significant challenge to theoreticians, and hence experimentalists, working in the field. The crux of the issue remains; is the Crab pulsar unique[1], or do other pulsars also exhibit the same behavior in the VHE regime, and, in either case, what are the underlying mechanisms? To try and answer this question, while also learning more about the pulsar population and the physics of VHE gamma-ray production, this work will present the results of a search for pulsed emission in the VHE band from six Millisecond Pulsars (MSPs) in the archival VERITAS data-set, the first such survey of MSPs, and the most sensitive VHE measurements ever made for the targets. I test to see if significant pulsed emission is detected, report the observed VHE pulsed flux and gamma-ray conversion efficiency of these MSPs, to determine if there is an appearance of a VHE flux element at these energies, for the sources studied here. As the analyses result in non-detections, in every case, upper limits are placed on the aforementioned quantities. The upper limits are compared with a modern, comprehensive pulsar model energy spectrum and are found to be compatible with the proposed theoretical scenario, although we are limited by a lack of target-specific predictions. In addition, PSR J0030+0451 is proposed as a promising candidate for future study with CTA; as the limits placed here indicate that, with similar exposure and assuming a non-detection, CTA would likely produce flux limits that chal-

[1] Although not as 'canonical' as the Crab pulsar, there are confirmed pulsed VHE gamma-rays from one or two other pulsars (see section 5.1), as of writing.

lenge the scenario of $F = k_{Crab}\ \sqrt{\dot{E}}/d^2$ for the MSP population.

Pulsars are also sources of non-pulsed gamma-rays. However, at the time of writing, there has been no decisive detection of the TeV emission expected by current models from any pulsar tail that is also seen in the X-ray or radio bands. An observational campaign has been carried out by VERITAS to hunt for VHE gamma-ray emission from the candidate tail regions associated with three nearby pulsars (PSR B0355+54, PSR J0357+3205 and PSR J1740+1000) that move supersonically and exhibit significant X-ray tails. The results of this analysis provide quantification of the TeV flux and luminosity, from the tail regions of the targets, for comparison with other pulsar wind nebulae observations and the predictions of modern pulsar tail models. The results of this search also provide guidance for the selection of additional candidates, and quantifying the properties of pulsar tails, for new pulsars tails that may be observed in the VHE regime.

In order to analyze data from IACTs, such as VERITAS, detailed and extensive simulation works are necessary to understand the gamma-ray-induced EASs and the detector response. I will detail the work I undertook to produce the most modern and comprehensive simulation set for VERITAS to date.

In addition to the aforementioned research, that aims to further our understanding of pulsars in the VHE domain, in this document, I will describe my contributions to the building of the Cherenkov Telescope Array (CTA), the most sensitive IACT instrument ever constructed to observe the gamma-ray sky. As the timescales of such huge projects are so long, it is natural for researchers to work with an existing instrument (in this case, VERITAS) and help run and improve the experiment, along with analyzing data products, while also contributing to the building of future instruments, that build on the previous observatory's endeavors. The research, herein, will be the most up to date analysis of the target sources, and so provides the most modern insights into the nature of these objects, but also serves as an excellent guide for source-selection, and even the models to be tested, for future works. For example, the improved sensitivity that CTA will achieve, over the current

generation IACTs, will allow even deeper investigation of the pulsars studied here. Directly quantifying the standards that need to be met for the next generation of IACTs is a hugely important task and works, such as this one, aid in achieving this goal and also help bridge the gap between the generations of IACTs. This is an integral part of the evolution of the field and this thesis ties together the current era with the future research in the CTA era.

I will also include details on my contribution to a novel study of Lorentz-Invariance Violation and, hence, what we can learn about possible quantum substructure of space-time through VHE gamma-ray observations, via collaboration with the other major IACT groups.

Statement of Additional Contribution

As a member of the VERITAS collaboration throughout his PhD studies, the author of this thesis has made several contributions to the consortium effort, in terms of the advancement of the scientific goals, along with operation of the instrument itself and also representing VERITAS in two cross-collaboration studies (coordination of, and analysis of the data products from, joint observations of the Crab Nebula, along with providing the necessary source simulations for a Lorentz Invariance Violation study) with the two other main IACT collaborations, MAGIC and H.E.S.S.

While the primary focus of this thesis, and the research herein, is the investigation of the nature of pulsed emissions from MSPs and the interaction of SPWNe with their surrounding media, and the resulting emission seen, the author has also been an active member of the VERITAS collaboration, taking on numerous observing shifts at the VERITAS site in Arizona, operating the telescopes during data-taking, as well as participating in the 'start-up' shift on two occasions, which involves the re-cabling of the instrument and bringing it back online after the necessary shutdown for the summer monsoons. Also, the author has been an active member of the VERITAS 'Analysis and Calibration' working group, in particular, overseeing and managing the production of extensive simulations, on the Open Science Grid, necessary for the production of instrument response functions that are vital to data analysis. This contributed to being awarded the 'Simon Swordy Outstanding VERITAS Contribution Award'. "An award to recognize significant VERITAS service work completed by a graduate student"[2]. Along with contributing to commissioning and the upgrade from the initial camera of the pSCT, a novel telescope that aims to vastly improve upon the technology and capabilities of IACTs, and be a candidate for use in CTA.

[2]https://veritas.sao.arizona.edu/news/513-outstanding-2019

Thesis Outline

The following dissertation manuscript is organized as follows:

- Chapter 1 - In this chapter I give an introduction to the field of VHE astronomy & astrophysics, along with a brief foundational discussion of pulsars and observations of pulsed emission, as a basis for Chapter 2.

- Chapter 2 - This chapter contains a more in-depth insight into modern theory and models of the pulsar magnetosphere, and beyond, along with VHE gamma-ray production mechanisms and how they are thought to manifest in pulsar theory, and simulations.

- Chapter 3 - An overview of the physics of extensive air showers and Cherenkov radiation, with a short lead-in to the imaging atmospheric Cherenkov technique, is given in this chapter.

- Chapter 4 - In this chapter I give an in-depth narrative of the VERITAS instrument itself, operation and observational details and a description of the procedures for data analysis. In the final section of this chapter I discuss the simulation work necessary for the understanding of the instrument and data analysis, along with details of the latest full-scale VERITAS simulation project that I undertook on the Open Science Grid and GT computing clusters.

- Chapter 5 - This chapter describes the motivation, methods and results from a survey searching for pulsed emission that I conducted, through observations made with VERITAS, of MSPs in the VHE regime. This work is planned to be the focus of a publication that will be submitted in summer 2022.

- Chapter 6 - This chapter contains a mostly unedited reproduction of a journal article published in The Astrophysical Journal, that was led by myself, from the VERITAS

side, and investigates the extended tails of three nearby supersonic pulsars for any hint of VHE gamma-ray radiation, with collaboration from X-ray scientists.

- Chapter 7 - Details of my contribution to the construction and commissioning of a cutting-edge prototype Schwarzschild-Couder telescope for use as part of CTA, are found in this shorter chapter.

- Chapter 8 - In this brief chapter I give an overview of my efforts in a multi-collaboration working group studying LIV. My responsibilities were producing the simulation data-sets and coordinating as the VERITAS representative.

- Chapter 9 - This chapter contains some final conclusions and remarks of this thesis as a whole.

CHAPTER 1
INTRODUCTION AND BACKGROUND

In this chapter I will give an overview of the current field of gamma-ray astronomy along with a brief summary of the history that has led us to this point. I will also introduce pulsars, in context, as they will be the main focus of the content of this thesis.

1.1 The Field and History of Gamma-Ray Astronomy & Astrophysics

The field of gamma-ray astronomy has vastly evolved over the last several decades. Advances in theory, technologies and experimental technique, has furthered the study of the gamma-ray sky and, indeed, our universe towards the highest energies in the EM spectrum.

1.1.1 Cosmic-Ray Curiosity & Early Gamma-Ray Astronomy

Humans have always had a fascination with the sky above us; 'traditional' astronomy began with observations of optical light coming from the night sky, with radio astronomy following as the next band of the EM spectrum to be able to be studied well, as radio technology became more advanced.

The uncovering of cosmic 'rays', once thought to be radiation but now known to be highly energetic nuclei, brought about great curiosity regarding what kind of object(s) were responsible for producing these messengers with such tremendous energies, and where in the universe they come from, in relation to Earth. With origins in trying to understand these mysterious cosmic rays, detecting gamma rays on Earth, and hence studying the sources that emit them, has become a powerful tool for scientists to understand the wider universe, and particularly some of the most violent and energetic particle accelerators, along with their mechanisms for producing said highly energetic particles. As photons carry no electric charge, their path to us is 'straight', allowing us to trace the origins of gamma rays

back to the source linearly on the sky. Any particle that carries an electric charge is subject to its path being altered by the EM fields that are present in many areas in space, between stars and even in the regions between galaxies. Some of the most fascinating and mysterious objects in the observable universe produce photons in the High-Energy (HE: $\sim$30 MeV - 100 GeV) and Very-High-Energy (VHE: $\sim$100 GeV - 100 TeV) bands, giving an opportunity to study phenomena in ways that would not be possible in human-made experiments. Evidence of high-energy emission is a signature of an energetic source. This is because it must be powerful enough to overcome the substantial difficulty of producing a significant population of particles with enough energy to produce noteworthy gamma-ray radiation. Hence, it intrinsically draws interest to sources identified as such through their 'gamma-fingerprint'. Popular areas of study include black holes (AGN/blazars etc.), along with galactic objects; some of the most notable are pulsars and the nebulae they often reside in. Since the first detection of the Crab Nebula in the VHE regime, with the Whipple telescope, the number of identified gamma-ray emitters has rapidly expanded. Indeed, most of the identified galactic objects that are seen to emit VHE gamma-rays are pulsars (PSRs) and pulsar wind nebulae (PWNe).

In the late 1940s and early 50s, several prominent scientists (see [2], [3], [4], and references therein) produced works showing that several mechanisms were possible for creating gamma rays, and that they likely existed in nature. The varied proposals for possible emitters of HE photons included supernovae, cosmic-ray scattering and radiation from electrons, accelerated in magnetic fields. Here, the experimental prowess lagged the theory, and it was over a decade before any such gamma rays were detected.

Gamma rays are most likely to interact in the atmosphere of our planet to produce a shower of many particles, meaning that few, if any, gamma rays make it to sea level and so these early detections involved balloon experiments (similar to the first measurement of ionization in the atmosphere, due to cosmic-rays, by Victor Hess in 1912, in his famous balloon experiment) to bring the detectors to a suitable altitude to directly measure them. Satellite-

based gamma-ray telescopes followed over the years, initially detecting a homogeneous 'gamma-ray background' from the universe. This implied some directionally-independent mechanism, now known to be the scattering of cosmic rays from interstellar material. The first sources of more localized gamma-ray radiation were identified by the mapping produced by the SAS-2 and COS-B telescopes. On top of the homogeneous gamma-rays seen before, these experiments were able to see coincident radiation originating from a very confined area on the sky. These were the first glimpses of 'point-like' sources of HE photons.

1.1.2 Advancements in the Field and Technology

As is often the case, technology designed for a completely unrelated purpose was the source of great intrigue and interest at the turn of the 1970's, when satellites that were designed to keep watch on international nuclear bomb tests also saw brief flashes of gamma rays with directionality that meant they must be of extra-terrestrial origin. It took several decades to correctly identify the source of these 'eruptions' of gamma-rays as GRBs, from violent events outside the Milky Way.

Space-Based Gamma-Ray Astronomy

In the last $\sim$13 years the *Fermi* satellite's 'Large Area Telescope' (LAT), and 'Gamma Burst Monitor' (GBM), have been the defacto focal point of space-based gamma-ray detection. But, prior to the satellite's launch, the Compton Gamma Ray Observatory (CGRO) was the premier space observatory, launched in 1991 and operating until the turn of the century. The Energetic Gamma Ray Experiment Telescope (EGRET) aboard the CGRO successfully produced quantifiable measurements of the HE sky. However, as is predicted in theory and experimentally seen, the resulting energy spectrum from the relativistic particles, that produce the observed gamma-ray emission, often follows a power law distribution; meaning that the number of gamma rays decreases as a function of energy. So while

'small'[1] telescopes like the LAT can detect a significant number of gamma rays in the HE range, a much larger detector area is needed to build up events at higher energies, as to be able to reliably quantify emission in the VHE regime.

Ground-Based Gamma-Ray Astronomy

The development of the Imaging Atmospheric Cherenkov Telescope[2] (IACT) has allowed the indirect measurement of gamma rays arriving at Earth. The method employs measuring the radiation produced from the cascade of 'secondary' particles, that are created in the atmosphere by the primary gamma-ray, bypassing the need for the detector to leave the atmosphere. This ingenious technique capitalizes on the large interaction cross-section[3] for a VHE gamma-ray in the atmosphere, to essentially use the atmosphere as a large target for the VHE photons. This results in an effective area of over ten-thousand times that of the LAT. The brief flashes of blue-ish light seen on the ground are comprised of 'Cherenkov' photons, emitted by relativistic electrons & positrons that move faster than the speed of light in the medium. The primary electron/positron pair are produced from the initial gamma-ray interacting with an atmospheric molecule. Secondary pairs are also created by emitted bremsstrahlung photons, as the extensive air shower (EAS) progresses through the atmosphere. The evolution of the conglomerate of particles, along with the swathe of radiation they produce, is highly complex in form but all the underlying processes are well understood. The eventual Cherenkov light, produced by particles that move superluminally[4], can be used as a basis to 'work back' to the gamma ray that initiated the whole process. Detailed simulations are needed to model this process, but the technique is powerful and robust; the energy and direction of the incident gamma-ray can be accurately calculated and the background due to unwanted light in the telescopes, or from cosmic-ray induced

[1] Small in the context of ground-based telescope sizes.

[2] Or 'Technique'

[3] The high probability for an incident gamma ray to scatter with atmospheric molecules was historically problematic, when experiments were trying to directly detect gamma rays on the ground.

[4] Again, relative to the speed of light in the medium in question, not vacuum.

showers, can be rejected with high efficiency. The final 'pancake' of light detected on the ground by the IACTs lasts less than 10ns. The 'pool' of photons is typically around 250m in diameter for a typical 1 TeV gamma-ray. The resulting ability to detect gamma rays in the range of tens-of-GeV to tens-of-TeV, given good observing conditions, has meant that these ground based experiments work well in tandem with space-based telescopes and can study selected sources for long exposures and take regular scheduled data. This has allowed scientists to expand the catalogue of known gamma-ray sources and extend the energy range that can be probed to measure spectra into the TeV regime.

1.1.3 The Modern-Day and Beyond

Three major IACT collaborations are currently operating: VERITAS (as featured in this work) is located close to the Mexican border in southern Arizona, USA; MAGIC, also in the northern hemisphere, is hosted on the Canary Island of La Palma; and, finally, H.E.S.S. which is located in the Khomas Highlands of Namibia, in the southern hemisphere. All three experiments operate on the same principle, and similar technologies, but have design differences that lead to slight variations in performance strengths and weaknesses. Given the different geological locations on Earth, and hence the different parts of the sky seen, the collaborations often join forces in attaining scientific goals.

Containing scientists involved with all three of the aforementioned collaborations, The Cherenkov Telescope Array (CTA) consortium plans, and is in the process of building, two massive observatories with vast arrays of state-of-the-art telescopes, with cutting edge designs and modern cameras. This will create amazingly sensitive instruments and take the age of ground-based gamma-ray astronomy to the next level; allowing observations at an unprecedented level of sensitivity and detecting sources that have proved elusive in the past.

1.2 Pulsar Background

1.2.1 Supernovae & Neutron Star Formation

Neutron stars are the remnants of massive stars, formed in the violent collapse of their progenitor supergiant star (of mass 10-25 $M_{\odot}$, depending on its metallicity) at the end of their main-sequence lifetime. After the star has used most of its light-element fuel for nuclear fusion, the only available nuclear processes, of fusing heavier elements, begin to consume more energy than they release. This leads to the loss of outward thermal pressure and, therefor, gravitational collapse. As the stellar material increases in density and temperature, heavier elements can be fused and hence even heavier elements produced, eventually leading to an iron-rich core of the star. This process repeats until there is little fusion able to occur and the outward pressure, from nuclear processes releasing binding energy, is completely overcome by gravity. At this point a core-collapse is imminent and, resultantly from the energy released during this final collapse, a supernova occurs, releasing vast amounts of energy in a relatively short time. This type of core-collapse supernova is known as either a type Ib, Ic or II supernova, classified by their light curves and spectral absorption lines, due to the mechanisms involved and their progenitor type. For example; the stars that lead to type Ib/Ic supernovae are Wolf-Rayet stars, which are massive stars that have not retained their exterior hydrogen layer. Type II supernovae are usually from supergiant progenitor stars.

On the other hand, type Ia supernovae are due to a different 'evolutionary path' of the progenitor star: if a remnant white dwarf gains new mass, either from accretion from a partner giant star or main sequence star, or from the merger of two degenerate white dwarfs, a 'thermal runaway' period of carbon/oxygen fusion occurs and heavier elements are produced in a very short period (believed to be only a matter of several seconds [5]) the rapid and significant increase in temperature completely disrupts the constituent material.

The remnant white dwarf from the core of less massive stars can further collapse un-

der the immense gravity, if a new equilibrium is not achieved. The electron degeneracy pressure that supports white dwarfs is due to the nature of fermionic matter and the Pauli exclusion principle. As no two identical fermions can occupy the same quantum state, there is a resultant spatial 'repulsion' that the, in this case, electrons feel, due to their wavefunctions overlapping in space with that of other fermions. This 'degeneracy pressure' aids in balancing the inwards force of gravity as the outwards pressure can counteract the compression of the matter into a smaller space. This is explained by the need for the fermions to occupy higher and higher energy levels as more fermions are added to a compact system. This requires additional energy input as the particle density increases and so if the gravitational energy release from said compression is not sufficient to offset this cost, the result is a resistance to the decrease in size and increase in density. However, if the mass of the white dwarf is not less than the Chandrasekhar limit ($\sim$1.4 $M_{\odot}$ = 2.765 x 10^{30} kg) then electron degeneracy pressure is not enough to overcome the force of gravity. In this case, the gravitational energy is enough to force the combination of electrons and protons into neutrons (and an electron neutrino) in a process known as electron capture (or inverse beta decay). This mass of neutrons only survives further collapse by neutron degeneracy pressure and repulsive nuclear forces [6] [7].

The outer layers of the star, that initially fall towards the center of gravity, are violently accelerated outward by the massive neutrino flux that is the by-product of the neutron formation from electrons and protons, causing a supernova event. The front of shocked stellar material spreads into the surrounding gas and dust, creating the supernova remnant that surrounds the leftover core object. The incredibly dense neutron star (NS), roughly as dense as an atomic nucleus, formed is of the order 1.4 solar masses (also known as the 'canonical neutron star mass') and has typical diameter of about 20km [8]. For more massive remnants, above the Tolman–Oppenheimer–Volkoff limit[5] of around 2 solar masses [9], further collapse is unavoidable and the core continues to collapse under gravity, forming

[5] Analogous to the Chandrasekhar limit for white dwarfs.

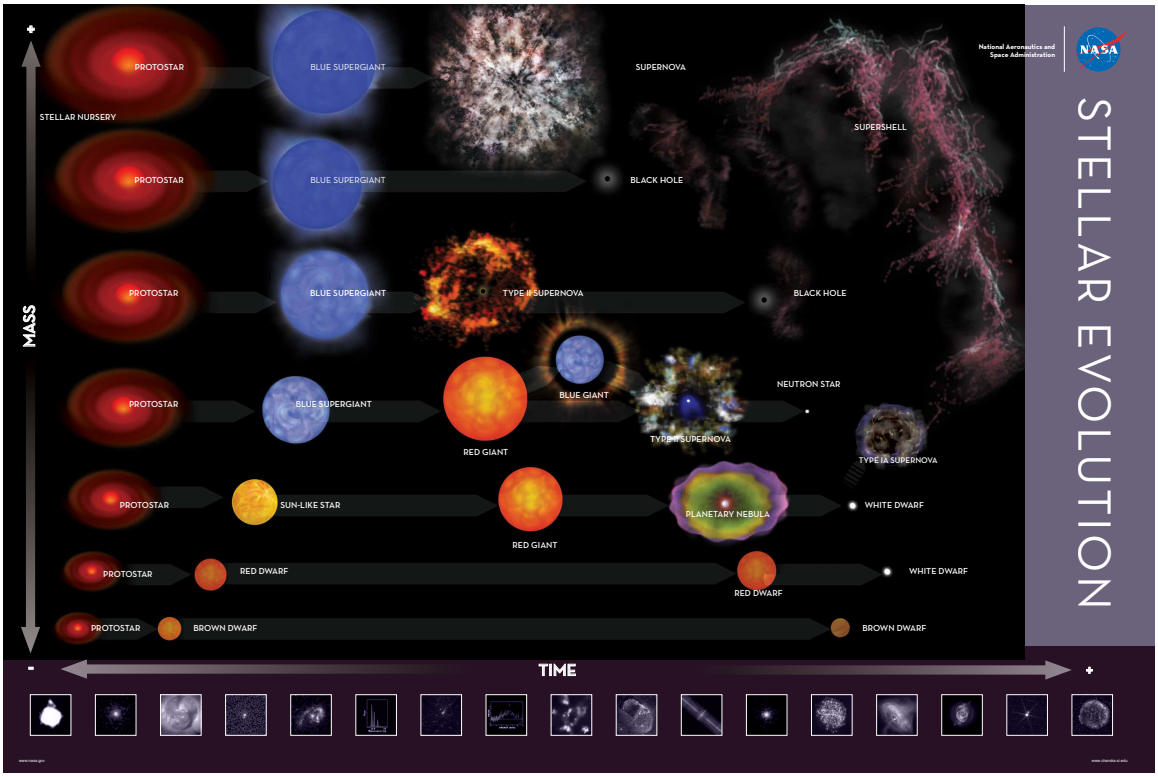

Figure 1.1: A chart showing the possible evolution routes of stars of different masses, from https://chandra.harvard.edu/edu/formal/stellar_ev/. Image credit: CXC.

a black hole. This is because the short-range neutron-neutron repulsion, mediated by the strong nuclear force, that contributes, along with the Pauli exclusion principle for the neutrons, to neutron degeneracy pressure, is eventually overcome by the immense gravity of the body, forming a spacetime singularity. Black holes and neutron stars form the category of the densest known 'family' of objects in the universe, with only some, purely theoretical, entities that could come close to their relatively compact size and large mass.

1.2.2 Neutron Star and Pulsar Characteristics

Neutron stars do not undergo further fusion processes, as their parent star did. Hence, the energy that they are formed with only dissipates, through various processes, unless matter, from a companion star or gas cloud, for example, is accreted onto the neutron star[6].

[6]Or the rare event of a neutron star merging with another compact object, as observed with LIGO gravitational wave observations.

Exhibiting extreme properties; neutron stars have typical surface magnetic field strengths of between 10^4 T and 10^{11} T (see [10] and references therein) and have archetypal surface temperatures of around 600,000K. The mechanical properties of newly formed neutron stars are truly staggering. Given that the size of the star has collapsed to roughly the size that it's core was, and hence the moment of inertia of the remnant decreases drastically too, the rotation rate of the remnant is increased immensely. This is expected, due to the conservation of angular momentum, and newly born neutron stars can have rotational periods of only a few milliseconds. Estimates of a newly-formed neutron star's rotation rate and surface magnetic field strength can be attained by applying conservation of angular momentum:

$$M_p \, R_p^2 \, \Omega_p \; = \; M_{ns} \, R_{ns}^2 \, \Omega_{ns} \tag{1.1}$$

and magnetic flux;

$$B_p \, R_p^2 \; = \; B_{ns} \, R_{ns}^2 \tag{1.2}$$

With 'p' and 'ns' denoting the properties of the progenitor and neutron star, respectively; the radius, R, is greatly reduced after the collapse of the progenitor, and so (with some change in the mass, M, certainly) the rate of rotation, Ω, and surface magnetic field strength, B, increase by a factor of $\approx \left(\frac{R_p}{R_{ns}}\right)^2 \approx 10^{10}$.

The NS Interior

Neutron stars are thought to be comprised of layers of different materials, of differing composition and density, on and below its surface. The surface and outer crust of the neutron star is understood to be mostly atomic nuclei forced into a rigid lattice with a free-flowing population of shared electrons. Due to the immense gravitational pressure the outer crust is confined to being exceptionally smooth, as any deviations from the lowest energy gravita-

tional state, due to some deformation, would be immediately corrected by gravity. Delving deeper into the interior of the star the number of free neutrons rises, along with the neutron number density. The exact nature of the matter inside the neutron star is not understood well, although some theory exists describing the formation of depth-dependent structure colloquially known as nuclear 'pasta'(see [11] for a 'yummy' take). To form a full equation of state for the central matter the interplay between magnetohydrodynamics, superconductivity, superfluidity and even quantum chromodynamics, would need to be fully understood and applied. We do not currently have the theoretical tools to do this.

NS Radiation and Pulsar Classifications

A subset of the neutron star population emit EM radiation than can be detected. When the axis of rotation and the magnetic axis of the neutron star is misaligned[7] the emission is beamed across the sky, as in the classic 'lighthouse analogy', and so can be seen from many positions in space as the beam sweeps the observer, resulting in seemingly pulsed emission. If this is not the case one must get lucky and the observers location must be looking 'down the barrel of the gun', directly at one of the poles[8] and hence the emission zone.

Neutron stars can also be seen in binary systems, where the signature X-ray emission observed is due to matter being accreted onto the neutron star. The gravitational potential of this matter is given off in the X-ray band (known as 'accretion-powered pulsars). Accretion from a companion object is thought to be how older neutron stars can be seen with such fast rotation rates; the angular momentum of the matter falling on to the neutron star increases its angular momentum, leading to a 'spin-up' or 'recycling' of neutron stars. This is how the so-called 'Millisecond pulsars' (MSPs) are thought to be formed (see Chapter 5 for details on the MSP study), as the 'final form' of binary systems.

Pulsars (PSRs: a portmanteau of 'pulsating radio source'), rapidly-rotating neutron

[7]The magnetic poles of the neutron star determine much of the geometry of the emitted particle population, and hence their emitted radiation.

[8]Depending on what energy range one is looking for, see section 2.3.

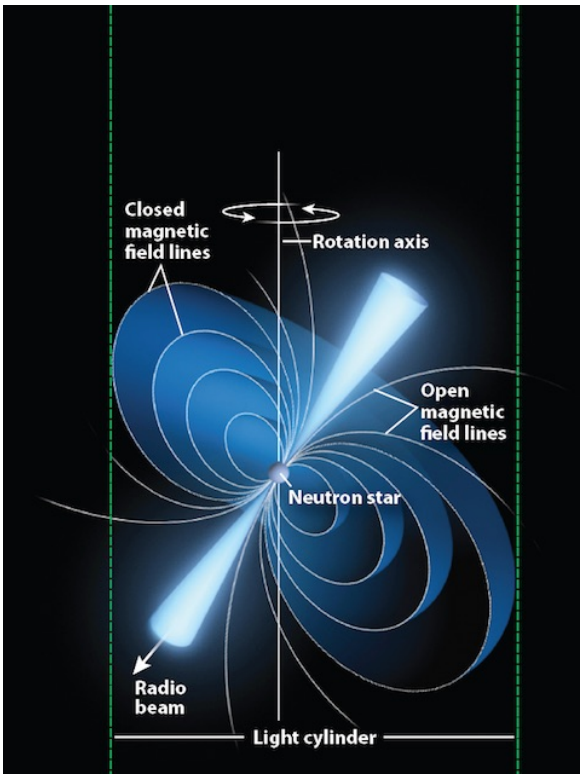

Figure 1.2: This diagram shows a simple model of the field lines around the pulsar, and the light cylinder. The radio emission is depicted as a cone aligned with the magnetic poles. Also depicted is the outer magnetic field lines that cannot close, as they are limited by the maximum propagation speed of the EM field but would need to move superluminaly to reconnect. From https://astronomy.com/magazine/ask-astro/2018/06/radio-waves-from-pulsars

stars with misaligned rotational and magnetic axes, offer an excellent opportunity to study particle acceleration in 'astrophysical laboratories'. The particle outflow, generally dubbed the 'the pulsar wind', is highly energetic. It is fueled by the phenomenal 'spin-down' energy transferred from the pulsar's immense rotational angular momentum, as the pulsar slowly spins slower and slower over very long timescales (dubbed 'rotation-powered PSRs'). In accordance with Maxwell's equations; the rapidly changing magnetic field creates a very strong electric field, that strips particles from the neutron star's surface and accelerates them. The magnetic field lines generated by the pulsar remain closed up to a certain radius, called the 'light cylinder', defined as the distance at which the co-rotating plane moves at the speed of light. At distances greater than this, the field lines cannot close.

A third type of pulsar class is known: the magnetar. These types of object are powered by the decay of an incredibly strong magnetic field, orders of magnitude stronger than even that of rotation-powered pulsars. Although these three families of objects are all neutron stars, the mechanisms for producing the emission seen and the physics responsible for their behavioral characteristics are unique. However, during different situations and times of their life, neutron stars can belong to different categories. For example; in its 'old age' an ancient rotation-powered pulsar might have radiated away most of its angular momentum, but might start accreting matter from a companion, and begin emitting X-rays as a binary system. Eventually, in the above scenario, angular momentum can be transferred back to the pulsar and it can reach a very high rotation rate, entering into the category of the MSPs. There are many such scenarios that can occur given different systems of objects, various initial conditions, and time for the system to evolve. MSPs seem to exhibit a much weaker surface magnetic field than the regular pulsar population. This is thought to be due to the accreted matter screening part of the total magnetic moment of the neutron star, as the new material does not necessarily follow the same magnetic alignment as the original neutron star material.

Pulsar Timing

Many pulsars exhibit incredibly regular rotational periods, and so can be used in many ways as 'astronomical clocks', for various studies of general relativity, for example. MSPs seem to have particularly low spin-down rates, and so are particularly apt candidates for such studies. However, observations have been made where abrupt changes to a pulsar's spin frequency have been seen, changing from one regular period to another, almost instantaneously. This can lead to additional parameterization needed to analyze data: see section 5.3.1). This phenomena is not well understood, but could be a possible result of a 'star-quake', when the outer crust of the neutron star suddenly shifts under gravity to a new, lower potential state. Other possibilities exist, where the 'glitch' (so-called as it is an unforeseen interruption to regular, expected, behavior) is caused by superconducting-superfluid material, that forms the interior of the neutron star, either coupling to (or decoupling from) other layers in the star, that usually rotate at a different rate. Regardless of the underlying mechanism, a change in inertia occurs and, consequently, a different rotational period results. Over time the rotation rate usually returns to its 'pre-glitch' state. Such events have been studied for the Crab and Vela PSRs.

1.2.3 The History of Pulsar Discovery and Study

The history of the evolution of our understanding of pulsars is an interesting topic in it's own right. The first regularly-repeating pulsed emission seen was so remarkably periodic it was thought that its only explanation could be that of extra-terrestrial life and their technology (leading to the first source, which later was confirmed as a pulsar was dubbed 'LGM-1', for 'Little Green Man 1'). Initially working in a group studying quasars, in 1968, Jocelyn Bell Burnell found, on the paper charts that were used at the time, startlingly regular periodic radio waves [12]. At the time there was no certain explanation for the regularity of the emission seen, Bell's co-workers were convinced that the periodicity seen in the data must be due to some interference or noise in the signal, as even the neutron star was still

an unconfirmed theory at the time. Now known as PSR B1919+21, this was found to be a rapidly rotating neutron star. Later the same year, one of the most famous objects in all of astronomy, the Crab Nebula, was confirmed to play host to another rotating neutron star, the Crab Pulsar. This fit with the observations that the Crab Nebula was actually increasing in size and one possibility for this was put forward by Pacini; that the emission expected from a pulsar rotating at such a rate could fuel the development seen [13]. Gold's work [14], in the same seminal year, has remained the cornerstone of our understanding of the nature of pulsars ever since.

1.2.4 Detection of Emission: Steady and Pulsed

Synchrotron radiation from Pulsar wind nebulae and synchro-curvature radiation from the pulsars themselves, spans lots of the electromagnetic spectrum. The synchro-curvature component is expected to be radiation-reaction suppressed at an energy of a few GeV, leading to an expected 'cutoff' far below the IACT detections above 100 GeV. Hence, an invocation of a new component to the emission spectrum is needed and it is thought that PWN are also seen at high GeV and TeV energies due to Inverse-Compton (IC) 'up-scattering' of a photon seed field by charged particles, in the Klein-Nishina [15] regime.

With the only VHE pulsed emission detected from the Crab pulsar, (with VERITAS [16] and MAGIC [18] [17]), and some more recent claims from H.E.S.S on the Vela pulsar [19], the search for other candidate sources of pulsed VHE emission is ongoing.

This work will focus on the fastest-spinning pulsars; thought to have been spun up or 'recycled' by ablating their stellar companions. Typical MSPs exhibit rotational periods of tens of milliseconds. Their characteristic ages (τ) , derived from the pulsar's period (P) and spin-down rate ($\dot{P}$) are typically greater than one billion years.

$$\tau = \frac{P}{2\dot{P}} \tag{1.3}$$

With more compact magnetospheres than the 'regular' pulsar population, due to the

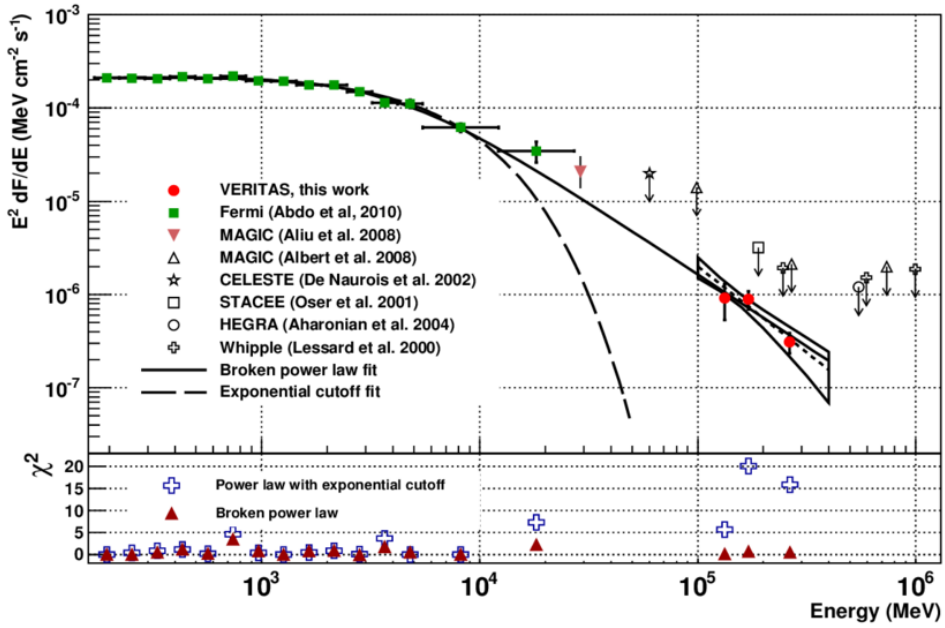

Figure 1.3: The VERITAS Crab Pulsar Spectral Energy Distribution (SED) from [16]. Spectral points are also shown from other gamma-ray detectors for comparison. The broken power law fit is clearly favored, over the exponential cutoff, for measurements with the IACTs.

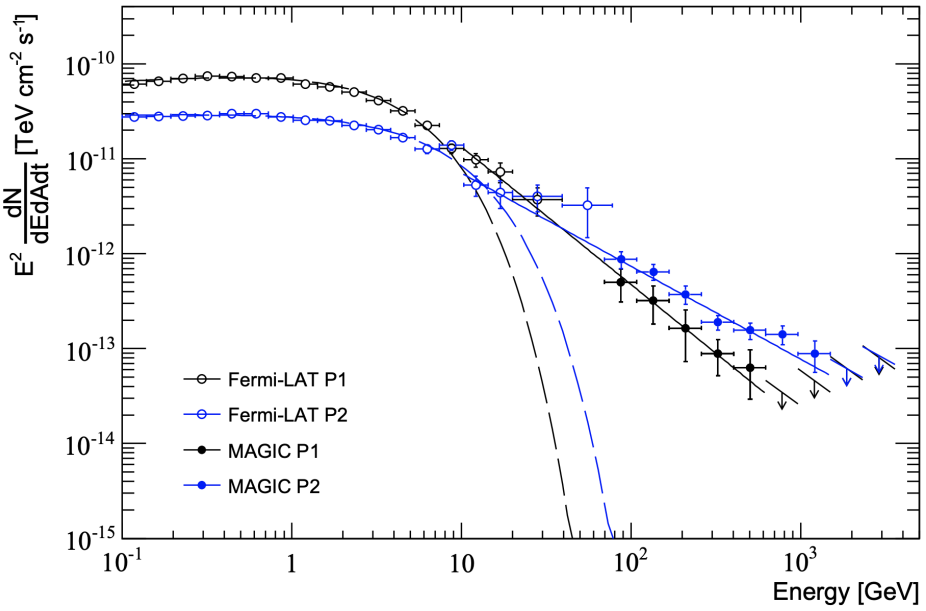

Figure 1.4: The joint *Fermi*-LAT - MAGIC spectral energy distributions for each individual peak in the Crab PSR phaseogram [17]. Power-law fits to the $E > 10\ GeV$ data points are shown in solid lines. ULs at 95% CL are shown as arrows.

constraint on the size of the light-cylinder by the high rotation rate, MSPs offer an alternate type of probe into the emission mechanisms [20] . It is theorized that older, more rapidly rotating pulsars may also be more efficient at converting their spin-down power,

$$\frac{dE_{rot}}{dt} \equiv \dot{E}$$

into gamma rays [21] (see [22] and references therein) and, therefor, may be good candidates to probe VHE pulsed emission with ground based IACTs.

1.2.5 Current Unknowns and Present-Day Research

Until recently [19], the Crab pulsar has been the only source of pulsed VHE emission to challenge the 'curvature radiation' scenario, where the spectral shape from pulsars is thought to have a cut-off, so that the highest energy emission is naturally limited to a few GeV [25]. Currently, the observed lightcurve and spectrum cannot be simultaneously de-

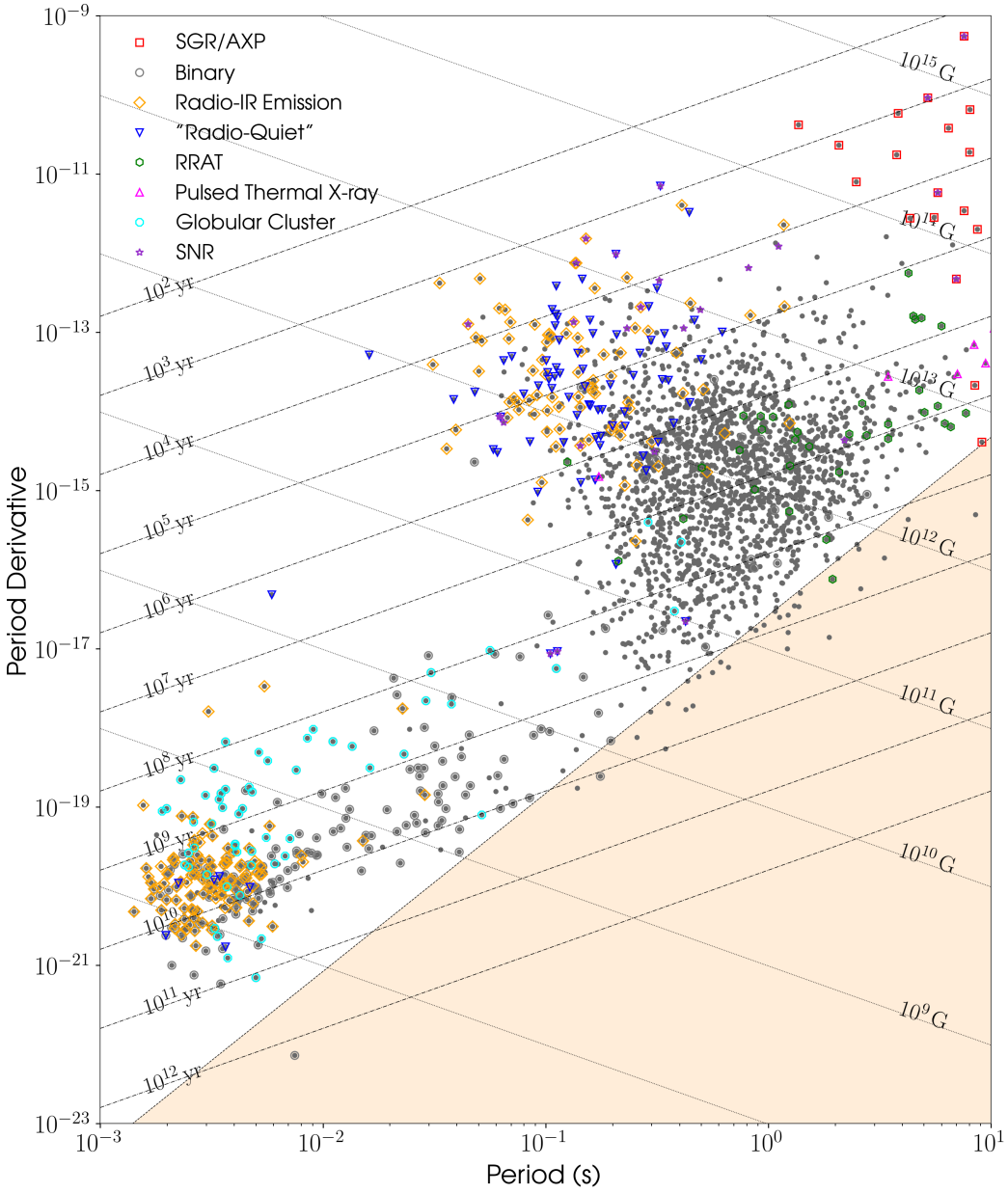

Figure 1.5: The ubiquitous '$P - \dot{P}$' plot: showing all known pulsars from the ATNF Pulsar Database [23] the data was extracted and formed into this plot using the Python package 'psrqpy' [24]. Lines of constant characteristic age and surface magnetic field strength are shown. The 'regular' pulsar population is shown in the mid-upper right, while the MSP population is in the lower left.

rived from models of the Crab PSR (see [26]), unlike the successful modeling done for *Fermi* PSRs [27]. It is of great interest and import to further study the pulsar population for more evidence in support of, or in aversion to, an inverse Compton (IC) component explaining observations. To study the validity of an IC component, that could well model the VHE Crab emission [28] [29], my work will provide quantification of the VHE pulsed flux observed from the MSPs. The analysis results will also provide the conversion efficiency seen in these MSPs, possibly constraining theoretical predictions on emission. Further investigation of any type of pulsar is of import to the direct field, and other areas of physics as well; as the detection of even a single new VHE pulsar could provide vital information in furthering our understanding of these cosmic particle accelerators. In addition, study of such extreme objects and their unique environments might glean unique insight into more exotic processes, such as quantum processes in powerful magnetic fields (see, for e.g., [30] [31]) and more generally allow testing of gravitational and electromagnetic theory in a way that would not be possible in a collider experiment.

The six MSPs presented in this work were selected as part of the VERITAS 'Long Term Plan', based on their spin-down luminosity[9], and their RA band, as to fit with competing observations of other sources. The candidates also all exhibit optical or X-ray emission from either within their own magnetosphere or, at the very least, the direct vicinity of the source[10]. Each target was assigned 20 hours of observations but only some come close to the projected observation time for a variety of reasons; bad weather, conflicting ToOs etc. A survey of these six MSP sources was proposed to be the first comprehensive VHE survey of MSPs, between several-hundred GeV and tens-of-TeV, and hence provide crucial information for guiding and constraining VHE pulsar emission models.

[9]The spin-down luminosity of each pulsar is scaled by the inverse of the square of their distance from Earth, a standard metric for the predicted observable flux.

[10]This criteria is included as it confirms there is a population of lower-energy photons to undergo IC processes.

CHAPTER 2

GAMMA RAY PRODUCTION AND THE PHYSICS OF PULSARS

In this chapter I will detail our current understanding of the mechanisms that lead to the emission of VHE photons from pulsars, along with the underlying physics of said neutron stars and their magnetospheres, which are of interest in this thesis.

2.1 Photon Production Mechanisms

The broad-band emission seen from pulsar magnetospheres[1] is produced through three main processes; synchrotron radiation (SR), curvature radiation (CR), and inverse-Compton (IC) scattering. The plasma in the magnetosphere of pulsars is accelerated, and the relativistic particles produce radiation in several ways, that are detailed in the next sections. Emission of synchrotron photons produces radiation from the radio band through to the low-energy gamma-ray regime, while the production of curvature photons can continue higher in energy, up to a few GeV[2], into the HE band[3]. Gamma rays with energy higher than this are not directly created by emission, but instead lower-energy photons can be boosted to higher energies by scattering with relativistic electrons [29] [32]. It is worth noting that almost all of the radiation observed that is caused by particle acceleration in pulsars comes from the electron/positron population as they are accelerated more than any heavier, and more rare, particles.

[1] From both young pulsars *and* MPSs

[2] Perhaps even tens-of-GeV in the ECS [32]

[3] This is because of the limit on the available radius of curvature of the magnetic field, in the pulsar magnetosphere, due to it's physical size being constrained by the light cylinder. To produce VHE photons the radius of curvature would have to be at least an order of magnitude greater.

2.1.1 Synchrotron Radiation

As follows from Maxwell's equations; if a charged particle, moving at relativistic velocities, has a component of its acceleration in the plane perpendicular to its velocity, it will radiate synchrotron photons. This emission is beamed in a conical geometry, oriented on the particle's velocity vector direction. If the particle is moving at velocity, $\mathbf{v}$, with Lorentz factor

$$\gamma = \frac{1}{\sqrt{1 - \frac{v^2}{c^2}}}$$

then the opening angle of the cone in which the synchrotron emission is beamed into is γ^{-1}. Hence, the more relativistic the particle's motion, the more tightly beamed the synchrotron emission cone appears to an observer. The synchrotron mechanism is the relativistic analogue to cyclotron radiation and is mechanistically similar to bhremsstrahlung radiation (which occurs when the acceleration component is parallel to the particle's velocity, see the section on CR, below).

For a single particle emitting synchrotron radiation (SR), an observer would see a time-varying pulse, with characteristic frequency;

$$\omega_B \equiv \frac{|\mathbf{v}_\perp|}{r} = \frac{eB}{\gamma m_e c}$$

as the particle moves in a helical motion around the magnetic field line and the emission beam moves into and out of the line of sight, depending on the geometry of the situation. The overall synchrotron component from astrophysical sources is seen as a non-pulsed[4], continuous spectrum as the population of radiating particles move asynchronously with each other and are likely of differing energies, following some overall particle population energy distribution (a power law is a common occurrence). From the relativistic Larmor

[4]Non-pulsed in the sense of the helical motion of the emitting particles. Clearly, with the example of the pulsar, the overall emission may be pulsed due to macroscopic rotational motion.

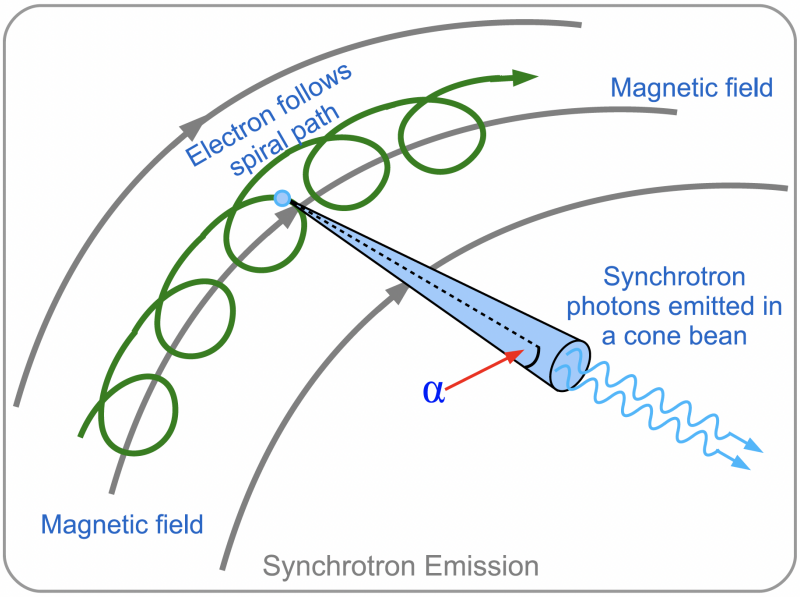

Figure 2.1: A cartoon representation of a lone particle emitting SR in a weak magnetic field. Shown in green is the helical path of the electron around the magnetic field line. From [33].

formula, the power of the emission is given by;

$$P(\gamma) = \frac{1}{6\pi\epsilon_0}\frac{q^2a^2}{c^3}\gamma^4$$

The power spectrum seen from pure SR follows a power law up to a critical frequency, $\nu_c \sim \gamma^2\nu_L \approx \gamma^2\frac{eB}{2\pi mc}$, where ν_L is the Larmor frequency. Above ν_c, the power spectrum follows an exponential cutoff, rapidly limiting emission beyond this point.

2.1.2 Curvature Radiation

In the presence of a strong magnetic field, the charged particles are restricted to more tightly confined paths: following the field lines closely. The given gyroradius (which leads to the helical motion in the synchrotron case), varies inversely with the magnetic field strength and so, in areas of a strong magnetic field, confines the particles to motion parallel to the overall large curvature-radius field lines. In such a case, any orbital momentum

causing motion around (i.e. transverse to) the magnetic field lines is rapidly radiated away as synchrotron photons, on a timescale of;

$$\tau_{synch} \approx \frac{c}{\omega_B^2 r} \approx 10^{-15} s$$

until the particle reaches the lowest allowed, quantized, cyclotron energy state (known as 'Landau Levels'). The allowed energy levels are [34]

$$E_n^{Landau} = \sqrt{\left(p_\parallel^2 c^2 + m_e^2 c^4 \left(1 + (2n + 2s)\,\frac{B}{B_c}\right)\right)}$$

where n and s are the quantum numbers associated with the occupied energy level and particle spin, respectively. Now, the charged particle will only have an acceleration component in the plane of the magnetic field curvature, and so primarily[5] emits CR. The energy of the curvature photons

$$E_{curv} = \hbar\omega_{curv} \approx \frac{\hbar c}{R_{curv}} \left(\frac{E_e}{m_e c^2}\right)^3$$

where R_{curv} is the radius of curvature of the magnetic field line in question.

This mechanism can be seen as a different, but related, facet to SR, in a strong-field limit. SR and CR have many similarities in their characteristics, for example, following the same spectral shape of $P(\nu) \sim \nu^{1/3}$ below the cutoff frequency, and an exponential cutoff at higher frequencies, beyond the cutoff frequency [29]. The cutoff frequency is defined in terms of the local radius of curvature of the trajectory, R_{curv}, as; $\nu_c = \frac{3c}{4\pi R_{curv}}\gamma^3$ The curvature photons are beamed tangentially to the radius of curvature that the particle follows, again, with an opening angle γ^{-1} [36]. CR exhibits a spectrum that extends to higher energies than the synchrotron photon population, but is limited by the maximum-energy of the radiating particles, which is not sufficient to create VHE photons in pulsars,

[5]Particles can absorb radio photons that are seen, in their rest frame, as being at the cyclotron resonant frequency. This can influence the pitch angle relative to the magnetic field line it follows, and excite it to a higher Landau level, therefor allowing for further SR. See [35].

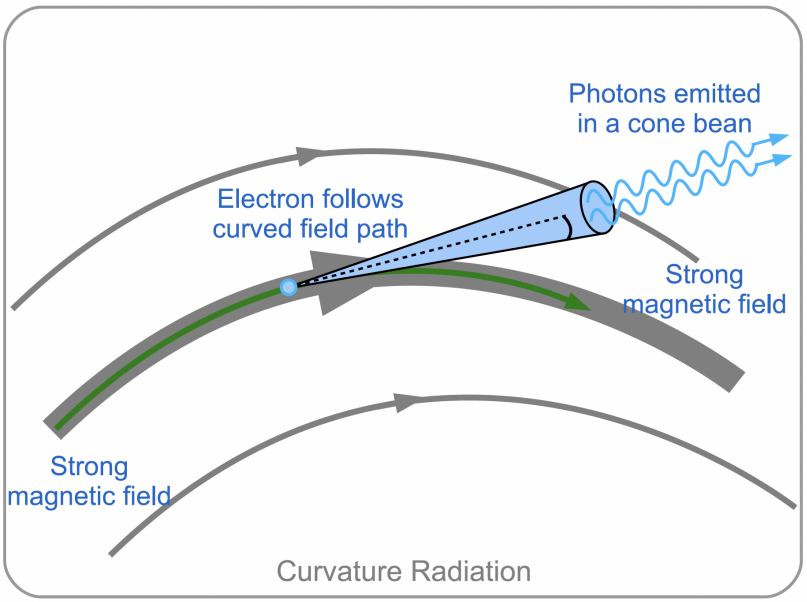

Figure 2.2: A cartoon representation of a lone particle emitting CR in a strong magnetic field. The electron is confined to a path (green) closely following the curvature of the magnetic field line. From [33].

as discussed below.

Radiation-reaction limit

The radiation from a charged particle carries both energy and momentum. In order to jointly satisfy energy and momentum conservation, the charged particle must experience some recoil at the time of photon emission. This 'kick', a necessary additional force on the charged particle, is known as the Abraham–Lorentz–Dirac force, in relativistic scenarios:

$$\mathbf{F}_{total} = \frac{d}{dt}\left(\gamma m_e \mathbf{v}\right) = q\left(\mathbf{E} + \mathbf{v} \times \mathbf{B}\right) + \mathbf{g}$$

where $\mathbf{g}$ is the recoil force felt by the electron, due to radiating synchro-curvature (SC) photons, as defined by the Landau-Lifshitz formula [37]. As a particle is accelerated more and more and therefore emits more and more CR, there exists a limit at which the energy

gain is balanced by the energy loss due to CR. Equating the accelerating and recoil forces:

$$e|\mathbf{E}_{\|}| \approx \frac{e^2\gamma_{max}^4}{R_{curv}^2}$$

This is known as the 'radiation-reaction' limit (see [38] and references therein for a nice discussion). The energy 'ceiling of the curvature-radiating accelerated particles is then

$$E_{max} = m_e c^2 \gamma_{max} \approx m_e c^2 \left(\frac{R_{curv}^2 |\mathbf{E}_{\|}|}{e}\right)^{1/4}$$

and so photon production, along with electron energy loss, per time, follows: $\dot{\gamma} \propto \gamma_{max}^4 \propto |\mathbf{E}_{\|}|$ [39].

2.1.3 Inverse-Compton Scattering

Inverse Compton (IC) scattering is a specific process in which a photon and a charged particle (an electron/positron) interact and the photon is boosted to higher energy, absorbing momentum from the charged particle. It is a very important mechanism for the production of the highest-energy gamma rays, particularly in pulsars, as the radiation-reaction limit places an upper bound on the photon energy produced from CR. IC processes, involving ultra-relativistic electrons (and positrons) and soft seed photons, are thought to be the main channel that can bypass this limit and produce detectable VHE radiation.

In their seminal work, Blumenthal & Gould [15] derive, with simple relativity, kinematics, and energy conservation, the relationships governing such scattering processes. In the rest frame of the electron, the incident photon energy E_γ^I, is boosted to;

$$E_\gamma^S = \frac{E_\gamma^I}{1 + \frac{E_\gamma^I}{m_e c^2}(1 - cos\phi)}$$

where ϕ is the scattering angle and the superscript S denotes the scattered photon.

When considering ultra-relativistic particles, such as those accelerated in a pulsar mag-

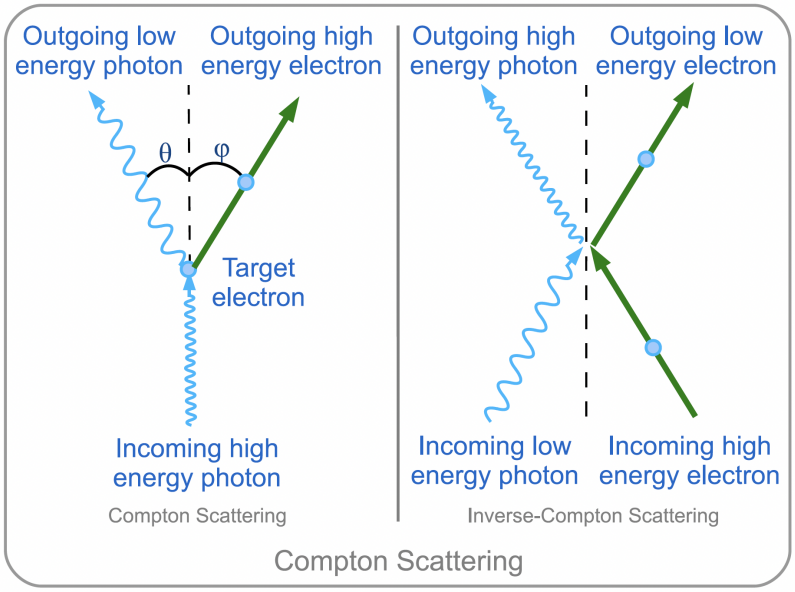

Figure 2.3: A cartoon representation of Compton scattering and IC up-scattering. From [33].

netosphere, the IC up-scattered photons have their energies boosted by a factor γ_e^2, leading to VHE gamma-rays. In the low energy limit, where the seed photon energy is less than the rest mass energy of the electron, this scattering channel occurs unimpeded; this is known as the Thompson limit. However, when $E_\gamma^I > m_e c^2$ the cross section for the interaction is quantum-mechanically reduced from the Thompson cross section, σ_{TH}, to the Klein-Nishina limit;

$$\sigma_{KN} \approx \sigma_{TH} \left(\frac{m_e c^2}{E_\gamma^I} \right) \left[ln \left(\frac{2E_\gamma^I}{m_e c^2} \right) + \frac{1}{2} \right]$$

This presents a potential problem for VHE gamma-ray production; either a population of low energy target photons need to be present, so that scattering happens more frequently in the Thompson regime, or there needs to be a very large population density of higher energy photons and electrons so that, even in the KN limit, the VHE flux produced can be at a level detectable by modern experiments (see subsection 2.2.3).

Synchrotron Self-Compton

One mechanism that can satisfy both of these criteria is the synchrotron self-Compton (SSC) scattering process. It is a sub-category of more general IC processes. In this special case the target photons are SR photons that are IC up-scattered by the very population of particles that create them. Particularly in the case of soft SR photons (UV or even IR/Optical), this leads to a scenario where there is an abundance of relatively low energy photons in the same region as energetic electrons to scatter with. SSC has become a noted possible contributor to the VHE flux component from pulsar models [28] [29]. The SSC spectrum takes the from;

$$\frac{dN_{SSC}\left(E_s\right)}{dE_s dt} = \int d\Omega \int dE\; n_{ph}\left(E,\Omega\right)\;\left(1-\beta\mu\right)\frac{d\sigma\left(E,\Omega\right)}{dEd\Omega}$$

Where $n_{ph}\left(E,\Omega\right)$ is the local SR photon density, $\sigma\left(E,\Omega\right)$ is the relevant IC scattering cross section and μ defines the incident photon directionality/scattering angle [29][6].

2.2 Pulsar Magnetospheric Structure and Dynamics

2.2.1 Overview

The modern theoretical picture of a pulsar and, in particular, it's magnetosphere has evolved from the seminal work of Goldreich and Julian [40] where the authors proved that a plasma-filled magnetosphere, encircling the pulsar, was necessarily the case, despite the immense gravity of the compact object. They made the assumption that, even with the rapid rotation rate, inside the NS itself the conductivity was high enough that any induced electric fields in the interior could be effectively canceled by the movement of charged particles, giving

[6] As the calculation of the SSC radiation requires the SR component to be computed first, a 'two stage' method is often used in simulations. The SR produced as particles follow their trajectories is done in the first pass and then the particles re-trace their trajectories and the SSC radiation is realized.

the force-free condition in the interior:

$$\mathbf{E} + \left(\frac{\mathbf{\Omega} \times \mathbf{r}}{c} \times \mathbf{B} \right) = 0$$

so that the Lorentz invariant quantity, $\mathbf{E} \cdot \mathbf{B} = 0$. If one first works from the assumption that the quickly-rotating and persistently-highly-magnetized pulsar exists in a vacuum and directly solves Laplace's equation (i.e. Poisson's equation where there is no charge density, as per the assumption of a vacuum), then it results that there must exist a component of the electric field, which is in the same direction as the magnetic field emanating from the surface of the pulsar outer crust. Furthermore, by, in the usual way, demanding continuity of non-radial field components at boundaries, this electric field component turns out to be of sufficient magnitude to overcome gravity at the surface, and forcibly eject particles into the surrounding medium. The strength of the electric field at the surface of the pulsar is enormous; around the order of magnitude of $\omega BR \approx 10^{13}\ Vm^{-1}$. This magnitude of discontinuity in the radial electric field necessitates a surface charge density of;

$$\sigma_s = -B_0 \frac{\Omega R}{4\pi c} \cos^2 \theta$$

to be physical. Indeed, in comparison to the incredible EM fields, the, already extreme, gravitational force is relatively negligible. Estimating their ratio in such a case;

$$\frac{F_{EM}}{F_G} = \frac{eE_{\|}R^2}{GMm_e} \approx 10^{12}$$

shows that the star cannot retain surface particles in this non-equilibrium state. The conclusion is that a pulsar cannot exist in a vacuum and is encompassed by a (at least partially) plasma-filled magnetosphere, with mobile plasma that follows the dynamics dictated by the strong magnetic and electric fields present there. Extreme magnetization in the vicinity of the pulsar confines the charged particles to path the magnetic field lines, with perpendicular

drift motion $\mathbf{V}_d = \mathbf{E} \times \mathbf{B}/B^2$. The omnipresent 'Goldreich-Julian charge density' [40], ρ_{GJ}, where $E_\parallel$ is screened by the plasma charge, is[7];

$$\rho_{GJ} = -\left(\frac{\mathbf{\Omega}}{2\pi c}\right) \cdot \left[\mathbf{B} - \frac{1}{2}\left(\nabla \times \mathbf{B}\right)\right]$$

In the polar cap[8] (PC) zone, where we can approximate the $B \approx B_0$ field to be purely radial, this expression simplifies to (see, for example, [41]);

$$\rho_{GJ,PC} \approx \frac{\Omega B_0}{2\pi c}\, cos\alpha$$

To further solve the case of a rotating and conducting pulsar, a choice for the internal magnetic field must be made. The most ubiquitous, and reasonable in terms of implication and observation, is either choosing to consider a uniform internal magnetic field, or a dipole with origin at the star center. In both cases the result is an external magnetic dipole field and, in vacuum, an external electric quadrupolar field [42]. In [43] it is proven that the vacuum EM field, outside the pulsar itself, is completely defined, purely, by the radial component of the magnetic field, B_r, at the stellar boundary. As B_r is the same for either choice of internal magnetization, the resultant external EM field is also the same for both cases.

The exact distribution, morphology and composition of the particle population in the magnetosphere is not precisely understood. Although most of models assume only electrons/positrons are present, and, indeed, fill most, if not all, of the pulsar surroundings, it is possible that a non-negligible, non-leptonic, hadronic proportion of particles are present, too. The results of such a paradigm, and discussion of possible regions depleted of signifi-

[7]This is the charge density everywhere in the magnetosphere in the force-free and ideal MHD regime, but is also a useful metric in other situations as well. Given here is the 'full-form' of ρ_{GJ}. The subtracted term, sometimes not-applicable, depending on the frame of reference used, represents the effect of moving charges on the magnetic field morphology, as per the Ampère-Maxwell equation.

[8]The 'polar cap' zones are regions around each of the magnetic poles of the neutron star. Magnetic field lines emanating from these regions no not reconnect inside the light cylinder, and so provide an avenue for particles to escape the magnetosphere. The angular size of the polar caps are defined by; $sin^2\theta_{pc} = \frac{R_0}{R_L}$

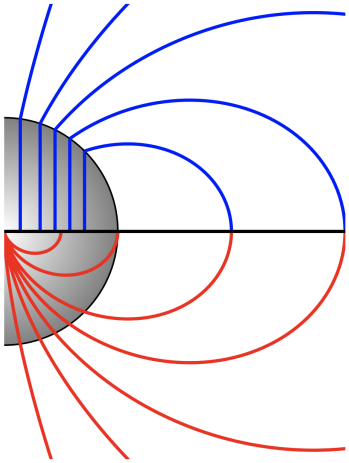

Figure 2.4: A cartoon showing how an external dipolar magnetic field is the result of choosing either a uniform (in blue) or dipolar (red) internal magnetic field. From [42].

cant plasma density, is discussed in [42].

This is in contrast to the more common 'force-free'[9] electrodynamics (FFE) model of the magnetosphere, as particle injection from the surface fills the magnetosphere with charged particles, as is discussed in [44] and [45]. This prescription, while an idealization, is a cornerstone 'starting point' for investigation of more realistic magnetospheric properties. In this paradigm the time-dependent Maxwell equations;

$$\frac{\partial \mathbf{B}}{\partial t} = -c\nabla \times \mathbf{E} \quad , \quad \frac{\partial \mathbf{E}}{\partial t} = c\nabla \times \mathbf{B} - 4\pi \mathbf{J}$$

are solved, numerically, applying the usual force-free axioms[10] (discussed in [46] and references therein);

$$\mathbf{E} \cdot \mathbf{B} = 0 \quad , \quad \rho \mathbf{E} + \frac{1}{c}\mathbf{J} \times \mathbf{B} = 0$$

resulting in knowledge of the EM fields. However, this gives no information on the formation of charged particles or their behavior, which is crucial.

[9] Often extended to 'nearly' force-free when vacuum gaps are allowed in specific regions

[10] The first asserts that the electric and magnetic fields are orthogonal and the second is a statement of the net force on a volume element containing charges being zero.

So, on one hand, we have frameworks where some (or most) of the star's surroundings are lacking notable plasma concentration and significant areas of the magnetosphere have un-screened 'longitudinal' (i.e. parallel to the local magnetic field lines) electric fields ($E_{\parallel} = \mathbf{E} \cdot \mathbf{B}/B$) that can accelerate particles in the direction of the magnetic field and cause emission of radiation. Clearly, from discussion above, there must be some plasma present, and with no/very-low plasma density, no high energy radiation would be emitted. This tells us that this cannot be the full picture, but could describe a low 'plasma fill-factor' scenario where the behavior in the magnetosphere is not strongly coupled to the plasma characteristics. On the other hand, at the opposite extreme, we picture an all-encompassing plasma density that effectively shorts the electric field, and so screens the particle population from accelerating electric forces (hence the label; '(nearly) force-free', depending on the remaining areas with accelerating electric fields not screened by charged plasma).

A compromising scenario somewhere in between these extreme cases seems most plausible. The popular models and their applicable assumptions, along with the predicted resultant emission, is summarized in figure 2.5, with the relevant magnetospheric plasma density dictating the left-right placement. The chart illustrates the fact that, even for the case of an almost full magnetosphere, there exist regions of lower density plasma, and hence partially unscreened accelerating fields. These 'gap' regions [47], and their local dynamics, are of particular interest in the effort to fully understand the source of VHE gamma-rays emitted by pulsars.

For very low plasma density scenarios, the so-called 'electrosphere', as the electric field influences particles with little opposition, forming regions of with charge-separated (non(-quasi)-neutral) plasma population. These distinct zones exhibit differing morphologies dependent on the choice of EM field shape chosen and can give rise to complex non-linear plasma particle wave models [48].

The nature and quantity of pair production occurring is one of the most important indi-

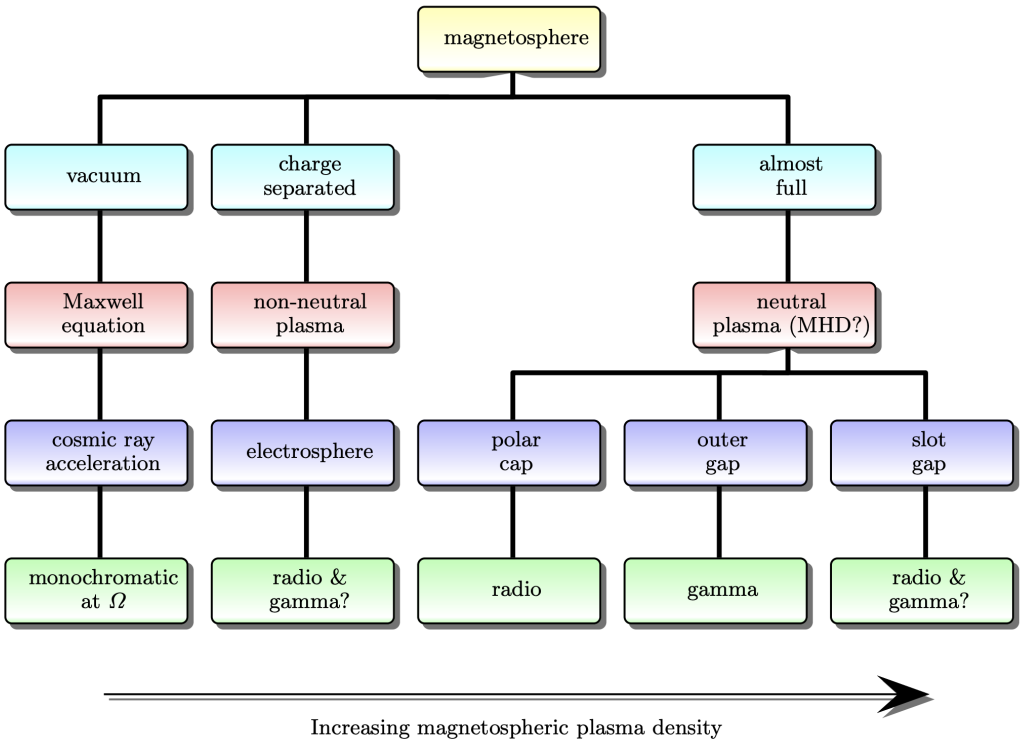

Figure 2.5: A flowchart representation of different magnetospheric models, separated by the relevant magnetospheric plasma density. The descending rows show: 1st) the base nature of the magnetosphere, with regard to plasma presence, 2nd) the mechanism governing plasma behavior, 3rd) the noteworthy characteristics that arise in the model, 4th) type of emitted radiation predicted. From [42].

cators of the relevant scenario, and is critical in relation to the observed radiation, particularly in the VHE regime. Applying a 'mix' of the above frameworks to different regions of the pulsar magnetosphere, and beyond, is necessary to capture the true dynamics observed in the real surroundings of pulsars. For further comparison and indicative numerical characterization see [49]. Fully understanding the complex magnetohydrodynamics is a very challenging endeavor, but, particular cases exist where analytic solutions can be derived [50].

An interesting alternate strategy, used in special cases, is to 'work backwards' from a radiation-reaction limited particle population to determine the particle motion, and hence the accelerating EM field (see [51] [52]). Given an equilibrium state, between energy gain from acceleration and energy loss from radiation, of the plasma particles, information about the velocities in the direction of the fields, and an additional drift component, can be deduced [53].

2.2.2 Numerical Approach to Magnetosphere Simulations

For most cases, however, where a realistic, non-idealized scenario is being considered, an exact analytical solution to understand the magnetosphere dynamics can range from highly unwieldly to completely unattainable. As such, numerical simulations (see [54] for details on the numerical differential equation techniques), with as much detail as desired, often offer the best available insights into authentic, time-dependent magnetospheric behavior. The treatment of the physics in these models, and assumptions made, give variations in complexity, often dictated by the particular area the individual study wishes to investigate.

Simplifications made to ease the simulation process can include: neglecting particle mass and inertia, assuming no energy losses, only accounting for certain kinematic current terms and condensing the computationally-intensive Vlasov-Maxwell equations (that describe how plasma distribution evolves with time when influenced by EM fields [55] [56]). Drawbacks and difficulties associated with the above approaches include: necessarily tying

the low (high) plasma particle density to the assumed charge-separated (quasi-neutral, not charge-separated), which should be variable depending on the speed and efficiency of particle creation/injection, non-conservation and divergent values for the total system charge, difficulty matching realistic boundary conditions between zones, trouble producing consistent light curves that also match observations [39] [57], matching the overall luminosity to the model predictions, discontinuities and artifacts arising in current flow structure and not fully localizing the acceleration/emission zones.

The most complex cases involve full MHD treatment [58], comprehensive solutions to the stress-energy tensor, particle and field dynamics, treating the electron/positron plasma as two discrete, but coupled, populations (as is not possible with the standard MHD mass-ordering) and solving the full Vlasov-Maxwell system of equations. This produces a computationally intensive and costly simulation to prepare, and run, with interconnected factors that are often difficult to jointly properly consider. However, it seems this exhaustive approach is necessary to fully understand the magnetosphere dynamics and, crucially, accurately explore zones of particle acceleration and radiation.

Balancing insight with complexity, so-called 'Particle in (a) Cell' (PIC) [59] family of simulations have had success over the years, and can often encapsulate most physics from first principles. Starting from Wada and Shibata's work such as [60], evolving to [61] and such modern publications, studying; luminosity and energetics [62], and [63] for one of the most detailed simulations focusing on light curves to date. Comparison of *Fermi*-LAT HE light curves with theoretical predictions is an effective tool to evaluate emission model. This procedure is relatively robust due to the large gamma-ray sample size available in the HE energy band. If significant pulsed emission is found in the survey of MSPs (Chapter 5), the VHE light curve can also be compared to models, although it is possible that the flux level could be too low to provide sufficient events to make any strong claim about the light curve features [64].

2.2.3 The Equatorial Current Sheet

In [63], Cerutti et al. conclude a very important result: that the equatorial current sheet[11] (ECS) and the 'Y-point'[12] [66] are the locations of the greatest particle acceleration, and most highly-relativistic particles [67] [68], and so are the best candidate regions for the generation of (V)HE emission [41] (see figures 2.6 & 2.7), in addition to the gap regions around the last closed field lines (i.e. the outer gaps) that they discuss in [69].

Likewise, in [70] the authors discuss the conversion of radiation energy flux into particle momentum in the ECS. Aside from the Poynting flux dissipation in this region, they also note the contribution of magnetic reconnection effects [71] that are though to inject significant energy density [72], into the plasma, from the fields converting to a lower energy state [69]. The ECS and Y-point [73] are excellent candidates for where this magnetic reconnection might occur [74], and, again, could explain the observed VHE pulsed emission through IC processes [72] [75]. These results arise from consideration of the domain of an almost filled magnetosphere, thought to be a realistic choice when investigating gamma-ray pulsars [45].

The first models of pulsed gamma-ray emission from the ECS assumed energy from the wind was transferred to particles, that then radiated Doppler-boosted SR at a distance of $\sim 10 - 100\ R_L$ [76], but more modern works favoring SSC, from accelerated secondary pairs, up to ~ 1 TeV[13] [29] and IC from accelerated primary particles scattering off of SR from secondaries forming a new component > 10 TeV [77] [32]. However, solid quantitative predictions for the expected VHE flux from the ECS models are still lacking in the literature, as the methods require various nonphysical scaling factors due to simulation

[11] Named as such as it describes the the flow of charges that is established in the equatorial plane, with reference to the pulsar's spin orientation.

[12] The Y-point is the location of intersection of the ECS and the last closed field line, near, but not always exactly at, the light cylinder [62]. Named so, as the magnetic field lines are thought to form a 'Y-like' configuration there. It is an important location when considering magnetic reconnection [65].

[13] Although, for MSPs, the secondary particles possess higher energy, due to the higher energy threshold for photons to initiate pair production in the weaker magnetic fields, and so it is possible that for these higher energy particles, Klein-Nishina suppression lowers VHE fluxes below the sensitivity of current instruments [64].

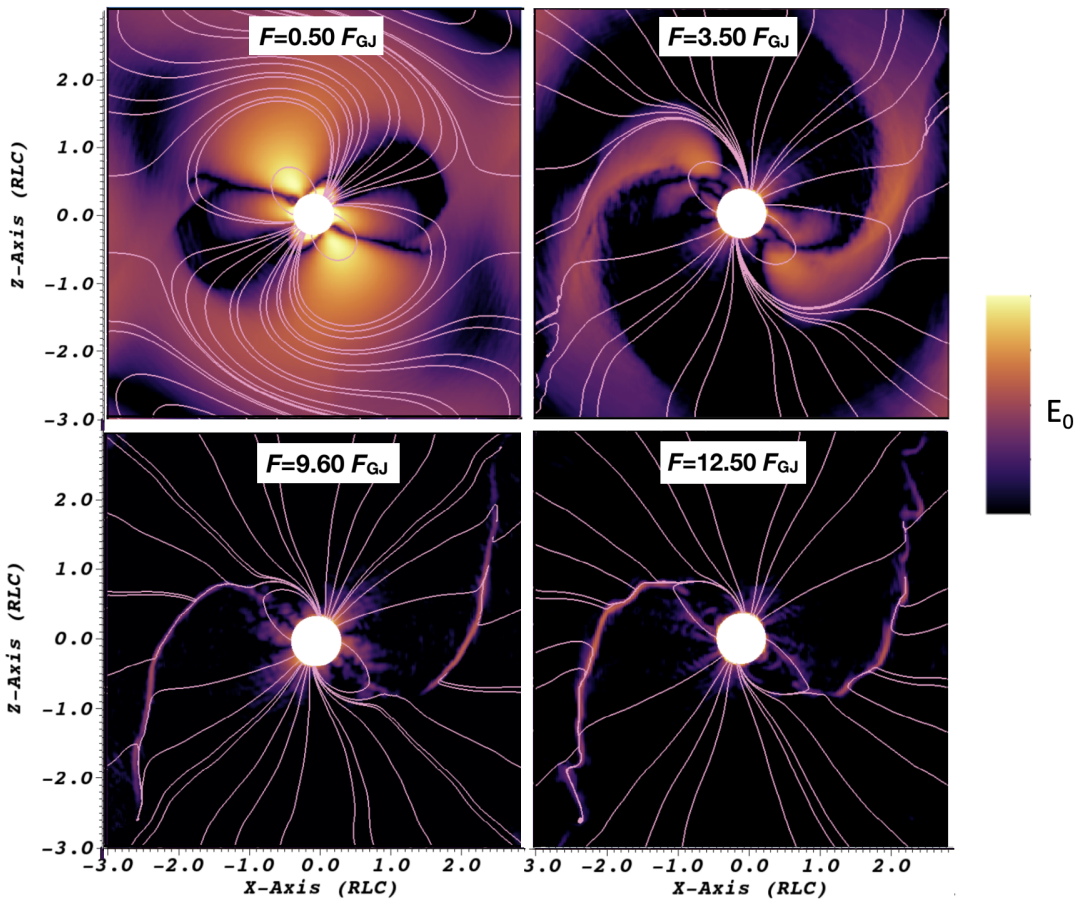

Figure 2.6: From modern PIC simulations [41]. Showing the pulsar magnetosphere; pink lines show the magnetic field lines and the color scale quantifies the unscreened accelerating electric field, for four different plasma particle injection rates. Clearly shows the vacuum gap regions and the ECS, and how they change with plasma density.

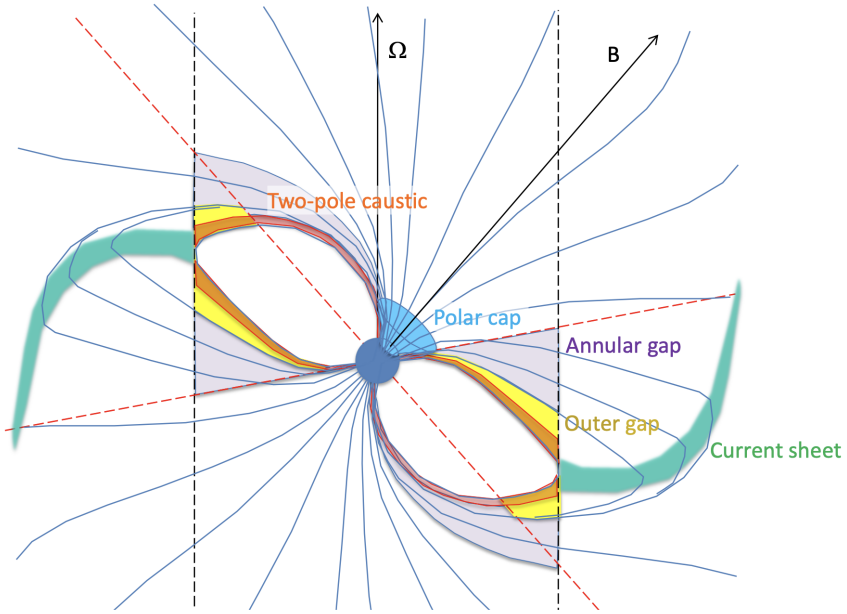

Figure 2.7: A cartoon that shows regions of interest in the magnetosphere and beyond the light-cylinder. Of particular note is the ECS and Y-Point. From [64].

limitations (see [64] and references therein). Due to this intrinsic uncertainty on the flux scale that is present in these modern models, any flux information that can be extracted from VHE MSP pulsar data is of fundamental import to fully realizing a more robust modelling process. Despite this inherent lack of robust theoretical predictions, the detection of significant pulsed emission would confirm an emission component in the VHE energy range and allow the quantification of lower limits on the highest particle energies that IC scatter photons to VHE gamma-rays, at the energy level of the most energetic gamma-rays detected.

2.2.4 The Outer Magnetosphere & Pulsar Wind

As mentioned previously, the assumption that the magnetic field lines, and the particles that comprise the magnetospheric plasma, can rotate completely jointly with the pulsar only holds out to a certain distance, as to not violate causality. Indeed, when not considering the idealized case of an entirely force-free magnetosphere, assuming plasma co-rotation, even

inside the light cylinder, is disputed [78], and has been shown to be, perhaps, impossible in situations with significant vacuum gaps [79]. Beyond a certain distance from the pulsar the field and any particles that follow said fields, would have to move faster than the speed of light to keep up with the rotation. An imaginary cylinder, placed such that the axis of the cylinder is co-linear with the pulsar axis of rotation, is used to denote this phenomenon. The radius of which, R_L, known as the light cylinder radius, is defined as to co-rotate at the speed of light.

$$R_L \equiv \frac{c}{\Omega}$$

Where Ω is the angular velocity of the pulsar. For example, with a period of 33ms, the Crab pulsar has a light cylinder radius of $R_L \approx 1500km$. Further out from this imaginary surface the picture of field lines of a 'perfect' spinning dipole breakdown and the field lines cannot hope to re-connect to the star, instead creating a 'whirlpool-like' structure and allowing the outflow of particles. This stream of particles that are no-longer bound to the magnetosphere forms the 'pulsar wind', and imparts energetic particles to the surroundings. Inside the light-cylinder, in the closed-magnetospheric region, the behavior of the medium is dictated by strong electromagnetic forces, while outwards of the light-cylinder particle inertia and momentum play a more crucial role.

As these released particles radiate, primarily, SR, they are seen as, what is denoted, a 'pulsar wind nebula' (usually defined this way, rather than the 'classical' definition of a nebula, as just gas and dust, instead, as the zone of emitting particles was the subject of interest in these structures). Although PWNe are extremely interesting astrophysical objects, and can produce steady VHE gamma-rays, the pulsed VHE emission is thought to originate inside, or at least very close to, the magnetosphere. Models that adopt relativistic wind particles up-scattering soft pulsed photons, from the pulsar, at any significant distance ($> 2R_l$) from the pulsar, tend to over-predict the HE flux at levels already constrained by *Fermi*-LAT data.

The particles that comprise the PW are worthy of study in many aspects, including

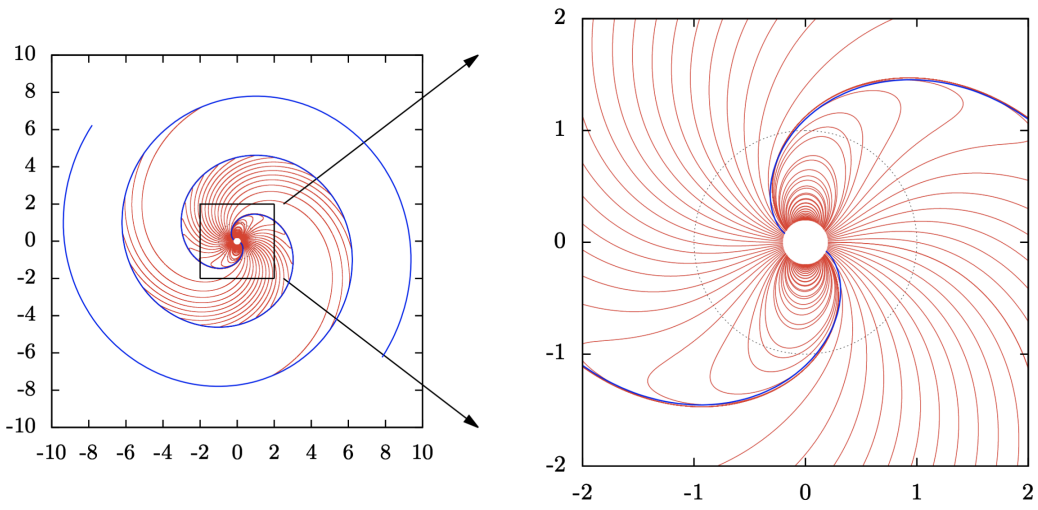

Figure 2.8: Shown here are the resultant magnetic field lines (red) and the overall spiral-like structure (blue) that result from solving orthogonal rotator. The image on the right is a zoomed in version of the left, showing the field closer to the star in more detail. Units are multiples of R_L. From [42].

their emission mechanisms. Particular cases of interest are binary systems, when the wind interacts with the NS's companion in some way, or other exotic cases such as when the remnant NS moves out of the host SNR and exhibits ram-pressure induced 'heads' and 'tails' from the pulsar, as it moves supersonically through the ISM. Modern models suggest that the tail regions around these supersonic pulsars should produce a detectable level of VHE gamma-rays, through IC processes. However, no VHE emission has been detected to date and so in Chapter 6 we detail a survey of 3 such candidates in an attempt to confirm, or deny the model predictions.

2.2.5 Advanced Considerations in the Presence of Complex Physics

We have given a reasonably comprehensive description of the usual treatment and understanding of the canonical pulsar magnetosphere: to this point, the overarching approach has been to investigate the results of Maxwell's equations with the assumption of non-curved spacetime and only the presence of a dipole-like magnetic field contribution. How-

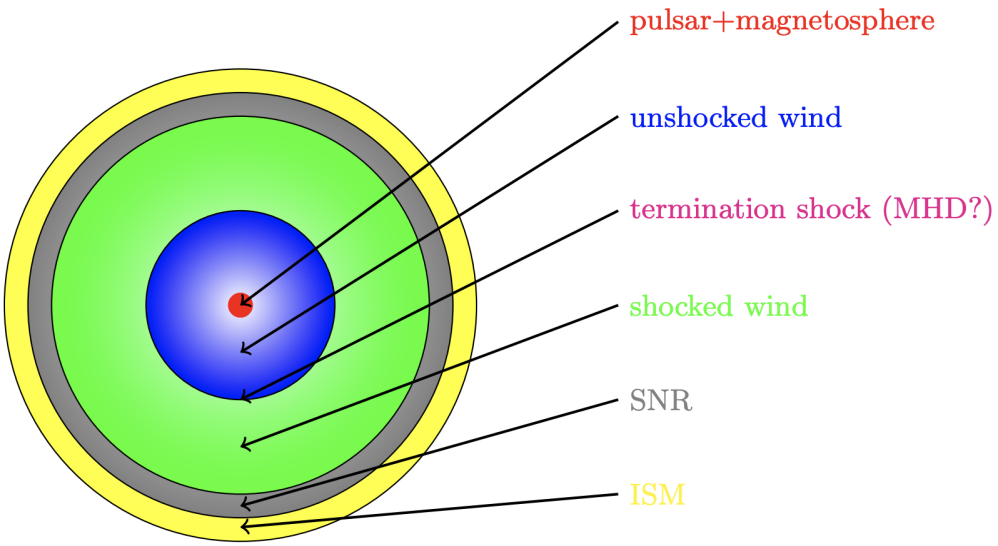

Figure 2.9: A cartoon, showing a simplified picture, far zoomed-out from the pulsar and magnetosphere, of the interfacing layered zones between the neutron star and the surrounding ISM. From [42].

ever, additional phenomena and theory-complicating physics may also be present. Indeed, they may be contributing factors that could help in bridging the gap between current models/simulations and puzzling, unexplained behavior, such as VHE pulsed emission, from some pulsars. A brief introduction to these ideas is given in this section.

Gravitational Considerations

Due to the very strong gravitational effects, particularly near the surface, relativistic effects on the EM field being warped in the bent spacetime could change the assumptions made on the field structure. Indeed, it was made clear that such 'corrections', needed to model frame-dragging (Lense–Thirring) effects on the fields without GR considerations, could produce behavior of the same order of dynamical influence as the originally assumed fields, in the absence of intense gravity [80] [81]. Lense–Thirring frame-dragging effects manifest

themselves as a reduction to the effective rotation rate such that;

$$\mathbf{\Omega} \rightarrow \mathbf{\Omega}_{LT} \approx \mathbf{\Omega} \left(1 - \frac{2GI_r}{c^2 r^3} \right)$$

hence altering many equations defining physics properties, for example, in the expression for the plasma density ρ_{GJ}. Models for the effects of an extreme gravitational influence on a magnetic field have existed for the time-independent dipole [82] and time-independent multipole [83], for decades. Introducing the same physics for the dynamic case is much more complex, although some 'tools' exist [84] to build partial frameworks. Building on the work of [85] and [86], the work of [87] exemplifies the overall outcome. That is; considering frame-dragging effects and a proper Schwarzschild metric treatment of the scenario, a significant enhancement to the accelerating electric field, increased injected particle population and also more effective plasma acceleration in the vicinity of the neutron star. Most pertinent to this work is that this may have radical consequences on the pulsar emission in the highest energy regimes. It seems that the effects of strongly curved spacetime on the production of electron/positron pairs, close to the pulsar surface, is of great import [74] [88].

Possible Presence of Higher-Order Multipole Moments

Although it seems clear that the overarching magnetic field near a distance of R_L, and beyond, is purely dipolar, the exact magnetic field in the inner magnetosphere is not completely infallible. The EM field contribution from additional (beyond the widely adopted pure-dipole) higher-order multipole-moments may also be present in the space surrounding the pulsar, and have non-negligible effect on the plasma behavior and emission properties [89] [90]. The presence of higher order multipole moments in the region close to the pulsar would not dispute the wholly dipolar picture at larger distances, as the contributions of higher order moments drop off as increasingly-negative exponents of r; i.e. a dipolar field

component drops off as $1/r^3$, a quadrupolar component goes as $1/r^4$ etc. It is thought that these magnetic moments of higher order could manifest themselves, producing polar cap morphology that deviate significantly to the simple dipolar case [91], while also enhancing secondary particle formation through stronger and more highly-curved fields [92], for MSPs in particular [93]. This could also have the effect of modifying radio and higher-energy pulse profiles, particularly in MSPs[14] [94]. If VHE light curves can be produced from VHE MSP data, then the observed light curves can be compared to simulated data that attempt to model the effects of these higher order multipole moments. Deviance from a simple aligned-dipole could be induced by, for example, the rotating dipole field being eccentric with the center of the pulsar, the neutron star deviating from a perfect spherical shape [95], or be a result of the recycling process, as older pulsars accrete new matter from a companion. These ideas are further applied to specific pulsar observations in [96] and [97], along with radio pulsars in general [98].

QED Treatment for Strong Fields

Treatment of the cases of the strongest magnetic fields, in magnetars and even regular pulsars, should account for quantum electrodynamical processes and amendments to the norm of lower-energy physics. The 'scale' at which these effects become important is of the order; $B_c = m^2c^3/e\hbar = 4.413 \times 10^{13}G$, when the electron rest-mass energy is exceeded by it's cyclotron energy [99]. This has direct implications for additional creation of particle pairs, allowed for in QED, but not necessarily accounted for in more 'classical' theory. Although possible influence of advanced QED effects could be of significance, they are tricky to assimilate properly into a comprehensive model, those that have made forays into this line of investigation that the resultant corrections to pulsar and magnetosphere properties are likely small and relatively unimportant [100] [101], although future studies

[14]Due to the more compact magnetosphere, from a restricted R_L, due to the large rotational rate, any higher-order magnetic multipole moments would have larger effects on emission zones near R_L for MSPs vs. regular pulsars.

could change this paradigm (see discussion in [102]).

2.3 Electromagnetic Emission From Pulsars

2.3.1 Emission Overview

For a idealized, rotating, magnetized sphere in vacuum, perhaps the most naive starting point to work from, the expected, overall, energy carried away by the Poynting flux, which is equal to the spin-down power, is given by

$$\dot{E} = I\Omega\dot{\Omega} = \frac{\Omega^4 R_0^6 B_0^2}{6c^3} \sin^2 \alpha$$

[103], and the equation obtained 'empirically', from force-free electrodynamics simulations and analysis, differs slightly, in the form: [104]

$$\dot{E} = \frac{\Omega^4 R_0^6 B_0^2}{4c^3} \left(1 + \sin^2 \alpha\right)$$

Clearly, these are hyper-simplified cases to picture, but can provide a rough benchmark for numerical comparisons as the equations above give upper and lower limits for the expected luminosity of a more realistic pulsar magnetosphere (as they represent the most extreme cases, which the actual scenario should lay between, see [46] and references therein). They are also, historically, a starting point for gauging more complex models for emission.

However, a lone magnetized rotator, in a vacuum, would only produce a EM wave of a single frequency, that of the rotation rate. The addition of some plasma population is needed to generate EM radiation, from particle acceleration, that could be detectable at Earth. This was first proposed by Gold [14] and results in a broad spectrum of emitted radiation. Building on this work, Pacini put forward an early model for a radiating neutron star [13] and then expanded on this idea to propose the revolutionary idea that a neutron star was the power source for the Crab nebula [105], laying the foundation for the scenario that the

star's rotational energy is transferred, through the formation and acceleration of relativistic particles by the strong fields surrounding the neutron star, to any surrounding nebula. The expected luminosity was quantified in terms of the luminosity of a 'perpendicular rotator' (where the angle, χ, between the magnetic dipole axis and the rotation axis, is 90°) in a vacuum, $L_{\perp}^{vac}$ is;

$$L_{\perp}^{vac} = \frac{8\pi B^2 \Omega^4 R^6}{3\mu_0 c^3}$$

Then the more general expression for different magnetic and spin axis orientations ('oblique' rotators) can be parameterized as $L^{vac}(\chi) = L_{\perp}^{vac} \sin^2 \chi$. This can then be further modified by some additional function, $f(\chi)$, which encompasses all additional magnetospheric effects when plasma, and not purely vacuum, surrounds the neutron star, resulting in such a formalism as; $L(\chi) = f(\chi) L_{\perp}^{vac} \sin^2 \chi$.

The power necessary for such emission comes from the loss of rotational kinetic energy of the pulsar, gradually slowing the spin-speed as the induced fields impart energy to accelerate particles and therefor also apply a slowing torque to the pulsar. The rotational kinetic energy of the neutron star is

$$E_{rot} = \frac{1}{2} I \Omega^2 = 2\pi^2 \frac{I}{P^2}$$

and so the energy lost over time, as the emitted luminosity is

$$L_{rot} = -\frac{dE_{rot}}{dt} = -I\Omega\dot{\Omega} = 4\pi^2 \frac{I\dot{P}}{P^3}$$

2.3.2 Particle Injection and Pair Creation

Now we have discussed energy injection into the magnetosphere we must return to the origin of the plasma particle population. Introduction of particles into the magnetosphere from the polar caps of the neutron star was proposed as the earliest non-idealized model by Sturrock [106] [107]. In this case (furthered in [108]), to try and explain radio emis-

sion from pulsars, the polar caps are the site of primary particle injection, and, with an accelerating electric field that leads to radio emission. Wherever the location on the pulsar that they are sourced from: particles that are ripped from the surface of the pulsar by the enormous EM field are called 'primary' particles and, to a reasonable estimate, are almost immediately accelerated to ultra-relativistic velocities, by the same fields, very soon after they are liberated from the neutron star surface.

In turn these highly-energetic primaries can induce the production of pairs of 'secondary' electrons and positrons through pair production, from gamma-ray photons emitted as CR, in, either, rapid and frequent interactions with the strong EM field, or, more rarely, other photons.

Up to a few stellar radii above the polar cap, where it is thought that the most significant plasma creation occurs [109], the preferred channel involves photons[15] interacting with the strong magnetic field [99], leading to QED 'single-photon', or 'magnetic', pair creation [111];

$$\gamma + B_{field} \;\; \rightarrow \;\; e^+ + e^-$$

where the magnetic field transfers the necessary momentum. In this scenario the photon interacting with the field must have energy $> 2m_e c^2/sin\theta$, where θ is the angle between the magnetic field vector and the photon momentum vector. As the emission from relativistic particles is tightly beamed along the field lines they are being accelerated along, the pair-creation criterion is not met until the photons have moved to a region where the local curvature of the field is sufficient, compared to their original trajectory [64].

This highly important process repeats, and leads to a shower of additional charged particles (up to $\sim 10^4$ per primary), that aids in filling the magnetosphere, and also radiate further curvature, and some synchrotron, photons in the strong fields[16].

However, these cascades of charged particles are only formed when it is energetically

[15] Said photons are produced from relativistic particles, either through CR or IC up-scattering thermal X-rays from the NS [110].

[16] in an interesting analogy to the air-shower method used by IACTs to detect gamma rays arriving at Earth.

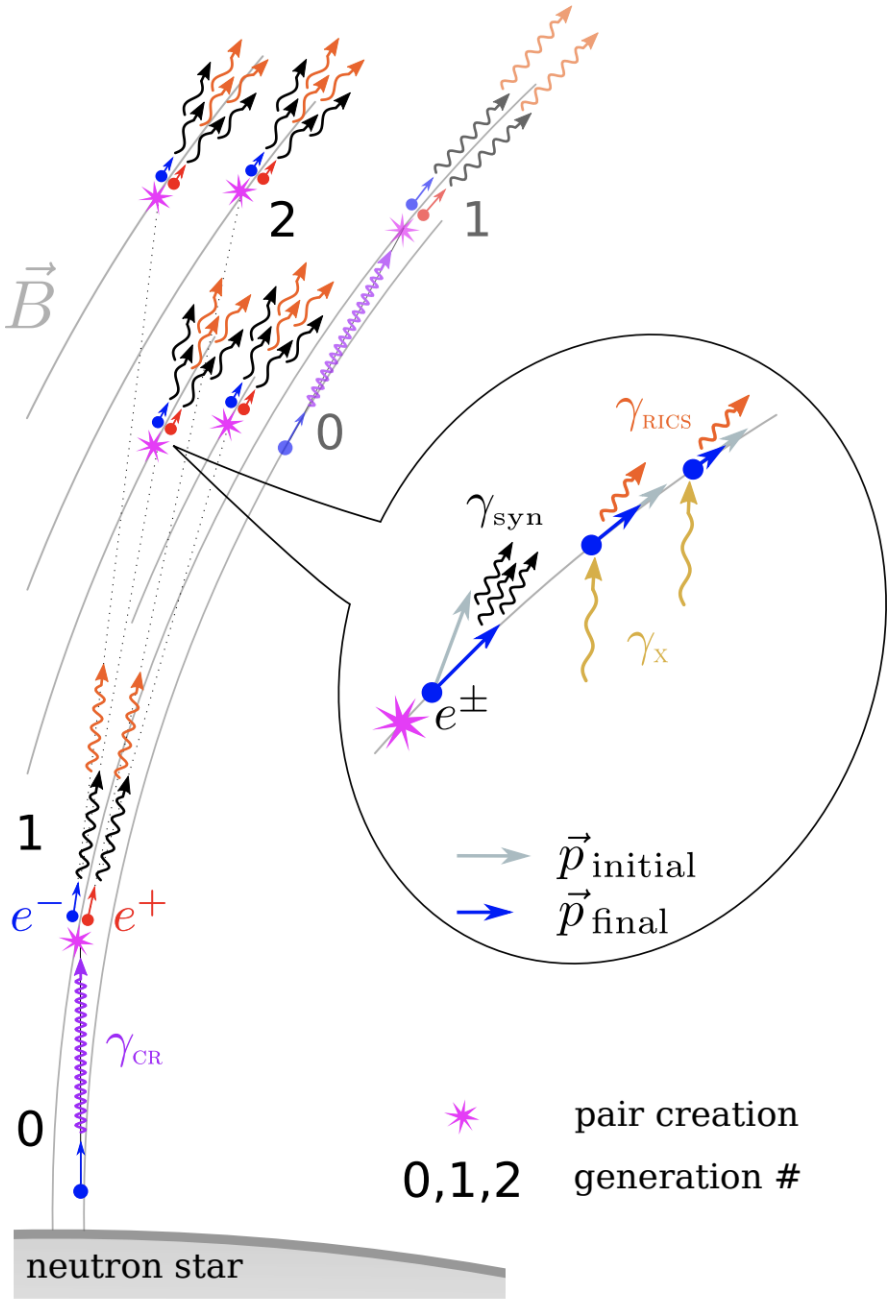

Figure 2.10: A diagrammatic representation of the stages involved in the development of a particle cascade near the polar cap region of a regular pulsar with strong magnetic field. From [109].

Table 2.1: The timeline of hallmark new models, and advancements in theory, that aim to describe and understand pulsar magnetospheres, from [42].

Model Description	***Reference & Publication Year***
Oblique Rotator in Vacuum	Deutsch (1955)
'Neutron Star'	Pacini (1967)
Bunch of Co-rotating Particles	Gold (1968)
Aligned Rotator and Plasma Source	Goldreich & Julian (1969)
Aligned Rotator and Pair Creation	Sturrock (1970)
Polar Cap, Cavities, Discharge	Ruderman & Sutherland (1975)
Outer Gaps	Cheng et al. (1986a)
Slot Gaps	Arons (1983)
Trapping of Charges	Krause-Polstorff & Michel (1985a)
Keplerian Disk	Michel & Dessler (1981)

favourable to do so; this can only occur when there is a region of sufficiently low plasma density, and the associated energetic fields are strong enough or, with photon-photon pair creation. Hence, for an idealized, fully-filled magnetosphere only primary particles are present, with no secondary particles, or their additional radiation, being created.

Photon-photon[17] pair creation, due to the lower cross-section (compared to the magnetic pair creation case when strong fields are present) is only prominent in outer/slot gap regions where the fields are too weak for the QED single-photon process, for regular pulsars (see [112], and references therein).

$$\gamma + \gamma \;\; \rightarrow \;\; e^{+} + e^{-}$$

However, due to their lower magnetic field strengths, this process is thought to be the primary channel to influence even the polar cap cascade, and for most, if not all, pair creation in MSPs, although further investigative simulation work is needed [64].

Also worthy of note is the work of Shibata [113] [114], that made clear that blindly focusing on only certain regions, and applying particular boundary conditions, would not

[17] In the case of the outer gap regions, the photons responsible are gamma-ray photons that interact with X-rays that are produced at the pulsar surface.

lead to a proper solution to solve the nature of plasma acceleration by the unscreened electric field in the gap regions, and that only by tackling the comprehensive system as a whole could a all-encompassing theory be attained. This 'broad-view' approach has been adopted more in more modern times.

2.4 Vacuum Gaps as Sites of Particle Acceleration

The examination and treatment of unscreened, accelerating, electric fields in the pulsar magnetosphere naturally leads to consideration of radiation produced by pulsars, and the two topics are intrinsically linked. Confined cases of the $E_{\parallel}$ field not being fully nullified by the local plasma (known as 'gaps' or 'vacuum gaps', the idea originating in [115]), manifest themselves due to nuances in the specific conditions required for a fully force-free magnetosphere. Some causes, and the associated scenarios, that can manifest themselves in such a way to produce unscreened volumes are: treatment of significant particle inertia in the plasma population [116], the structure and curvature of the magnetic field [117], incorporation of expected behavior from general relativity [118] [85] and even potential problems with effective particle extraction into the magnetosphere [108].

Many possible models emerge from considering different ways in which these zones of active fields, and therefor prominent EM activity, could arise. Already mentioned as a site of particle acceleration, and hence, emission of radiation, canonically for radio photons, is the polar cap. Two other main zones are thought to be candidates for areas of the magnetosphere with low enough plasma density to facilitate an unscreened electric field component strong enough to significantly accelerate the plasma particle population, to relativistic velocities, facilitating CR. These are the 'outer gap' (OG), and 'slot gap' (SG) illustrated in figure 2.11 (see [45] for a nice summary).

The slot gap is thought to be a relatively compact area surrounding the final magnetic field line to close successfully back to the pulsar. It is treated, most often, as a 'channel' (as seen in Figure 2.11) sometimes with a fixed cross-section and other times, more realis-

tically, with a geometry that is a function of spatial coordinates. With low enough particle density to give rise to possible electron/positron pair creation [119] [18] and, also, plasma acceleration, leading to emission of HE photons up to large fractions of R_L from the pulsar [120] [121]. Photons are radiated in a large opening-angle (compared to the polar cap cone) but 'hollow', conical geometry [122]. It encompasses a few percent of the open magnetic field lines, with an electric potential difference of $\sim 10^{13}V$ [122]. By some, the SG is likened to a 'high-altitude extension' to the polar cap cone, and can be further sub-divided into regions of differing altitude, for tailored treatment.

In the relatively extensive area, that is bounded by the null-charge surface[19], the light cylinder, and the last closed magnetic field line, exists the outer gap zone. The outer gap can form due to the loss of plasma, along open field lines, with no sufficient in-flow of particles, from polar cap cascades for example, to replenish it. The cross-section of this gap roughly takes the form of a 'triangle', with a curved side, that follows the last closed field line. Again, here, due to the lack of plasma population pair creation is expected[20] [123], and suitable conditions for acceleration and emission exist [124]. The expected electric potential difference in the OG is $\sim 10^{15}V$ and spans over 10% of the open magnetic field lines, thus presenting a larger volume for pair-creation 'sparking' and a higher acceleration potential compared to the SG. The general consensus seems that the properties of the OG are much preferred over the SG, for reproducing gamma-ray fluxes [125]. Lyutikov et al. [28] suggest SSC processes in the OG to produce VHE emission while Rudak & Dyks [126] present a model where IC emission above 10 TeV is produced when accelerated primary particles interact and up-scatter soft SR photons, in the optical/IR regime, from secondary particles in the OG of the Vela pulsar.

For investigations into HE/VHE gamma-ray emission, the outer and slot gaps are heav-

[18] Although, it seems that particles may not produce emission of high enough energy before they reach an altitude where the magnetic field strength is not sufficient to facilitate pair-production [64]

[19] (where the sign of ρ_{GJ} flips, and the magnetic field is perpendicular to the rotational vector: $\mathbf{\Omega} \cdot \mathbf{B} = 0$

[20] In this case, in the outer magnetosphere, two-photon pair production is the dominant mechanism for electron/positron formation.

ily favored over the polar cap [38]. High energy gamma-rays require a highly energetic population of particles to create or boost them. The theoretical maximum acceleration an electron could experience, accelerated from the polar cap, gives rise to maximal Lorentz factor of;

$$\gamma_{max} \approx \frac{\Omega^2 R_0^3 B_0 e}{m_e c^2}$$

[108]. In addition, because the restricted beam geometry and expected super-exponential-cutoff spectral-shape, intrinsic to polar cap models, has been challenged by *Fermi*-LAT data of pulsars such as the Vela pulsar [127], hence leaving the outer (as in [128]) magnetosphere (or, perhaps, beyond [129]) as the prime region of interest, as the source for the highest energy photons.

Other vacuum gaps have been proposed, as well (such as the 'annular gap' [130]), but the slot gap and outer gap are the primary candidates thought to be the source of pulsed VHE gamma-ray emission mechanisms [28] [131] [29], and therefor the areas of interest for study inside the light cylinder (such as in the study of MSPs in Chapter 5).

These SSC models are thought to be the most promising in explaining the observed spectra/fluxes and light curves, when considering intra-magnetospheric gap regions. They are self-consistent and fully form a coherent model of the pulsar magnetosphere, including it's dynamical behavior, composition and emission characteristics. This is of the utmost importance when forming a realistic and universal theory of the physics of pulsars. We aim to test the prediction of VHE emission components, that is present in such theories, in the MSP survey.

The behavior of particles outside the light cylinder, in the pulsar wind, is also an area of research, in Chapter 6.

2.4.1 Hadronic Emission Channels

Thus-far we have discussed the channels in with leptons emit gamma-ray photons. Hadronic interactions can also be responsible for VHE photons, an example is the decay of a neu-

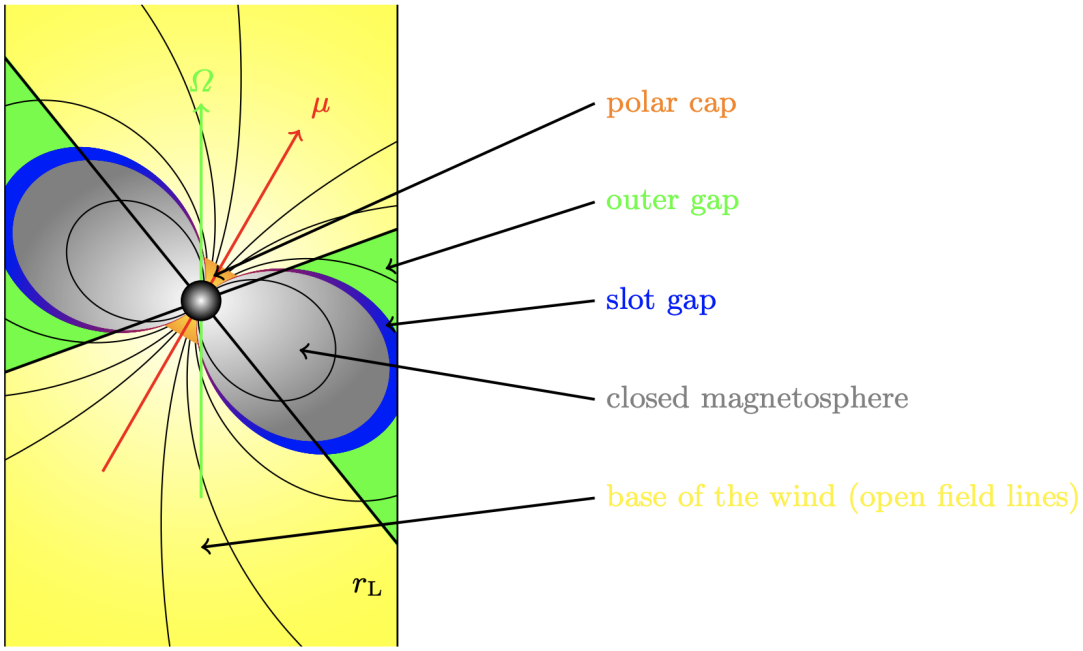

Figure 2.11: A cartoon showing some key components of the pulsar magnetosphere, inside the light cylinder, particularly the location of the vacuum gaps, from [42].

tral pion. As hadronic channels produce neutrinos as well as gamma-rays [132], searches for coincident detections, with experiments such as IceCube, can indicate such processes are present (see for [133] further discussion). If detections of the MSPs result, follow up investigations can be made with multi-messenger counterparts.

2.5 Summary of Modern Numerical Simulations and Models

Guided by the most up-to-date simulations and models [77] [32], focus has mainly shifted, in the last few years [64], from vacuum gaps inside the LC to the ECS [134] [135] and Y-point [63] [41], as the regions of interest for particle acceleration and (V)HE gamma-ray production. Although, the OGs [28] [131] [29] [126] still hold promise for explaining observed phenomena [75]. The MSP survey carried out in Chapter 5 aims to quantify the level of pulsed emission seen in the VHE regime. This will confirm the existence, or constrain the flux level, of the predictions of modern models, summarized in Table 2.2. If

Quantity	Estimate	Second	Millisecond
Mass ($M_\odot$)	M	1.4	1.4
Radius (km)	R	12	12
Moment of inertia ($\mathrm{kg\,m^2}$)	$I = \frac{2}{5}\,M\,R^2$	1.6×10^{38}	1.6×10^{38}
Period (s)	P	1	10^{-3}
Rotation velocity (rad/s)	$\Omega = \frac{2\,\pi}{P}$	6.283	6 283
Braking (s/s)	$\dot{P}$	10^{-15}	10^{-18}
Luminosity (W)	$L = 4\,\pi^2\,I\,\dot{P}\,P^{-3}$	6.3×10^{24}	6.3×10^{30}
Magnetic field at surface (T)	$B = \sqrt{\frac{3\,\mu_0\,c^3}{32\,\pi^3}}\,\frac{\sqrt{I\,P\,\dot{P}}}{R^3}$	7.4×10^{7}	7.4×10^{4}
Magnetic field at r_L (T)	$B_L = B\,\frac{R^3}{r_\mathrm{L}^3}$	1.6×10^{-3}	1.6×10^{3}
Magnetic moment ($\mathrm{A\,m^2}$)	$\mu = 4\,\pi\,\frac{B\,R^3}{\mu_0}$	1.7×10^{27}	1.7×10^{24}
Electric field (V/m)	$E = \Omega\,B\,R$	7.5×10^{12}	7.5×10^{12}
Gavitational/electric force	$\frac{G\,M\,m_\mathrm{e}}{R^2\,e\,E}$	9.7×10^{-12}	9.7×10^{-12}
Light cylinder radius (km)	$r_\mathrm{L} = \frac{c}{\Omega}$	47 700	47.7
Polar cap radius (m)	$R_\mathrm{cp} = R\,\sqrt{\frac{R}{r_\mathrm{L}}}$	190	6 017
Potential drop across a polar cap (V)	$\Delta\phi_\mathrm{cp} = \frac{\Omega\,B\,R^3}{r_\mathrm{L}}$	2.2×10^{13}	2.2×10^{16}
Potential drop from pole to equator (V)	$\Delta\phi = \Omega\,B\,R^2$	9.0×10^{16}	9.0×10^{16}
Particle number density at R ($\mathrm{m^{-3}}$)	$n = 2\,\varepsilon_0\,\frac{\Omega\,B}{e}$	6.9×10^{16}	6.9×10^{16}
Particle number density at r_L ($\mathrm{m^{-3}}$)		1.1×10^{6}	1.1×10^{15}
Particle flux (s^{-1})	$\mathcal{F} = \frac{4\,\pi\,\varepsilon_0}{e}\,\Omega^2\,B\,R^3$	7.5×10^{29}	7.5×10^{32}
Plasma frequency at R (Hz)	$\nu_\mathrm{p} = \frac{1}{2\,\pi}\,\sqrt{\frac{n\,e^2}{\varepsilon_0\,m_\mathrm{e}}}$	2.3×10^{9}	2.3×10^{9}
Plasma frequency at r_L(Hz)		9.4×10^{3}	2.9×10^{8}
Cyclotron frequency at R (Hz)	$\nu_\mathrm{B} = \frac{e\,B}{2\,\pi\,m_\mathrm{e}}$	2.8×10^{18}	2.8×10^{15}
Cyclotron frequency at r_L (Hz)		4.5×10^{7}	4.5×10^{13}
Characteristic age (years)	$\tau = \frac{P}{2\,\dot{P}}$	1.6×10^{7}	1.6×10^{7}
Gravitational potential energy (J)	$E_\mathrm{g} = \frac{3}{5}\,\frac{G\,M^2}{R}$	$2{,}6 \cdot 10^{46}$	$2{,}6 \cdot 10^{46}$
Rotational kinetic energy (J)	$E_\mathrm{k} = \frac{1}{2}\,I\,\Omega^2$	$3{,}2 \cdot 10^{39}$	$3{,}2 \cdot 10^{45}$
Magnetic energy (J)	$E_\mathrm{B} = \frac{4\,\pi}{3}\,\frac{B^2\,R^3}{2\,\mu_0}$	$1{,}62 \cdot 10^{34}$	$1{,}62 \cdot 10^{28}$
Thermal energy (J)	$E_\mathrm{th} = \frac{3}{2}\,N\,k\,T$	$3{,}4 \cdot 10^{40}$	$3{,}4 \cdot 10^{40}$

Figure 2.12: A table summarizing many important pulsar parameters and characteristics, along with typical values for both regular pulsars and MSPs. From [42].

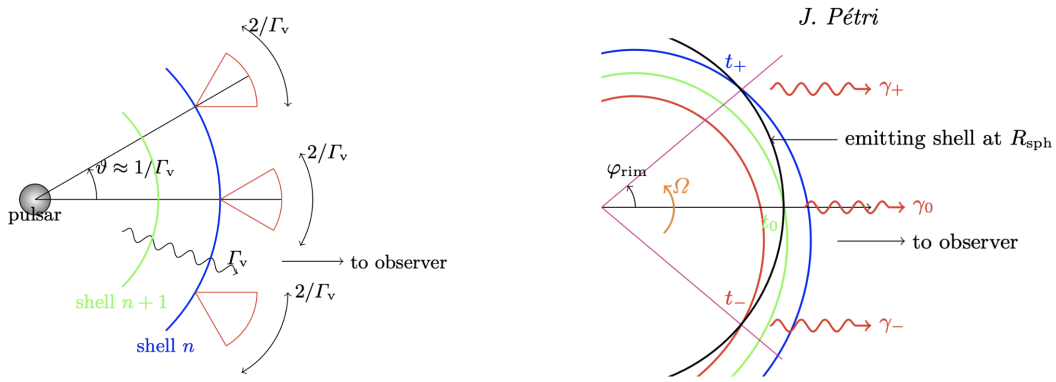

Figure 2.13: A simplified diagram showing concentric shells of plasma radiating at some point (blue arc), in this case the observer sees pulsed emission if the delay of arrival time of photons emitted by the shell is less than the time between adjacent sheets crossing the emission arc. From [42].

pulsed emission is detected with sufficient statistics to make claims about the morphology of the VHE light curve then comparison can be made to the expected phase-dependent features from simulations.

To properly model and understand the global pulsar magnetosphere, the plasma behavior must be fully, and realistically, realized. In particular, the rate of particle injection (particularly secondary pair creation) is one of the most decisive and important inputs to these simulations, and unfortunately, is one quantity that remains uncertain and unconstrained in literature [65].

Other challenges are yet to be tackled, in this endeavor for a fully-fledged model: it is proposed that GR adjustments to the models are necessary [74] [136] as discussed in section 2.2.5 and it is also clear that the limitations that the most modern simulations are subject to, need to be further investigated and addressed [64]. The recent flurry of interest and activity in pulsar modelling sure points towards further advances in modeling in the near future, making observations and analyses, such as this work, all the more valuable.

Table 2.2: A summary of applicable models considered for studying pulsars in the VHE regime, based on OG and CS scenarios. The Harding 2018 model also contains the mechanism in Harding 2015 and treats the accelerating E-field separately inside and outside R_L, improves the SC modeling and extends the considered energy range. Harding 2021 is an improved version of the Harding 2018 model; considering an even wider energy range, properly accounting for $\gamma - \gamma$ attenuation for IC photons and numerous other smaller improvements. As noted, explicitly for some models, softer SR seed photons are preferred to produce measurable VHE flux as higher energy photons undergo scattering in the K-N regime and so suffer suppression effects. The uncertainties in the older OG models meant that it was not certain that TeV photons would survive absorption.

Label & Reference	***VHE Production Mechanism***	***Scattering Plasma Population***	***Scattering Location***	***Target Photon Population***	***Expected Gamma-ray Energy***
Harding 2015 [29]	SSC	Secondaries	ECS	Soft Self SR	A few TeV
Harding 2018 [77]	IC	Primaries	ECS	SR from Secondaries	$\sim$ 10 TeV
Harding 2021 [32]	SSC/IC	Primaries & Secondaries	ECS	SR from Secondaries	A few TeV & $\sim$ 10 TeV
'Old' OG Models [137]	IC	Primaries	OG	SR from Secondaries	$\sim$ 100 GeV to $\sim$ TeV
Rudak & Dyks 2017 [126]	IC	Primaries	OG	Soft SR from Secondaries (Optical/IR)	$\sim$ 10 TeV
Lyutikov 2012 [28]	SSC	Secondaries	OG	Self SR (UV)	100s of GeV

CHAPTER 3

THE ATMOSPHERIC CHERENKOV TECHNIQUE

In this chapter I will briefly detail the physics of air-showers, in Earth's atmosphere, and how this leads to a powerful technique that can be used to detect the signature of primary gamma-rays coming from astrophysical sources.

3.1 Extensive Air Showers in Earth's Atmosphere

Unlike space-based gamma-ray telescopes, such as the *Fermi*-LAT, IACTs do not directly detect gamma-rays, but instead detect light from the air shower that is induced when a gamma-ray enters the Earth's atmosphere. When a 5 GeV[1] or higher energy gamma-ray interacts in the upper atmosphere with a molecule it creates an electron and a positron, imparting its energy to the newly created pair.

The primary particles undergo bremsstrahlung interactions with other atmospheric constituents, inducing energetic photons that also pair-produce to create secondary electron-positron pairs, quickly building an extensive shower of particles.

The conglomerate of charged particles radiate Cherenkov light (see [138] for a nice derivation and discussion), because the particles propagate with a velocity exceeding the phase velocity of light in the atmosphere.

3.2 Cherenkov Radiation

Any charged particle with $v > c/n$, in a dielectric medium, causes the formation of a light 'shock-front' as it polarizes the local medium in an anisotropic fashion. This occurs as the 'upstream' particles are only affected by the particle's EM field *after* the particle has

[1]Of course any photon with energy above twice the rest mass of the electrons can produce an electron/positron pair, but for a gamma-ray of less that $\sim$5 GeV the energy losses are so rapid that the shower never manages to develop, c.f. the dissipation that occurs towards the end of an EAS.

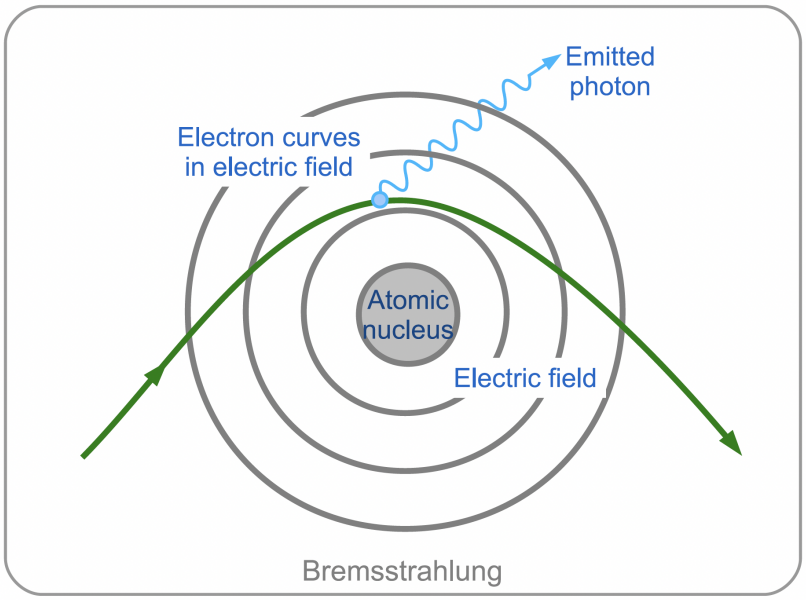

Figure 3.1: A cartoon representation of a particle emitting bremsstrahlung radiation in the presence of an atomic nucleus. The curved path of the electron is shown in green. From [33].

passed them, due to it's faster-than-light speed. As the local atoms/molecules relax, after the charged particle has moved on, they induce a net EM wave that is Cherenkov radiation. It is this blue-ish Cherenkov light is detected on the ground with IACTs (see [33]).

The spectrum of emitted Cherenkov radiation, by a charged, per unit length it moves and per frequency unit, follows the Frank-Tamm formula:

$$\frac{\partial^2 E}{\partial L \partial \nu} = \frac{q^2}{4\pi}\,\mu(\nu)\,\nu\left(1 - \frac{c^2}{v^2 n^2(\nu)}\right)$$

where $\mu(\nu)$ and $n(\nu)$ are the permeability and index of refraction of the medium, crucially, they are functions of frequency. The Cherenkov photons are emitted an an angle, θ_{ch}, such that $\theta_{ch} = cos^{-1}\left(\frac{1}{n\beta}\right)$. The Cherenkov angle in air is about $1.4°$, although it varies slightly with altitude, as the atmospheric density, and therefor local refractive index changes too.

As the shower quickly builds into a complicated combination of electrons/positrons and photons, it needs to be extensively modeled by simulations to allow the reconstruction of

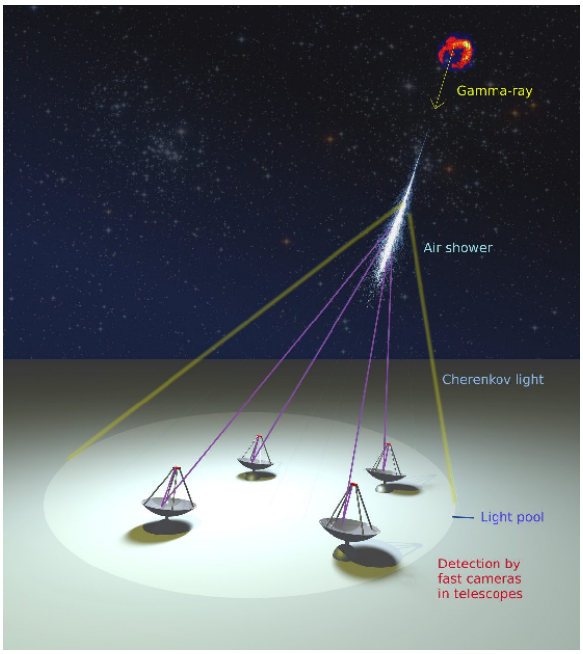

Figure 3.2: An artist's impression of the IACT technique, from [139].

the air shower, and hence the incident VHE gamma-ray that is responsible for it, from the recorded data.

A useful characteristic of the EAS, that is used in data analysis, is the definition of the 'shower maximum' (or shower max), where there exists the most charged particles in the shower's total development. This happens around an altitude of $\sim$10km, for typical target IACT gamma-rays. For all altitudes below, this the shower begins to dissipate energy[2] as the shower energy decreases due to ionization losses that dominate as the average particle energy become lower and lower. The shower is curtailed and the Cherenkov photons travel to ground-level. The 'pool' of Cherenkov light seen at the telescope level is typically $\sim$100m in size, for a TeV gamma-ray, and consists of approximately 150 photons m^{-2}, all arriving on the ground within several nanoseconds. The energy spectrum of the Cherenkov light increases as ν^2, but is cutoff around $350nm$ as atmospheric ozone absorbs lower wavelength photons (see [36] for further information and some nice diagrams).

[2]With respect to pair creation and Cherenkov radiation

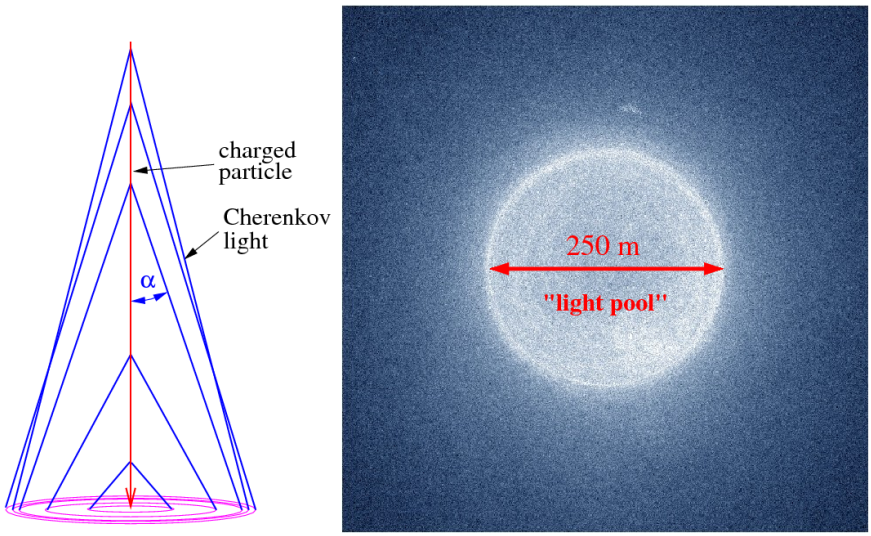

Figure 3.3: A diagram showing shower evolution, along with the Cherenkov angle, alpha, and a typical light pool from a zenith gamma-ray. From [139].

CHAPTER 4

INSTRUMENTATION AND ANALYSIS

In this chapter I will describe the VERITAS telescope array, along with the methods of data collection standard analysis.

4.1 The VERITAS Instrument

Operating since first light in 2007, at the historic site of the Whipple 10m telescope, the Very Energetic Radiation Imaging Telescope Array System (VERITAS) is the only of the three current IACT experiments that views the Northern Hemisphere.

4.2 VERITAS Signal Chain Overview

The Very Energetic Radiation Imaging Telescope Array System (VERITAS) is comprised of four IACTs located in southern Arizona (31 40N, 110 57W, 1.3km a.s.l.) at the Fred Lawrence Whipple Observatory (FLWO) [140]. The four Davies-Cotton telescopes each have spherical 12m focusing mirror arrays, consisting of 345 facets, and 499 photomultiplier tubes (PMT) pixel cameras, resulting in a $\sim 3.5^{\circ}$ field of view [141]. VERITAS is designed to be sensitive to gamma-rays in the energy range $\sim$85 GeV to above 30 TeV [142] and can detect a source exhibiting a flux of approximately 1% of the Crab Nebula in approximately 25 hours. The angular resolution of the array is better than 0.1° at 1 TeV and the pointing error is less than 50 arcseconds.

The High Voltage (HV) supplied to the PMTs is non-uniform across the camera pixels but is calibrated to maintain uniform performance across the detector channels[1], as each

[1]Throughout this these the words 'channel' and 'pixel' will be used interchangeably, unless explicitly stated. Strictly speaking, the precise VERITAS verbiage is: A 'channel' follows the numbering on the FADC boards, i.e. it conforms to *C*-style enumeration starting at 0 and running to 498. A 'pixel' follows the numbering in the camera, enumerated by 'physical' numbering with the first pixel at 1, and the last at 499

Figure 4.1: This classic image shows the four VERITAS telescopes and the control buildings at the base-camp. From https://veritas.sao.arizona.edu/about-veritas
image credit: SAO.

PMT delivers a slightly different response due to subtle manufacturing differences and intrinsic performance degradation over time (see section 4.9.1).

The single photoelectrons are detected, and the signal amplified, by fast, sensitive and high-efficiency Hamamatsu PMTs. The PMTs form the 'start' of the data-acquisition and digitization chain, that forms the back end of the instrument. The signal from each channel in the array is read out when a three stage trigger system is activated. The first (second) levels of the trigger requires a set amount of light in one (a neighboring group) of pixels. The third and final level requires L2 triggers in multiple telescopes within 50 nanoseconds of each other, and then the array is read out. This is a hardware implemented background rejection technique that both eliminates spurious events, such as muons, for example, and reduces the rate at which data is acquired to a more manageable frequency, typically on the order of several hundred times a second, while the flash analogue-to-digital converters (FADCs) are capable of digitizing signals up to 500 mega-samples per second (MS/s) with minimal read dead-time.

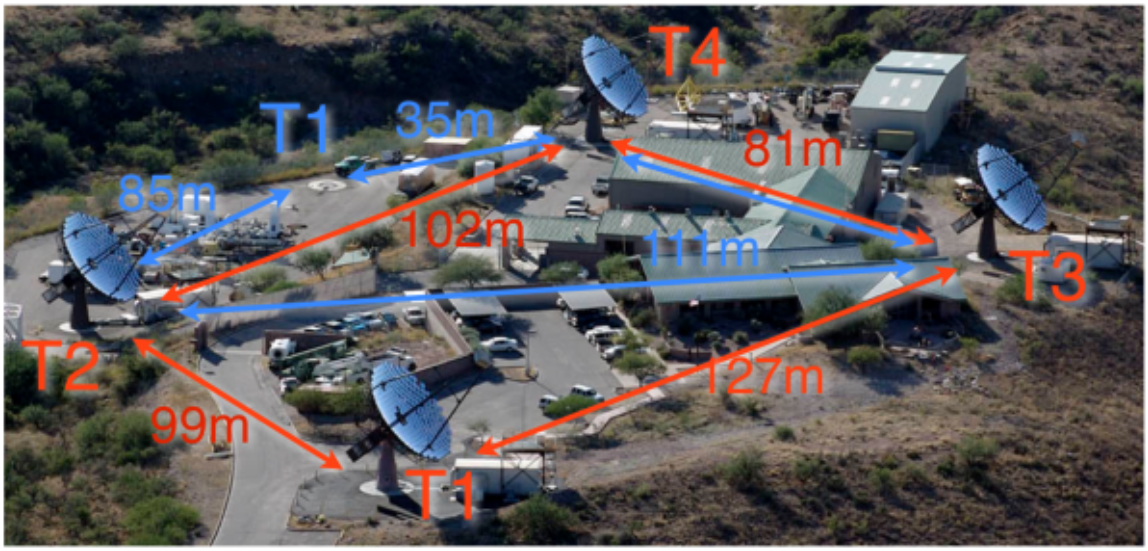

Figure 4.2: This image shows the layout, and distances involved before and after the relocation of T1, from [143].

4.3 Upgrades to the Array & Instrument Epochs

The four VERITAS telescopes are arrayed in a rhombus, with approximate side length of $\sim$100m, with the telescopes located at the vertices. Since first light, in 2007 (known as the 'Old Array' configuration), when all four telescopes were completed (with the first of the four finishing construction in 2005), the first telescope (known as 'T1') was moved to a new location on-site in 2009 (known as the 'New Array' configuration). This relocation of T1 increased the effective collection area for, and sensitivity to, EASs, but maintains a close enough proximity of each telescope to another to ensure that showers can be views by more than one telescope (see [143] for further details), ensuring the advantages of stereoscopic imaging (see section ...). In 2012 an overhaul of the cameras upgraded the PMTs to high-quantum-efficiency tubes, the epoch after the camera upgrade is know as the 'Upgraded Array' configuration.

4.4 Optics

As with the other current-generation of IACTs (see section 7 for the details on the realization on a novel telescope design) the VERITAS telescopes are designed around the Davies-Cotton (DC) style [144] single spherical reflector, 12m in diameter, resulting in a focal length of also 12m. The overall mirror comprises of 345 hexagonal facets, made of anodized and highly-polished aluminium-coated glass (see [145] for more details). Regular re-coating, re-anodizing and re-polishing of the mirror facets is a continual process as the typical local weather, along with monsoon and desert conditions, damage the mirrors over time, reducing reflectively. The on-site lab cannot keep up with the rate of degradation, resulting in a loss of sensitivity (see section 4.9.6 for more details) this problem is addressed in data analysis and a grant has been secured to contract a company to rectify the deterioration seen, in particular, over the last few years.

The overall mirror is formed by mounting said mirror facets on a rigid optical support structure (OSS), manufactured from steel, resulting in a manageable weight for telescope maneuvering. Each mirror facet is separately mounted on dynamic suspension mounts, which is essential for robust, and re-adjustable optical alignment. The DC design is deliberately a relatively simple one, consisting of a single reflector (originally designed for the U.S. Army see [146] for an interesting read on how this 'solar furnace' became a telescope optic standard). Unlike, say, a reflector of parabolic design, the mirror facets are all identical. This results in cheaper manufacturing costs and also allows replacement of any facet with any other. The DC reflector gives superior focusing quality over a parabolic reflector. The drawbacks of the configuration is a slight path-length difference for light reaching the camera focal plane, although the temporal dispersion caused to a Cherenkov light flash is less than about 4ns, and does not negatively impact the data.

The OSS is mounted on top of the telescope positioner (or 'tower') and also supports the camera, and housing, along with an adjustable counterweight to provide a more stable

Figure 4.3: A photo showing one of the VERITAS telescopes. The profiles of the profile of the camera housing along with the reflector can be seen. Also shown is the trailer that contains the necessary electronics and computing equipment specific to each telescope.

center of gravity for operation and slewing. The whole telescope assembly can be moved in elevation and azimuth, as fast as 1° per second, but is limited in the number of uninterrupted rotations it can make by various cables eventually restricting motion. Various systems assist in the correct pointing of the telescope (see section 4.8.5), resulting in a typical error of less than 100 arcseconds.

4.5 Cameras

The cameras of the VERITAS telescopes each comprise of a hexagonal lattice of 499 PMTs, forming the front end 'pixels' of the camera.

PMTs are vacuum phototubes that transform low light flux, down to individual photons, into a measurable electronic signal. The primary electron is released from the photocathode, by the photoelectic effect, with the energy of the incoming photon minus the work function of the conducting layer that forms the cathode. This single electron is focused by

a first electrode and then accelerated through multiple dynode stages, and finally collides with an anode that is connected to output terminals. By applying an increasing potential voltage to each dynode in the sequence, the electron(s) are rapidly accelerated and collide with each subsequent dynode, resulting in the release of further electrons and increasing the total charge of the signal. The population grows in this way until the electron population reaches the anode, producing an abrupt current pulse that is passed down the chain.

Each of the four telescopes in the array require two HV crates to supply the the VERITAS High Voltage (VHV) to the camera; one CAEN Model SY1527 (the larger of the two crates, labeled as 'crate 0') and a Model SY2527 (the smaller crate, 'crate 1'). The crates are turned on/off as observing is setup for/ends, as the HV can be potentially dangerous for personnel and the PMTs can be damaged if the HV is left on and they are flashed with too much light (observers can clearly see the effects of a car's headlights in the software GUIs, for example). There are 11 HV modules (CAEN A1932AN) per telescope, 8 in the large crate and 3 in the small, each providing HV for up to 48 channels (sub-divided into 6 groups of 8 channels per group). The exact voltage applied to each PMT pixel can be adjusted individually, however, the HV can only be turned on/off at the group level.

PMTs can exhibit extremely high gain (often amplifying the current from incident light by a factor of tens-of-millions), low noise and ultra-fast response through the UV, visible and near-IR parts of the EM spectrum. Although the technology is old (being first developed in the 1930s) and SiPMs (see section 7 for details on the pSCT camera) are being used in more modern instruments, PMTs work extremely well in this use for detecting Cherenkov light. The camera PMTs were swapped out in 2012 for an upgraded model of PMT. These new high-quantum-efficiency Hamamatsu tubes (model R.10560-100-20MOD) provide a $\sim$10% better peak quantum efficiency (the probability that an incident photon produces a photoelectron, usually expressed as a percentage) value than the old Photonis XP 2970/02 PMTs, and also move the peak of the sensitivity spectrum to close to 350nm (c.f. the old peak at 320nm) which is more desirable for detecting Cherenkov light,

while rejecting a larger proportion of unwanted background light. This has the effect of reducing the energy threshold of the instrument for increased sensitivity to the EASs, that it is designed to detect. This can be critical to gather sufficient statistics of lower energy gamma-ray events during observations of sources whose spectra may not extend far into the VHE regime, a good example of this could be the pulsars studied in this work.

To improve the signal-light collection efficiency of the camera each pixel PMT is married to a light cone, in the form of a custom shaped Winston cone (only passing incoming photons with an incidence angle of less than 30° from the optical axis, so helping to prevent background photons, with a large incidence angle, from making it to the camera focal plane), that gathers light through the hexagonal front aperture and passes it through the circular back aperture. This waveguide-like function maximizes the amount of light, that hits the camera plane, that is seen by the PMTs. This is easy to see geometrically, as the roughly cylindrical PMTs leave a significant fraction of 'dead space' between them when they are tiled into the hexagonal camera plane lattice. This system of having a smooth transition from the hexagonal cell structure to the lattice of circular PMT cross-sections nets a roughly 65% gain in effective light collection area, compared to having the raw PMTs, and gives every channel a field of view of $\sim 0.15^{\circ}$ (resulting in integral FOV of $\sim 3.5^{\circ}$ for each camera).

4.6 FADCs

The, now amplified, signal pulse from the incident photon is still analogue, and must be digitized for the back-end electronics further down the signal chain. This is accomplished by ultra-fast 'flash' analogue-to-digital converters (FADCs)[2]. These custom built boards

[2] 'Direct-Conversion', or 'Flash', ADCs consist of numerous comparators, each responding to its dedicated input-voltage range, so that sampling of the analogue signal proceeds in parallel, rather than sequentially, as in other types of ADC. One of the advantages of using FADCs is that the sampling and conversion of the input happens concurrently, allowing for a very fast response and therefor a high conversion rate (into the GHz regime, if required). This allows very rapid sampling of the PMT signal, which is necessary due to the shortness of the Cherenkov flashes to be detected, but comes at the cost of extensive comparator circuitry and complex encoder logic.

constantly monitor the output of each PMT channel at a sampling rate of 500 MHz, with a RAM 'ring' buffer with look-back depth of $65\mu s$ and a dynamic range of 8-bits. For the greatest precision possible, it is desirable to have the digitizer input signal span as much of the dynamic range as possible. To this end, two different pre-amplifier paths exist in the FADCs, known as the high/low gain stages, that are used to further expand the fraction of the dynamic range used by each individual signal event. The high gain circuit features a gain of 6, the low gain stage has a gain of 1 and is artificially delayed w.r.t. the high gain circuit. If the high-gain stage causes saturation, i.e. the signal exceeds the usable range in the digitizers, then the output from the low-gain channel is used instead. Understanding the nuances of this 'hi/lo gain switch' has proven non-trivial over the years, and takes considerable effort to accurately reproduce the behavior when tailoring the simulations used for the analysis chain of the instrument (see section 4.12). The noise stays below one digital count on all channels, as does crosstalk on adjacent channels, even when a maximum amplitude pulse is seen.

Clearly, constantly polling every PMT channel at all times would accrue lots of useless information (indeed this isn't actually possible as there is a non-zero dead-time when the array is readout) and so deciding when to record the low-level readout from the cameras requires some kind of trigger logic, which we discuss in the next section. When the array trigger occurs the digitization is paused and the data acquisition process begins and the memory of all channels are checked for a signal, above a set threshold level.

4.7 Multi-Level Trigger

The VERITAS array employs s three-level trigger system to algorithmically decide when the camera signals should be readout and stored.

4.7.1 The First (L1) Trigger Level

This lowest level, also known as the pixel-level trigger, is a channel-by-channel threshold set to minimize possible triggers due to unwanted night-sky background (NSB) light. 'Constant fraction discriminators' (CFDs) are used to set this lowest threshold. They are signal processing devices that trigger not only on a 'hard preset' voltage level, but instead when the signal reaches a set fraction (the 'constant fraction') of the peak of the pulse, giving 'accurate timing information for signals of differing peak height but similar same rise time' (see: https://jrm.phys.ksu.edu/Resource/Pubs/CFD/CFD.html for a brief explanation). Requiring certain characteristics of the PMT pulse to be above a certain pre-set, but relative to the event, level. This gives a robust temporal trigger flag and to be non-errant in avoiding tine walk while fitting the given threshold parameters, regardless of the exact pulse shape, to reject background-induced triggering. The minimum threshold value that the CFDs need to report a trigger is determined by regularly taking runs where the CFD threshold is ramped through a series of values while the trigger rates are recorded. The rate vs threshold relationship is examined for the point where NSB triggers are suppressed enough to leave, predominantly, air shower events.

4.7.2 The Second (L2) Trigger Level

When any individual channels fit the criteria for a positive L1 trigger, this information is passed to the L2 trigger. Also known as the 'pixel-group' or 'telescope-level' trigger, the L2 trigger threshold is set on identifying if a set of pixels in the camera (of a single telescope) pass the L1 criteria in a given window. This is a very important step in the background rejection, as a flash of Cherenkov light will be expected to be seen in many channels, where as sporadic L1 triggers from NSB, or even noise in the electronics themselves, should have no overall spatial correlation with each other. The required 'geometry' of a successful L2 trigger stipulates that at least 3 adjacent pixels provide a positive L1 output in a space of $5ns$, the number of required channels and the length of the time window has been found

to be optimal in studies looking at the peak rejection of background and acceptance of gamma-ray shower images. The current field-programmable gate-arrays (FPGAs) that are used for the modern L2 system were an upgrade (in late 2011) from the original hard-wired system, for more details see [147]. The hardware employed consists of three Xilinx Virtex-5 FPGAs (which each monitor a sector of one third of each camera) and a single Virtex-4 FPGA board, which collates the signals from the three sectors, and, if the conditions are met, passes this information on to the next stage in the trigger. The upgraded system allows improved accuracy in timing alignment of different pixels, and also allowed for custom delays to be set at the channel level (this is used to account for path-length differences in the signal cabling that is physically required to connect the hardware) and, as a result, allowed the tightening of the L2 trigger window (previously it had to be as long as 8ns) for the temporal co-occurrence in the triggered hit-map of pixels. This gave the opportunity to lower the L1 threshold, hence lowering the overall array's energy threshold, without resulting in more background triggers.

4.7.3 The Third (L3) Trigger Level

The final stage in the complex trigger system is the 'multiple-telescope' or 'array-level' trigger. The output from the L2 hardware, hosted in the electronics trailer next to each individual telescope, is fed to the L3 system in the central control building. When the light pool of Cherenkov photons from a gamma-ray induced EAS reaches the ground it typically covers around $\sim$100m. Given that the spacing of the telescopes is slightly less than this, looking for coincidence in separate telescopes is another powerful way to reject background triggers. While nuisance showers, such as muon-induced hadronic showers for example, can frequently result in an L2 event, it is usually confined to the area on the ground seen by just a single telescope. The multiplicity of required telescopes is typically set to 2 (or more) for standard observing. As in the L2 system (there at the channel level), delays in the path length need to be accounted for (now at the telescope level), before checking if the

triggers arrive in the desired window. In addition to this, the geometry of the evolution of the Cherenkov light pool, and therefor timing differences due to the light propagation time, are also taken into account in telescope-pointing dependent processing modules. After this book-keeping is done, the L3 system looks for successful L2 triggers in a window of time of 50ns, if this condition is met, finally, the array is readout and the data is saved; the relevant 16 sample ($32ns$) data block is dumped to a separate 8MB buffer.

When a successful L3 trigger flag is achieved the central L3 computer tells the electronics (known as the 'Event Builder' program) for each individual telescope, to record the FADC traces (including a time-tag) along with a binary mask that enumerates the participating pixels (telescopes) in the L1/L2 (L3) trigger (i.e. which channels caused the L1/L2 trigger), so that the participating pixels in each event are saved. As this data is being readout from the array systems the L3 is artificially blocked by a 'busy' signal, the array cannot trigger another L3 event during this time leading to a 'deadtime'[3] fraction, during data-taking, that is a function of the L3 rate. All this information becomes the lowest level of data product from the array. The centralized event 'Harvester' machine collects the prior mentioned data and creates 'banks' in a file that records all events in each observing run, typically each run consists of around 30 minutes of observation time but can be extended, shortened or ended, by the observers, as needed. An in-house, specially created format known as 'VERITAS Bank Format (or VBF) is used for the data files (along with MC simulation files) for storing the data. The relevant libraries and software to interact with the VBF files, written in C++, are distributed with the VERITAS analysis software. The complete VBF files, roughly 10 GB in size, are hosted locally until they can be sent to a centralized archive, hosted by UCLA, and from there individual analyzers can retrieve the raw data to begin their offline analysis.

While data is being taken, a rudimentary real-time event reconstruction is handled by 'Quicklook'. This online analysis employs a stripped-down version of the full, standard,

[3]It takes about 400μs to finished the readout of a single array event, this leads to an approximate 12% deadtime fraction for standard observational rates of around 300Hz.

Hillas analysis (see section 4.11) and therefor lacks the robustness and accuracy of the full offline analysis packages. It can be useful in some situations, for the observers to get a rough idea of the events being recorded, and is also used as a coarse benchmark to decide if a signal might be being seen (when tracking a transient alert, for example) where the time dedicated to an observation is variable in extent.

4.8 Maintenance and Calibration

For optimal operation of the VERITAS array several peripheral systems are used, both during observing, and on a non-continual but regular basis, to ensure that data-taking and analysis is standardized in time.

4.8.1 Allsky Cloud Monitor

To monitor the sky about the observatory a CCD 'Allsky Cloud Monitor' camera that gives an upward facing view of the overhead conditions for observers to check for clouds etc., is used. This camera can be viewed, via the web, from remote and is used as a very quick sanity check of the local weather and atmosphere.

4.8.2 Far-Infrared Radiometers & LIDAR

In addition to the CCD cloud monitor, two far-infrared radiation pyrometers ('FIRs') are deployed on two separate telescopes to directly monitor the area of sky targeted during observing runs. If any cloud is present, the recorded temperature of the pyrometers increases, allowing real-time tracking of weather effects that might scatter air shower light, or introduce polluting background light. In 2012 the monitoring system was augmented with a Vaisala CL51 LIDAR device, that measures the fraction of reflected light from an InGaAS laser pointed to zenith, operating at 910nm, to quantify cloud influence as high as 13km in altitude. Data from the FIRs and LIDAR is recorded and can be used to assign a quality rating to the weather during a run (usually in tandem with any changes in the L3 rate) or

Table 4.1: Images showing the Allsky Cam view in the evening, the camera itself and some control software, with an image of the night sky. From the VERITAS internal wiki page for the Allsky Camera.

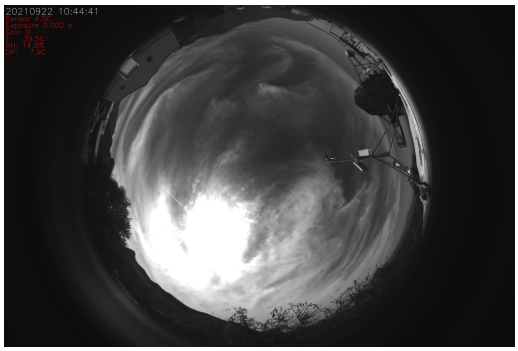

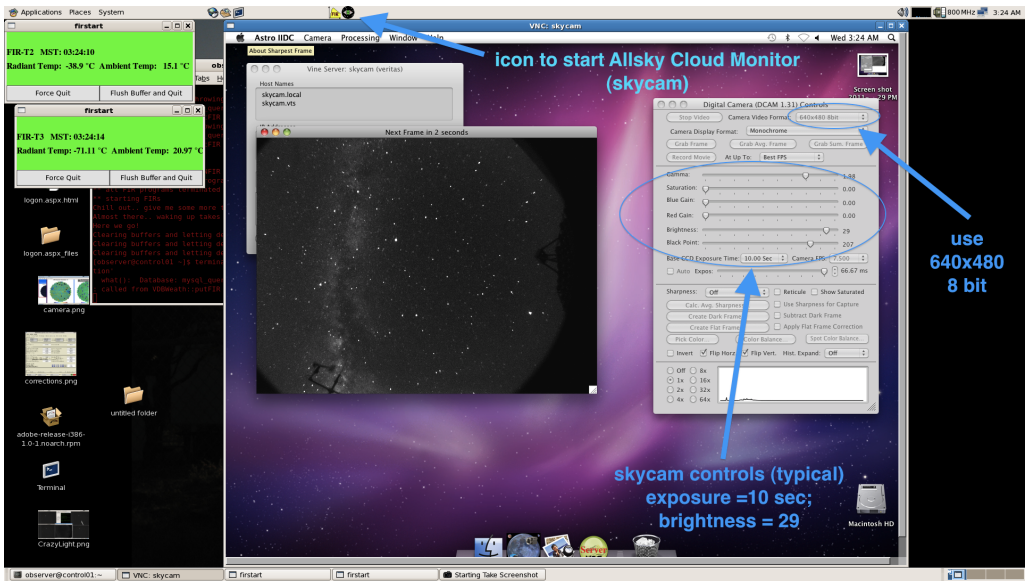

by offline analysts, who may have differing needs in terms of data selection criteria.

4.8.3 Mirror Alignment

To check and hone the alignment of the mirror facets a special CCD camera is mounted in the center of the focal plane, where all rays parallel to the telescope axis, should be focused. The usual procedure involves scanning about a bright star and measuring the intensity of reflected light, from each individual mirror facet. The required adjustments to the alignment of the facet are derived from the brightest reflection in the process, which also give its current orientation.

4.8.4 Whole-Dish Reflectivity

To monitor the empirical reflectivity of each telescope (a function of the quality and alignment of the mirror facets) a relatively simple procedure has been devised to monitor both the direct light from a bright star, and the light reflected back from a target of known reflectivity that is mounted in the focal plane of the camera. A dedicated camera is mounted on the OSS of each telescope and a special plate (called the 'Spectralon target') with reflective material covering where the pixels would be if the plate were not mounted, is temporarily attached over the focal plane. The telescope is then pointed at a chosen bright star such that the camera has both the star and the Spectralon target in its FOV. Given that the target is of known reflectivity, the overall whole-dish reflectivity can be calculated from the ratio of the two intensities.

4.8.5 Pointing Monitor and Cross-Calibration

The VERITAS Pointing Monitor (VPM) System uses measurements of the position of stars to determine the actual pointing orientation of the telescopes, with arcsecond-level of precision. There is one pointing monitor apparatus per telescope, each consisting of; two sets of twin reference monitoring LEDs mounted on the focal plane (physically attached

Figure 4.4: A picture showing the dedicated camera mounted on the OSS of one of the VERITAS telescopes. From the VERITAS internal wiki page for Optical Reflectivity.

to the same plate that houses the light cones), a sky camera (a Prosilica EC1380 CCD Camera), to track the stars in the FOV, a focal plane camera (again a Prosilica EC1380 CCD Camera) and a dedicated computer, mounted on the OSS that controls the system. The VPM equipment is turned on during night time observation startup, and the images from the cameras can be monitored from the control room as a peripheral tool. During gamma-ray observations the focal plane and sky monitoring cameras process the positions of stars in the sky, and their images on the focal plane relative to the reference LEDs, and write this information to a general VERITAS database. Images of the star positions are taken with a cadence of 0.5 Hz, with a detection threshold that can be manually changed (although it remains static, as standard) typically detecting between 50-70 stars per image for good observing conditions. This information is processed, using the star-matching software 'astrometry.net', to get the calibrated pointing of the CCD camera, which can then be converted into the raw orientation of the VERITAS camera, so that the actual precise telescope pointing can be calculated and used during analysis of the taken gamma-ray data.

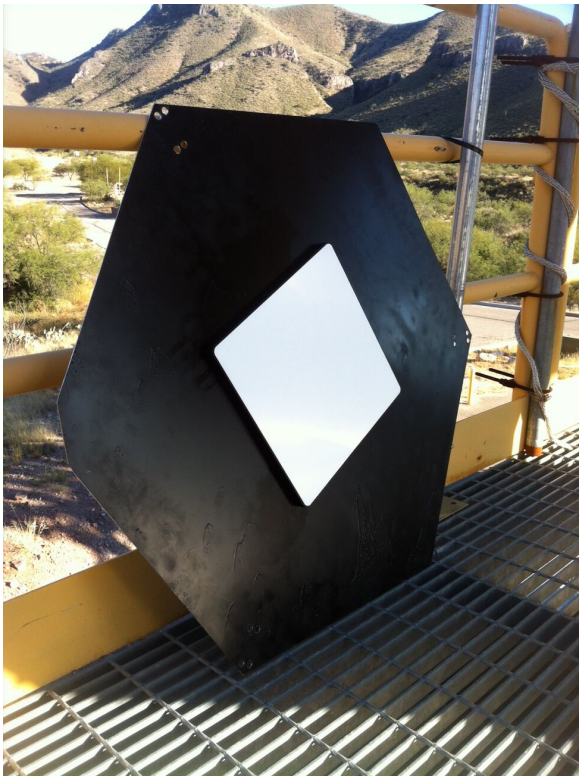

Figure 4.5: A picture of the custom Spectralon reflectivity plate, placed on the access platform of one of the telescopes. From the VERITAS internal wiki page for Optical Reflectivity.

The VPM system is cross-calibrated with the telescope at the start of every 'Dark Run' (the name given to the roughly month-long period of time when the nights are sufficiently dark at the observatory to gather quality data, while the moon does not interfere significantly with gamma-ray observations) or if any maintenance work is done that could have an effect on any hardware that might offset the telescope pointing. The necessary measurements for the VPM calibration are taken simultaneously with measurements of the On-Axes Point Spread Function (PSF). To perform the measurements required for calibration a dedicated hexagonal screen, reinforced with aluminium struts, is placed atop the light cones. It has cut-outs to expose the monitoring LEDs and only a thin covering of the central pixels of the camera. Next, a list of candidate stars and their coordinates on the sky is generated from software, containing bright (brighter than magnitude 4.5) stars in order of current zenith angle. The list deliberately excludes stars that can cause problems with the procedure such as those that are; near the south celestial pole, in double star systems or in bright clusters. These $\sim$30 selected stars are then sequentially slewed to, as to obtain measurements from throughout the phase space of elevation angle, and an image is saved as a FITS file from both the focal plane and sky cameras. For each set of these pairs of images the centroid of each star is computed, from a routine fitting algorithm, in both the sky and focal plane images, along with the positions of the LEDs. From the position of the LEDs the exact position of the center of the PMT camera is known. The offset between the center of the camera and the actual location of the star centroid is calculated, with reference to the star position in the sky camera FOV, and these offsets are tabulated as a function of elevation. The data can be fit and compared to the last calibration results as a sanity check. The results of consecutive calibrations should agree to within a few pixels, unless a telescope as been knocked into significantly by something. The PSF is then parameterized by fitting a Gaussian function to the image of the star on the focal plane. The containment diameters (the size at which the desired fraction of the light on the focal plane, from the point source, is within) are calculated for 68%, 80% and 90%. The 68% containment value is usually

the quoted value of interest, but the others are monitored too to check for uncharacteristic behavior.

4.8.6 T-Point

In addition to the cross-calibration of the telescope and pointing monitor the so called 'T-Point' measurement is made to enhance the framework used by the telescope pointing/source tracking software, to orient the telescopes in RA/Dec on the sky. A raster scan of suitable stars is performed, in a similar way to the VPM calibration discussed in the previous subsection, covering the whole sky in grid-steps of about 30° in Azimuth and 15° in elevation. The targets are selected, the nominal coordinates that the star should be precisely seen at are slewed to and then each star centroid is further manually aligned in the focal plane image by making small adjustments to the telescope pointing (these adjustments can be as fine as changes in pointing corresponding to moving focal plane images less than 1% of the size of the PMTs) the pointing of the telescopes is recorded when the image is positioned within the acceptable window. The measurements of these telescope corrections (the required input corrective offset needed to exactly align the focal plane centroid with the central channel) are then compared with the current set of corrections in the database. A simple model with a few free parameters that represent El/Az offsets and angular dependent changes in the OSS rigidity along with telescope velocity hysteresis effects, for example, is fit in an attempt to reduce the RMS residuals between the corrections and the expected pointing. If the RMS of the 'disagreement' between true and expected pointing can be decreased (typically required to be less than 0.005 in RMS residual) then the new model is adopted. This new model is then checked by slewing to a target star and checking that, with the new pointing model, the star centroid is closer (it should now be very close) to the center of the camera.

Table 4.2: Images showing the GUI used for the T-Point fine adjustments, along with some of the model parameters that are used to fine-tune the pointing software, and the screen used for VPM and PSF measurements. From the VERITAS internal wiki page for Pointing Calibration.

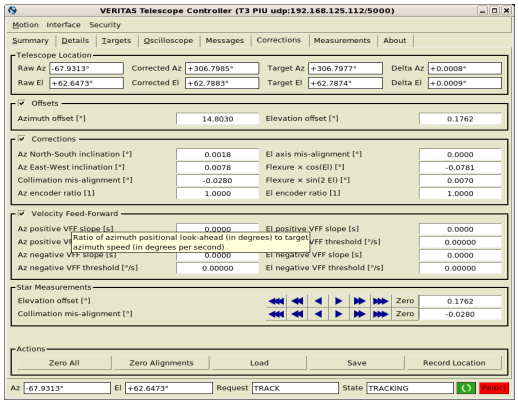

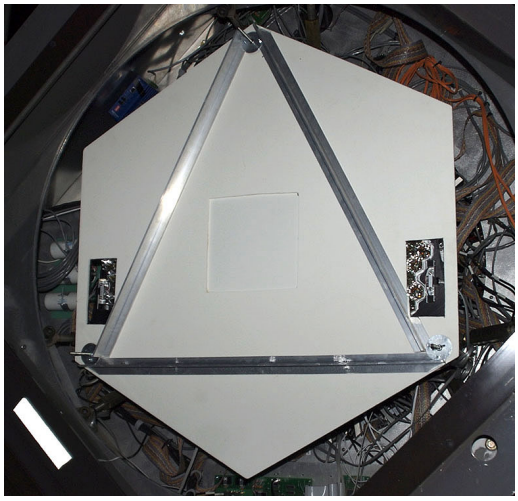

4.9 The VERITAS Flasher System & Flasher Runs

A system of blue LEDs is used to flash the VERITAS camera PMTs in order to regularly surveil, and keep track of, their actual gain and timing profiles. The LED flasher is also used to check the overall linearity of PMT/FADC system and can be adapted, with a neutral density filter, to evaluate the channel's behavior when a single photoelectron is incident, as to understand the response of the front end at the most fundamental level. Each flasher module consists of 14 (upgraded from the initial 7) identical InGaN LEDs (originally Optek OVLGBOC6B9 LEDs, but upgraded to Nichia NSPU510CS UV LEDs) with a nominal brightness of 3200mcd and a peak wavelength of $\sim$375nm. The flasher LEDs are protected by the housing of an altered flashlight, offering good protection from the desert conditions, which permits the system to be permanently mounted on the telescope without issue. The flasher units are placed around 6m away from each camera, mounted on the quad-arms, pointed at the focal plane.

The light from the LEDs is spread among the PMT channels with a 50mm opal diffuser

(Edmund Optics NT46-106), so that each pixel experience the same light intensity. After tweaking the driving electronics from the LEDs, the flashes delivered to the PMTs are sufficiently narrow ($\tilde{1}$0ns) to mimic Cherenkov events (and are satisfactory, compared to the old laser system, retired in favor of this LED system due to cost-effectiveness and robustness). Using the fast-responding LED flashers allows quick accumulation of photo-statistics, as the highest possible rate of the illumination of the PMTs is limited by the maximum DAQ rate (of several hundred Hz), rather than the flasher hardware (which can be pulsed faster than 1000Hz). This means that methods that require the acquisition of large statistics, such as the 'single photoelectron' calibration check can be taken in runs of relatively short duration (of the order of a few minutes), which then minimizes the observational dark time that has to be allocated and set aside for such dedicated calibration time-requirements. The robustness of the LED system, which does not require optical fibres, as the laser system did, alongside its cheap cost (meaning spares can be readily produced), limits any potential impact a failure of the system would have, and reduces potential down-time of the telescopes because of it, significantly.

A simple IC is used to provide power to the LEDs, which can be triggered externally by a NIM-level pulse or internally by the 10Hz oscillator built in. The control also moves the flasher through a sequence of turning on the individual LEDs, between no illumination and all fifteen on, sequentially, so that the light intensity ramps, step-wise, through fifteen different levels. This ability is used to probe the PMT and FADC behavior throughout the operational range of the channel front-end, in both the low-gain and hi-gain FADC channels.

A two-minute long dedicated flasher run is taken on a dark patch of sky every night of observing (and taken more than once per night if the observing conditions change, like changing to RHV for moonlight observing, for example), every data run taken that night is coupled to this flasher run and is used in the analysis of said data run (see section ... for more details).

4.9.1 HV Calibration

The flasher system, described in the previous section, is primarily used to monitor the gain characteristics (and changes to said gains) of the camera PMTs, but also provides timing information for each channel. Assessment of the channel gains is done in two main ways; looking at the 'Relative Gains' of different channels in each camera, compared to the average for the entire camera, and changing the HV to make this as uniform as possible, in a process known as 'Flat-Fielding', and calibration of the Absolute Gain of the channels (measured in digital counts per photoelectron or 'dc/pe'). Although flasher runs are taken every night, the dedicated single PE calibration runs discussed further below, are only necessary every few weeks.

4.9.2 Relative Gains and 'Flat-Fielding'

Ideally, for the same incident light we would want to see the same pulse-height, for the trigger electronics, and the same integrated charge, for the analysis. Due to inherent, and practically in-avoidable, channel-to-channel variations this is generally not the case in practice. The gain of each channel, in each VERITAS camera, is compared with all other channels in the same camera by comparison of said channel's average pulse size to the aggregated, average, pulse size of all channels, from a uniform illumination from the flasher system.

The procedure is as follows: for every LED flash, the integrated pulse size for every channel is recorded, along with the calculated-average of all the camera channels. This information is stored in different histograms for each channel, and a separate histogram for the camera-averages from which the reference size (or 'monitor') value is determined.

As all the PMTs in the camera participate in this check any random fluctuations in photostatistics on a channel-to-channel level should be averaged out, along with probabilistic fluctuations of the PMT gain due to the internal gain stages, over tens-of-thousands of flasher pulses. This is done for all fifteen light levels of the flasher intensity ramp, and results in a distribution of recorded pulse sizes for each channel (and the calculated aver-

ages) that inhabits fifteen non-overlapping Gaussian distributions, each individual Gaussian corresponding to one of the different flasher light intensities. The means of these fifteen (denoted with 'i' to differentiate the part of the overall distribution that is due to each light intensity level) Gaussians are calculated for each channel, giving $\mu_{channel,i}$, and for the camera-average giving $\mu_{monitor,i}$. The variances, $\sigma^2_{channel,i}$, of the distributions are also calculated for use in the 'photostatistics method'.

The individual channel-specific means $\mu_{channel,i}$ can be plotted vs. the monitor camera-mean size $\mu_{monitor,i}$, as a function of light intensity, and fitted with a straight line. The gradient of which, gives the resulting relative gain of the channel in question. For an ideal camera, where all channels are perfectly uniform, the slopes of all such plots are unity.

The derived quantity that is the slope of the fitted line indicates the channel performance, which incorporates the nuances of all parts of the pixel response, for the amount of light seen, such as; the PMT quantum efficiency, the probability of the photoelectrons successfully impacting the initial dynode stage, the realized gain of the following dynode stages, the gain of the pre-amplifier, any subtle differences in the FADC channel, gain-drift, cathode degradation, etc. If a non-uniformity (or a change as a result of use/aging etc.) occurs then the slope of the plot will vary and, rather than trying to compensate by changing the hardware in any way, the gain can be altered, by directly changing the applied HV to each channel, to make up for these discrepancies. In reality it is sufficient, and more trouble than it is worth to do better than, to have relative gains that differ by about 1%. This is what is accepted in practice and the small deviation from the ideal scenario is taken into account in data analysis suites.

Although the aforementioned plots can be made with only two data-points (in order to determine the gradient), for example a pedestal 'dark' light level and one illuminated light level, the linearity of the channel front-end is demonstrated with the ramp through the difference light intensities, and their respective points in the set of plots. This process yields a response across the entirety of the PMT population, that is as uniform as possible.

The relative gains are derived from a standard flasher run, of extended duration $\tilde{3}$ minutes, with an event capture rate of around 300Hz.

The 'theoretical' HV value needed to flat-field a camera can also be calculated by taking the same measurements as in the above procedure but for several different values of the HV settings. For example, flasher runs can be taken at 95%, 100% and 105% of the nominal HV values to extract the pixel charge dependence on the applied voltage. This relationship can then be inverted so that each channel gives a standard pulse size. However, as changes to the set HV values can take as long as several minutes to fully settle to their true values, this process can consume an unwanted amount of observational dark-time, and if one tries to take the calibration data before allowing the HV to fully equalize deviations from the expected levels introduce error in the results.

4.9.3 Absolute Gains

While the practice of flat-fielding each camera is an important factor in maintaining a uniform and stable response to incoming shower photons, measurement and understanding of the actual or 'absolute' gain response to light, of every PMT channel, is of vital importance as well for robust reconstruction of EASs. Determination of the absolute gains on a per-pixel basis is achieved in two ways, with the VERITAS telescopes. Firstly, the method of 'photostatistics' exploits the statistical link between the mean and variance seen in the size of the pulses, due to quanta of charge being amplified. The second, uses analysis of very low light intensities to probe the distributions seen when only a very small number of incident photons are allowed into the PMTs. The two methods employed agree to better than 5% discrepancy, which is taken to be the level of the systematic uncertainty of the absolute channel gain.

4.9.4 The Method of 'Photostatistics'

In the method of photostatistics, the relationship of interest is that of the link between variance of an individual channel's pulse size distribution and of the mean size of the pulses, for the different flasher intensities. A statistical argument can now be made for the absolute gain of the channel: considering the, strictly Poissonian, but in the limit of the relatively large mean number of photoelectrons involved in each event, distribution of the photoelectrons, there is some average N_{pe} of photoelectrons at the first dynode stage, then, given the relatively large number of incident photons, an approximately Gaussian fluctuation level of $\sigma_{pe} \approx \sqrt{N_{pe}}$. For a particular channel (and, as before in the relative gains methodology, considering each flasher intensity separately), after all the amplification has taken place we have, $\eta_{channel}$ photoelectrons, with gain denoted $G_{channel}$ then;

$$\eta_{channel} = G_{channel} N_{pe}$$

and, due to the nature of multiplying a normally distributed variable by a constant,

$$\sigma_{channel} = G_{channel} \sigma_{pe} = G_{channel} \sqrt{N_{pe}}$$

Hence, after amplification the variance in the charge distribution seen is

$$\sigma^2_{channel} = G^2_{channel} N_{pe} + \sigma^2_{Pedestal}$$

In the above equation $\sigma^2_{Pedestal}$ has been included to account for the contribution to the fluctuations seen due to the real-world effects of noise in the channel electronics and from stray (unwanted background) light entering the PMT. Combining this equation with our previous expression for $\eta_{channel}$ we obtain;

$$\sigma^2_{channel} = G_{channel} \eta_{channel} + \sigma^2_{Pedestal}$$

From this relation we see that by plotting the pulse sizes, which is simply recording the integral of the digitized charge, and is directly due to photoelectrons at the anode, against the variances in the sizes, an independent measure of the absolute gain is made. This is done for each flasher intensity, again, mimicking the procedure taken for the relative gain assessment, with the offset in the plots due to the pedestal noise level that is independent of the LED light level.

As mentioned previously, there is some inherent statistical fluctuation in the pulse sizes seen that is solely due to the probabilistic nature of the photoelectron multiplication mechanism at each dynode stage (i.e. there is a stochastic broadening in the number of electrons emitted and that successfully impact on the next dynode). This is because there is an intrinsic variance in the number of additional electrons released, and therefor amplifying the signal, for each successive gain stage. Our derived expression only accounts for fluctuations due to the variance in the number of initial photoelectrons and so a correction needs to be applied to consider these 'internal' (to the PMT) variances. This additional factor can be measured by studying the response to only a single indecent photoelectron. If this is the case, then N_{pe} is know to be one, with no deviation, and so any further fluctuations that broaden the pulse distribution are due to effects in the gain stages. The required statistical model has been thoroughly investigated throughout the 20th century [148] and the resultant distribution is established as the Polya (also known as the 'negative binomial') distribution. The Polya distribution arises when a series of sequential processes occur that all follow Poissonian statistics, but with differing mean parameters [149], this is exactly the situation for the multiplication of the electron population that occurs at each dynode stage in the tube. Sufficient for the method in this case is the modification by a Polya correction factor to be applied (see [150] and [151] for further discussion). In situations such as this, we account for the spectral broadening of the single photoelectron response with the introduction of the additional variance term $\phi^2_{channel}$. The resultant effective distribution leads

to the following expression for the gain, taking all the above into account:

$$G_{channel} = \frac{\sigma^2_{channel}}{\eta_{channel}} \left(\frac{1}{1 + \phi^2_{channel}} \right)$$

The value for $\phi^2_{channel}$ is ascertained as part of the parameterization and fitting done in the 'Single Photoelectron' procedure, discussed in the next section. It is, perhaps, of no surprise that to fully characterize the pixel response, rigorous understanding of how the PMTs react to a single light quanta is required.

4.9.5 'Single Photoelectron' Runs

A more direct, but with its own practical challenges, measure of the gain is also possible. This is achieved by analyzing the average pulse size distribution, due to individual (or, at least, small numbers of) photoelectrons (see [152] for a similar methodology practiced by another experiment). The expected charge delivered by a single photoelectron that is liberated from the anode, and successfully amplified is, simply, Ge. Where e is the magnitude of the elementary charge, and, as before, the gain includes all amplification down-stream of the first dynode stage. This is achieved, with the VERITAS cameras, with the so-called 'holey plate'; a sheet of aluminium with a precisely placed hole over the center position of each PMT. This plate attenuates incident light by a factor of $\tilde{1}00$. By physically blocking light access to the PMTs, and using a low enough flasher intensity, the light level seen by the camera is a distribution of traces that are due to mostly zero photoelectrons, some single photoelectrons, fewer pairs of photoelectrons, even fewer triplets of photoelectrons, and so on. The attenuation from the holey plate also limits the background light entering each PMT.

The probability of a pulse pertaining to N photoelectrons is given by the Poisson distribution;

$$Poisson(N, \lambda) \equiv P(N, \lambda) = \frac{\lambda^N e^{-\lambda}}{N!}$$

With λ being the mean number of photoelectrons observed. Using a statistical model, the trace-sizes recorded can be analyzed and a fit to the data is performed. The charge recorded, from each individual photoelectron amplified through the dynode chain, is normally distributed; parameterized by a mean, δ, and a variance ϕ^2. In this formalism the value of the mean-parameter δ is the value of the absolute channel gain, that is to be determined. We define the Gaussian distribution (also known as the 'Normal distribution') here, with mean μ and variance σ^2, as;

$$Gaussian(\mu, \sigma^2, x) \equiv G(\mu, \sigma^2, x) = \frac{1}{\sqrt{2\pi}\sigma} exp\left[-\frac{(x-\mu)^2}{2\sigma^2}\right]$$

When no photoelectrons are released there is a so-called 'pedestal offset' charge contribution (thus named as it 'raises' the pulse values seen on the ever-present background pedestal value), in this context[4], this is purely determined by characteristics of the channel electronics chain and its consequence is the 'zero-photoelectron' contribution to the overall charge distribution. The pedestal peak in the charge distribution is also characterized by a Gaussian function, now with mean (sometimes referred to as the pedestal/pedestal value/pedestal offset) β and variance (referred to as the pedestal variance or 'ped var') γ^2.

Combining the above contributions, for N flasher pulses, we obtain a charge (q) distribution of;

$$F(q) = N \sum_{n=1}^{m} P(n, \lambda) G(n\delta + \beta, n^2\phi^2 + \gamma^2, q)$$

With P & G indicating the Poissonian and Gaussian distributions, defined previously, λ is the average number of photoelectrons released from the anode (here, it is related to the PMT quantum efficiency) and n being the number of photoelectrons impacting the initial dynode stage. The overall distribution is formulated of overlapping Gaussians, whose

[4]In general IACT terminology, 'pedvar(s)' are due to electronic noise, internal to the signal chain ***and*** external sources of background light, such as NSB, that are always present in the FADC readout when there is not signal (i.e. Cherenkov) light in the trace. A known DC voltage pedestal-offset is deliberately introduced to the PMT signal output, so that both upward and downward variations in the pedestal-level value can be quantified and corrected for.

relative amplitudes are determined by the Poisson probability of the corresponding given number of photoelectrons, contributing to the charge-peak, having impacted the first dynode, and the means, and characteristic widths, of said Gaussians, increase with the number of initial photoelectrons involved. An example of the resultant charge distribution, and the individual 'sub-distributions' that contribute, from the above equation, and are used to fit for the specific parameters is shown in figure... . This is where the value of the Polya correction, that is used in the photostatistics method, is numerically ascertained.

To gather sufficient statistics, of roughly 120,000 events, takes 10 minutes if triggering at a typical 200Hz. Single PE runs are typically taken in pairs; with one of the runs at nominal HV and one at a 10% over-voltage of the nominal value. This is done as the higher gain gives a more pronounced peak in the data due to the single PE distribution, which can be masked by the pedestal peak, and so gives more robust fit results. Comparison of the two results is taken, as the ratio of the gains at different HV values is well understood.

4.9.6 Instrument Ageing and 'Crab Nebula Flux Issue'

As the VERITAS telescopes age, naturally, due to exposure, use and weather, components deteriorate in certain ways. This can have an impact on the array's response to EASs, particularly the energy reconstruction of gamma-ray events and the measured flux of gamma-ray sources. Over the last few years (m̃id 2019 present) there has been significant work done by members of the VERITAS collaboration to quantify the changes seen, and to be able to correct for, whenever possible, the changes in throughput of the optics and overall detector efficiency, including making necessary changes to the simulations and Instrument Response Functions (IRFs) that are used in analysis of data. In a recent publication [153] the methodology, describing all contributing factors in the signal chain and how to calibrate the changing response, relevant to all IACT experiments, using over seven years of recorded data of the most pertinent 'standard candle' in VHE astronomy, the Crab Nebula. The work, which represents a significant effort and time investment by the group, find

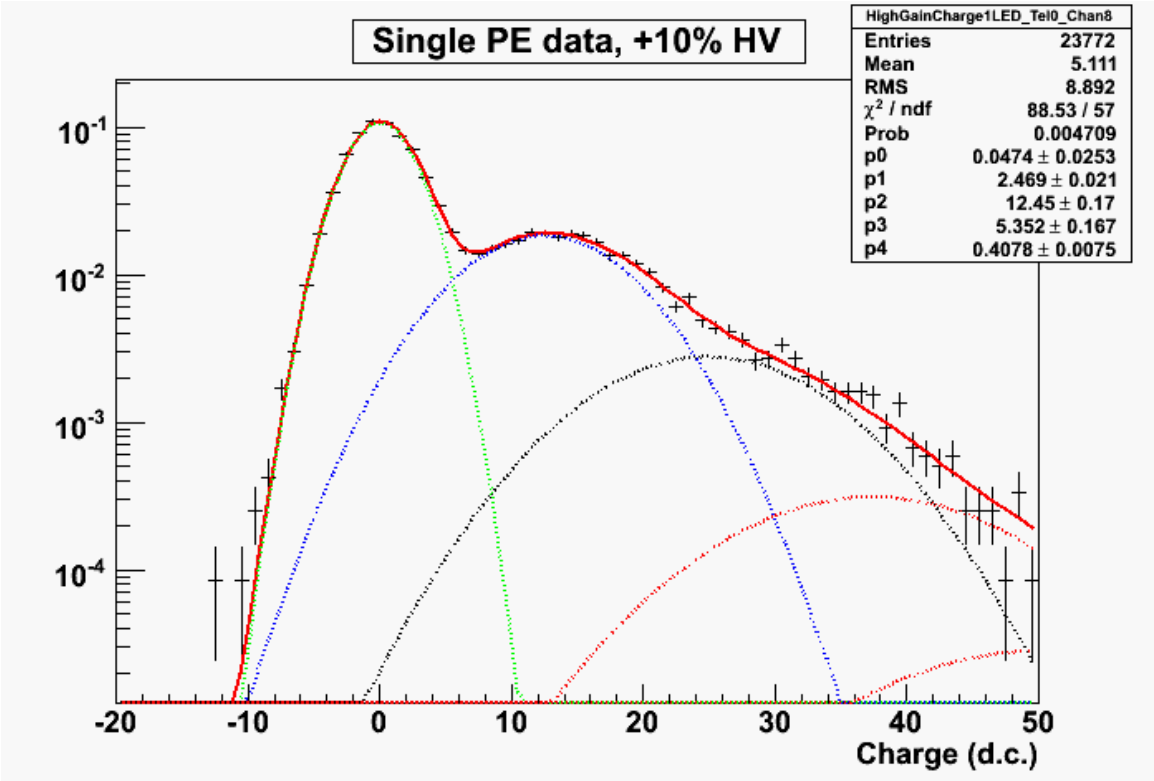

Figure 4.6: Here is an example fit of the charge data from a single PE run (Telescope 0, channel 8) with 110% HV, shown are the Gaussian distributions corresponding to different numbers of PE liberated from the photocathode. From VERITAS wiki Flasher page.

regular monitoring of the optical response, along with the related calibration approaches employed, can produce correction factors (to the PMT signals seen, for example) that are folded into the telescope performance simulations to provide adjusted and corrected IRFs[5].

The three derived correction factors are: 1) the 'gain factor' $g_i = \frac{G_i}{G_{i,MC}}$ a channel-specific correction that is the ratio of the measured channel gains to those that are assumed in the Monte-Carlo simulations 2) the 'optical throughput factor' or 'reflectivity factor' $r_i = \frac{R_i}{R_{i,MC}}$ a telescope-specific correction that is the ratio of the wavelength-averaged whole-dish reflectively measurement, that includes reflectivities convolved with a representative Cherenkov spectrum from a gamma-ray EAS, to the reference simulation value 3) the overall 'throughput factor' t_i which is the product of the relevant g_i and r_i, for each channel in each telescope camera. The correction factors are applied to the simulation events by scaling the signals in the PMT traces, before they are summed for further analysis[6].

The project also shows that using these updated IRFs, which will be generated regularly, for each observing season (with plans for more potentially even further finer temporal granularity, where as before the IRFs were produced only for the different epochs of the array) bring the observed flux and spectral properties of the Crab Nebula back to the reference level seen before the causal degradation took place. While the method is very successful in re-normalizing these observational characteristics there is an unavoidable loss of low-energy events, near the array threshold. Here some very dim showers are lost, as they don't pass the trigger threshold and therefor don't cause the readout of the array, or the uncertainty of the shower morphology, caused by loss of light, leads to them being classified as background hadronic showers, and being cut in analysis.

[5]These factors are introduced in a way that allows for scaling of the extensive simulation set that had already been produced when the need for such factors became evident. The huge resources required to re-do the simulations made this a highly undesirable option

[6]Studies found that by using the factors to modify the pre-processed simulation event images, after the standard cleaning methods have already been applied, gave acceptable energy and flux reconstruction it did not correctly model the morphology of the image as seen by the camera, when comparison was done between MC and data. As such, even though this approach is less computationally intensive, the prior method was adopted to correctly model the shower images from the lowest-level onward

Table 4.3: From [153]. Left: shown is the differential sensitivity comparison of the 2012-2013 season and the 2019-2020 season, after the correction factors have been applied. This exemplifies the effective change in the energy threshold of the instrument, over time. Right: A table of the considered sources of systematic uncertainty for VERITAS.

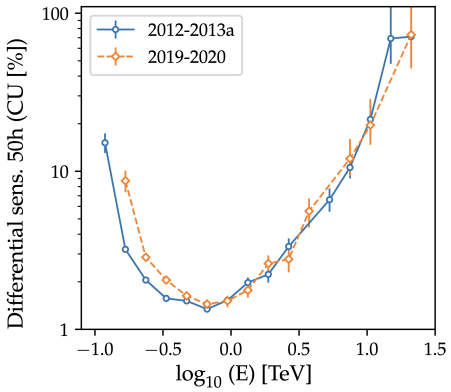

Type	Flux
Photo-electron response and gain	5%
Signal pulse shape	5-10%
Low-gain modeling	5-10%
Efficiency of photo detection	< 5%
Unavailable pixels	3-5%
Shadowing	1%
Mirror reflectivity	10%
Winston cone efficiency	4%
Point spread function	5-10%
Atmospheric profiles, Absorption, scattering	10-15%
Analysis	10%
Total	~ 25%

4.10 The *Fermi* LAT

The Large Area Telescope (LAT) has greatly expanded the catalogue of detected pulsars [154] in the HE band, although Vela remains the only pulsar, aside from the Crab pulsar from which pulsed emission is detected above ∼50 GeV [155]. The LAT is a pair-conversion telescope which operates aboard the *Fermi* spacecraft and is very useful for providing photon information well below the energy threshold for ground based IACTs, this allows the joining of spectra through a large energy range and also provides high statistics, in the HE regime for determining possible peak locations in the VHE pulsar lightcurve. The LAT is sensitive to gamma rays in the range of ∼ 20 MeV to 300 GeV and with a large FOV of ∼2.5 steradians is does not perform targeted observations but surveys its full sky every few hours (see more details in [156] and [157]).

4.10.1 HE Data Analysis

Data from the *Fermi* LAT is barycentred and phasefolded with Fermitools (v11r5p3) and TEMPO2 [158], both to check the validity of the timing solution and to define on and off phase regions for the later VHE analysis.

We select *Fermi* LAT data that falls in the valid region of the appropriate timing solution for each pulsar. The LAT data includes events with an energy above 100 MeV and within 2° of the pulsar position from the parameter file used for timing. Events that intersect with the Earth's limb are cut, as this introduces unnecessary background, and other standard data quality selection is applied [159]. The *Fermi* Tempo2 plugin (as described in [160]) is used to generate barycentric Times of Arrival (TOAs) using ephemeris information along with parameterization of the PSR in question. The TOAs are 'phase-folded', converted to a phase corresponding to the pulsars rotational state, using the pulsar timing information in the relevant timing solution. We note that no overall convention for the definition of 'zero' phase is adopted. The 'time zero' in the relevant timing solution, which is arbitrary to define unless comparison between different timing solutions for the same PSR is necessary, is taken for this reference purpose. The resulting 'phaseogram' can then be used to define the peak(s), which are used as 'On' counts, and background region(s), where the Off counts are drawn from for later use in the Li&Ma significance test. This process is colloquially know as 'phase-gating'. The algorithm to define the phase gates is described in detail in [161] and [162]. It scales the *Fermi* LAT lightcurve by the expected VERITAS excess seen from a 1 percent Crab Nebula flux-level source, and then calculates the On and Off regions in phase as to maximize the significance expected. It is important to note that our approach here assumes an approximate flux of the source and that the VHE peaks are not shifted in phase from the HE peak location(s). We adopt the procedure in [163] and choose the number of bins in the presented phaseograms based on the H-Statistic from the weighted H-Test (see [164] along with [36] and references therein).

4.11 VERITAS VHE Data Analysis

4.11.1 Analysis Chain Overview

The data used in this publication was collected from September 2014 through to March 2017 in standard 'Wobble Mode'. The so-called 'Wobble Mode' allows for simultaneous and unbiased accumulation of 'On Target' and 'Off' data; the source position is displaced from the centre of the FOV by 0.5°, alternating through the four cardinal directions to reduce any intrinsic bias and collect as accurate as possible measurement of background [165].

Quality selected data is passed thought the calibration, reconstruction and cuts stages of the VERITAS Gamma-ray Analysis Suite (VEGAS), detailed in [166] [167] , along with overall approach discussed in [168]. The secondary analysis of VERITAS data was done with Eventdisplay see [169], this secondary analysis is in principle the same as the primary and is only done as a sanity check to ensure no spurious results are reported. Both of the analysis packages used by VERITAS are original software suites, with different parts of the code written in either *C* or *C++*, and heavily feature use of the *ROOT* [170] framework.

The camera readout is calibrated, cleaned and the Hillas parameters are extracted from the images [171]. Using the combined moments from all participating telescopes, the reconstruction of the gamma-ray energy and incident direction is performed, if the images are deemed of sufficient quality to contribute, as determined by sets of parameter cuts that also form the background rejection (gamma/hadron separation) method [172]. Geometric identification of gamma/cosmic ray initiated showers is possible due to the distinct elliptical images produced from gamma-ray initiated showers. Physically this is caused by the narrow morphology, compared to the cosmic ray showers that produce hadrons that are more likely to have relative motion out of the transverse direction, and hence much more spread-out images. The final stage calculates the estimated background and, from that, the statistical significance of the results of the gamma ray data-set, according to the formalism

of Li & Ma [173]. 'Post-analysis' products such as spectra and sky-maps can also be produced. Also, as of great import in this analysis, the pulsed properties of the data can be evaluated, using specific plugins for VEGAS that utilize TEMPO2 for the barycentering and phasefolding of arrival times. There are a number of additional macros that produce visualization plots and other output.

As no spectral quality is assumed a-priori we test for three standard data cut types; optimized for soft, medium and hard spectra sources, each assuming a standard power law spectrum. The H-Test [174] for periodicity is performed as well as an On/Off Lima & Ma test of the phase binned counts, to quantify the level of significance of pulsation seen.

Many steps comprise the VERITAS analysis software chain. It begins with the digitized PMT pulses, and other auxiliary information recorded when the array is triggered, and culminates in high-level scientific products, such as gamma-ray flux or source spectral information. The first analysis stages begin with the raw-data described in the L3 Trigger section (see 4.7.3), when the array is readout.

4.11.2 Low-level Initial Analysis

The digital FADC traces (along with the other peripheral quantities such as timing and trigger information) for each event are processed, first, by performing a removal of the injected pedestal offset, NSB contribution and electronics noise by subtracting the expected background level that is extracted by using force-triggered 'pedestal' events, that typically contain no Cherenkov signal.

To quantify the amount of light seen by each channel in each camera, for every Cherenkov shower, a 'charge' value is calculated[7]. The charge seen in each channel is the time-integrated PMT pulse, over a given number of FADC samples, and is directly related to the number of photons detected by the pixel. These are not all EAS Cherenkov photons

[7]Named as such as the pulses seen from the PMTs are due to the current of electrons, amplified from the photoelectrons released by the light-flashes, and when summed over a specific window of time, the strength of the signal seen is related to this total charge. i.e. $Q = IT$

however, and, as previously mentioned, the baseline level signal returned, by each individual channel, in the absence of a Cherenkov flash, must be determined for later subtraction.

As the output from every PMT channel is digitized by the FADC system, the signal amplitudes are quantified in units of digital counts, as are the integrated traces, if the number of samples is taken as a dimensionless quantity in this context. Given that the FADC sample rate and dynamic range is known, along with the response of each channel to a single photoelectron, the digital counts can be converted to voltages or charges (in terms of the corresponding number of photoelectrons, rather than digital counts), if it is necessary to do so.

As the level of NSB (and possibly even electronics noise, due to temperature changes, for example) can vary during even during the same observing run, each observational run is broken down into segments of 180 seconds in length. For each of these time-windows, a histogram of the summed traces (corresponding to the same number of samples that will be used for the final integration window width) for every force-triggered pedestal event in that particular segment is created and from these histograms the mean value of the pedestal, along with its variance (the pedestal variance, or '*pedvar*' to be used later in image cleaning), can be extracted. These force-triggered readouts are injected into the data-stream during gamma-ray observations at a rate of 1Hz. Named 'pedestal events', which are assumed to be free of any Cherenkov light and be solely a measure of the Night Sky Background light level from stray photons (and therefor purely contain information about the pedestal offset voltage level and variations, in the absence of a signal from an EAS); they are used to calculate the necessary charge quantity to be subtracted from each respective channel's event charge.

Now that the average background level is known for each time-slice of the data run, the other events that organically caused the array to trigger can be assessed. A 'Double Pass' method is used to, firstly, determine the arrival time spread of the traces in the event and, secondly, to apply an integration window to each channel's trace based on this timing in-

formation. Due to the geometry of the observed EAS, and the fact that the Cherenkov light emitted later in the EAS's development reaches the ground earlier that those Cherenkov photons produced at higher altitudes, a natural gradient in arrival times of the photons is expected. This effect is due to the orientation of the EAS relative to the telescope pointing.

If a fixed 'absolute' time window was used to sum the traces from every channel, then signal light would be cut out and removed from traces where parts of the signal pulse fall outside the central time section, around the average arrival time. Alternatively, to catch more of all of the traces, a larger integration window could be used. This approach would introduce more noise contribution, as more samples simply contain excess and unnecessary pedestal baseline, and fluctuations, and not Cherenkov signal. Hence, the Double Pass method is adopted.

The first pass employs a long summation window, conventionally 16 FADC samples (corresponding to $32ns$), to integrate the signal. This first pass also calculates the precise point-in-time where the signal rises to half[8] of the maximum value seen in the integration window for that specific channel, known as the *T-Zero* value. A fit is then performed to the *T-Zero* distribution[9] for all channels in the event, upon which the final integration window, typically 7 FADC samples (corresponding to $14ns$), for each pixel is determined and applied. Fitting to the *T-Zero* in every pixel across the camera helps to average out any timing fluctuations and also reduces the contribution of background light, as it is uncorrelated with the Cherenkov signal, and then may fall out of the final sample-summation region.

The respective mean pedestal charge values are then subtracted from the final integrated trace values, from the smaller summation window, giving the *pedestal-corrected charges*. These *pedestal-corrected charges* are the fundamental quantities used for generating and parameterizing the whole-camera images. The cleaning and calibration steps that are ap-

[8]Using the half-maximum value, of the peak, as the reference provides the best timing resolution as the pulse shape is at its steepest there, giving a more robust estimation of the pulse timing, while still maintaining most of the signal charge for integration

[9]Timing information gathered from the corresponding flasher run is also used to adjust the exact *T-Zero* values used for the fitting procedure, to account for any intrinsic timing offsets in the channel.

plied to such images are discussed in the next section.

Image Cleaning and Data Calibration

We now have pedestal-corrected charge information for every camera channel in the event. Now, the relative gains calculated from the flasher run (see section 4.9.2) that is associated with the data run, are used to scale the integrated signal on a channel-by-channel level. The next step in the analysis takes this scaled image and eliminates channels that are judged to be not actually associated with the Cherenkov signal, or whose inclusion in the image would result in an incorrect reconstruction of the event, and are simply unwanted contributions from spurious background light or noise. Various approaches can be taken to produce an algorithm to provide this cleaning, with their own advantages and drawbacks, and are often more or less appropriate depending on the type of source of interest or style of analysis that is being performed. Two such methods are described below.

An elementary routine is to set a fixed threshold and cut all channels from the final image if their recorded signal strength is below said threshold. This allows for a straightforward, non-varying cleaning threshold throughout all images and events, but necessarily requires a relatively strict (high-value) threshold, as to not allow random fluctuations in the background/noise level to remain in the images and pollute any Cherenkov signal. However, as a good understanding of the characteristic fluctuations seen in each channel has been gained by aggregating the channel pedestal information, particularly the pedestal variances, it is natural to use these as time-varying channel-specific thresholds, as they quantify the range of expected charge values recorded (for a fixed number of samples in the summation window), due to background and noise. For standard analyses, the cutoff for channels to be retained is typically set to require a pixel's pedestal-corrected charge to be greater than five times the standard deviation of the relevant pedestal charge distribution ($Q^{5\sigma}_{Thresh}$). Any channels passing this threshold are deemed 'Picture' pixels. In addition to this, due to the expected 'cluster-like' topography of a gamma-ray-induced shower's Cherenkov signal in

the camera, often, only, a second, lower, threshold is required of channels that have a neighboring pixel that meets the $Q^{5\sigma}_{Thresh}$ criterion. This lower threshold is set to require a pixel's pedestal-corrected charge to be greater than two-and-a-half times the standard deviation of the relevant pedestal charge distribution. Channels that meet this second benchmark are dubbed 'Boundary' pixels, and join the Picture pixels, as 'Image' pixels, in further analysis. This technique of 'island cleaning' has shown to be effective, as adjacent pixels are more likely to contain additional Cherenkov signal than isolated pixels that show, potentially, a higher charge but are disconnected with the main body of the contiguous 'signal island' in the image. Individual, secluded pixels that meet the lower threshold are statistically more likely to simply be upwards fluctuations in the noise, given that the noise across the camera is expected to be roughly equal in magnitude. This approach is more complicated than the set-threshold method, but is more adept at accounting for non-static observing conditions during data-taking.

In addition to the above, so called 'Simple Cleaning' method, an additional process can be applied to pixels that do not make up the main-body of charge, seen in the image. The simplest choices for this additional cleaning pass are the 'Single (Double) Isolated Pixel Cleaning' algorithms, setting all pixels that do not have at least one (two) Image pixel neighbors, to a zero value. This is necessary as many Hillas images can be badly skewed by outlying channels and the probability of these outliers increases if the cleaning thresholds are lowered (for example, in an attempt to have a lower overall analysis energy threshold). In such a case, where the cleaning thresholds need to be lowered a third technique can be employed: known as 'Cluster Cleaning'. In this method all island groupings of pixels are evaluated by summing their total charge, and only the cluster with the highest charge value is retained in the image, offering a superior method of vetting images and aiding event reconstruction.

However, any approach that limits the participation of channels in the final image can potentially eliminate shower information, and should only be used if the benefits to recon-

struction of the primary gamma-ray outweigh the drawbacks. We've already mentioned the benefits of using the timing gradient of the image in the assignment of integration windows to limit the impact of potential contributions from noise that do not match the expected time-evolution of the primary signal (see [175] and more recently [176] for further discussion), but, removing clusters of pixels from the event image can also cause problems for gamma/hadron separation. As will be explored in more detail later, the primary way to differentiate between events caused by gamma-ray-induced showers and those that are instead due to cosmic-ray-induced showers, lies in their distinct image morphology. 'Gamma-like' events are consistently seen to be unbroken, uniform and ellipsoidal in shape, while 'hadron-like' events form irregular, but often more circular and less elongated overall, images with additional independent structures that are not spatially connected to the main body of the image. These extra clumps of triggered pixels, from a cosmic-ray event, can be mistaken for noise and cleaned from the image, thus removing a characteristic that might have marked the event as a likely background shower event, and instead disguising it as a gamma-like candidate.

In any case, while managing the background contribution in event images is very important, due to the nature of the Hillas parameterization and reconstruction methods, keeping all valid pixels, and therefor signal information, is key to maintain the highest possible quality gamma-ray reconstruction and angular resolution.

Event Image Parameterization

The distribution of Cherenkov light seen on the ground by the telescopes is a cross-section of the evolution of the EAS at the observatory altitude. The morphology of the images seen are parameterized by the geometric 'Hillas' parameters [171] and, hence, the traits of the shower itself can then be reconstructed in the analysis. This robust method reduces the moments of the resultant camera images to variables in the description of the well-understood shower shape. The camera images expected for a gamma-ray induced EAS are

that of a 2-dimensional Gaussian distribution that is elliptical in nature (i.e. non-degenerate in the X-Y camera coordinates).

It would not be much of an understatement to say that Hillas parameterization and method of classifying EASs has radically influenced how ground-based gamma-ray astronomy has evolved over the previous decades, and still underpins the state of the field today. The seminal paper [177] describes its use in the famous Crab Nebula detection with the ground-based Whipple 10m Telescope, where over 98% of the background was able to be rejected, even with the method in its early days. As Hillas himself did originally: through the use of extensive and detailed simulations of EASs, and the telescope response to them, we can build up a strong understanding of how the breakdown of the image, into basic measurable quantities of the 2D images, can then be used to reliably and accurately 're-assemble' the shower characteristics and infer information about the primary particle that caused it. In addition, by simulating showers that result from cosmic rays and investigating the resultant telescope images through a comparison of the Hillas parameter phase-space distributions from gamma-like and hadron-like primaries, we can develop criteria from which to discriminate between true gamma-ray events and contamination from background cosmic-ray events. Aside from background rejection techniques, other information tied to the physical EAS properties, which the different geometrical parameters represent or characterize, is exploited to determine, for example, the principle shower core orientation, and hence the arrival direction of the incident gamma-ray. Through simulation, again, the resulting Hillas parameters are derived for millions of showers of varying gamma-ray energy (and numerous other variables), so that the image parameterizations can also be used, with knowledge of the instrument, to determine the energy of the incoming gamma-ray, before it interacted in the atmosphere. So, for example, the orientation of the derived major axis of the ellipsoid image determines a plane of possible primary-particle incidence-angles and the total charge, or 'brightness', of an image is characterized by the *size* parameter which, when combined with other parameters can be used to estimate the

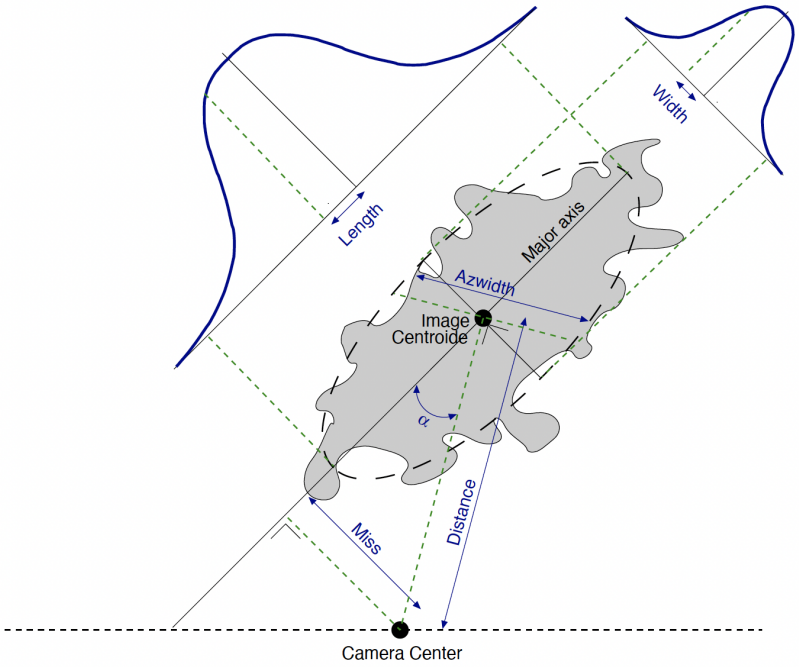

Figure 4.7: Shown here is the definitions and visual representation of the Hillas parameters of a gamma-ray image, from [33].

energy of the gamma-ray. In practice so called 'mean-scaled' parameters are actually used, for superior background rejection and gamma-retention. These are simply the measured value of the parameter in question *scaled* by the expected value from simulation lookup tables, and *averaged* over all participating telescopes, hence the name (see [33] [133] for further discussion).

More detailed discussion on the exact methodology followed in the analysis to take the Hillas image parameters and produce higher-level data products follows in the next sections.

Table 4.4: The most commonly use Hillas Parameters: many other quantities can be derived from the images and can be useful in certain situations, listed here are those usually considered the 'standard' parameters.

Hillas Parameter	***Definition***	***Used For/Describes***
Length	The Standard Deviation of the distribution of charge on the image major axis	Quantification of ellipsoid length
Width	The Standard Deviation of the distribution of charge on the image minor axis	Quantification of ellipsoid breadth
Distance	The distance from the center of the camera to the centroid of the image	Measures the shower's impact parameter
Alpha	The acute angle between the vector that points from the image centroid to the camera center and the major axis	Quantifies the orientation of the image with respect to the camera
Azwidth	The Standard Deviation of the distribution of charge perpendicular to the *Distance* vector	Quantification of image orientation and shape
Miss	The perpendicular distance between the major axis and the camera center	Quantifies the orientation of the image with respect to the camera
NTubes	The total number of channels that are present in the image after cuts	Assesses the quality of the image and robustness of potential reconstruction
Size	The sum of the pedestal-corrected charge across all channels that are present in the image after cuts	Quantifies the brightness of the shower as seen on the ground
Max(i)	The charge magnitude of the *'i'th* brightest individual pixel in the image	Quantifies the upper bound on channel charge for the image
Frac(i)	The ratio of the summed charges of the *'i'* highest-charge channels, to the total *Size* of the image	Indicates how concentrated the image charge is
Loss	The fraction of the image *Size* that is from the channels at the edge of the camera	Indicates how well the image is contained by the camera FOV
Length / Size	The ratio of *Length* to *Size* (often abbreviated to *LoS* or even *L / S*)	A metric of the compression of the image with respect to its total brightness, used to discriminate against muon events

Primary Direction Reconstruction

The reduction of images from each telescope then allows the stereoscopic combination of said images together with the other participating telescopes, which is a powerful tool to reject background and also gives a more accurate reconstruction of the shower axis, and so the gamma-ray incidence direction, and the shower brightness, and so the energy of the primary gamma ray.

The point on the ground where the gamma ray would have impacted, if it did not interact in the atmosphere, is where the major axes from all participating telescope images intersect. This gives the shower core location and hence the incident direction of the original gamma ray. In practise, due to uncertainties in measurements and reconstruction, the major axes from all images rarely, if ever, all intersect at just one point. Therefor, various methods are used to 'weight' the images for quality, and so their contribution to the true shower core placement and direction reconstruction. For example, options include: using the (log of) the image sizes as a measure of robustness and weighting each image as such, weighting by the square of the sine of the angle between each pair of axes, to attempt to improve accuracy, including image ellipticity as a quality check, or all of the above together (see [36] for further information).

Energy Reconstruction

The total charge, along with several other quantifications of the phase-space, seen by the telescopes is used to 'look-up' the reconstructed energy of the gamma-ray event from data tables produced from detailed simulations of the telescopes' response to simulated air-showers. The energy lookup tables are specific to the instrument epoch, observing conditions and other factors so be as specific and realistic as possible, containing any nuance of the real detector that is modelled in the simulations.

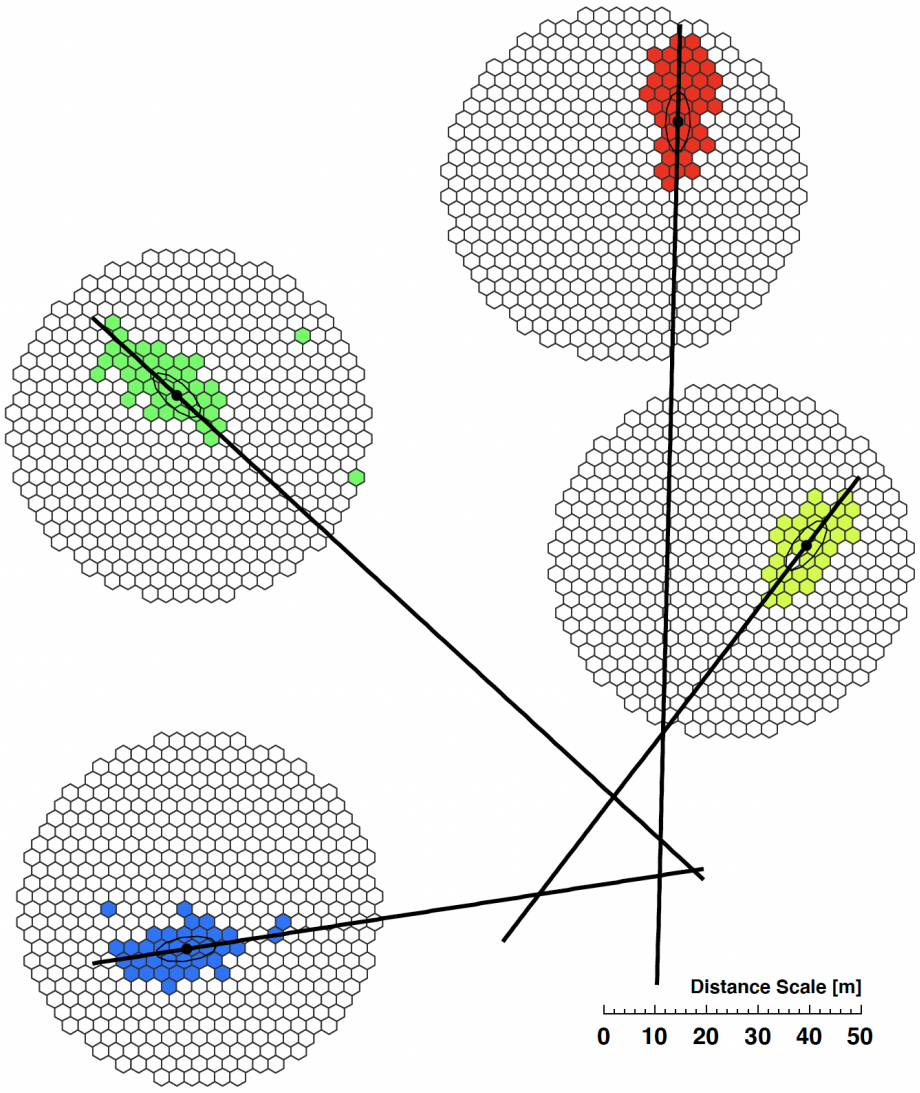

Figure 4.8: A visual representation of how the camera images from the four VERITAS telescopes are combined to reconstruct the incident gamma-ray shower core position in the camera plane. Due to uncertainties in the images it is exceedingly unlikely that the image axes all intersect at the same point, a relative weighting procedure is needed as discussed in section 4.11.2.From [33].

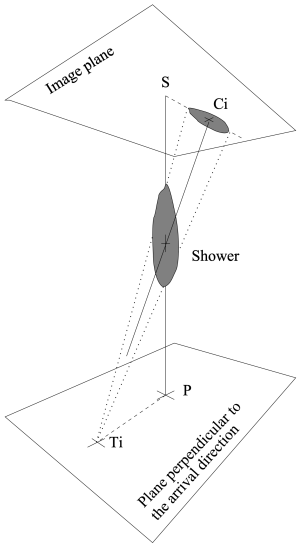

Figure 4.9: A schematic showing the geometry of the shower reconstruction process, from [178]

Event Selection & Rejection

The candidate gamma-ray events are now passed through a set of selection criteria (or quality '*cuts*') to remove background events that are judged to be non-gamma-rays (such as hadronic showers).

The chosen *cuts* values define a set of requirements that the event images but meet, or exceed, to be retained in the pool of accepted events. If an image falls below the set criteria then it is set aside ('cut') and not used to generate higher level data products. The standard sets of *cuts* mandate two types of discriminatory measures: firstly, those that are shared across all analysis types and check that the event is suitably robust to contribute meaningful information to the analysis (*NTubes*, *Size*, *Loss* etc.) and, secondly, those that are specific to the type of analysis, or presumptions about the source candidate being observed, that tune the allowed parameter phase-space, based on prior understanding or inference of the target, to give superior reconstruction or background rejection [10]. The most rudimentary method of performing event selection is the '*Box Cuts*' method. In this procedure a 'hard' cut is

[10]Of course, one must be extremely careful when 'artificially' tuning these parameters as, at best, a certain trials factor may be introduced, or, at worst, an artifact in the data might be misconstrued as a real signal

made and all events are removed/kept, based only on the single parameter value in question, individually, with zero tolerance. This is the most common choice for a standard analysis and has shown to be sufficient and robust in almost all cases. More advanced techniques exist, however, such as using Boosted Decision Trees (BDT reference), the Image Template Method (ITM reference) or simply modifying the *Box Cuts* method to weight events around the threshold in some way, rather than simply removing them, often considering not just a single parameter alone, but instead in conjunction with other related parameterization values.

Cut values can be derived and optimized in several ways, but using a well understood MC simulation data-set together with a standard source, usually the Crab Nebula, data-set is the most commonly adopted approach. The standard cut values are, most basically, a function of the instrument epoch, as hardware changes greatly impact the telescope response, the source extension (the angular size of the source in the FOV; there also exist more advanced methods to analyse very extended sources) and the expected spectral hardness of the source in question (if no *a priori* knowledge is assumed than all three standard spectral cuts can be used). In the analysis of MSP data contained here point-source cuts, for all three spectral types was performed. For the analysis of the 'pulsar tails' data, less constriction was placed on the expected emission characteristics, and both point and extended cuts were used, along with all three spectral cuts, to potentially capture any concentrated, or more diffuse gamma-ray emission.

4.11.3 High-level Dataset analysis

When the final list of events passing the desired cuts for the specific analysis has been generated, the energies and origin direction are then collated onto a map of the sky, which is then used to test for potential gamma-ray sources.

[11] Strictly speaking, in the VEGAS configuration files there is actually a separate flag to apply the angular distance cut for the Ring Background Method $-$*RBM_SearchWindowSqCut* and the Wobble Method $-$*S6A_RingSize*, the purpose is the same, however.

Table 4.5: The standard VERITAS V6 'Upgraded Array' Box Cut values. The looser cut for θ^2 in the case of a SOFT point-source analysis is due to the worsening of the VERITAS PSF at lower energies.

Parameter Name	***Parameter Cut Description***	***Cut Value For SOFT/MEDIUM/HARD Cuts***
DistanceUpper	Upper bound on the distance from the center of the camera to the centroid of the image (°)	1.43/1.43/1.43
SizeLower	Lower bound on the sum of the pedestal-corrected charge across all channels that are present in the image after cuts	400/700/1200
NTubesMin	Lower bound on the total number of channels that are present in the image after cuts.	5/5/5
MeanScaledWidthLower	Lower bound on the *MeanScaledWidth*	0.05/0.05/0.05
MeanScaledWidthUpper	Upper bound on the *MeanScaledWidth*	1.1/1.1/1.1
MeanScaledLengthLower	Lower bound on the *MeanScaledLength*	0.05/0.05/0.05
MeanScaledLengthUpper	upper bound on the *MeanScaledLength*	1.3/1.3/1.4
MaxHeightLower	Lower bound for the height of the shower maximum (Kilometers)	7/7/0
ImpactDistanceUpper	Upper bound for the impact distance (Meters)	1200/1200/1200
ThetaSquareUpper (*POINT SOURCE*)[11]	Upper limit for the angular distance, squared, from the nominal source location ($\circ^2$)	0.030/0.010/0.010
ThetaSquareUpper (*EXTENDED SOURCE*)[11]	Upper limit for the angular distance, squared, from the nominal source location ($\circ^2$)	0.055/0.055/0.055

Source and Background Estimation

To account for the gamma-ray background seen with any observation, a method to quantify the level of 'On-source' (signal) gamma-rays over the 'Off-source' (background) is needed. Several such approaches are used in modern gamma-ray analysis packages. The simplest technique is to take a dedicated background region (or regions, as is often done in practice) and subtract the size-scaled number of gamma-rays seen from the background region away from the supposed source/signal region. What is left is called the gamma-ray 'excess';

$$N_{Excess} = N_{On} - \alpha N_{Off}$$

Where α is the fractional size of the On region with respect to the Off region.

$$\alpha \equiv A_{On}/A_{Off}$$

The size of the signal/background regions is often parameterized in terms of an angular size θ or more commonly, the square of this angle, θ^2. It is measured from the putative source location. By applying a cut on this parameter you effectively limit events to this region and, as background events are expected to be isotropic, for the best sensitivity it should be matched to the anticipated source extent. For targets that are expected to appear point-like to VERITAS the tightest cut that can be applied is limited by the instrument PSF (see section 4.8.5).

VERITAS analysis can use either the 'Ring Background' method (RBM) along with the 'Reflected Region'[12] (also known as the 'Wobble' analysis) method to define these regions in sky coordinates, as standard options in the suite.

The RBM method defines a circular region of interest as the on region and a concentric, but non-overlapping, annular region surrounding it as the off region. As the camera has a

[12]Other, more advanced methods exist for particularly tricky scenarios, such as the analysis of very extended sources.

response that varies with camera coordinate, this is not an ideal approach.

The Wobble procedure involves taking observations with the target location offset from the center of the camera, by half a degree for standard Wobble mode, and cycling through the 'points of the compass' to change the Wobble offset direction for every data-run. The On region, around the expected source location, is matched with an Off region that is the reflection of the On region, in the camera coordinates[13]. The purpose of this approach is that it allows for unbiased and simultaneous collection of signal and background data, as any systematic effects should nullify each other [179].

Statistical Significance of Results

Any excess of gamma-rays seen could be the exciting indication of a hint, or detection, of a source. It could also just be a statistical fluctuation in the gamma-ray background. The standard detection criteria is held to be at a threshold of 5 times the standard deviation of the background level. While the idea is similar, there are many methods used to quantify the significance seen in a signal, from an electronic pulse in a noisy channel, to searching from emission of an astrophysical object. The standard for gamma-ray astronomy has been the likelihood-based approach developed in the seminal paper of Li & Ma [173].

A rudimentary derivation, following 'propagation of uncertainties', of the standard deviation of N_{Excess} leads to the expression;

$$\Delta N_{Excess} = \sqrt{N_{On} + \alpha^2 N_{Off}}$$

and thus leads to the significance ration taking the form;

$$S \equiv \frac{N_{Excess}}{\Delta N_{Excess}} = \frac{N_{On} - \alpha N_{Off}}{\sqrt{N_{On} + \alpha^2 N_{Off}}}$$

[12]Despite the effects being theoretically accounted for by the analysis procedure and simulations

[13]Hence the name of 'Reflected Region' method. 'Wobble' mode is a descriptor of the behavior of the telescopes switching from run to run as they 'wobble' about the source coordinates

The derivation of this expression implicitly assumes that the On and Off counts are drawn from independent Poisson distributions. This somewhat naive approach does not properly address the situation when the On and Off regions are not the same size (i.e. $\alpha = 1$) which is rarely, if ever, the case. To address, this Li & Ma derive an alternate expression for the significance, using a likelihood ratio test that performs more accurate assignments of confidence for cases when $\alpha \neq 1$.

The crux of the idea is that a true test of the significance is against a pure null-hypothesis. That is: that one should assume that there *actually is no source* of On counts, and that N_{On} is purely a fluctuation from the background. In addition, Wilks' theorem [180] should be applied, determining the maximum likelihood ratio, λ, and assigning S to the test statistic; $S = \sqrt{-2ln\,(\lambda)}$

This method is universally adopted throughout the field of gamma-ray astronomy, fully derived in [173], is;

$$S = \sqrt{2}\sqrt{N_{On}\; ln\left[\frac{1+\alpha}{\alpha}\left(\frac{N_{On}}{N_{On}+N_{Off}}\right)\right] + N_{Off}\; ln\left[(1+\alpha)\,\frac{N_{Off}}{N_{On}+N_{Off}}\right]}$$

and will be used for all calculations of significance level in this thesis.

Flux and Spectral Calculations

The measured gamma-ray excess is a number specific to the VERITAS instrument and sensitive to the exact observing conditions. Clearly, this is not of much use and needs to be converted to a flux measurement for comparison with other scientific results. This is done through quantifying the various aspects of the detector, through regular measurements of various experimental quantities and extensive analysis of detailed simulations, given the observing conditions. The vital quantities needed for the excess to flux conversion are; the total 'exposure time' of the data set T_{Exp} and the 'effective area', $A_{Eff}(E)$, that is the effective gamma-ray collection area of the telescope. This is derived from millions of

simulations, for different observing conditions, cuts values etc. and can be described as the efficiency of gamma-ray collection. If a simulations injects N_{Actual} gamma-ray events over an area A_{Actual} and, after simulation the full optics/electronics chain and analysing the simulated data, $N_{Detected}$ gamma-ray events are left, then the effective area can be defined as;

$$\frac{N_{Detected}}{N_{Actual}} = \frac{A_{Eff}}{A_{Actual}}$$

The gamma-ray flux seen, which can be expressed in many different ways, but most simply as;

$$N_{Flux} \equiv N = \frac{N_{Excess}}{A_{Eff}\ T_{Exp}}$$

A commonly calculated quantity is the 'differential flux', with respect to the gamma-ray event *reconstructed energy*, here labeled simply as 'E', which describes how the flux changes with expected photon energy;

$$\frac{dN}{dE} = \frac{d}{dE}\left(\frac{N_{Excess}(E)}{A_{Eff}(E)\ T_{Exp}}\right)$$

If an observing campaign spans multiple epochs or different observing conditions, as is almost always the case, the data is broken into segments so that the effective area used is always appropriate to the data.

If the calculated significance of a data set is not high enough (i.e. $> 5\sigma$, post trials) to claim a detection result, then important information on how constrained any possible gamma-ray flux is can still be derived. For calculating upper limits on the excess counts in this work we use the method of Rolke [181]. This involves choosing a confidence level at which to ascertain the limit, here we use 95%, and requires an assumption of the intrinsic statistical distributions that govern any measurements of the On and Off counts, along with a choice for the expected spectral properties of the source in question[14]. This allows the

[14]It comes as no surprise that these distributions follow Poissonian/Gaussian statistics and that the spectral shape is a power-law.

calculation of N_{Excess}^{UL}[15], and from that, an upper limit on the flux;

$$N_{Flux}^{UL} = \frac{N_{Excess}^{UL}}{T_{Exp}} \left(\frac{\int E^{-\Gamma}\, dE}{\int A_{Eff}(E)\, E^{-\Gamma}\, dE} \right)$$

where the $A_{Eff}(E)$ in the previous equation is an event-weighted average over all the effective areas involved. This flux upper limit, N_{Flux}^{UL}, which has dimension of $A^{-1}t^{-1}$, is often referred to as an 'integral UL', as it requires an explicit integration over a chosen energy range, E_{Min} to E_{Max}. E_{Min} is usually set to the energy threshold of the detector E_{Thresh}, which is defined as the energy at which the convolution of the averaged effective area and expected source spectrum is at it's maximum. E_{Max} can be set to a certain limit to evaluate the flux in a particular energy range, or set to a high value to include all events. A limit on the differential flux, F_{Diff}^{UL}, of dimension $A^{-1}t^{-1}E^{-1}$, can be calculated in an analogous way:

$$N_{Flux}^{UL} = \int F_{Diff}^{UL} \left(\frac{E}{E_{Thresh}} \right)^{-\Gamma} dE$$

where a power-law spectrum is assumed for the source. We see that the differential limit plays the role of an upper limit on the 'normalization' of the spectral distribution. Energy fluxes can be trivially computed as well, by adding a factor of E, the gamma-ray energy, to the integrand:

$$E_{Flux}^{UL} = \int E\, F_{Diff}^{UL} \left(\frac{E}{E_{Thresh}} \right)^{-\Gamma} dE$$

which are then used to calculate a luminosity for the source, given a known distance, from the VERITAS VHE flux. The above methods for calculating ULs are standard for the field.

4.12 Monte Carlo Simulations

Over the last several years I have been in charge of the production of a modern set of these simulations, as to derive new and improved IRF products for use in cutting-edge VERITAS

[15] Which is a dimensionless number

analysis. In this section I detail the work that went into the production of said simulations.

To be able to accurately reconstruct the original gamma ray that initiated the EAS, of which the resultant Cherenkov light is imaged with the VERITAS telescopes, extensive study and analysis of MC simulated air showers, and how they interact with the telescopes, is necessary. This involves simulating millions of gamma-ray-induced showers, that evolve as they move down through the atmosphere and produce Cherenkov light in the telescope FoV. Large statistics are necessary to to quantify the morphology of the EAS and the uncertainties involved, due to the inherently probabilistic nature of the shower evolution and detection process.

The simulation chain is broken into three main parts; air shower simulations, telescope optics simulations and detector simulations, as detailed below. This process is time-consuming and involved, requiring many measured 'real-world' parameters. However, it is a requisite task to allow the collaboration to analyse data, and hence the observatory to function.

Ongoing comparison of older simulations to real data has been a necessary precursor to this new generation of simulations, from which the V6 IRFs are produced. Much of the tuning and assessment of the parameter phase-space has been an ongoing process since the previous simulation set was realized in 2016, and has been worked on by a subset of the VERITAS collaboration, including N. Otte, N. Park and G. Maier. Setup of the software and enabling distribution of programs to the OSG was done with assistance from UChicago team, particular thanks go to P. Paschos and M. Rynge, who have extensive knowledge of the involved processes for effective job distribution to the hosts. Streamlining and running of the simulations, monitoring workflow output, cleanup and final preparation of the simulation files for the IRF production (on NERSC) was done by A. Gent.

Millions of CPU hours are used for this production and resources on the Open Science Grid [182] [183] and on computing clusters at GT (HIVE and Phoenix [184]) were of huge import.

4.12.1 Simulation Usage and Simulation Chain Overview

The final goal for the project is to be able to produce IRF files for the V6 epoch (see Section 4.3) that include up-to-date atmospheric profiles, contemporary simulation software and improved treatment of the instrument response, along with greater statistics[16] than have been produced in previous generations of simulations. The IRF files are essential to VERITAS data analysis as they contain realistic information on the detector's effective area, as a function of gamma-ray energy, and lookup tables that are used to estimate the energy of the primary gamma-ray from an event. To produce these IRFs, simulated data is produced, with the 'initial conditions' being known and controlled, and then analyzed with the relevant VERITAS analysis package. In this way the detector response is quantified and lookup tables are generated to be able to reconstruct the primary gamma-ray's properties from the parameterization of the event image.

Air Shower Simulations with CORSIKA

The first stage in the MC chain is the production of detailed air shower simulations, which is done with CORSIKA [185][17]. This package models particles and their interactions as the EAS develops in the atmosphere (see also Chapter 3). The IACT package [186] is critical as it allows a modern and flexible implementation of the Cherenkov emission mechanism. While the aforementioned package contains the ability to implement the telescope optics and detector response, separate specialized software programs are used instead, for flexibility and veracity.

The scale of the EAS simulation is truly massive: resulting in over 400TB of data. Almost 350 million showers have been simulated, spanning 11 zenith angles and 2 atmospheric profiles. The showers are simulated for primary gamma-rays drawn from a

[16] In particular, the number of gamma-rays at higher energies has been greatly increased, by an order of magnitude, from the last epoch simulation.

[17] See also https://www.iap.kit.edu/corsika/index.php

spectrum of the form[18];

$$\frac{dN}{dE_0} \propto E_0^{-1.5}$$

with the lower energy bound varying from 30 GeV - 100 GeV, depending on the zenith angle of the shower. The upper bound on the primary energy is 200 TeV. The core locations of the showers are scattered over the area of a circle of radius 750m - 1500m, again, dependent on the simulated zenith angle. The profile of the Earth's magnetic field is parameterized for the Whipple observatory location.

Following this first stage, the corsikaIOreader program[19] takes the simulated CORSIKA shower data and applies atmospheric extinction, requiring the desired atmospheric template, while also converting the photon information to a format that can be read into the next stage of the chain: the optical simulation with GrOptics.

Telescope Optics Simulations with GrOptics

Before the response of the camera can be simulated, the paths of the Cherenkov photons from the EAS must be calculated. This process is called 'ray-tracing', and maps the mirror-incident photons to the camera focal plane using a detailed model of the telescope optics, developed with the ROBAST 'telescope factory' libraries[20]. A specialized program called 'GrOptics'[21] has been developed for this task, allowing the implementation of the specific telescope model and parameterization of the VERITAS mirror/optics system. Once the photons from each shower have been tracked through the telescope optics to the focal plane the output is passed to the next stage of the chain that simulates the camera response. After the production stared, the scripts were modified to allow the optics and camera simulation to be run as a single compute job, thus eliminating the need to store the $\sim$50TB of intermediate files, for the whole production.

[18]Note the relative hardness of the spectral index here: ensuring that many very energetic gamma-ray primaries are simulated.

[19]https://github.com/GernotMaier/corsikaIOreader

[20]https://github.com/ROBAST/ROBAST

[21]https://github.com/groptics/GrOptics

Camera and Readout Electronics Simulation with CARE

Previous VERITAS simulation productions have used 'GrISUDet'[22], an older 'in-house' program for the optics and camera simulation, while this project makes use of the 'Camera and Readout Electronics' (CARE)[23] software. CARE is a modular program that simulates the detector response and the behavior of the electronic components in the VERITAS camera chain. The improvements made in the simulation of the VERITAS camera response, over the previous GrISU model, are numerous. Parameters related to the calibration of the instrument, such as; the photo-detection efficiency, absolute gain, trigger threshold nuances, point-spread function etc. have been extensively investigated as to be accurate to the real-world case. The configuration files input many parameters of the system, including; the trigger VERITAS logic, FADC specifications, pixel information, along with carefully measured pulse shapes for both the High and Low Gain channels, and other subtle behaviors related to the 'hi/lo gain switch' (see section 4.6) have been implemented in CARE.

More than 3.5 million simulation files were processed through 11 standard-observing HV noise levels and 6 RHV noise levels, to cover all VERITAS observing conditions.

4.12.2 Production of Simulations with the Open Science Grid

The entire production pipeline makes extensive use of the Pegasus Workflow Management System [187] for optimal handling of jobs and distribution to OSG resources. In 2020 some of the highlights of the VERITAS production project have been documented in a publication [188] by the OSG collaboration services.

The final, relatively small in size, files were transferred to the HIVE and Phoenix clusters for merging into fewer files, around $\sim$10GB in size. This was done off of the OSG as the merging process is memory-intensive and hence more suited to the PACE resources available at GT[24]. Thus far, the simulation chain has consumed more than 15 million CPU-

[22] https://www.physics.utah.edu/gammaray/GrISU

[23] https://github.com/nepomukotte/CARE

[24] Interfacing problems were encountered with the dedicated high memory 'stashworker' nodes on the

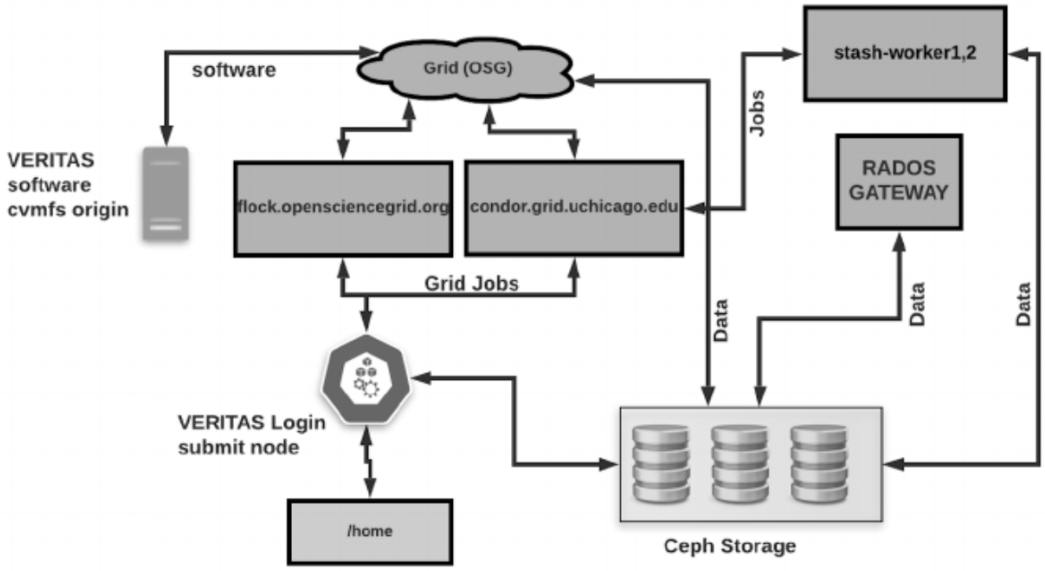

Figure 4.10: The VERITAS OSGConnect infrastructure hosted at UChicago that underpins the simulation production, from [188].

hours. The merged files, totalling some ∼45TB were then copied to NERSC for archiving and to be further processed to produce the final IRFs.

Now, as GT deploys its own OSG resources[25], the simulation scripts[26] and software has been migrated to the new Buzzard OSG cluster, along with being integrated into the 'StashCache'[27] service.

OSG.

[25] https://docs.pace.gatech.edu/osg/openScienceGrid/

[26] Hosted on GitHub: https://github.com/agent3gatech/VERITAS

[27] https://osg-htc.org/docs/data/stashcache/overview/index.html

CHAPTER 5

A SEARCH FOR PULSED VHE EMISSION FROM SIX MSPS

This chapter details the survey carried out to investigate VERITAS data on six MSP targets for any hint of pulsed emission in the VHE gamma-ray regime. Firstly, I give a recap on the theoretical and experimental motivation for investigating pulsars, and particularly MSPs, at GeV-TeV energies. Secondly, I will introduce the survey methods, give background on the target PSRs, present the HE and VHE analysis results, and discuss the conclusion and impact of the results.

5.1 Motivation for Investigating MSPs

As has been the case for several years now (see [36] for a nice summary of the timeline), the Crab pulsar [16] [17] remains the only pulsar to have been authoritatively[1] detected in the VHE regime. The *Fermi*-LAT has confirmed the presence of pulsed gamma-rays, and light curves that closely match those of the regular pulsar population, from a significant number of MSPs. The well-documented, extensive, curvature-radiation component seen by *Fermi*-LAT [1] fits the expected behavior of a radiation-reaction-limited population of emitting electrons/positrons; that have reached their maximum energy limit, and radiate energy at the same rate as they gain it. Although the sensitivity of the LAT drops off above a few tens-of-GeV, the HE data clearly prefers an exponential cutoff in the observed pulsar spectra. This makes the case for a separate mechanism being responsible for producing the VHE photon population (see [192] and [193] for a nice summary). The process could be capable of producing either a higher-energy population of source particles, or for directly producing

[1] i.e. adhering to the usual 5-sigma detection threshold using *only* gamma-rays in the VHE regime, and not below. Some claims have been made, but they do not adhere to this criteria; see [19] and [189] for HESS probing of the Vela PSR, and PSR B1706-44 [190], and also [191] for MAGIC observations of Geminga, with a nice summary in [32].

VHE gamma-rays, up to the energies seen in the aforementioned Crab and Vela [19], pulsar data. Here, our primary goal is to test to see if any significant pulsed emission is detected from the MSP targets: to confirm, or dispute, emission as seen from the Crab pulsar and the VHE component(s) predicted by theoretical modeling [32] [28]. The detection of pulsed emission would allow a VHE data-to-theory light curve comparison, and also place explicit lower limits on the highest particle energies that produce said pulsed emission, at the level of the most energetic gamma-rays detected [64]. Any proposed scenario has to explain the apparent power-law-like spectral shape when the HE and VHE data are fitted, when combined, and so the data herein help guide broad-band modeling.

5.1.1 Current Understanding and Theoretical Questions

Although a comprehensive theoretical framework does not yet exist, that can fully explain the observed VHE behavior of the Crab pulsar, there exist several promising models for particular mechanisms producing VHE gamma-ray emission inside the magnetosphere (see [194] [195] and references therein). These 'intra-magnetospheric' theories can be broken down into three main categories, with variations on each existing, based on the proposed acceleration zones that are responsible for creating the relativistic particle population, which then go on to radiate and IC up-scatter seed photons to VHE energies. The proposed models include the predictions of particle acceleration happening primarily in the; 'Polar Cap', 'Outer Gap' and 'Slot Gap' regions, and are detailed by the associated frameworks (see section 2.4). In particular: in Lyutikov et al. [28], a promising work that could explain the VHE emission seen from pulsars, the authors adopt a scenario where synchrotron photons are up-scattered to VHE energies by the very population of electrons that produce them. This process is known as synchrotron self-Compton (SSC) scattering and provides a possible mechanism for the production of VHE gamma-rays from the particle cascades formed in the outer gap [28] of the magnetosphere.

An alternate mechanism that could offer a possible explanation for gamma-ray emis-

sion, but, in this case, lies outside the magnetosphere, is VHE photon production in a 'cold ultra-relativistic wind' [129]. This proposed scenario involves the conversion of the radiated Poynting flux to particle momentum, by rapidly accelerating the wind particles, but at a large distance of $\sim 30R_L$ from the pulsar.

Finally, there exist models that are currently in favor, where the Y-point and equatorial current sheet regions (i.e. at, and beyond, the light cylinder) are responsible for producing the highest energy particles and VHE gamma-rays. This could be through processes linked to magnetic reconnection and efficient conversion of radiation, to accelerate particles to ultra-relativistic energies[196]. Or, alternatively, through secondary particles being accelerated by the EM field in the ECS and then radiating SSC[29], possibly with additional IC photons from accelerated primary particles up-scattering SR from secondary particles [77], to explain pulsar emission from radio through to the TeV regime[32] (also see section 2.2.2).

With some models seeming more favorable than others, further evidence is needed to hone existing predictions, further theoretical understanding and constrain the parameters of possible scenarios. In this work, the aim is to probe (or constrain) such predicted components (as detailed in section 2.2), if pulsed emission is observed (not detected). New detections in the VHE regime, but also constraining upper-limits would greatly help to provide particular insight into exact emission mechanisms (or interplay of separate mechanisms), the structure of the pulsar magnetosphere and the behavior of the particle populations as they are accelerated [32].

5.1.2 Drivers of the VHE MSP-Specific Survey

A search for pulsed emission from archival VERITAS data of *young pulsars* has already been carried out (see [36] & [162]) and while valuable constraints, in the form of upper limits on pulsed emission, were obtained, none of the 13 targets where detected. This work aims to extend the hunt for a detectable source of pulsed VHE gamma-rays, through obser-

vations of 6 separate MSPs. While less luminous at lower energies than the most energetic younger pulsars, MSPs are thought to possibly have higher gamma-ray conversion efficiencies (i.e. a higher proportion of the spin-down energy being converted into VHE gamma-rays) [197] [38] and so could be excellent candidates to investigate for pulsed VHE flux from rotation-powered pulsars [64].

Despite having lower surface magnetic field strength[2], and thus presenting a potentially problematic situation to reconcile[3] with necessary single-photon pair-production (see 2.3.2), MSPs' high angular velocities can lead to large accelerating electric fields, and values of $\dot{E}$.

In addition, the tighter limit on the light cylinder radius, due to the rapid rotation rate of MSPs, means that the area of the magnetosphere with closed field lines is confined to a smaller volume, which may lead to a larger pair-production density. High pair multiplicity is essential for significant SSC emission; the SSC flux scales with the square of the particle density. The compact nature of the MSP magnetosphere also means that the highest energy particles, located in the ECS, are physically closer to the soft photons emission inside the LC, thus enhancing the probability of IC scattering events. Due to having more energetic pairs, than Crab-like pulsars, MSPs should show a SSC component extending to TeV energies. However, it may be that MSPs do not have sufficient pair multiplicity to generate SSC flux at a level that can be seen with modern IACTs[29] and that the high pair energies lead to suppression of scattering processes due to Klein-Nishina effects[32]. Also, crucially, due to relatively small values of R_L, MSPs can exhibit magnetic field strengths in the outer magnetosphere and around the light cylinder[4] that even rival the most powerful young pulsars, and are necessary to enhance the SR emission level. Such a MSP was investigated by MAGIC [198], but no detection in the VHE regime resulted.

[2]In comparison with the regular, 'non-recycled' pulsar population.

[3]One solution, that also fits with modern publications, is the presence of additional magnetic field components (see 2.2.5), close to the NS.

[4]This is hugely important, given the current favor of theory where the outer gaps and the Y-Point near the light-cylinder and beyond in the ECS, are the primary sites of acceleration/emission: MSPs *can* provide the necessary magnetospheric morphology and conditions, around R_L, to produce VHE gamma-rays [64].

The high X-ray luminosity of some MSPs leads some to the belief that there could exist 'Crab-like' MSPs, with efficient pair creation in the vicinity of the light-cylinder [32]. The more concentrated particle population could produce sufficient IC radiation to produce the pulsed VHE emission we probe. Questions have also been raised about the presence of an exotic magnetic field structure in MSPs, either manifesting offsets in the field core position and/or non-dipolar field contributions [199] which can be investigated through features of VHE pulsar light curves. If detection of significant pulsed emission can be claimed, then we can assess if the MSP population exhibits emission characteristics in line with current models, or, that significantly deviate from the regular pulsar population. This work will be the first survey of MSPs in the VHE regime, comprising of more than 100 hours of quality-selected IACT gamma-ray data.

5.1.3 Investigation into the Energetic Trends of all Pulsars

Aside from directly probing for pulsed VHE gamma-rays from MSPs, to investigate different emission scenarios, any observed trend in the gamma-ray luminosity of all the MSP targets here is an additional useful diagnostic tool, to test proposed models [122] [28]. In a regime where particle acceleration is restricted by the available potential energy in the gap region ('potential-limited' acceleration), the gamma-ray luminosity is predicted to vary as a function of $\sqrt{\dot{E}}$ [5], rather than as a linear function of $\dot{E}$, as would be expected in a scenario where the particle energy is limited by radiation-reaction. This relationship, often expressed as;

$$\int_{E_{thresh}}^{E_{max}} F_\nu \, d\nu \propto \frac{1}{d^2} \left(\dot{E}\right)^{\alpha_{eff}}$$

[5] As seen, early on, by EGRET [200] [201]

where the index, α_{eff}, to be investigated [135] is at most unity [122] and represents a measure of energy conversion efficiency[6]. An alternative formulation is;

$$L_\gamma = k_{pulsar} \left(\dot{E}\right)^{\alpha_{eff}}$$

where L_γ is the observed luminosity of the pulsar, in the pulsed gamma-ray regime.

As shown by Hirotani [125], factors that contribute to α_{eff}, such as acceleration gap thickness and 'effective' charge density, are smaller in younger pulsars but grow with characteristic pulsar age[7], leading to the hypothesis that older pulsars are more efficient at converting their spin-down energy into radiative luminosity. The 'net effective accelerating' charge density assumed, in a non-idealized scenario, parameterized as; $\kappa = (\rho_{GJ} - \rho)/\rho_{GJ}$, the difference between the Goldreich-Julian charge density and the real charge density, normalized to ρ_{GJ}, it enters into the equation for luminosity linearly. The gap thickness $h_{gap} \equiv (\theta_{max} - \theta_{min})/\theta_{max}$, is defined as the dimensionless difference between the polar angles of the last open field line, θ_{max}, and the upper bound on the gap region, θ_{min}, the pulsar luminosity is expected to depend on h_{gap}^3. For the Crab, a young pulsar, considering an OG[8](see [125] for more discussion) model $h_{gap} \approx 0.1$ & $\kappa \approx 0.3$ but, for older pulsars, these parameters can be $h_{gap} > 0.5$ & $\kappa \approx 1$, leading to possible values of $\alpha_{eff} > 0.5$.

No conclusive luminosity dependence has been confirmed in the regular pulsar population, from observations by VERITAS and other experiments, thus far. The MSP survey carried out here will add more 'data points' to further probe this relationship between pulsar luminosity, in VHE gamma-rays, and the spin-down power of said pulsars. Confirmation of a firm relationship would be very valuable [134], and, if a distinct behavior is seen in MSPs, theorists could gain even more precise information, to narrow the phase-space of

[6]The limits of integration here represent the VERITAS energy range: we are investigating the dependency of this relationship in the VHE regime

[7]Due to changes in the pulsar kinematics and EM fields, rather than anything 'intrinsically' age-dependent.

[8]For SG models the gap thickness is less than half of this value.

model parameters, such as h_{gap} & κ [64] [32]. Even constraints on the possible values for α_{eff} would give insight into the mechanisms and regions responsible for the production of VHE gamma-rays. This is because potential-limited acceleration and radiation-reaction limited acceleration are thought to exhibit different dependencies of the gamma-ray luminosity on the spin-down energy loss rate [28], as discussed above. The possible values of uncertain parameters, such as κ and h_{gap} could also be narrowed down by constraints on α_{eff}.

5.2 The Sources

Here we discuss the characteristics of the six MSPs analyzed in this work.

5.2.1 PSR J0030+0451

PSR J0030+0451 (hereafter J0030) is an isolated MSP in the disk of the Galaxy, discovered by Arecibo [202], with a rotation period of 4.8 ms and a spin-down luminosity of $3.5 \times 10^{33}\ erg\ s^{-1}$ [203] at a relatively close distance of approximately 303pc [204] [205]. There is no candidate for the companion from which the accretion that, presumably, spun up this pulsar. It is possible that J0030 completely consumed its companion [206] and so offers an interesting insight into a rare member of the pulsar 'evolutionary chain'. There has been recent interest in the pulsar as NICER X-ray date implies surface hot-spots and magnetic field morphology that is non-dipolar in nature [93].

5.2.2 PSR J0751+1807

PSR J0751+1807 (hereafter J0751) exhibits a rotation period of 3.48ms [207], this MSP, discovered as part of a binary system with a white dwarf. The binary system has an orbital period of $\sim$6.3h [208] and is located at a distance of $\sim$1.15kpc [209] or possibly a distance of $\sim 1.51 \pm 0.35$ kpc according to [210]. The derived spin-down luminosity for J0751 is $7.3 \times 10^{33}\ erg\ s^{-1}$.

5.2.3 PSR J1024-0719

PSR J1024-0719 (hereafter J1024) was discovered, along with three other isolated MSPs, in the Parkes survey of the southern sky [211] and in then confirmed in X-rays [212]. With a rotational period of 5.2 ms [203], leading to an $\dot{E}$ of $5.3 \times 10^{33}\ erg\ s^{-1}$. Initially reported at a distance of 200pc [213] but this estimate has since been updated to $\sim$1.20kpc [214] after correcting for Lutz-Kelker bias [215] [216] and, even more recently, to 1.22kpc (see [217] and references therein). This is an extremely wide binary system, consisting of the PSR and Main Sequence star that only complete an orbit of each other every 200yrs. This is a very interesting scenario to observe as the MS star cannot have been the companion that caused J1024 to spin up to the MSP state. It is thought that the 'missing' object was completely ablated [218] or possibly escaped from the triple object system [219], either way a rare scenario.

5.2.4 PSR J1816+4510

PSR J1816+4510 (hereafter J1816) is an eclipsing binary, belonging to the so-called 'redback' system population (see [220] and references therein for a comparison of 'black widow' and 'redback' systems and their formation and properties). The binary orbital period is $\sim$8.7h [221]. The MSP has a rotational period of $\sim$3.2 ms and an $\dot{E}$ of $5.2 \times 10^{34}\ erg\ s^{-1}$. J1816 is a high-mass pulsar with a companion exhibiting abnormally high metallicity [222] [223] at a distance of 4.36kpc using the model of [204] or 4.5kpc with [224]

5.2.5 PSR J1939+2134

PSR J1939+2134 (also known as PSR B1937+21, hereafter J1939) was the first discovered MSP [225] with a period of $\sim$1.56ms [203], this rapid rotational rate leads to high energetics, giving a spin-down luminosity of $1.1 \times 10^{36}\ erg\ s^{-1}$. At a distance of 3.58 kpc [213] [226] this isolated and very luminous MSP has been extensively studied in the past

Table 5.1: A summary of the properties of the MSP targets for the survey. The distances and $\dot{E}$s listed here are used for the luminosity and gamma-ray conversion efficiency calculations. Also shown are the properties of J0218+4232, for reference and for comparison of results to model expectations in Subsection 5.4.1.

Pulsar Name (J2000)	P (ms)	$\dot{F}$ ($10^{-16}\ s^{-2}$)	Distance (pc)	$\dot{E}$ ($10^{33}\ erg\ s^{-1}$)	$\dot{E}/d^2$ ($10^{33}\ erg\ kpc^{-2}\ s^{-1}$)	$B\ (R_{LC})$ ($10^4\ G$)	VERITAS Exposure (hr)
J0030+0451	4.8	4.29	303	3.5	33	1.83	20.0
J0751+1807	3.5	6.45	1150	7.5	5.9	3.71	23.0
J1024-0719	5.2	6.96	1220	5.3	3.6	2.13	21.0
J1816+4510	3.2	42.2	4500	52	2.8	10.8	4.5
J1939+2134	1.6	433	3580	1100	90	102	42.0
J1959+2048	1.6	65.1	1730	160	82	37.6	5.0
J0218+4232	2.3	143	3150	240	25	32.1	N/A

several decades.

5.2.6 PSR J1959+2048

PSR J1959+2048 (hereafter J1959) is another well known 'black widow' pulsar, J1959 has a brown dwarf companion and together they form an eclipsing binary system [227]. With a rotational period of $\sim$1.6ms [228] and a spin-down luminosity of $1.6 \times 10^{35}\ erg\ s^{-1}$. A lower limit on the distance to J1959 of $\sim$2kpc was placed [229] but more recent electron density model places the distance at $\sim$1.73kpc [204].

5.3 Data Analysis Method & Results

5.3.1 Pulsar Analysis With VERITAS Data and Peripheral Software

Pulsar-specific analysis of VERITAS data requires an extra stage, beyond the regular analysis chain. Once the standard analysis procedure (described in Chapter 4) has been completed, gamma-like events that have passed all required quality and selection cuts are then assessed again, regarding their temporal profile. This, in theory, allows for extra sensitivity to low pulsed-fluxes by introducing an additional discriminant between the expected 'On pulse' regions, in phase, and the 'Off pulse' phase bin.

The pulsar analysis software 'Tempo2'[158] is, as per the procedure for *Fermi*-LAT

Table 5.2: The resultant *Fermi*-LAT HE gamma-ray phaseograms, from the phase gating procedure, that define the 'On/Off' phase regions for the VERITAS pulsed analysis. The background regions ('Off' gates) used are shown in dark blue and the pulse regions ('On' gates) are shown in green. Zones colored white, often corresponding to inter-peak, so called 'bridge emission' are considered neither 'On' nor 'Off'. The plots are generated with varying bin coarseness, dependent on the H-Test result.

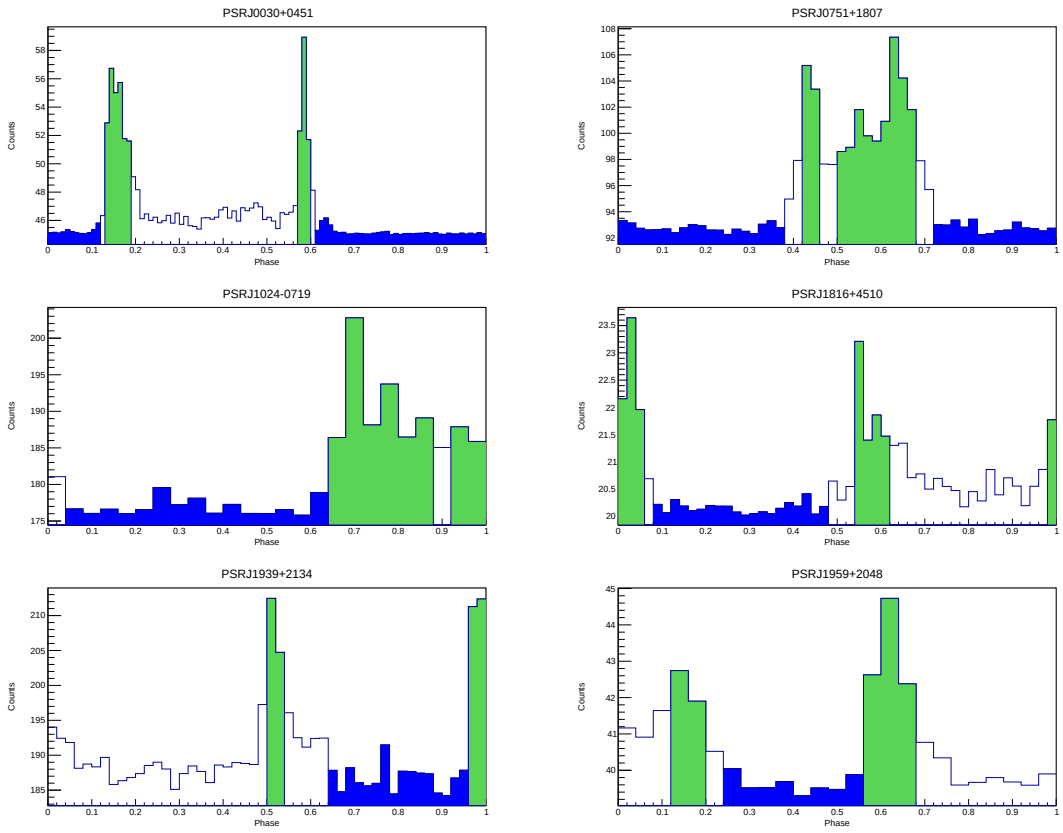

Table 5.3: Displayed in this table are the numerical values of the phase gates, from the phase gating procedure, that are used for the VERITAS pulsed analysis. Also shown are the percentages of a whole pulsar rotation, which the 'On' & 'Off' phase gates correspond to.

Pulsar	'On' Gate 1	'On' Gate 2	'Off' Gate	'On' Fraction	'Off' Fraction
J0030+0451	$0.13 \rightarrow 0.19$	$0.57 \rightarrow 0.60$	$0.61 \rightarrow 0.12$	9%	51%
J0751+1807	$0.41 \rightarrow 0.47$	$0.50 \rightarrow 0.69$	$0.72 \rightarrow 0.38$	25%	66%
J1024-0719	$0.67 \rightarrow 0.85$	$0.91 \rightarrow 0.93$	$0.03 \rightarrow 0.63$	20%	60%
J1816+4510	$0.99 \rightarrow 0.06$	$0.54 \rightarrow 0.63$	$0.08 \rightarrow 0.49$	16%	41%
J1939+2134	$0.49 \rightarrow 0.54$	$0.96 \rightarrow 1.00$	$0.63 \rightarrow 0.95$	9%	32%
J1959+2048	$0.12 \rightarrow 0.18$	$0.59 \rightarrow 0.68$	$0.26 \rightarrow 0.56$	15%	30%

data, detailed in section 4.10.1, used to generate Solar-system-barycentric TOAs using the most accurate ephemeris information available for each pulsar, along with parameterization of the PSR rotation and spin-down dynamics, knows as a 'Timing Solution'. These timing solutions are produced from observations of said pulsar in different parts of the EM spectrum (through radio or lower-energy gamma-ray data, from the *Fermi*-LAT, for example). Some timing solutions are regularly published and made available, but others have been obtained by direct correspondence with other scientists. This work makes use of timing solutions from: M. Kerr's LAT pulsar timing tool [230], NANOGrav MSP timing [203] and from private communications. They are usually chosen, from what can be attained, by what is the most up-to-date, but the timing solution must be valid for the time period that the VERITAS observations were taken.

The barycentering and phase-folding functions of Tempo2 are invoked via a script to interface with VEGAS and process the event time-stamp data. Barycentered[9] VERITAS timestamps are assigned a phase value, corresponding to the pulsar's relevant rotational phase when the gamma-ray in question was emitted, by comparison to a simple time-series model of the pulsar's spin characteristics that Tempo2 formulates and analyzes, by utilizing the timing solution (see [33]).

The VHE gamma-ray events are then assigned to contribute to either signal or background event counts, in terms of the pulsed analysis, depending if they fall in the 'on pulse' (pulsed signal + background) or 'steady emission' (pulsed background) bins, that are determined from the HE gamma-ray analysis.

The number of events falling into each bin are then taken to calculate an excess number of signal events and quantify the level of significance of any pulsations seen, compared to the null hypothesis of a completely time-independent profile (see [161] and [162] for further reading). This process is analogous to the method described in sections 4.11.3 &

[9]Properly accounting for various relativistic and geometrical corrections, such as: the observatory location on Earth, Earth's rotation, Earth's movement around the Sun and also delays due to gravitational energy of massive objects in the photons path. Accuracy to the nanosecond level is achieved, which is far below the rotational period of even MSPs. See [231] for an in-depth calculation.

4.11.3, but now searches for a gamma-ray excess in phase, rather then spatially, and again uses the Li & Ma significance formulation. If a low test statistic is returned, then upper limits can be placed on the pulsar's pulsed flux.

Again, we note that this approach assumes the VHE emission is in-phase with the HE emission pulses[10] although, if obvious emission peaks were observed in the visual inspection of the VHE phaseograms a separate test of the level of these pulsations could be applied.

This procedure is applied to the VEGAS data-products for all six MSPs, for SOFT, MEDIUM and HARD cut values, as we assume no prior spectral shape (see section 4.11.2). With the phase-gate significance test and the H-Test a total of 6 trials must be accounted for if detection-level confidence results.

5.3.2 Results From the Analysis

No significant VHE pulsed emission[11] is observed from any of the 6 MSP targets in this survey. Tables 5.4 - 5.9 report the results for the pulsed analysis of each MSP, giving details on the analysis energy threshold, significance level of possible time-dependent emission[12] and ULs in various forms, for comparison with literature.

For the 95% CL flux (procedures for calculating these values are given in Subsection 4.11.3) and luminosity ULs, the method assumes an intrinsic source spectral index of 3.8 to match the Crab pulsar in [16] and the archival pulsar search [162]. The ULs on VHE gamma-ray luminosity are calculated as such;

$$L_{\gamma}^{UL} = 4\pi\ d^2\ f_{\Omega}\ E_{Flux}^{UL}$$

where d is the distance to the pulsar and f_{Ω} is the 'beam correction factor' [163]. f_{Ω} accounts for the fraction of the sky that the pulsed emission is assumed to be beamed into.

[10] For this reason, the, unbinned H-Test is also automatically applied as a check.
[11] No evidence of unpulsed emission is detected using the standard VERITAS analysis chain, either.
[12] Above the null hypothesis of a constant flux in time.

It is a function of the pulsar's magnetic inclination angle, α, and ζ, the angle between the rotational axis and the line-of-sight to Earth, and is highly model-dependent. f_Ω can take a range of values: for a polar cap model (where emission is tightly beamed) $f_\Omega \approx 1/4\pi$ but for models assuming VHE gamma-ray production in the outer magnetosphere or beyond, in a more diffuse beam that encompasses the whole sky, $f_\Omega \approx 1$ [232]. In line with the current theory to be tested, we adopt the latter value.

Values for the significance level of possible pulsations seen, vary from -2.7σ to 1.6σ, and follow approximately[13] the expected normal distribution of the null hypothesis, that is: observing no excess in the 'On' phase region. We note the particularly negative excess for J1024 for Soft cuts, resulting in a significance of -2.75σ and, hence, an exceptionally stringent UL. This value is consistent with a statistical outlier from a downward fluctuation in the excess counts in the phase test.

The VEGAS results and ULs are corroborated by an analysis cross-check, done with the EventDisplay package, by Tony Lin.

Table 5.4: The pulsed analysis results for the pulsar J0030+0451, shown across two tables for clarity. The limits on luminosity assume a distance of 303pc. Details of the quantities and calculations are given and discussed in sections 4.11.3 & 5.3.2.

Spectral cuts	$\mathrm{E_{threshold}}$ [GeV]	Significance (Pre-Trials) [Sigma]	95% CL flux UL ($> \mathrm{E_{threshold}}$) [10^{-13} cm^{-2} s^{-1}]	95% CL flux UL (1–10 TeV) [10^{-15} cm^{-2} s^{-1}]	95% CL luminosity UL (1–10 TeV) [10^{30} erg s^{-1}]
Soft	166	-0.21	4.56	2.98	0.0804
Moderate	263	0.71	2.72	6.43	0.173
Hard	417	-0.26	0.750	6.47	0.174

Spectral cuts	95% CL Differential UL (@ $\mathrm{E_{threshold}}$) [10^{-12} TeV^{-1} cm^{-2} s^{-1}]	95% CL Energy flux UL ($> \mathrm{E_{threshold}}$) [10^{-13} TeV cm^{-2} s^{-1}]	95% CL luminosity UL ($> \mathrm{E_{threshold}}$) [10^{32} erg s^{-1}]	Gamma-ray efficiency UL ($> \mathrm{E_{threshold}}$) [%]
Soft	7.69	1.18	0.0208	0.0593
Moderate	2.89	1.11	0.0196	0.0559
Hard	0.504	0.487	0.00857	0.0245

[13] We have a 'relatively small' sample size of 6×3 measurements.

Table 5.5: The pulsed analysis results for the pulsar J0751+1807, shown across two tables for clarity. The limits on luminosity assume a distance of 1150pc. Details of the quantities and calculations are given and discussed in sections 4.11.3 & 5.3.2.

Spectral cuts	$E_{threshold}$ [GeV]	Significance (Pre-Trials) [Sigma]	95% CL flux UL ($> E_{threshold}$) [10^{-13} cm^{-2} s^{-1}]	95% CL flux UL (1–10 TeV) [10^{-15} cm^{-2} s^{-1}]	95% CL luminosity UL (1–10 TeV) [10^{30} erg s^{-1}]
Soft	138	0.86	18.9	7.39	2.87
Moderate	200	0.70	9.92	10.9	4.25
Hard	316	0.73	4.21	16.6	6.49

Spectral cuts	95% CL Differential UL (@ $E_{threshold}$) [10^{-12} TeV^{-1} cm^{-2} s^{-1}]	95% CL Energy flux UL ($> E_{threshold}$) [10^{-13} TeV cm^{-2} s^{-1}]	95% CL luminosity UL ($> E_{threshold}$) [10^{32} erg s^{-1}]	Gamma-ray efficiency UL ($> E_{threshold}$) [%]
Soft	38.5	4.08	1.03	1.38
Moderate	13.9	3.09	0.784	1.05
Hard	3.73	2.07	0.525	0.699

Table 5.6: The pulsed analysis results for the pulsar J1024-0719, shown across two tables for clarity. The limits on luminosity assume a distance of 1220pc. Details of the quantities and calculations are given and discussed in sections 4.11.3 & 5.3.2.

Spectral cuts	$E_{threshold}$ [GeV]	Significance (Pre-Trials) [Sigma]	95% CL flux UL ($> E_{threshold}$) [10^{-13} cm^{-2} s^{-1}]	95% CL flux UL (1–10 TeV) [10^{-15} cm^{-2} s^{-1}]	95% CL luminosity UL (1–10 TeV) [10^{30} erg s^{-1}]
Soft	219	-2.73	0.0452	0.0641	0.0280
Moderate	347	-0.69	1.14	5.90	2.58
Hard	550	0.38	1.07	20.1	8.83

Spectral cuts	95% CL Differential UL (@ $E_{threshold}$) [10^{-12} TeV^{-1} cm^{-2} s^{-1}]	95% CL Energy flux UL ($> E_{threshold}$) [10^{-13} TeV cm^{-2} s^{-1}]	95% CL luminosity UL ($> E_{threshold}$) [10^{32} erg s^{-1}]	Gamma-ray efficiency UL ($> E_{threshold}$) [%]
Soft	0.0577	0.0154	0.00439	0.00829
Moderate	0.925	0.619	0.177	0.333
Hard	0.549	0.922	0.263	0.496

Table 5.7: The pulsed analysis results for the pulsar J1816+4510, shown across two tables for clarity. The limits on luminosity assume a distance of 4500pc. Details of the quantities and calculations are given and discussed in sections 4.11.3 & 5.3.2.

Spectral cuts	$E_{threshold}$ [GeV]	Significance (Pre-Trials) [Sigma]	95% CL flux UL ($> E_{threshold}$) [10^{-13} cm^{-2} s^{-1}]	95% CL flux UL (1–10 TeV) [10^{-15} cm^{-2} s^{-1}]	95% CL luminosity UL (1–10 TeV) [10^{30} erg s^{-1}]
Soft	138	0.52	27.6	10.7	64.0
Moderate	200	1.66	20.0	22.0	131.
Hard	316	-0.42	3.66	14.5	86.3

Spectral cuts	95% CL Differential UL (@ $E_{threshold}$) [10^{-12} TeV^{-1} cm^{-2} s^{-1}]	95% CL Energy flux UL ($> E_{threshold}$) [10^{-13} TeV cm^{-2} s^{-1}]	95% CL luminosity UL ($> E_{threshold}$) [10^{32} erg s^{-1}]	Gamma-ray efficiency UL ($> E_{threshold}$) [%]
Soft	56.0	5.92	23.0	4.42
Moderate	28.0	6.22	24.2	4.64
Hard	3.24	1.80	7.00	1.34

Table 5.8: The pulsed analysis results for the pulsar J1939+2134, shown across two tables for clarity. The limits on luminosity assume a distance of 3580pc. Details of the quantities and calculations are given and discussed in sections 4.11.3 & 5.3.2.

Spectral cuts	$E_{threshold}$ [GeV]	Significance (Pre-Trials) [Sigma]	95% CL flux UL ($> E_{threshold}$) [10^{-13} cm^{-2} s^{-1}]	95% CL flux UL (1–10 TeV) [10^{-15} cm^{-2} s^{-1}]	95% CL luminosity UL (1–10 TeV) [10^{30} erg s^{-1}]
Soft	138	-0.67	2.90	1.13	4.28
Moderate	200	-0.07	2.26	2.48	9.37
Hard	316	0.70	1.51	5.99	22.5

Spectral cuts	95% CL Differential UL (@ $E_{threshold}$) [10^{-12} TeV^{-1} cm^{-2} s^{-1}]	95% CL Energy flux UL ($> E_{threshold}$) [10^{-13} TeV cm^{-2} s^{-1}]	95% CL luminosity UL ($> E_{threshold}$) [10^{32} erg s^{-1}]	Gamma-ray efficiency UL ($> E_{threshold}$) [%]
Soft	5.92	0.627	1.54	0.0140
Moderate	3.16	0.703	1.74	0.0157
Hard	1.34	0.744	1.83	0.0166

Table 5.9: The pulsed analysis results for the pulsar J1959+2048, shown across two tables for clarity. The limits on luminosity assume a distance of 1730pc. Details of the quantities and calculations are given and discussed in sections 4.11.3 & 5.3.2.

Spectral cuts	$E_{threshold}$ [GeV]	Significance (Pre-Trials) [Sigma]	95% CL flux UL ($> E_{threshold}$) [10^{-13} cm^{-2} s^{-1}]	95% CL flux UL (1–10 TeV) [10^{-15} cm^{-2} s^{-1}]	95% CL luminosity UL (1–10 TeV) [10^{30} erg s^{-1}]
Soft	138	-0.46	10.7	4.18	3.68
Moderate	200	1.37	12.3	13.6	11.9
Hard	316	0.69	5.62	22.2	19.6

Spectral cuts	95% CL Differential UL (@ $E_{threshold}$) [10^{-12} TeV^{-1} cm^{-2} s^{-1}]	95% CL Energy flux UL ($> E_{threshold}$) [10^{-13} TeV cm^{-2} s^{-1}]	95% CL luminosity UL ($> E_{threshold}$) [10^{32} erg s^{-1}]	Gamma-ray efficiency ($> E_{threshold}$) [%]
Soft	21.8	2.31	1.32	0.0828
Moderate	17.3	3.85	2.21	0.138
Hard	4.98	2.76	1.59	0.0991

5.4 Discussion and Conclusion

5.4.1 The Individual MSP Targets

The analysis of the VERITAS MSP data-set results in no indication of pulsed emission being present. As such, upper limits have been placed on the pulsed flux at competitive levels that constrain any pulsed emission component, in the given energy range, and also of the gamma-ray conversion efficiency in the VHE regime. The limits presented here are at comparable levels to recent ULs derived, also at 95% CL, from the MAGIC observations of PSR J0218+4232[198].

Modern models do not, anymore, expect a pure power-law extension of the energy spectrum into the VHE regime, and so individual emission components (see table 2.2) must be explicitly calculated for a range of possible parameter spaces for each PSR in question.

In addition, the most advanced models still suffer from intrinsic limitations in the simulations (see discussion in Subsection 2.2.2 and [32]). The model predictions are presented with the caveat of 'artificial' scaling factors being necessary, which, one might argue, pre-

vents completely concrete quantification of the expected VHE flux. However, said scaling can be reconciled with theory and the simulations seem to produce consistent and reliable results when comparisons are made to data from other experiments (see Figures 5.4, 5.5 and 5.6).

If the theoretical framework can be amended to produce completely 'organic' flux-scale predictions, they must be compatible with the limits from this work. This will either corroborate predictions of low flux, or possibly push favor towards further development of the theory and simulation models. Low VHE pulsed flux from MSPs may be due to the production mechanisms themselves not having sufficient participant particle-populations to sustain higher emission levels[29] or by VHE gamma-rays being attenuated before they can escape[14][32].

Limits on the VHE Pulsed Flux

The resulting flux limits from this survey are plotted in figures 5.1, 5.2 and 5.3 for Soft, Medium and Hard cuts, respectively. Shown are the differential flux upper limits, calculated at the analysis energy threshold (from tables 5.4 through 5.9), multiplied by the square of the energy threshold[15] and are plotted vs. $\sqrt{\dot{E}}/d^2$ for each MSP. The, often asymmetric, error in the distance to each pulsar is used to calculate the relevant error in $\sqrt{\dot{E}}/d^2$ and corresponds to the error bars shown:

$$\Delta\left(\frac{\sqrt{\dot{E}}}{d^2}\right) = \frac{\partial}{\partial d}\left(\frac{\sqrt{\dot{E}}}{d^2}\right)\Delta d = -2\frac{\sqrt{\dot{E}}}{d^3}\Delta d$$

In general, the limits here constrain the pulsed emission[16] from these MSPs, in the VERITAS energy range, to be[17] lower than that of the Crab pulsar ($\sim$1% of the Crab nebula

[14]The predominant channel for this attenuation of VHE emission is through interactions with other photons to produce $e^{\pm}$ pairs, thus partitioning the energy of the VHE gamma-rays to multiple lower energy particles

[15]This is a somewhat standard procedure for plotting spectra, historically adopted to highlight changes in spectral shape with energy. The factor of E^2 gives a dimension of $EA^{-1}t^{-1}$.

[16]For a new VHE component, or extension of HE component into the VHE domain.

[17]At 'worst' (least constraining), the flux limits are around the flux level of the Crab pulsar.

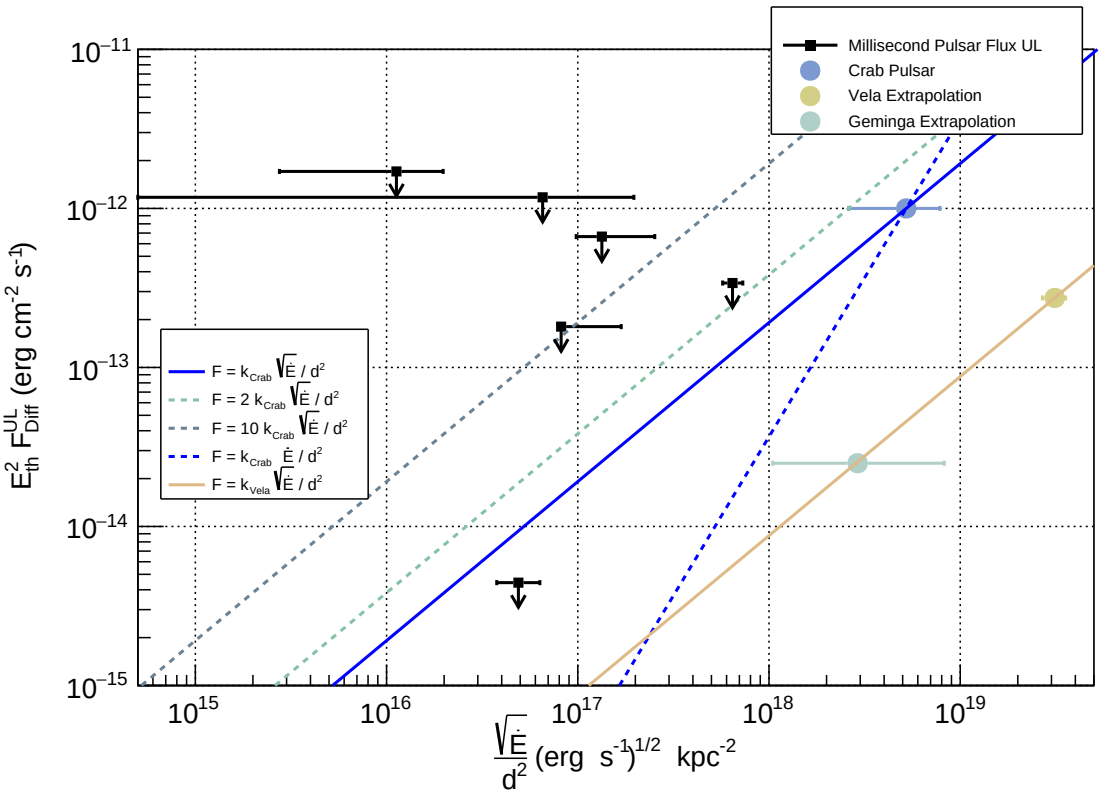

Figure 5.1: Plotted here are the *SOFT* cuts 95% CL ULs (at $E_{threshold} = E_{th}$) from the VEGAS pulsed analysis vs. the square root of the spin-down energy loss rate of the pulsar, scaled by the square of the distance to the pulsar. The flux values (y-axis) are calculated by multiplying the differential UL, F^{UL}_{Diff}, by the square of the threshold energy. The error bars are calculated accounting for the uncertainty on the distance to the pulsar, and propagating this error as it pertains to the $\sqrt{\dot{E}}/d^2$ value, as detailed in Subsection 5.4.1. Also shown are the flux values for the Crab, Vela and Geminga pulsars, for comparison. These values for the Crab are extrapolations of the VERITAS differential Crab pulsar flux seen at 0.2 TeV, to 0.3 Tev and 0.5 TeV, to roughly match the energy thresholds seen for the different cuts, by the usual power law of index -3.8. The Vela and Geminga points are extrapolated in the same way, from their *Fermi*-LAT spectrum above 10 GeV. This plot was produced following the methods in [36] to be able to compare the results directly with the VERITAS archival pulsar survey. The solid blue and gold lines represent a relationship of $F = k_{pulsar}\ \sqrt{\dot{E}}/d^2$, with values of k_{pulsar} such that they intersect the Crab and Vela flux points, respectively. The dashed green and gray lines follow the same proportionality but have k_{pulsar} set to 2 and 10 times k_{Crab}, to guide the eye. The blue dashed line represents a Crab-level flux that follows $F = k_{Crab}\ \dot{E}/d^2$, representing the case $L_\gamma \propto \dot{E}$.

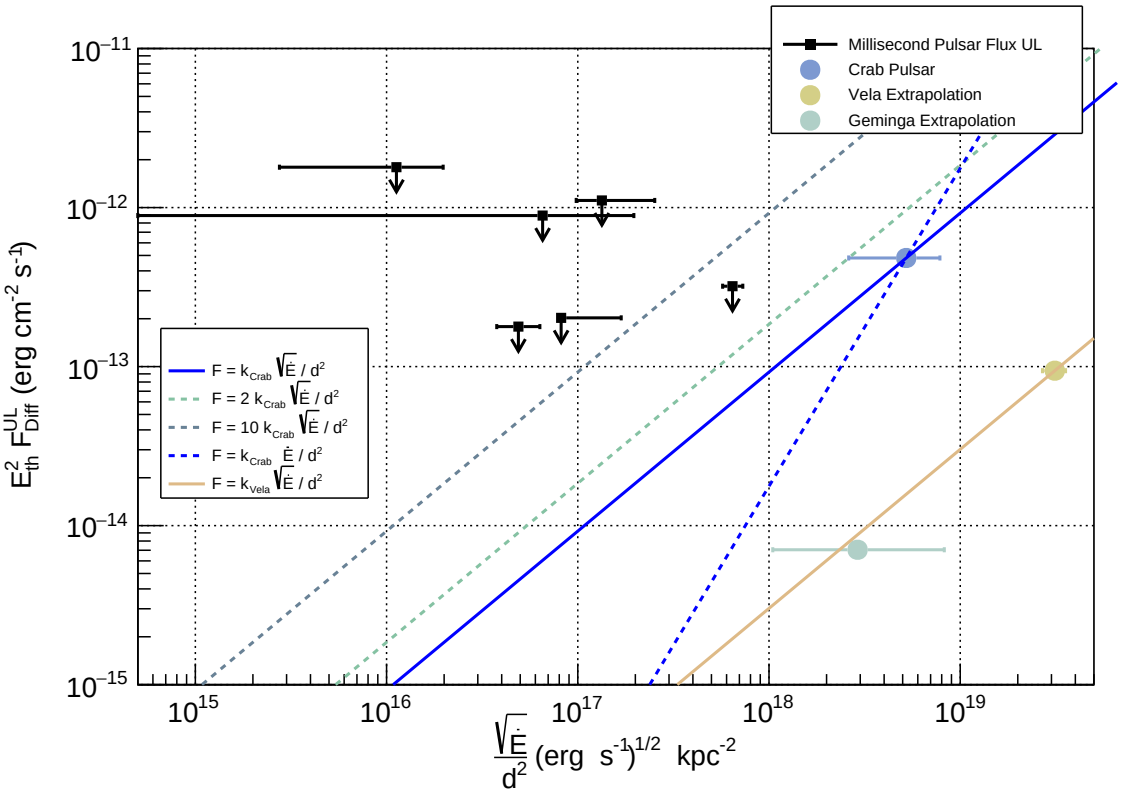

Figure 5.2: Plotted here are the *MEDIUM* cuts 95% CL ULs (at $E_{threshold}$) from the VEGAS pulsed analysis vs. the square root of the spin-down energy loss rate of the pulsar, scaled by the square of the distance to the pulsar. See 5.1 for further information.

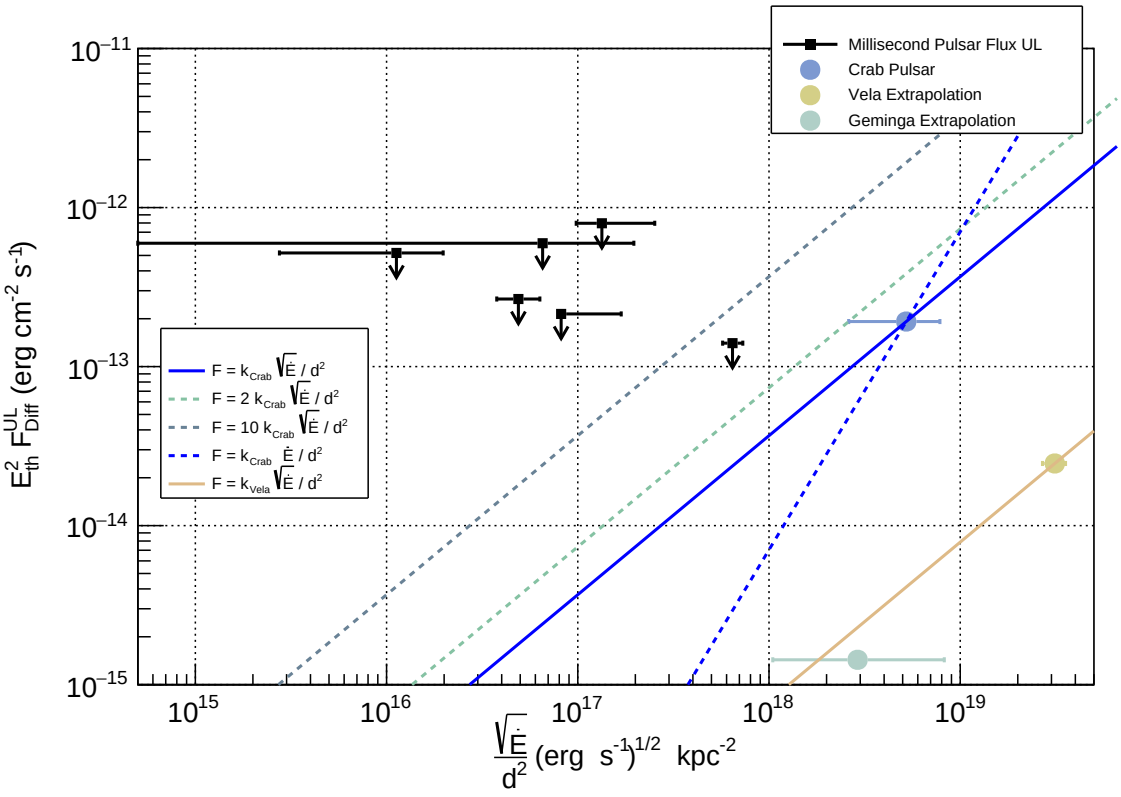

Figure 5.3: Plotted here are the *HARD* cuts 95% CL ULs (at $E_{threshold}$) from the VEGAS pulsed analysis vs. the square root of the spin-down energy loss rate of the pulsar, scaled by the square of the distance to the pulsar. See 5.1 for further information.

flux). This agrees with the conclusion found for young pulsars: that any pulsed emission present must be at a flux level too low for current generation IACTs to detect [162]. If we pose that, following the $F \propto \sqrt{\dot{E}}/d^2$ scenario, pulsars whose points on plots 5.1, 5.2, 5.3, are located around the solid blue line, intersecting the Crab flux point, would be successfully detected by such observations as these, only one case challenges this: J1024-0719 for *Soft* cuts[18]. Therefore, this survey does not constrain such a claim in most cases. Similar can be said for the $F \propto \dot{E}/d^2$ case (blue dashed line), as no flux UL points fall below the trend-line. It may be that the proportionality is correct, but the 'flux constant' of other pulsars is below that of the Crab. For all cut types the limit for PSR J0030+0451 falls closest to the $\sqrt{\dot{E}}/d^2$ line corresponding to the Crab pulsar, and in all cases is within an order of magnitude from this proportionality. This makes J0030 an excellent target to observe with CTA, as the improvement in sensitivity should mean that, if pulsed emission is not detected given the same exposure, then the corresponding limit should challenge the case of $F = k_{Crab}\ \sqrt{\dot{E}}/d^2$, which would be an important result in showing that the trend for the Crab pulsar is not to be expected for all MSPs.

Comparison of Limits with Current Models

Here we compare the VERITAS flux limits with the model of Harding, Venter & Kalapotharakos (hereafter: **HVK21**) [32]. Featuring all applicable emission channels (SC, SSC and IC), this model can produce spectral predictions across 18 decades in energy, up to 100 TeV, defining the fields throughout the magnetosphere, and so is the most comprehensive model to date. The best model-data available is for the Crab PSR and PSR J0218+4232, another MSP, as none of the MSPs in this survey have been explicitly modeled. As always the Crab is an interesting reference point, but certainly over-predicts emission that might be observed from MSPs.

Although the simulations are pulsar-specific, taking $P, \dot{P}, \alpha, \zeta$ and M_+[19], as parame-

[18] However, this particular limit, as noted previously, seems to be a statistical outlier.

[19] M_+ is the pair cascade multiplicity. It is taken as an input parameter to such simulations and deter-

ters, the characteristics of the separate spectral components[20] of the J0218+4232 simulation should be similar to what might be expected, if/when specific simulations become available for for the six MSPs targeted here. As seen in Table 5.1, PSR J0218+4232 exhibits properties typical of the averages of the VERITAS survey MSPs, and so provides the best comparison simulation available. We note that J0218+4232 would be ranked *2nd*-highest in $\dot{E}$, so it is expected to be fairly energetic, although it is placed only *4th*-highest in terms of expected luminosity at Earth.

To provide the most reasonable comparison we apply scaling to the model of J0218, assuming that the separate emission components appear at the same energy scales, but the expected flux levels are modified. We can correct the model flux to account for the different distances to the targets, and for the relative spin-down luminosities of the MSPs, which governs their overall energetics. The final scaling factor, ϵ, calculated for each MSP, which the flux of J0218 is multiplied by is calculated as:

$$\epsilon = \left(\frac{d_{J0218}}{d_{MSP}}\right)^2 \frac{\dot{E}_{MSP}}{\dot{E}_{J0218}}$$

In an earlier work by Harding & Kalapotharakos (hereafter: **HK15**) [29], a simulation was performed for PSR J1939+2134, which *is* one of the MSP targets here. However, this older simulation does not include any IC scattering from primary particles, only SSC from secondary particles. The predicted flux levels of the more modern simulation for PSR J0218+4232 matches well the features of the older simulation for PSR J1939+2134, except for the lack of the IC component, of course. Hence, we opt to show the modern, more comprehensive, simulation from **HVK21** for comparison here[21]. The expected phase-averaged spectral energy distributions (SEDs) from these three simulations are shown in

mines the number of secondary particle pairs that are produced from a single injected primary particle, see Subsection 2.3.2

[20]Explicitly; we are effectively assuming that the energy scales at which the different components, from the individual emission mechanisms, appear and the interplay/relative size of said components will be similar to J0218, for other MSPs.

[21]The conclusions drawn are the same when making comparisons with the J1939 model from **HK15**.

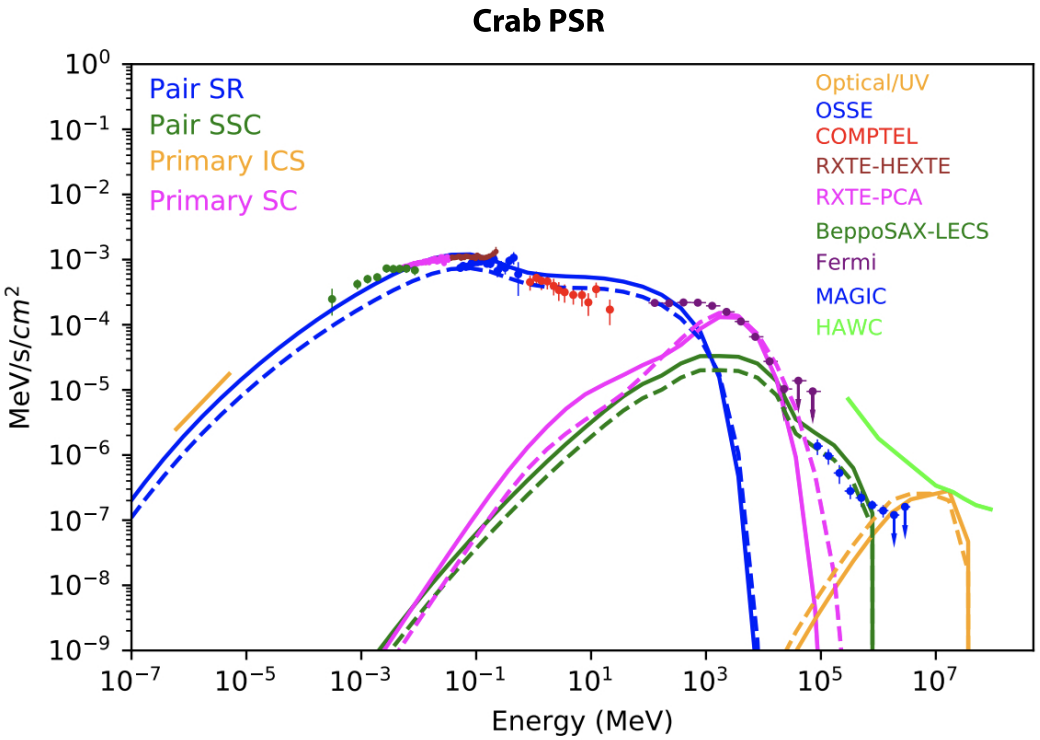

Figure 5.4: The phase-averaged SED for the Crab pulsar from the model of **HVK21**, taken from [32]. The simulations assume; $M_+ = 3 \times 10^5$, a rotational-magnetic inclination angle $\alpha = 45°$ and the dashed lines indicate the choice of rotational-viewing inclination angle $\zeta = 72°$, while the solid lines represent $\zeta = 60°$.

figures 5.4, 5.5 and 5.6. The models, for these pulsars take $M_+ = 3 \times 10^5$, which is a moderate value in **HVK21**.

In figures 5.7 - 5.12 we show the VERITAS differential flux ULs for each pulsar, for all three cut types, plotted with the model SED of PSR J0218+4232 from **HVK21**, that has been scaled by a factor of ϵ, as described above. As the simulations of **HVK21** produce phase-averaged SEDs, the VERITAS ULs are also averaged over one pulsar rotation for a proper comparison. To achieve this the ULs are scaled by a factor determined by comparing the size of the 'On' phase regions to a full rotation. Also shown are phase-averaged *Fermi*-LAT flux points, calculated using a standard Fermitools likelihood analysis[22], for each

[22]The spectral analysis used to generate the HE flux points employs the same data selection procedure as detailed in section 4.10.1, but extends the observation time-window to between 2008-10-27 and 2022-06-13.

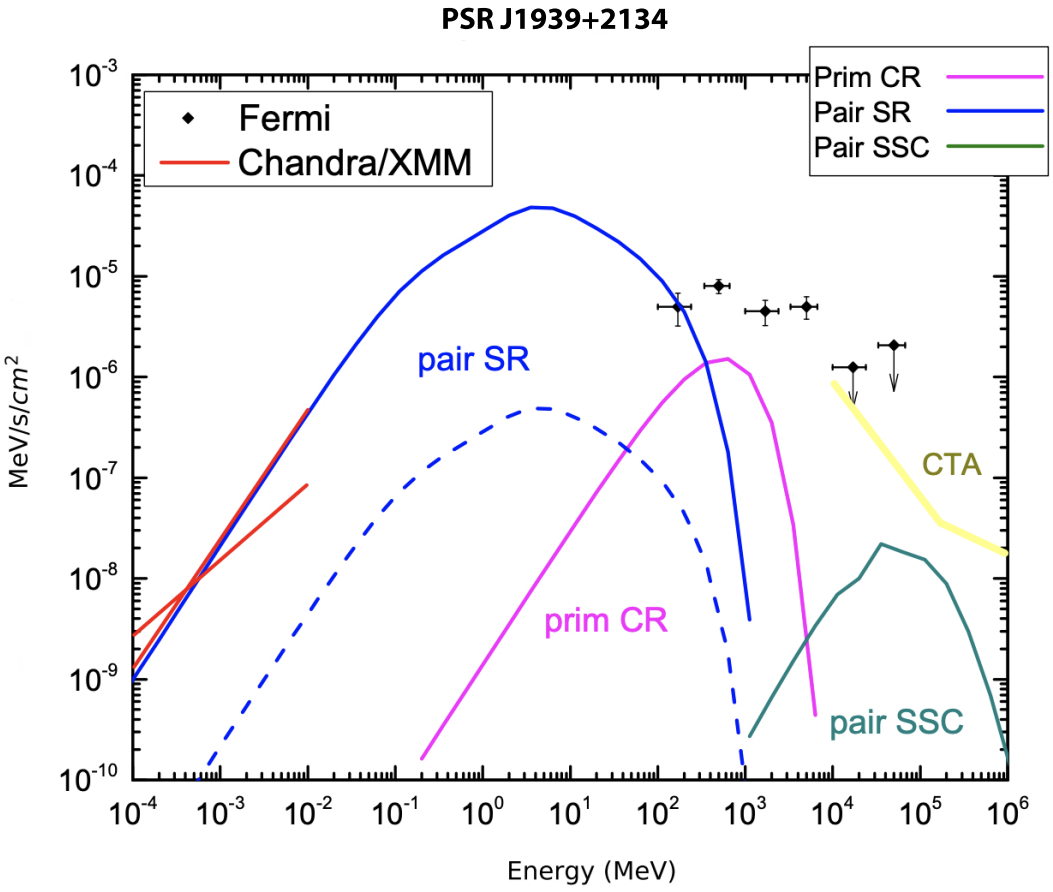

Figure 5.5: The phase-averaged SED for PSR J1939+2134 from the model of **HK15**, taken from [29]. The simulations assume a rotational-magnetic inclination angle $\alpha = 75°$ and rotational-viewing inclination angle $\zeta = 70°$. The dashed line indicates $M_+ = 1 \times 10^3$ while the solid lines indicate $M_+ = 1 \times 10^5$.

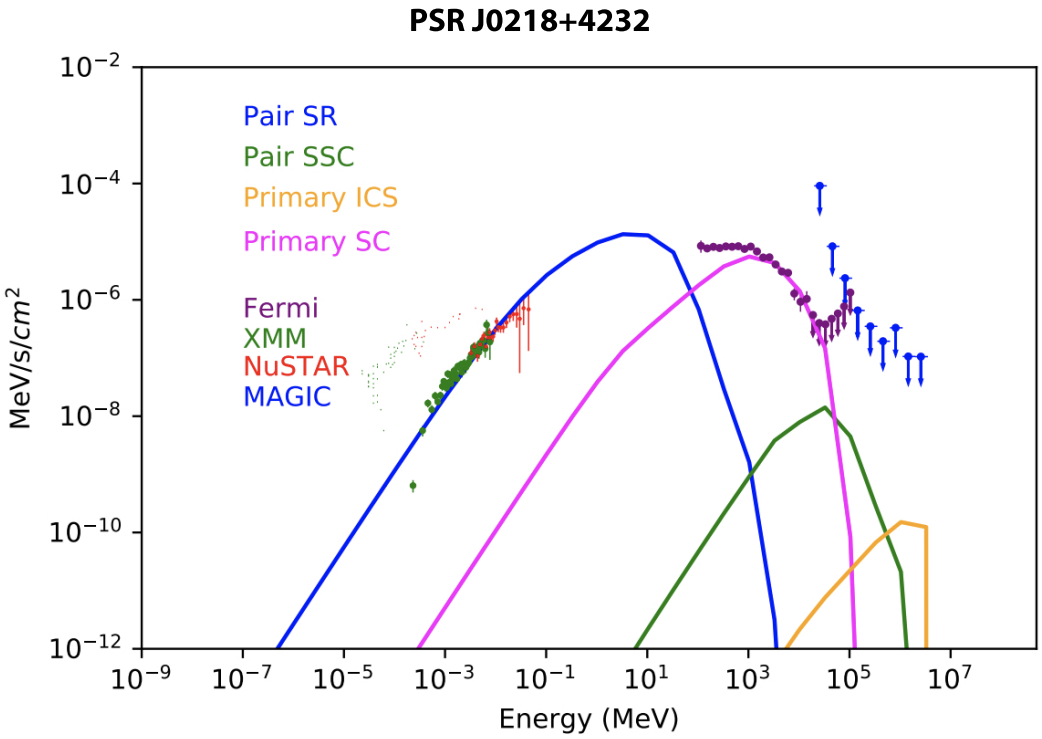

Figure 5.6: The phase-averaged SED for PSR J0218+4232 from the model of **HVK21**, taken from [32]. The simulations assume; $M_+ = 3 \times 10^5$, a rotational-magnetic inclination angle $\alpha = 60°$ and rotational-viewing inclination angle $\zeta = 65°$.

pulsar. While the HE flux points have the potential to be used as a metric for the scaling factors applied to the simulations, they are shown here to primarily highlight the intrinsic uncertainty introduced through unconstrained factors, such as α & ζ, when target-specific models are unavailable.

In each case we see that the limits are compatible with the scaled models: the ULs do *not* constrain a flux level that is below that of the scaled simulations. The limits for J1939 are closest to its scaled model, with other limits being around an order of magnitude, or more, greater than the model flux values. The VHE limits are placed in the region of a few hundreds-of-GeV, and in this domain the pair SSC component dominates the model SED, but is still at too low a flux level for detection. The primary SC component falls off below the VERITAS energy range and the primary IC component only becomes dominant, over the SSC, around 550 GeV. For all six of the MSPs the ULs constrain the flux level seen to be below that of the Crab pulsar, as expected[32].

The above conclusion agrees with the results of Harding et al. [32], who also deduce that the flux levels predicted by their model imply that current generation IACT instruments are not sensitive enough to detect the VHE spectral component. Confirming this result for the six MSP targets here[23] is a valuable corroboration and also assists in the constraint of uncertain model parameters, that can predict a variety of flux levels.

As no hint of pulsed emission is seen in the VERITAS observations, it will require deeper observations with an instrument more sensitive to lower fluxes to provide even more constraining limits, potentially challenging model predictions. If pulsed VHE emission *is* present in the MSPs surveyed here, it could be that IC component, predicted at the level of $\sim$1 - 30 TeV, will be the component that can be first isolated from the steady background level, given sufficient exposure. Almost all models predict that the emission peaks in the pulsar light curve become narrower, with increasing energy[24], and so pulsed emission becomes even more pronounced against the lower-energy time-independent back-

[23] Along with making as best a comparison as possible to our scaled versions of the J0218 model.
[24] Up to the energy cutoff that the model ascribes to.

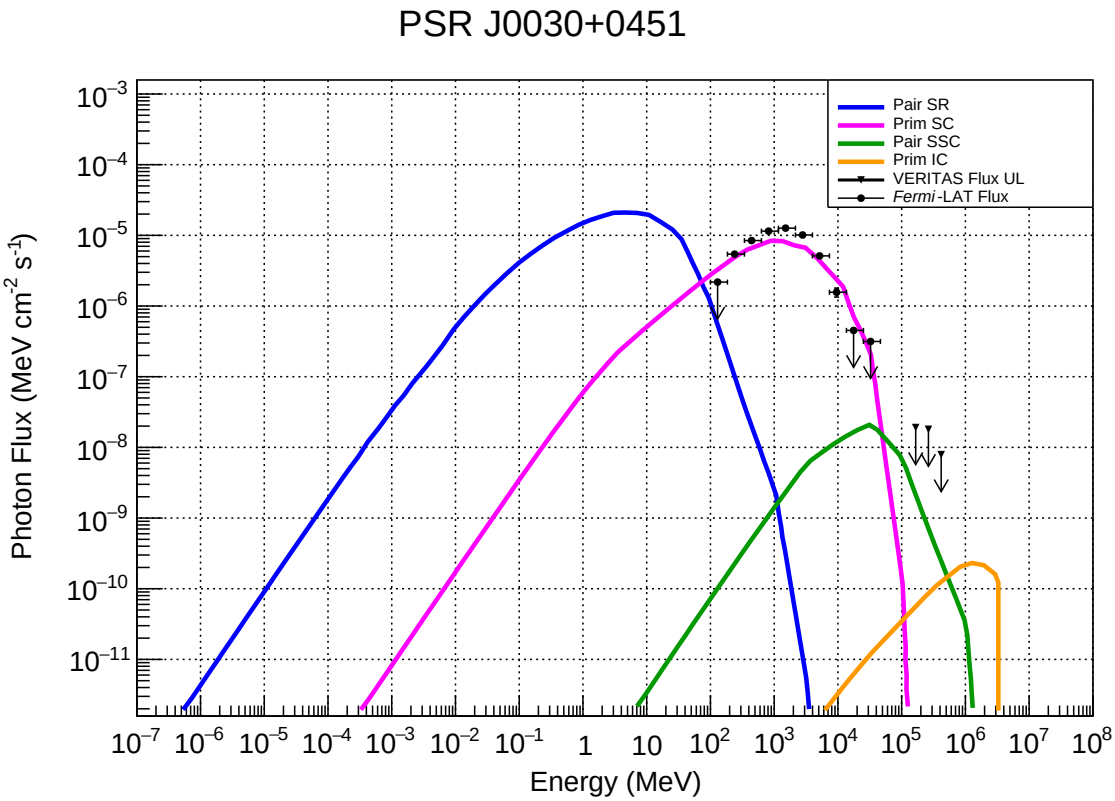

Figure 5.7: The model SED of **HVK21** for PSR J0218+4232, scaled by a factor of $\epsilon = 1.6$, with the 95% CL ULs (at $E_{threshold}$) for **J0030** from the VEGAS pulsed analysis, for all three cut types, plotted on top. The flux UL values are calculated by multiplying the differential UL, F^{UL}_{Diff}, by the square of the threshold energy and averaging over one rotational phase.

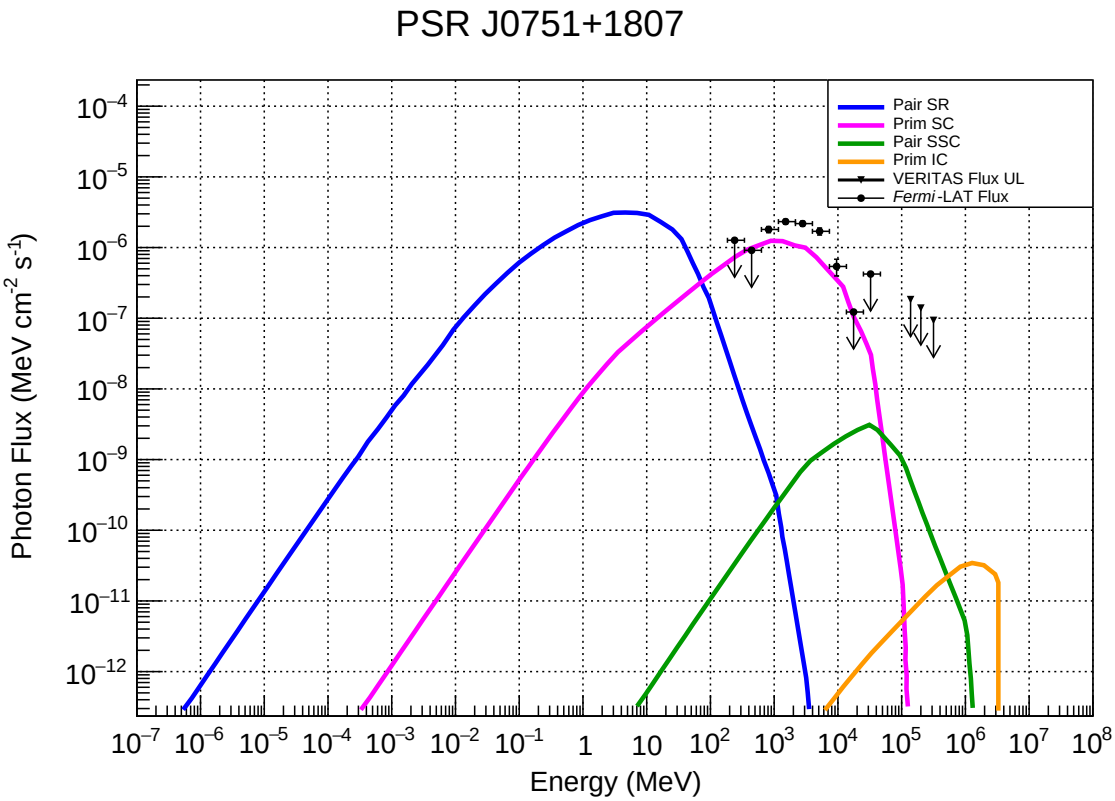

Figure 5.8: The model SED of **HVK21** for PSR J0218+4232, scaled by a factor of $\epsilon = 0.23$, with the 95% CL ULs (at $E_{threshold}$) for **J0751** from the VEGAS pulsed analysis, for all three cut types, plotted on top. The flux UL values are calculated by multiplying the differential UL, F^{UL}_{Diff}, by the square of the threshold energy and averaging over one rotational phase.

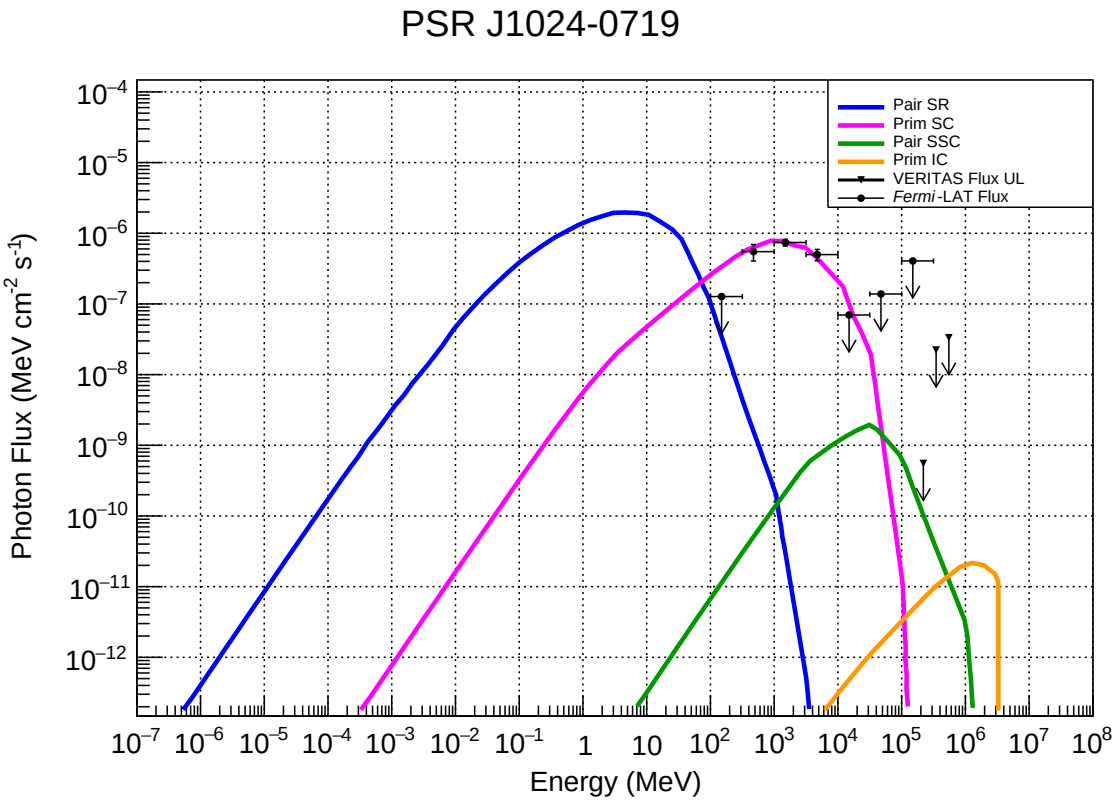

Figure 5.9: The model SED of **HVK21** for PSR J0218+4232, scaled by a factor of $\epsilon = 0.15$, with the 95% CL ULs (at $E_{threshold}$) for **J1024** from the VEGAS pulsed analysis, for all three cut types, plotted on top. The flux UL values are calculated by multiplying the differential UL, F^{UL}_{Diff}, by the square of the threshold energy and averaging over one rotational phase.

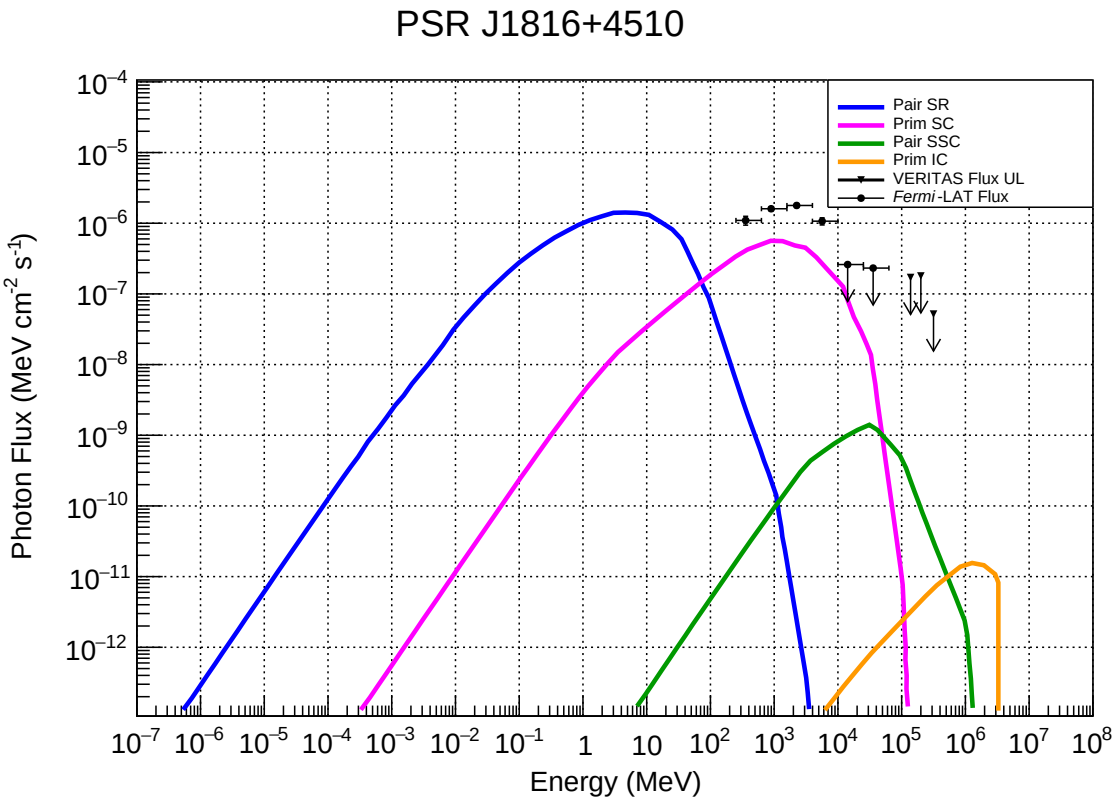

Figure 5.10: The model SED of **HVK21** for PSR J0218+4232, scaled by a factor of $\epsilon = 0.11$, with the 95% CL ULs (at $E_{threshold}$) for **J1816** from the VEGAS pulsed analysis, for all three cut types, plotted on top. The flux UL values are calculated by multiplying the differential UL, F^{UL}_{Diff}, by the square of the threshold energy and averaging over one rotational phase.

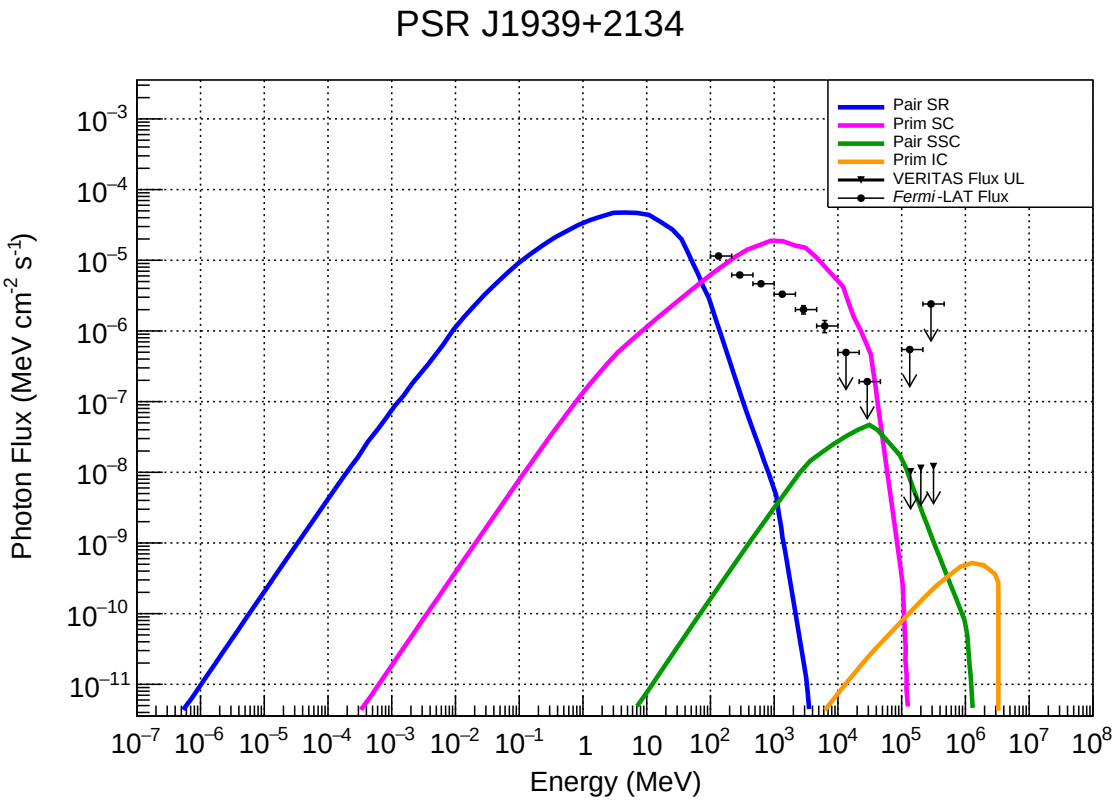

Figure 5.11: The model SED of **HVK21** for PSR J0218+4232, scaled by a factor of $\epsilon = 3.5$, with the 95% CL ULs (at $E_{threshold}$) for **J1939** from the VEGAS pulsed analysis, for all three cut types, plotted on top. The flux UL values are calculated by multiplying the differential UL, F^{UL}_{Diff}, by the square of the threshold energy and averaging over one rotational phase.

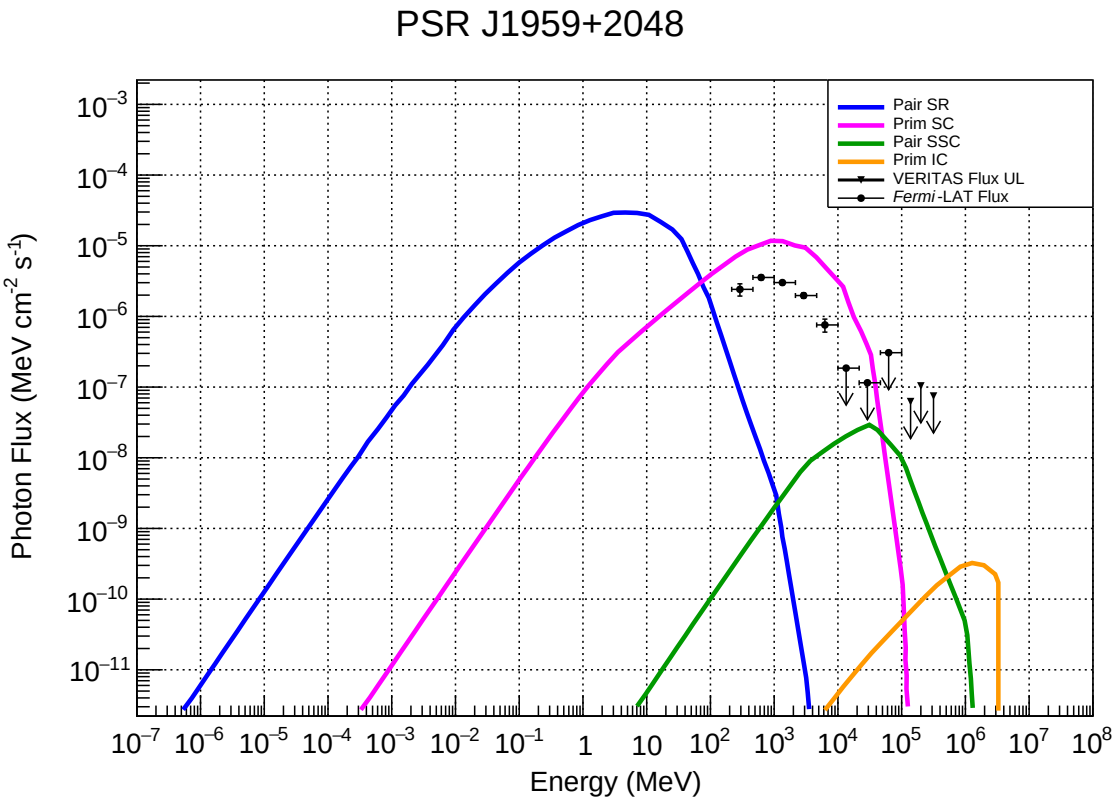

Figure 5.12: The model SED of **HVK21** for PSR J0218+4232, scaled by a factor of $\epsilon = 2.2$, with the 95% CL ULs (at $E_{threshold}$) for **J1959** from the VEGAS pulsed analysis, for all three cut types, plotted on top. The flux UL values are calculated by multiplying the differential UL, F^{UL}_{Diff}, by the square of the threshold energy and averaging over one rotational phase.

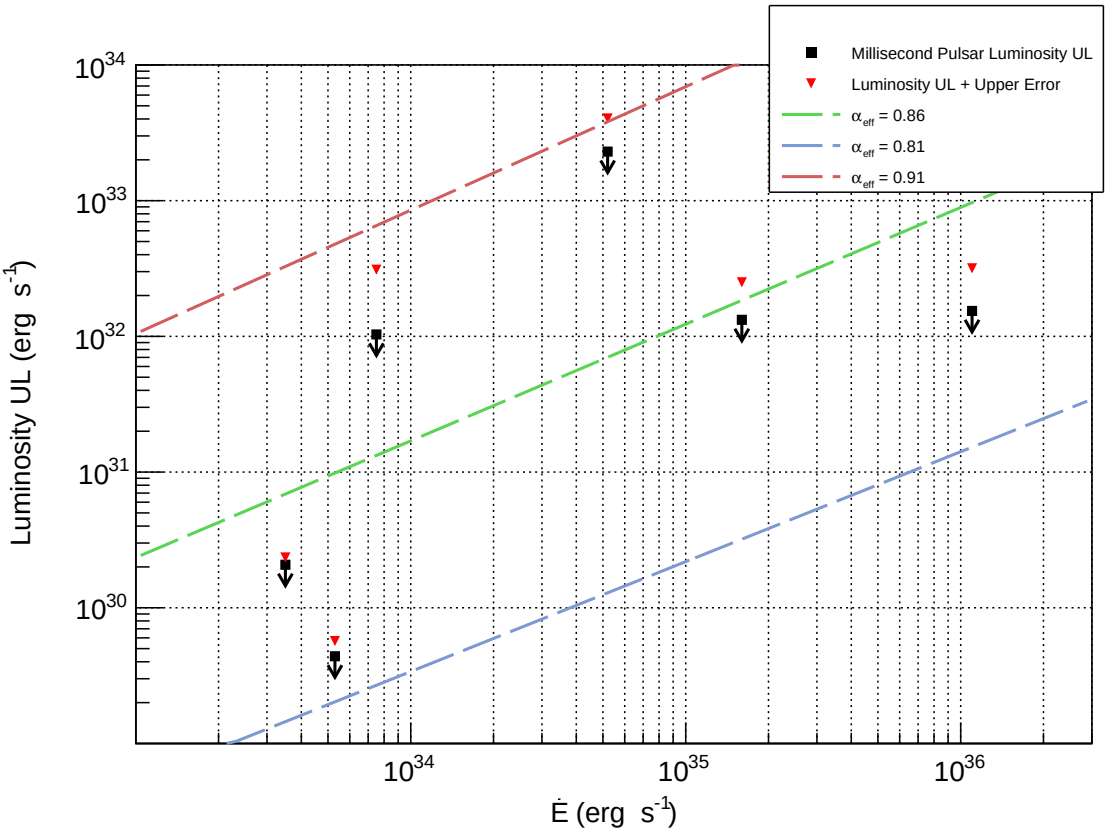

Figure 5.13: A plot of the *SOFT* cuts 95% CL gamma-ray luminosity ULs from the VEGAS pulsed analysis vs. the spin-down energy loss rate of the pulsar. The black squares are the raw luminosity ULs and the red triangles are the less-constraining limits, accounting for the upper uncertainty on distance as described in section 5.4.2. The function $L_\gamma = k_{pulsar} \left(\dot{E}\right)^{\alpha_{eff}}$ is overlaid for three values of index α_{eff}, purely to guide the eye in an attempt to illustrate any possible trend in the relationship between L_γ and $\dot{E}$, see section 5.1.3.

ground level[32]. The significant gain in sensitivity, throughout the VHE regime, that will be made by CTA will make these MSP targets interesting to revisit with the next-generation observatory, and the data provided herein will help guide optimal observation in the future.

5.4.2 The Survey Population as a Whole

Unfortunately, as none of the MSP analyses resulted in detections of pulsed emission, we cannot put a lower limit on the maximum energy of the particle population responsible for

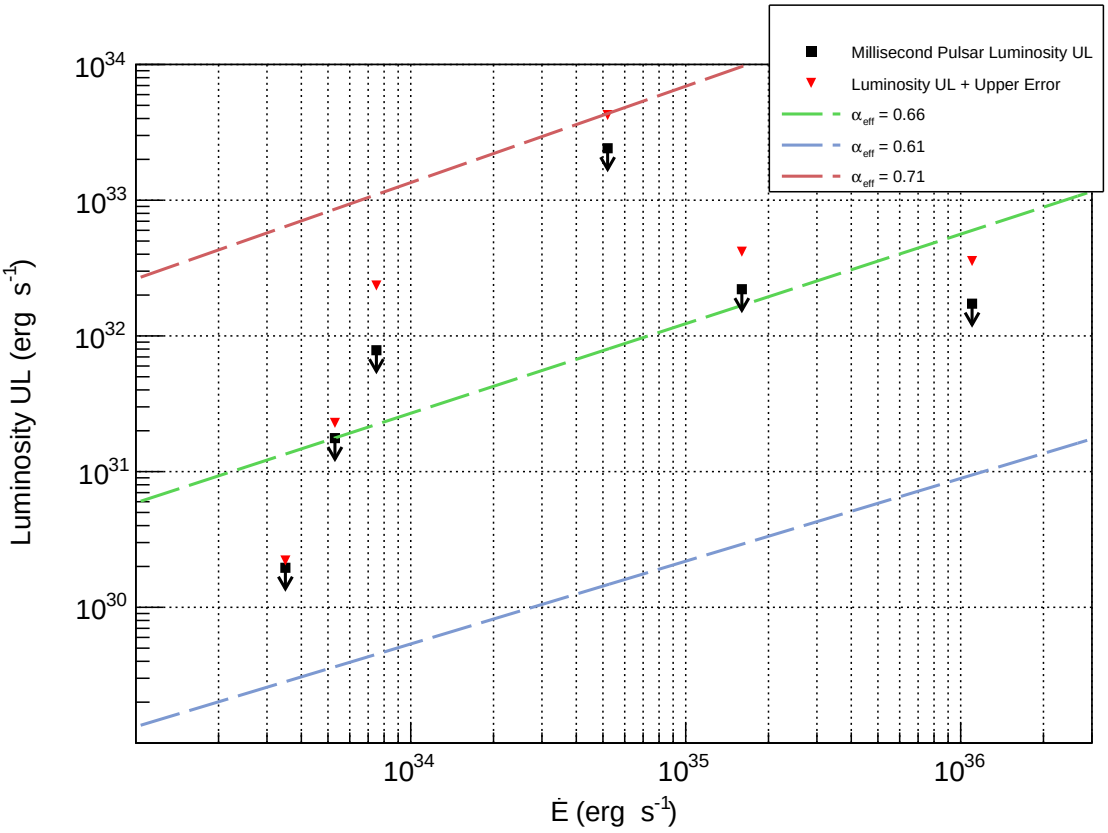

Figure 5.14: A plot of the *MEDIUM* cuts 95% CL gamma-ray luminosity ULs from the VEGAS pulsed analysis vs. the spin-down energy loss rate of the pulsar. The black squares are the raw luminosity ULs and the red triangles are the less-constraining limits, accounting for the upper uncertainty on distance as described in section 5.4.2. The function $L_\gamma = k_{pulsar} \left(\dot{E}\right)^{\alpha_{eff}}$ is overlaid for three values of index α_{eff}, purely to guide the eye in an attempt to illustrate any possible trend in the relationship between L_γ and $\dot{E}$, see 5.13 for further information.

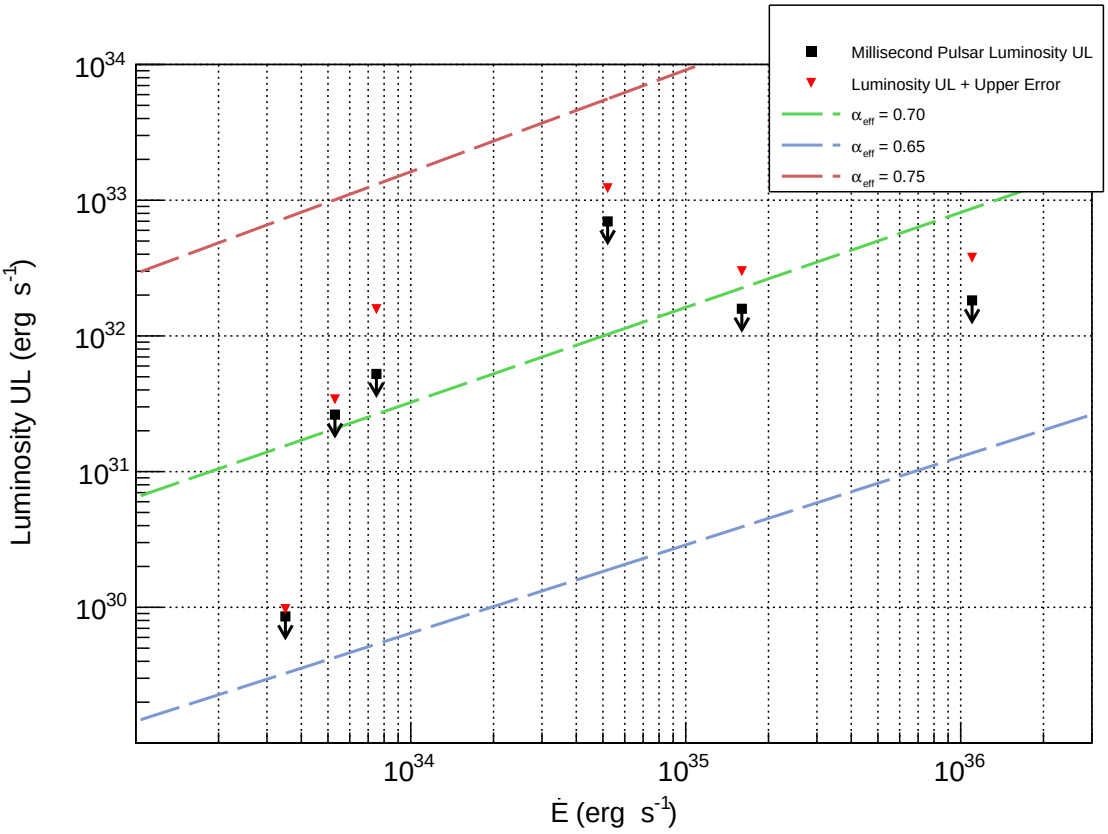

Figure 5.15: A plot of the *HARD* cuts 95% CL gamma-ray luminosity ULs from the VEGAS pulsed analysis vs. the spin-down energy loss rate of the pulsar. The black squares are the raw luminosity ULs and the red triangles are the less-constraining limits, accounting for the upper uncertainty on distance as described in section 5.4.2. The function $L_\gamma = k_{pulsar} \left(\dot{E}\right)^{\alpha_{eff}}$ is overlaid for three values of index α_{eff}, purely to guide the eye in an attempt to illustrate any possible trend in the relationship between L_γ and $\dot{E}$, see 5.13 for further information.

producing any VHE gamma-rays (as discussed in section 5.1). As the level of pulsations cannot be claimed to be above the phase-averaged background level, any conclusion drawn about the energetics of the VHE producing particles would not be unique to the pulsed component.

This also means that, as no indication of distinctive peaks is present in the VHE light curve morphology, we cannot make direct comparisons to simulation models that try to predict such features. Instead, the survey results are compatible with a scenario where MSPs exhibit only non-phase-dependent emission in the VHE regime. The significance levels of any possible pulsations fit the null hypothesis, of only phase-averaged background level emission being present, and so constrain the appearance of a VHE pulsed gamma-ray component at the levels reported. It could be that with deeper observations, to gather more statistics, a dependence on phase might be established, but no hint of such a scenario is seen here.

Limits on the VHE Pulsed Luminosity

As none of the MPSs are firmly detected in gamma-rays, it is difficult to perform an investigation into the displayed trend of gamma-ray luminosity vs spin-down energy loss rate, L_γ vs. $\dot{E}$ (as described in subsection 5.1.3), by using the results from the targets in this survey. The results are purely ULs and also show a relative scatter of behavior, hence no, even weak, universal trend can be claimed. The calculated ULs on the VHE gamma-ray luminosity, as described in section 5.3.2 are plotted against the pulsar's spin-down luminosity. The ratio of these two values, for each MSP, allows a direct calculation of an upper limit on the gamma-ray conversion efficiency (see tables 5.4 through 5.9).

In this procedure to investigate α_{eff} we account for the uncertainties in the pulsar distances and propagate them into the values of L_γ^{UL}, effectively making the ULs *less constraining* at the level of the upper error value. The error in L_γ^{UL} is then;

$$\Delta\left(L_{\gamma}^{UL}\right) = \frac{\partial}{\partial d}\left(L_{\gamma}^{UL}\right)\Delta d = 2\,L_{\gamma}^{UL}\,\frac{\Delta d}{d}$$

and the modified ULs for the plots become;

$$L_{\gamma}^{UL} + \Delta\left(L_{\gamma}^{UL}\right)$$

Although the relationship between L_{γ} and $\dot{E}$ should strictly be quantified with luminosity measurements from confirmed detections[25], the overall loose trend, even for ULs, fits with the *Fermi* findings in the HE regime [163] and the behavior seen in the VERITAS young pulsar study [36]. That is; values for α_{eff} of between 0.5 and 1 (as expected from literature [28]) are reasonable, but change noticeably for different cut values.

The uncertainties in VHE gamma-ray luminosities of the MSPs highlight the issue of the intrinsic lack of accuracy in the ascertained distance to each pulsar. The systematics involved in the gamma-ray analysis play a role (cf. the VERITAS energy resolution uncertainty, quoted at $\sim$20% at 1 TeV), but uncertainties in the distance to the pulsars (sometimes $\sim$100%) often dominate by a great amount. Different true values of f_{Ω} could explain variation in L_{γ} at the level of an order of magnitude reduction for some pulsars.

While a universal dependence of L_{γ} on $\dot{E}$ is claimed by some [134], it is possible that the scatter in such measurements is to be expected and that the scenario may not be as general as argued. Complex interactions between expected mechanisms [68] [32], along with the varying pulsar characteristics that models are very sensitive to [131] [42], could lead to the reality that all pulsars will *not* follow the same trend as each other, when it comes to overall gamma-ray luminosity. However, it is certain that more, and deeper, observations of these and other pulsar candidates are needed to pursue the nature of pulsar emission to

[25]For this reason we are hesitant to make any strict quantitative claims on actual values of α_{eff}. The ULs are *not* definitive measurements of the luminosity and are subject to biases associated with the assumptions under which they are derived and intrinsic uncertainty due to the fact that they are derived from statistically non-significant results. While the relationship is potentially constrained by the ULs, the constant of proportionality and index are free parameters, and so different values for α_{eff} are possible given that k_{pulsar} can be varied in tandem.

its fundamentals.

CHAPTER 6
A SEARCH FOR TEV GAMMA-RAY EMISSION FROM PULSAR TAILS BY VERITAS

Material in the following chapter is from the paper [233] and is left unedited for the most part. Published in the The Astrophysical Journal, August 2021, it was written by A. Gent in collaboration with Noel Klingler and Oleg Kargaltsev, who were primarily responsible for the sections detailing the X-ray observations and analysis and theoretical modelling. A. Gent is the corresponding author for the publication, authored sections on VERITAS/VHE observations and analysis, and contributed to the other sections of the manuscript.

6.1 Abstract

We report on the search for very-high-energy gamma-ray emission from the regions around three nearby supersonic pulsars (PSR B0355+54, PSR J0357+3205 and PSR J1740+1000) that exhibit long X-ray tails. To date there is no clear detection of TeV emission from any pulsar tail that is prominent in X-ray or radio. We provide upper limits on the TeV flux, and luminosity, and also compare these limits with other pulsar wind nebulae detected in X-rays and the tail emission model predictions. We find that at least one of the three tails is likely to be detected in observations that are a factor of 2-3 more sensitive. The analysis presented here also has implications for deriving the properties of pulsar tails, for those pulsars whose tails could be detected in TeV.

6.2 Introduction

Pulsars are among nature's most powerful particle accelerators, capable of producing particles with energies up to a few PeV. As a neutron star rotates, it imparts some of its immense

rotational energy into a magnetized ultra-relativistic particle wind. Although the wind bulk flow speed is initially highly relativistic, the flow decelerates abruptly at the termination shock (TS) to only mildly-relativistic speed, due to interaction with the surrounding medium. Beyond the TS, the pitch angle distribution of the wind particles becomes more isotropic and their synchrotron radiation becomes observable, from radio to gamma-rays, as a pulsar wind nebula (PWN, plural: PWNe).

In addition to pulsar properties (spin-down energy-loss rate $\dot{E}$, viewing angle ζ, magnetic-spin axis offset α, etc.), PWN sizes and morphologies depend upon the properties of the interstellar medium (ISM), such as the ambient pressure and local speed of sound, c_s. Since the "birth kicks" that pulsars receive in their progenitor supernova explosions, v_p, are typically on the order of a few hundred km s^{-1} [234], pulsars will only remain in their host supernova remnant (SNR) for a few tens of kyr. Once a pulsar leaves its SNR, it traverses an environment with a much lower speed of sound: in the ISM, c_s typically ranges from a few to a few tens of km s^{-1}. Consequently, most pulsars outside of their SNRs move supersonically (i.e., $v_p/c_s \equiv \mathcal{M} \gg 1$, where $\mathcal{M}$ is the Mach number). For supersonic pulsars, the ram pressure exerted upon the shocked pulsar wind (PW) by the oncoming ISM confines the shocked PW to the direction opposite that of the pulsar motion, forming a bow shock PWN "head" and an extended pulsar "tail".

Thus, pulsar tails are ram-pressure-confined outflows of the magnetized synchrotron-emitting relativistic particle wind. Radio and X-ray observations of pulsar tails have shown that they can extend distances of ~ 10 pc behind their pulsars (see, e.g., [235] and [236] for reviews), with the longest being the Mouse and Frying Pan PWNe, which both span about 18 pc in radio (see Figure 3 of [237], and [238]). We also note that, in some cases, the confinement of the particle wind by the ram pressure may be associated with the relative motion of the surrounding medium, rather than with the pulsar's motion. For example, the analysis of radio observations [239] suggests that for the Vela PWN the flow of the surrounding medium is mildly supersonic, after recent passage of the reverse shock and

could have been even more supersonic during the passage. H.E.S.S. observations [240] [241] revealed a strongly elongated TeV structure south of the Vela pulsar (which is also bright in radio) whose X-ray emission has both thermal and non-thermal components [242], of which the latter may belong to the PWN (as discussed in [236]).

PWNe typically emit most of their energy via synchrotron radiation from radio to MeV γ-rays, but PWNe can also be prominent sources of GeV and TeV γ-rays, through the upscattering of CMB photons by the ultra-relativistic wind particles. The higher energy particles which emit synchrotron radiation in X-rays cool on relatively short timescales ($\sim$ 1 kyr, for typical magnetic fields $B_{\rm PWN} \gtrsim 10\ \mu{\rm G}$). The lower energy particles which emit inverse-Compton (IC) radiation at GeV/TeV energies may cool on longer timescales ($\sim 10 - 100$ kyr, for typical ISM photon densities) if the magnetic field strength drops to few μGauss farther away from the pulsar. Therefore, PWNe can extend to larger scales in the TeV regime. In fact, most identified Galactic TeV sources are believed to be PWNe (and/or the SNRs in which they reside; [243], [244], [245]). However, puzzlingly, no supersonic PWNe (SPWNe) with long tails seen in radio and X-rays have been detected in TeV energies yet. Although the very nearby ($d \approx 250$ pc) Geminga pulsar is supersonic [246] and its PWN has been detected in γ-rays (see [247] & [248]), the extended tail has not been detected in X-rays.

Detecting IC TeV emission from long tails, whose synchrotron emission has been detected in X-rays, would enable an informative diagnostic of pulsar wind properties, since modeling for these SPWNe is simpler than for PWNe still residing within their host SNRs, where one can expect additional contributions to the TeV emission arising from the interaction between the pulsar wind and reverse shock of the SNR or the pulsar wind and dense material inside the SNR.

6.3 The Pulsar Tails Targets

PSR J0357+3205 (hereafter J0357) is a nearby radio-quiet pulsar discovered through a blind frequency search of the *Fermi* -LAT data [249]. Its spin-down power ($\dot{E} = 5.9 \times 10^{33}$ erg s^{-1}) is among the lowest of gamma-ray pulsars, even when selecting for pulsars of similar age ($\tau = 540$ kyr). The distance to J0357 remains uncertain, although [250] used a γ-ray "pseudo-distance" relation (see e.g. [251]) to estimate a distance of 500 pc (we adopt this distance below).

Deep *Chandra X-ray Observatory* (*CXO*) observations revealed an elongated X-ray tail [250] whose emission only becomes visible 20″ behind PSR J0357, and extends for an angular distance of $9'$, reaching maximum brightness $\sim 4 - 7'$ away from the pulsar (see Figure 6.1). No significant energy-dependent changes in morphology were seen. The strange morphology of the diffuse emission (i.e., the lack of a bright compact PWN head near the pulsar) is at odds with the morphologies of most other PWNe resolved by the *CXO*. One possible explanation could be that the compact PWN is simply unresolved due to its small angular size. This would imply a very large pulsar velocity.

Follow-up observations with *Chandra* revealed a proper motion of the pulsar well aligned with the main axis of the nebula, with a transverse velocity of $\sim 390(d/500$ pc) km s^{-1} [252]. Although the 3D velocity could be much higher, a large angle between the velocity vector and the sky plane would imply a significantly longer tail extent than that seen in projection. Similar to J1740, below, the pulsar is located far from the Galactic plane ($b = -16°$) with a proper motion angled slightly towards the plane (inclination $\sim 2°$).

PSR B0355+54 (J0358+5413; hereafter B0355) is a radio-loud pulsar with characteristic age $\tau = 564$ kyr and spin-down power $\dot{E} = 4.5 \times 10^{34}$ erg s^{-1}. Using very long baseline interferometry, [253] derived a parallax-determined distance of $1.04^{+0.21}_{-0.16}$ kpc and transverse proper velocity of 61^{+12}_{-9} km s^{-1}. [254] applied a Lutz-Kelker correction to this measurement, giving a distance of $1.0^{+0.2}_{-0.1}$ kpc.

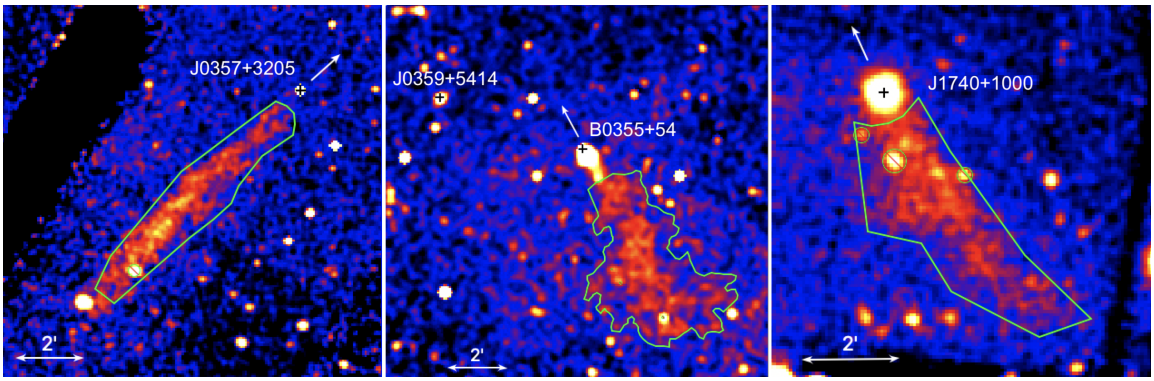

Figure 6.1: The tails of PSRs J0357+3205 (left, *Chandra*), B0355+54 and J0359+5414 (center, *Chandra*), and J1740+1000 (right, *XMM-Newton*). The X-Ray spectral extraction regions are shown in green, the black crosses mark the pulsar positions, and the white arrows mark their approximate/inferred directions of motion.

[255] reported on the analysis of the 66 ks *CXO* ACIS observation which resolved bright compact emission extending up to $50''$ from the pulsar, dubbed the 'compact nebula' (CN), and a fainter $7'$-long tail, both extending in the direction opposite the pulsar's direction of motion. Using a deeper (395 ks) set of subsequent *Chandra* observations, [256] reported a CN photon index of $\Gamma = 1.54 \pm 0.05$, and found that the tail exhibits no spectral cooling across its visible extent, with a best-fit $\Gamma = 1.74 \pm 0.08$ for the entire tail (excluding the CN).

The only source from the 3rd *Fermi*-LAT catalog (3FGL; [257]) within 2° of B0355 is 3FGL J0359.5+5413, offset from the pulsar's position by $5.5'$. 3FGL J0359.5+5413 was identified as a pulsar, J0359+5414 (hereafter J0359), in the Einstein@Home Gamma-Ray Pulsar Survey [258]. J0359 is a relatively young ($\tau = P/2\dot{P} = 75.2$ kyr), energetic ($\dot{E} = 1.3 \times 10^{36}$ erg s^{-1}), radio-quiet pulsar with period $P = 79$ ms, which exhibits a single broad peak in its γ-ray light curve (see [258]). The deep 395 ks of ACIS-I observations (ObsIDs 14688–14690, 15548–15550, 15585, and 15586) of B0355 contain J0359 in their field of view.

PSR J1740+1000 (hereafter J1740) is a young pulsar (characteristic age $\tau = 114$ kyr, spin-down power $\dot{E} = 2.3 \times 10^{35}$ erg s^{-1}) discovered well above the Galactic plane ($b =$

20.4°) by the Arecibo Telescope [259]. [260] saw no filamentary or bow-shock structures with the Very Large Array at 1.4 GHz, and noted that a high spatial velocity (oriented perpendicular to the Galactic plane) of $v_z > 4100\ \mathrm{km\ s^{-1}}$ would be required for the pulsar to reach its current Galactic latitude within its characteristic age, if it was born on the Galactic plane at the dispersion measure distance of ~ 1.4 kpc.[1] Using a pair of *CXO* observations with a 10-year baseline, [264] set an upper limit on the transverse proper motion which implies a displacement of $< 2^\circ$ within the characteristic age, supporting the premise that the progenitor star either originated in the halo or escaped from the disk long before the pulsar was born.

[265] reported the discovery of an extended (5.5′, possibly up to 7′) X-ray tail behind J1740 with an *XMM-Newton* observation (46.4 ks effective exposure). A power-law (PL) spectral fit to the tail emission showed a relatively hard photon index ($\Gamma = 1.4 \pm 0.2$), but high background rates and the limited angular resolution of *XMM-Newton* resulted in large uncertainties. The orientation of the tail implies that the pulsar is moving at an angle of $\sim 7\,\mathrm{deg}$ towards the Galactic plane, further corroborating a halo-star progenitor. No γ-ray emission (pulsed, nor unpulsed) from J1740 is seen with the *Fermi*-LAT.

In terms of their spin-down properties, J1740 and J0359 are typical representatives of the pulsar population associated with TeV sources (see the reviews by [266] [243]). The other two pulsars, B0355 and J0357, are older but relatively nearby (see Table 6.1 for a summary of the pulsar parameters), so it is reasonable to expect that TeV emission from their relic PWNe could be detected. This prompted us to carry out observations of these fields with the Very Energetic Radiation Imaging Telescope Array System (VERITAS).

In this paper we present the results of a search for TeV emission from three supersonic pulsars (B0355+54, J0357+3205, and J1740+1000) with VERITAS and compare the results

[1] However, a velocity of $\sim$4000 km s^{-1} is unrealistically high. The average 3D pulsar velocity has been found to be 400 ± 40 km s^{-1} [261], with the highest velocities being 765 km s^{-1} (PSR B2224+65; [262]) and $\sim$1000–2000 km s^{-1} (inferred; PSR J1101–6101; [263]). This implies that this pulsar was born above the Galactic plane, or that its true age is a factor of a few older than its spin-down age.

to the predictions of a multiwavelength emission model adopted to the case of SPWNe. In Section 2 we describe VERITAS observations and data analysis as well as X-ray data. The results of TeV and X-ray observations are presented in Section 3. In Section 4 we discuss the implications of the results in the context of a simple multiwavelength emission model of a SPWN (the model details are given in the Appendix). We conclude by summarizing our findings in Section 5.

Table 6.1: Pulsar parameters (from the ATNF Pulsar Catalog, [23]).

NAME	J0357+3205	B0355+54	J0359+5414	J1740+1000
R.A.	03:57:52.5	03:58:53.7	03:59:26.0	17:40:25.9
Decl.	+32:05:25	+54:13:13.7	+54:14:55.7	+10:00:06.3
μ_α (mas yr^{-1})	117	9.3	–	–
μ_δ (mas yr^{-1})	115	8.3	–	–
Gal. longitude (deg)	162.76	148.19	148.231	34.011
Gal. latitude (deg)	-16.006	0.811	0.883	20.268
Spin period, P (ms)	444.1	156.4	79.4	154.1
Period derivative (10^{-14}), $\dot{P}$	1.30	0.439	1.67	2.15
Dispersion measure (pc cm^{-3})	–	57.14	–	23.9
Distance (kpc)	0.83	1.04	–	1.23
Spin-down age, $\tau_{\rm sd} = P/(2\dot{P})$ (kyr)	540	564	75.2	114
Spin-down power, $\dot{E}$ (erg s^{-1})	5.88×10^{33}	4.54×10^{34}	1.32×10^{36}	2.32×10^{35}
Surface magnetic field, B_s (10^{12})	2.43	0.839	1.2	1.84

6.4 Data Analysis

6.4.1 VERITAS Instrument and Observations

VERITAS is comprised of four imaging atmospheric Cherenkov telescopes (IACTs) operating at the Fred Lawrence Whipple Observatory (FLWO) in southern Arizona, USA. Cherenkov light flashes from gamma-ray and cosmic-ray induced air showers are reflected from 12-meter Davies-Cotton reflectors onto the telescope cameras. Each camera has a field-of-view of 3.5° and is composed of 499 photomultiplier tubes (PMTs). A three-level

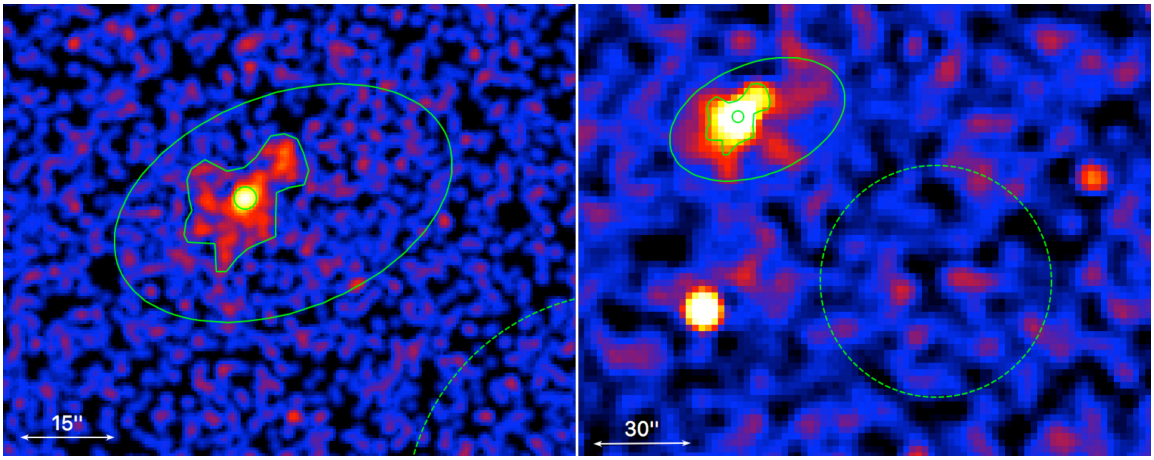

Figure 6.2: Deep *Chandra* ACIS-I (0.5–8 keV) images of J0359. *Left:* Image smoothed with an $r = 1.''48$ Gaussian kernel. *Right:* image binned by a factor of 4, and smoothed with an $r = 5.''9$ Gaussian kernel to better show the extended emission. The region shown by the $r = 1.''5$ circle is used to exclude the pulsar. The compact nebula (CN) region is shown by the polygon (excluding the pulsar region), and the extended nebula emission region is shown by the ellipse (excluding the CN region). The dashed circle shows the region used for background subtraction.

trigger requires coincident signals from at least two telescopes to initiate the array-wide read-out of the PMT signals [141]. The instrument is sensitive over the energy range 0.085–30 TeV, with a typical energy resolution of 20% and angular resolution of 0.1° at 1 TeV [142].

Observations of each source were taken in 'wobble' mode, where the telescope pointing is offset from the nominal source position to allow for simultaneous exposure of the source and background regions. The exposures were taken using an angular offset of 0.5° around the pulsar position, with the offset direction alternating between the four cardinal directions for each 20-30 minute run. VERITAS observed J1740 in 2008, April to May, resulting in 12.8 hours of livetime after performing quality selection to remove periods of poor weather and/or hardware performance. Observations of J0357 were taken in 2011 September to December, with selected livetime of 8.5 hours. Initial observations of B0355 were taken in 2014 September to October, with selected livetime of 10.2 hours. An additional 12.1 hours were taken in 2015 September to November, with the pointings wobbling around a position

in the middle of the X-ray tail (RA/Dec: 59.6864, 54.1755).

The data were processed using standard VERITAS analysis techniques. Independent analyses were conducted using two software packages, as described by [166] and [267]. The shower images are parameterized by their principal moments [171], with the shower direction and impact parameter calculated using the stereoscopic views from multiple telescopes [268]. Parameters for separating gamma-ray and cosmic-ray induced showers, as well as the energy of the initial particle, are estimated by comparison with Monte-Carlo simulation see e.g. [269] [270].

Three standard sets of gamma-ray selection criteria ('cuts') were used, optimized for sources with soft, moderate, or hard spectra (see [142] for details on VERITAS performance over the different epochs of the array). In the search for a possible extension in the very-high-energy (VHE; $E > 100$ GeV) emission, the following values were chosen for the radius of the source integration region (θ): 0.1°, optimized for point-source searches (0.173° for soft cuts), and 0.235° for extended emission. An *a priori* search region was also defined for each source, as the VHE emission could originate from a particle population which is older, and thus further downstream, than that which gives rise to the X-ray tail. To account for possible broadening of each tail at large offsets from the pulsar, a symmetric trapezoidal region was used, aligned with the X-ray tail. The areas were 0.4° wide at a distance 0.2° ahead of the pulsar and extended back along the tail with an opening angle of 20°, terminating at a distance of 0.2° beyond the TeV tail, which was assumed to be 4 times as long as the X-ray tail (c.f. the quoted VERITAS angular resolution of 0.1°). In the search for VHE emission in the region of interest, the background was estimated using the ring-background method [179] and the statistical significance of the excess was calculated using Equation 17 of [173].

6.4.2 *Chandra* observations of PSR J0357+3205

We analyzed 134 ks of *Chandra* ACIS-S observations of PSR J0357 (ObsIDs 11239, 12008, 14207, and 14208). The *Chandra* data were processed using the standard `chandra_repro` routine from the *Chandra* Interactive Analysis of Observations (CIAO) software package version 4.11, and Calibration Data Base (CALDB) version 4.8.3.

All spectra were extracted from each observation individually using `specextract` and then combined with `combine_spectra` (due to the low number of counts in each individual observation).

6.4.3 *Chandra* observations of B0355+54 and PSR J0359+5414

We also analyzed the 395 ks of ACIS-I data carried out to study B0355 (ObsIDs 14688–14690, 15548–15550, 15585, 15586), which, serendipitously, also contained PSR J0359+5414 in the ACIS field of view. The data were processed and the spectra were extracted and fitted the same way as for PSR J0357+3205.

6.4.4 *XMM-Newton* observations of PSR J1740+1000

We analyzed 532 ks of new *XMM-Newton* data carried out to study PSR J1740 (ObsIDs 0803080201, 0803080301, 0803080401, and 0803080501).[2] We only analyzed data from the EPIC MOS1/2 detectors, since the EPIC pn detector was operated in Small Window mode, and thus, half of the tail lies outside of the detector's small field of view. The data were processed using the standard `emproc` routine from the *XMM* Science Analysis Software (SAS; version 16.1). We manually filtered the data for periods of high background and flaring.

Spectra from each observation and corresponding response files were extracted and

[2] It is worth noting that a 5th exposure of similar length was also carried out (ObsID 0803080101), however we excluded this observation since the majority of the exposure was heavily contaminated due to periods of high solar flaring and/or particle background.

produced using the standard routines,[3] `evselect`, `arfgen`, and `rmfgen`, and grouped to 125 counts per bin using `specgroup`.

All X-ray spectra were fitted using XSPEC (version 12.10.1). In all spectral fits we used a simple absorbed power-law (PL) model (XSPEC's `tbabs(pow)`) which uses absorption cross sections from [271]. All uncertainties listed correspond to 1σ.

6.5 RESULTS

6.5.1 Upper Limits on VHE Emission

No significant emission was detected within the search regions using any of the analysis cuts. Upper limits (ULs) on the integral gamma-ray fluxes above the threshold energies[4] were calculated using the method of [272] at a 95% confidence level (CL). A bounded confidence interval was used to avoid the unphysical case of negative source counts. A power-law source spectrum was assumed, with an index $\Gamma = 2.5$. With no other *a priori* test positions in the search regions, the limits were taken at positions centered on the middle of the X-ray tails. The backgrounds were estimated using the reflected-regions method [179]. Tables 6.2, 6.3, and 6.4, list the results for each source.

6.5.2 X-Ray Emission from the J0357+3205 Tail

Using *XMM-Newton* data, [273] found that the spectrum of the tail fits a PL model with $\Gamma = 2.07 \pm 0.08$ and $N_{\rm H} = (2.61 \pm 0.23) \times 10^{21}$ cm^{-2}. Fitting the *CXO* data, we obtain compatible results, $\Gamma = 2.11 \pm 0.12$, $\mathcal{N} = (1.42 \pm 0.17) \times 10^{-4}$ photon s^{-1} cm^{-2} keV^{-1} (at 1 keV) and $N_{\rm H} = (3.5 \pm 0.5) \times 10^{21}$ cm^{-2} (with a reduced $\chi^2_\nu = 1.01$, for $\nu = 80$ d.o.f.). The entire tail was found to have a 0.5-8 keV luminosity $L = 9 \times 10^{30}$ erg s^{-1}. [250] found

[3] see https://www.cosmos.esa.int/web/xmm-newton/sas-thread-mos-spectrum

[4] The 'energy threshold' is defined as the energy at which the differential rate of reconstructed gamma-rays is at its maximum. It is a good indicator of the energy-scale of the analysis, but this threshold is higher than the trigger energy threshold, meaning that gamma-rays below the 'energy threshold' are present in the final data.

Table 6.2: Analysis results for the pulsar tail of PSR J0357+3205, taken at RA/Dec: (59.5313, 32.0372). The limits on luminosity assume a distance of 500 pc.

Spectral cuts	θ [$\circ$]	$E_{threshold}$ [GeV]	Significance (Pre-Trials) [Sigma]	95% CL flux UL ($> E_{threshold}$) [10^{-13} cm^{-2} s^{-1}]	95% CL flux UL (1–10 TeV) [10^{-13} cm^{-2} s^{-1}]	95% CL luminosity UL (1–10 TeV) [10^{31} erg s^{-1}]
Hard	0.100	417	0.2	6.2	1.6	1.6
Hard	0.235	417	2.4	33.9	8.8	9.0
Moderate	0.100	219	1.0	24.5	2.4	2.5
Moderate	0.235	219	1.0	68.4	6.8	6.9
Soft	0.173	151	0.2	50.4	2.9	2.9
Soft	0.235	151	0.7	59.3	3.4	3.4

Table 6.3: Analysis results for the pulsar tail of PSR B0355+54, taken at RA/Dec: (59.6864, 54.1755). The limits on luminosity assume a distance of 1.04 kpc.

Spectral cuts	θ [$\circ$]	$E_{threshold}$ [GeV]	Significance (Pre-Trials) [Sigma]	95% CL flux UL ($> E_{threshold}$) [10^{-13} cm^{-2} s^{-1}]	95% CL flux UL (1–10 TeV) [10^{-13} cm^{-2} s^{-1}]	95% CL luminosity UL (1–10 TeV) [10^{31} erg s^{-1}]
Hard	0.100	347	1.1	6.3	1.2	5.5
Hard	0.235	347	1.0	13.0	2.6	11.3
Moderate	0.100	263	0.4	5.0	0.65	2.9
Moderate	0.235	263	1.2	7.3	0.95	4.2
Soft	0.173	166	3.5	3.8	0.25	1.1
Soft	0.235	166	3.5	4.6	0.30	1.3

Table 6.4: Analysis results for the pulsar tail of PSR J1740+1000, taken at RA/Dec: (265.081, 9.96445). The limits on luminosity assume a distance of 1.36 kpc.

Spectral cuts	θ [$\circ$]	$E_{threshold}$ [GeV]	Significance (Pre-Trials) [Sigma]	95% CL flux UL ($> E_{threshold}$) [10^{-13} cm^{-2} s^{-1}]	95% CL flux UL (1–10 TeV) [10^{-13} cm^{-2} s^{-1}]	95% CL luminosity UL (1–10 TeV) [10^{31} erg s^{-1}]
Hard	0.100	501	0.5	4.1	1.4	10.6
Hard	0.235	501	1.2	9.0	3.1	23.3
Moderate	0.100	240	0.0	20.1	2.4	17.9
Moderate	0.235	263	1.6	95.5	12.5	93.7
Soft	0.173	166	0.5	104.9	6.9	51.2
Soft	0.235	182	1.1	195.3	14.7	110.3

there is no statistically significant evidence of spectral evolution along the tail. It is worth noting that [274] and [256] have shown that some pulsar tails can exhibit a lack of spectral softening over parsec-scale distances from the pulsar.

6.5.3 X-Ray Emission from the PSR B0355+54 Tail and PSR J0359+5414 PWN

[256] reported the detailed analysis of *CXO* observations of PSR B0355+54 and its X-ray tail. In particular, the spectrum of the entire tail is well fitted ($\chi^2_\nu = 1.13$ for $\nu = 135$ d.o.f.) by a single absorbed PL model with $\Gamma = 1.74 \pm 0.08$, $\mathcal{N} = 5.40 \pm 0.36$ photon cm^{-2} s^{-1} keV^{-1} (at 1 keV), and $N_{\rm H} = 6.1 \times 10^{21}$ cm^{-2}. No significant evidence of spectral cooling was seen between the near and far halves of the tail, as their photon indices were measured to be $\Gamma_{\rm near} = 1.72 \pm 0.10$ and $\Gamma_{\rm far} = 1.77 \pm 0.11$. The entire tail was found to have a 0.5-8 keV luminosity $L = 3.8 \times 10^{31}$ erg s^{-1}.

[275] reported the discovery of an X-ray PWN around γ-ray PSR J0359+5414 which is located just 5.5′ east of PSR B0355+54. The X-ray nebula of PSR J0359+5414 is much fainter than that of PSR B0355+54. The exposure-corrected images, shown in Figure 6.2, reveal a faint and rather amorphous nebula that lacks any clear indication of substantial (supersonic) pulsar motion. The total observed fluxes for the compact (within the polygon minus circle in Fig. 2) and extended (within the ellipse minus polygon in Fig. 2) fluxes are $8.6^{+0.6}_{-1.4}$ and $5.0^{+1.1}_{-1.8} \times 10^{-15}$ erg s^{-1} cm^{-2} in 0.5-8 keV, respectively. The corresponding best-fit PL photon indices are $\Gamma = 1.7^{+0.4}_{-0.3}$ and $1.4^{+1.3}_{-0.9}$. The pulsar and compact nebula (CN) spectral fits suggest a hydrogen column density $N_{\rm H} \sim (2\text{-}6) \times 10^{21}$ cm^{-2}. The spectral fits of the much brighter B0355 PWN (located 5.5′ west of J0359, at parallax distance $d = 1.04$ kpc) from the same set of *Chandra* observations yields $N_{\rm H,B0355} = (6.1 \pm 0.9) \times 10^{21}$ cm^{-2} [256]. The similar $N_{\rm H}$ values suggest that the distances to these two pulsars may be comparable. The combined (compact+extended) unabsorbed luminosity of J0359's PWN is $\approx 2.2 \times 10^{30}$ erg s^{-1} in 0.5-8 keV at $d = 1$ kpc.

6.5.4 X-Ray Emission from the PSR J1740+1000 Tail

The combined MOS1/2 image (shown in Figure 1) reveals an X-ray tail extending south-west up to approximately 6′ from the pulsar position. The initial segment of the tail appears slightly conical, with an opening angle of $\approx 15^{\circ}$, but after about 3′ it appears to taper off and maintain a seemingly cylindrical shape. The tail also appears to bend or curve slightly to the west with distance from the pulsar. Similar evidence of slight bending is also seen in the tails of PSRs B0355+54 ([256]; see also Figure 1) and J1741–2054 [276].

Based on the analysis of the PSR J1740+1000 spectrum,[265] found the best-fit absorbing hydrogen column density $N_{\rm H} \approx 1 \times 10^{21}$ cm^{-2}. However this value depends on the adopted spectral model, and the pulsar's spectrum requires multiple components for satisfactory fits. On the other hand, both the pulsar's dispersion measure and the HI column from radio data imply that the Galactic $N_{\rm H}$ in the direction of J1740 is 8×10^{20} cm^{-2} (see [277] and the HEAsoft/FTOOLs utility `nH`), which is close to that obtained by [265]. Therefore, while fitting the extended emission spectrum, we fix[5] $N_{\rm H}$ at 10^{21} cm^{-2}. The spectrum of the tail (extracted from the region shown in the left panel of Figure 6.1) fits an absorbed PL with $\Gamma = 1.75 \pm 0.04$ and a normalization $\mathcal{N} = (3.41 \pm 0.09) \times 10^{-5}$ photon s^{-1} cm^{-2} keV^{-1} (at 1 keV), with a reduced $\chi^2_\nu = 1.04$ (for $\nu = 202$ d.o.f.). The (absorbed) 0.3–10 keV flux $F_X = (1.93 \pm 0.06) \times 10^{-13}$ erg cm^{-2} s^{-1} corresponds to an (unabsorbed) X-ray luminosity $L_X = (5.20 \pm 0.16) \times 10^{31}$ erg s^{-1} (at $d = 1.4$ kpc), and an X-ray efficiency $\eta_X = 2.3 \times 10^{-4}$.

6.6 DISCUSSION

Considering the entire population of TeV PWNe (see Figure 6.3), we see that the three tails discussed here belong to pulsars that are older and have lower $\dot{E}$ compared to most of the others. The two exceptions are the nearby Geminga and B0656+14 pulsars. TeV sources

[5]When left as a free parameter, the best-fit $N_{\rm H}$ goes to zero, which is unrealistic considering the pulsar's DM distance $d \sim 1.4$ kpc. In this fit the other parameters are as follows: $\mathcal{N} = (2.69 \pm 0.18) \times 10^{-5}$ photons cm^{-2} s^{-1} keV^{-1} (at 1 keV) and $\Gamma = 1.54 \pm 0.06$, with a reduced $\chi^2_\nu = 0.97$ (for $\nu = 201$ d.o.f.)

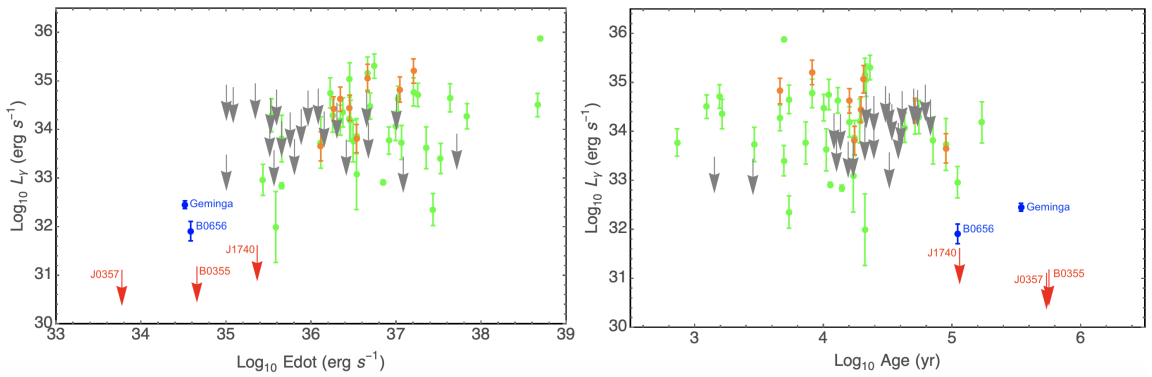

Figure 6.3: Plots of 1–10 TeV luminosities L_γ vs $\dot{E}$ and pulsar age. The green points are confirmed TeV PWNe (from [266] and the HESS Galactic Plane Survey (HGPS), [245], with values from the latter taking precedence for PWNe listed in both papers). The orange points represent candidate PWNe from the HGPS with no incompatible measurements (see HGPS Table 4). The gray arrows are the luminosity upper limits (also calculated at a 95% CL) of pulsars whose PWNe were not detected in the HGPS. The blue points represent the 1–10 TeV luminosities of Geminga and PSR B0656+14 (calculated from HAWC values for the 8-40 TeV range listed in [278] by assuming that the measured spectral slope remains the same in the 1-10 TeV range) and the red arrows are the luminosity upper limits of the targets observed in this study (using hard cuts).

associated with these PWNe have been detected by HAWC ([278], [247], [279]).

Due to their proximity as well as their large physical extent resolved by HAWC, the Geminga and B0656+14 PWNe take up a significant fraction of the VERITAS field of view. The standard source detection techniques common to IACTs (such as VERITAS), however, map gamma-ray sources using a round aperture of small angular size. This results in a limited sensitivity for two reasons: low surface brightness of the gamma-ray source relative to the cosmic ray background and difficulty obtaining a reliable background estimate from any location in the field of view. Thus, the current non-detection (see [280]) of these sources by VERITAS does not objectively characterize its sensitivity to a distant TeV PWN of comparable physical size and luminosity.

The VERITAS upper limit for the B0355 tail is already below the luminosity of the Geminga PWN inferred[6] from the HAWC measurements (see Figure 3). A more sophisti-

[6]Note that re-calculating the luminosity from the 8-40 TeV HAWC energy range to the 1-10 TeV range involved the assumption of a constant spectral slope fixed at the value reported in [278]. The actual luminosity

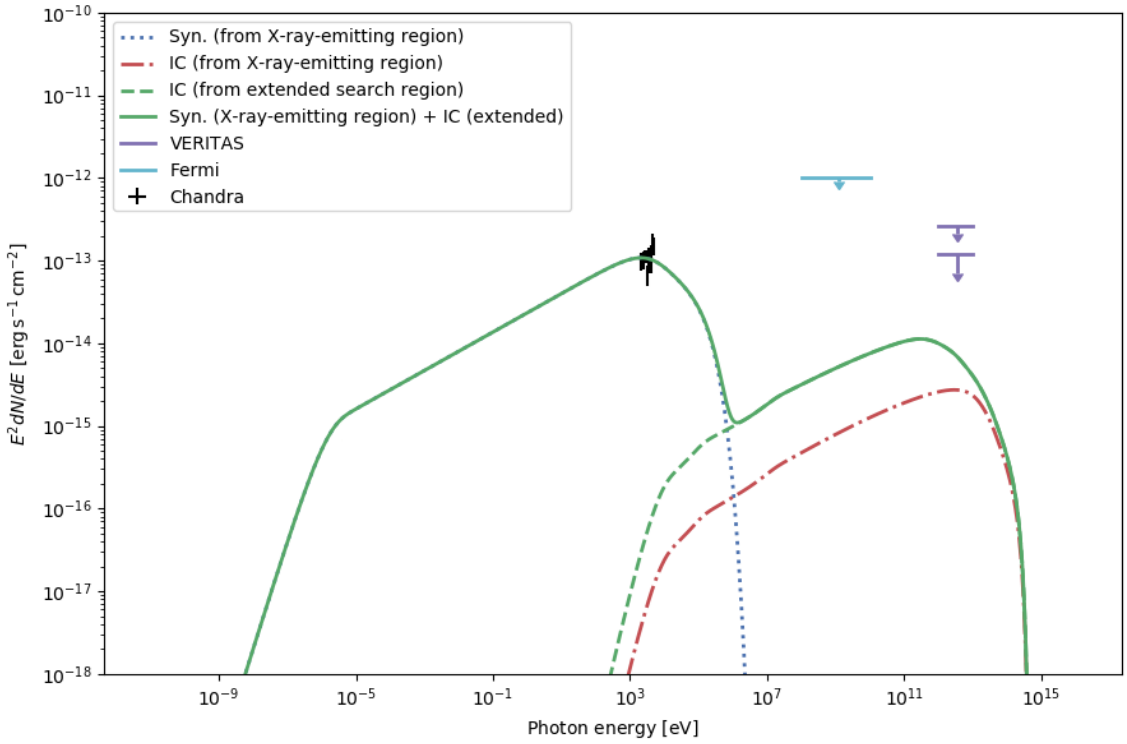

Figure 6.4: The multiwavelength spectrum of the B0355 tail calculated from the pulsar tail model (see Appendix). The blue (dotted) and red (dotted-dashed) lines represent the synchrotron and IC components (respectively) of the X-ray-emitting region of the tail (i.e., the regions shown in Figure 6.1). The green (broad dashed) line represents the IC component of the extended tail (see text). Shown in solid green is the sum of the synchrotron component from the X-ray-emitting region of the tail and the IC component of the extended tail (which includes the X-ray-emitting region). Also plotted are the measured *Chandra* spectrum of the X-ray tail (black data points), the *Fermi*-LAT upper limit on the B0355 tail (cyan arrow), and the VERITAS upper limits (purple arrows; the 'hard cut' limits for the extraction region sizes of $r = 0.1^\circ$ and $r = 0.235^\circ$ are shown, with the more stringent upper limit corresponding to the smaller region).

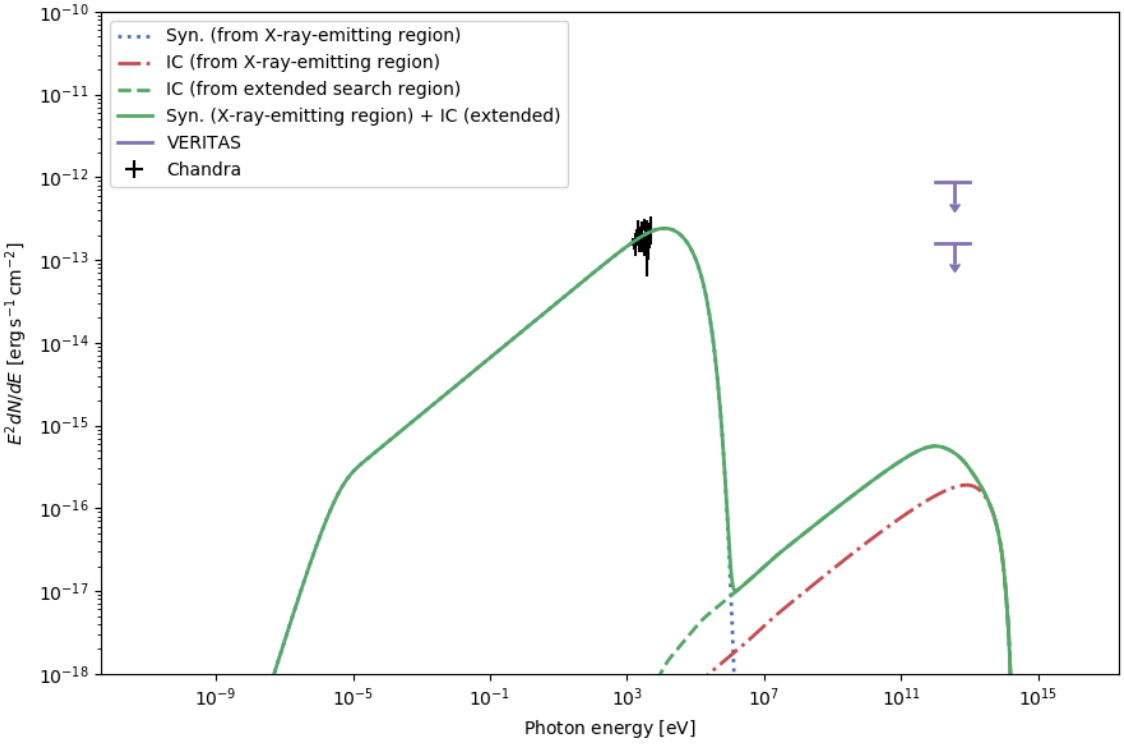

Figure 6.5: The multiwavelength spectrum of the J0357 tail obtained from our pulsar tail model, with the same labeling scheme as the previous plot.

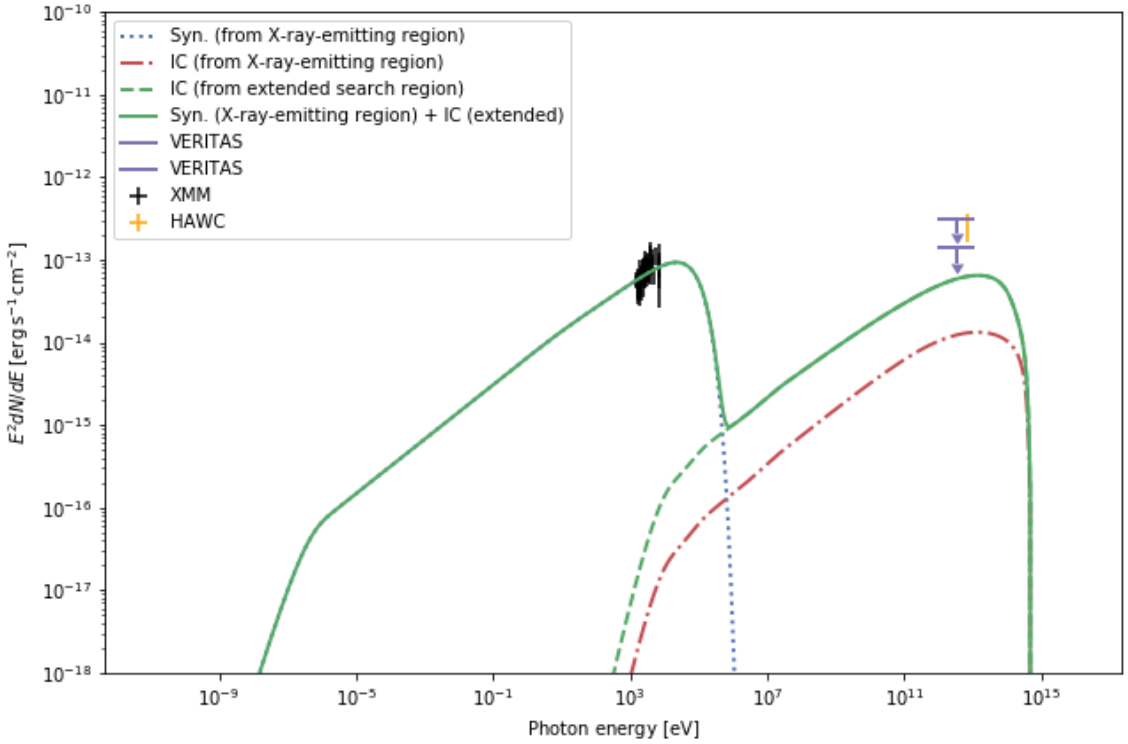

Figure 6.6: The multiwavelength spectrum of the J1740 tail obtained from our pulsar tail model, with the same labeling scheme as the previous plot. (See text for discussion on the HAWC limit.)

cated analysis (see [281]; beyond the scope of this paper) might further boost the sensitivity to the extended PWN of B0355, as the round aperture used by VERITAS is not optimized for detection of an elongated tail. The non-detection of B0355's PWN may also be attributed to the differences between the Geminga and B0355 PWNe. One such difference may be the morphology of B0355's PWN – the long tail with fairly soft X-ray spectrum. Such a tail has not been detected for Geminga so far although the morphology of the compact X-ray nebula was interpreted as an SPWN [246]. *eROSITA* should be able to tell whether Geminga lacks an extended tail or it is simply not detected due to its large size expected due to Geminga's proximity to Earth. Regardless, the Cherenkov Telescope Array (CTA), the next-generation IACT observatory, will have greatly improved sensitivity in the VHE range and should be able to easily detect pulsar tails like B0355's, thus enabling tests of the physical parameters associated with wind in pulsar tails. To demonstrate this and to independently estimate probable TeV fluxes for the PWNe of the three pulsars considered in this paper, we performed modeling of the multiwavelength emission from these tails.

The upper limits on the TeV flux from B0355 depend on assumptions about the size of the source. Determining the size of the tail is complicated. Firstly, the size of the TeV-emitting pulsar wind is expected to be larger than that of X-ray-emitting wind because of a factor of 10 longer cooling time for the TeV-emitting electrons. However, this is not the only factor that affects the length of the tail. The other two important factors are flow speed as a function of distance from the pulsar (which may be affected by the entrainment of the neutral atoms from the ambient medium; [282]) and diffusion timescale for TeV-emitting electrons. Once the flow slows down significantly, approaching the pulsar speed (in the reference frame of the pulsar), diffusion is expected to start playing a dominant role, therefore turning the end of the tail into more of a spherical structure (unless the magnetic field preserves an ordered geometry on large scales and/or the external field is ordered). This could happen over the distance where the time to traverse the tail in the transverse

value can be smaller if the spectrum hardens toward lower energies.

direction, $r(z)/v(z)$, at the local bulk flow velocity, $v(z)$, becomes of the order of the diffusion timescale, $r(z)^2/D$ (where $D \simeq 10^{26}(E_\gamma/1\ \mathrm{TeV})^{1/2}(B/10\ \mu\mathrm{G})^{-1}$ cm^2 s is the Bohm diffusion coefficient of electrons that up-scatter the CMB photons to the gamma-ray energy E_γ). However, calculating the tail's disruption distance requires a better knowledge of $r(z)$, $v(z)$, and $B(z)$ than we currently have. Theoretical models suggest that the flow and magnetic field may be more ordered closer to the pulsar becoming more chaotic and turbulent further downstream (e.g., [283] [284]). Observationally, these dependencies will become better constrained in the future if these tails are detected and resolved in TeV and radio. Moreover, the TeV emission may extend even beyond the disruption distance, in which case the morphology would appear more isotropic than a collimated tail (which may be happening in the case of Geminga). Therefore, in this paper we adopt a heuristic approach to estimate possible sizes of TeV sources. We note that synchrotron cooling time in radio is much longer than that in X-rays, and that radio tails (when detected) extend up to $10-20$ pc for highly supersonic pulsars like J1509–5850 [285] [274] and J1747–2958 [286] [237] which would correspond to $40'-80'$ at $d = 1$ kpc (a typical distance to the three pulsars analyzed in this paper). Since at least B0355 appears to have a lower Mach number [256], we picked a compromise size of $20' - 36'$ for the TeV emission search region.

To model the electron spectral energy distribution (SED) of the B0355 pulsar tail, we extend the one-dimensional (1D) model developed by [287] to account for variations in tail properties (cross-section, magnetic field strength, and bulk flow velocity with distance from the pulsar), adiabatic energy losses, and the variable (decreasing) particle injection rate of the pulsar with time. The derivation of the model is explained in the Appendix. Using the electron SED parameters obtained from the fits to X-ray synchrotron spectrum from *Chandra* data (i.e., the SED responsible for the X-ray emission seen up to $\approx 7'$ from the pulsar) and the tail properties constrained from those fits (i.e., the bulk flow velocity and magnetic field strength estimates, see [256]), we calculate the SED of the TeV-emitting particles up to 0.47° from the pulsar, and refer to these regions as the "extended search re-

gions" (e.g., in Figure 4) as opposed to smaller regions corresponding to the X-ray-emitting parts the tails (see Figure 1). This length corresponds to the angular size of the region used for extended TeV emission search (see Table 6.3 and Section 2.1) and is also comparable to the recently-detected extended TeV emission from the Geminga pulsar (see [247] & [248]). We used the Python package `Naima` [288] to calculate the synchrotron and IC emission from the volume-averaged electron SED (see Appendix), and present the multiwavelength spectrum of B0355 in Figure 6.4. The IC emission is calculated for the combined contributions of the CMB, thermal dust emission (30 K, 4.8×10^{-13} erg cm^{-3}), and starlight (4000 K, 8.0×10^{-13} erg cm^{-3}). We see that an observation more sensitive by a factor of 10 may be able to detect TeV emission. The modeling also demonstrates that, if the TeV spectrum is measured in addition to X-ray properties of the tail, one can put more stringent constraints on dependencies of the magnetic field strength and bulk flow velocity on the distance from the pulsar (see Appendix).

Unfortunately, despite the detailed X-ray information available for B0355, modeling its TeV emission (if it is detected) is complicated by the presence of another middle-aged pulsar, J0359, just $5.5'$ away. Having an angular resolution of $\sim 1'$ in the VHE range will be critical to establish the origin of any TeV emission. Indeed, the comparable absorbing hydrogen column density, $N_{\rm H} \sim (0.2 - 0.6) \times 10^{22}$ cm^{-1} for J0359 compared to $N_{\rm H} = 0.6 \times 10^{22}$ cm^{-2} for B0355, suggests that J0359 is located at a similar distance, if not closer than B0355. Given the relatively high $\dot{E} = 1.3 \times 10^{36}$ erg s^{-1} (compared to 4.5×10^{34} erg s^{-1}) the X-ray efficiency of J0359 PWN is very low, $\eta_X = L_X/\dot{E} \sim 10^{-6}$ for $d = 1$ kpc (compared to $\eta_X = 8 \times 10^{-4}$ for B0355), making it one of the least efficient in X-rays. It is currently unclear why X-ray efficiencies of PWNe vary so much[289] and whether there is a correlation between X-ray and TeV efficiencies for PWNe (see Fig. 4 in [243]). The non-detection in TeV suggests that the PWN of J0359 is also very inefficient in terms of its TeV emission.

We also repeated the same steps as above (see Appendix for details) to model the mul-

tiwavelength spectra of J0357 and J1740 tails (assuming a constant tail radius, flow speed, and magnetic field because we do not have as much information as for the B0355 tail from X-ray data), and obtain both the particle SED in the $8.'5$ X-ray-emitting part of the tail producing the observed synchrotron emission ($11z_0$; see appendix for definition of z_0), and the SED of the TeV-emitting particles up to a tail length of $30'$ ($50z_0$, comparable to the angular size of the region of sky analyzed, see Tables 6.2 and 6.4 along with Figures 6.5 and 6.6). The modeling suggests that detecting J0357 in TeV would be much more difficult compared to the other two pulsars.

TeV emission from an unresolved source located near the J1740 tail (at the HAWC resolution it can be considered as a match within the 2σ positional uncertainty of the 2HWC source) was recently reported in the 3HWC catalog [290] as 3HWC J1739+099. However, the source significance is fairly low (just above the threshold chosen for the 3HWC catalog). The source's differential flux at 7 TeV (plotted in Figure 6.6), 2.5×10^{-13} erg s^{-1} cm^{-2} is about a factor of 3-4 higher than predicted by our model. This can be attributed to the fact that we do not reliably know the shape and size of the tail (which also affects other assumptions and variables used in the model, like the bulk flow speed magnetic field's dependence on distance from the pulsar). There may also be a component from electrons that are still radiating in TeV in the tail's vicinity, but that are not necessarily in the tail anymore (in which case they are not subject to adiabatic energy losses and synchrotron losses due to the tail's magnetic field). At some point the tail flow is disrupted or ceases, and electrons diffuse out into the ISM, leading to so-called TeV halos, such as the one around Geminga, for example (this component is not modeled here).

6.7 Summary and Conclusions

We analyzed VERITAS observations and reported the upper limits on the TeV fluxes of three supersonically moving pulsars with long tails seen in X-rays. TeV emission from SP-WNe continues to remain elusive, although our modeling suggests that any TeV emission

could be detected with only a factor of 2-3 improved flux sensitivity, for J1740's tail, and a factor of 10, for B0355's tail, in deeper observations. In fact, when this paper was nearing completion the HAWC team reported a detection, albeit at a modest significance, of a VHE source located near the most promising tail, associated with PSR J1740+1000. We expect that CTA will be able to show conclusively whether the TeV emission from SPWNe is substantially different from that of slower moving or younger pulsars still residing within their host SNRs.

6.8 Appendix

We construct a pulsar tail model in order to calculate the electron SED and the corresponding IC and synchrotron spectra as a function of the distance from the pulsar. We compare these model predictions with the obtained TeV upper limits.

The simple one-dimensional (1D) model developed by [287] describes the impact of synchrotron losses on the electron SED as electrons (injected with some initial power-law SED at the TS) move along a cylindrical tail with constant bulk velocity. In that model, the tail's radius and magnetic field are assumed to be constant. We relax the model assumptions by allowing for a variable (with the distance from pulsar) magnetic field B, particle bulk flow velocity v, and tail radius r,

$$B = B(z) = B_0 \left(\frac{z}{z_0}\right)^{\beta} \qquad v = v(z) = v_0 \left(\frac{z}{z_0}\right)^{\alpha} \qquad r = r(z) = r_0 \left(\frac{z}{z_0}\right)^{\gamma} \quad (6.1)$$

where z_0 is the distance from the pulsar at which particles are injected into the tail, z_0, $z > z_0$ is the distance along the tail, and B_0, v_0, and r_0 are the initial values of the magnetic field, velocity, and radius, respectively. The constants β, α, and γ describe how these quantities change with distance, respectively. We pick the injection distance z_0 such that it corresponds with the "beginning" of the X-ray tail (i.e., the boundary between the compact nebula head and the beginning of the tail). The energy loss rate of an electron with energy

$\mathcal{E}$ (due to both synchrotron and adiabatic losses) is given by

$$\frac{d\mathcal{E}}{dt} = -c_1 B^2 \mathcal{E}^2 - \frac{1}{3}\left(\frac{\alpha+2\gamma}{z_0}\right) v_0 \left(\frac{z}{z_0}\right)^{\alpha-1} \mathcal{E} \tag{6.2}$$

where $c_1 = 4e^4/9m_e^4c^7$. Solving the differential equation yields

$$\mathcal{E}(z, \mathcal{E}_0, z_0) = \frac{\mathcal{E}_0 \left(\frac{z}{z_0}\right)^{-\lambda_1}}{1 + \frac{\mathcal{E}_0}{\epsilon\lambda_2}\left[\left(\frac{z}{z_0}\right)^{-\lambda_2} - 1\right]} \tag{6.3}$$

where $\epsilon = v_0/(c_1 B_0^2 z_0)$, $\lambda_1 = (\alpha+2\gamma)/3$, $\lambda_2 = 2\beta - \alpha - \lambda_1 + 1$, and $\mathcal{E}_0$ is the initial energy of the particle. Thus, the number density of particles with energy $\mathcal{E}$ at distance z, $n_e(\mathcal{E}, z)$, can be found from the continuity condition, $n_e(\mathcal{E}, z)\, \pi r^2 v = \text{constant}$. Assuming the injected particle distribution to be $n_e(\mathcal{E}_0, z = z_0) = K\mathcal{E}_0^{-p}$ ($\mathcal{E}_{0,\min} \leq \mathcal{E}_0 \leq \mathcal{E}_{0,\max}$), one obtains

$$n_e(\mathcal{E}, z) = K\mathcal{E}^{-p} \frac{\left(\frac{z}{z_0}\right)^{-2\gamma-\alpha-\lambda_1}}{\left\{\left(\frac{z}{z_0}\right)^{-\lambda_1} - \frac{E}{\epsilon\lambda_2}\left[\left(\frac{z}{z_0}\right)^{-\lambda_2} - 1\right]\right\}^{2-p}} \theta(\mathcal{E}_{\max} - \mathcal{E}), \tag{6.4}$$

where, $\theta(\mathcal{E}_{\max} - \mathcal{E})$ is the Heaviside step function, $\mathcal{E}_{\max} = \mathcal{E}(z, \mathcal{E}_{0,\max}, z_0)$, $\mathcal{E}_{0,\min} = 0$, and $\mathcal{E}_{0,\max}$ is assumed to be the energy associated with the maximum potential drop between the pole and the light cylinder, $\Delta\Phi = (3\dot{E}/2c)^{1/2}$ [40].

The particle injection rate is a function of $\dot{E}$, which decreases as the pulsar ages. Thus, at increasing distances z, the associated injection rate at the corresponding time of injection (in the past) t was higher than the current injection rate:

$$\dot{E}(t) = \frac{\dot{E}_0}{\left(1 + \frac{\tau - t}{\tau_0}\right)^{\frac{n+1}{n-1}}} \tag{6.5}$$

where τ is the current age of the pulsar, t is the time since injection, τ_0 is the spin-down

timescale, and n is the braking index (data from the HESS Galactic Plane Survey suggests that τ_0 ranges between $10^{2.5}$ and $10^{3.5}$ yr; see [245]; canonically, a simple spinning dipole corresponds to breaking index $n = 3$). One can take the variable injection rate into account in Equation (4) by multiplying it with $1/(1 + (\tau - t)/\tau_0)$ (assuming $n = 3$ and particle injection rate $\propto \dot{E}^{1/2}$; see [291]), after rewriting $t = dz/v(z)$ and integrating to z. Thus, the volume-averaged electron SED can be obtained by integrating $n_e(\mathcal{E}, z)$ over the volume of the tail. For the tail lengths, we picked $z_{\max}$ values that correspond to the size of the extended TeV search region ($0.47°$, see above).

To model the B0355 tail, we use the following parameters: $B_0 = 20\ \mu$G, $z_0 = 1 \times 10^{18}$ cm, $v_0 = 2,400$ km s^{-1}, $r_0 = 4.6 \times 10^{17}$ cm, $\gamma = 1$ (conical tail), $\beta = -0.35$, $\alpha = -0.65$ (constrained from $\beta = -\alpha - \gamma$), $p \equiv 2\Gamma - 1 = 2.48$, $\mathcal{E}_{0,\max} = 580$ erg (set by the maximum accelerating potential of the pulsar's polar cap, $\Phi = (3\dot{E}/2c)^{1/2}$), and $\tau = 560$ kyr. The magnetic field parameters, flow speed parameters, and particle spectrum p are consistent with those reported by [256]. The $z_0 = 1 \times 10^{18}$ cm corresponds to the distance at which the tail begins, downstream of the compact nebula. For this tail (as well as the others), we model the tail out to a distance corresponding to $0.47°$, as this angular distance corresponds to the angular size of the largest VERITAS search region (see Section 2.1 and Tables 2–4).

To model the J0357 tail, we use $d = 500$ pc (the distance inferred by [250]), $z_0 = 3.6 \times 10^{17}$ cm (the distance at which the tail becomes visible, $0.'8$), $z_{\max} = 50 z_0$, $r_0 = 2.7 \times 10^{17}$ cm (corresponding to the tail's $0.'6$ radius), and $v = v_0 = 15,000$ km s^{-1} and $B = B_0 = 50\ \mu$G (see [250] and [273]). In this case we assume a cylindrical tail (constant radius, $\gamma = 0$) with constant flow speed and magnetic field strength ($\alpha = \beta = 0$), $p = 2.64$ ($\Gamma = 1.82$, obtained by fitting the entire tail spectrum with $N_{\rm H} = 0.21 \times 10^{22}$ cm^{-2}: the maximum Galactic $N_{\rm H}$ in the direction of J0357, obtained by [273]), and set $\mathcal{E}_{0,\max} = 260$ erg and $\tau = 540$ kyr. Since the quantities here are less constrained than those of B0355 (e.g., B due to lack of multiwavelength observations, and d being only inferred), this model can only serve as a crude approximation in this case.

To model the J1740 tail, we use the dispersion measure distance $d \sim 1.4$ kpc, $z_0 = 8.4 \times 10^{17}$ cm (40″; we select this distance because it is the distance at which the bright pulsar's PSF (in the *XMM* data) no longer contaminates the tail emission), $r_0 = 8.4 \times 10^{17}$ cm, and $\gamma = 0$ (cylindrical tail; thus $\alpha = \beta = 0$). For the tail length we used $z_{\rm max} = 40 z_0$. To estimate the magnetic field strength, we use Eqn. (2) from [274], which is a generalization of Eqn. (7.14) from [292] for the case of arbitrary magnetization σ,

$$B = \left[\frac{L(\nu_m, \nu_M)\sigma}{\mathcal{A}V} \frac{\Gamma - 2}{\Gamma - 1.5} \frac{\nu_1^{1.5-\Gamma} - \nu_2^{1.5\Gamma}}{\nu_m^{2-\Gamma} - \nu_M^{2-\Gamma}} \right]^{2/7}. \tag{6.6}$$

Here, ν_1 and ν_2 are the characteristic synchrotron frequencies ($\nu_{\rm syn} \simeq eB\gamma^2/2\pi mc$ with $\gamma = \mathcal{E}/mc^2$) corresponding to the upper and lower energies of the electron SED ($dN_e/d\gamma \propto \gamma^{-p} \propto \gamma^{-2\Gamma+1}$; $\gamma_1 < \gamma < \gamma_2$), and $\mathcal{A} = 2^{1/2} e^{7/2} / 18\pi^{1/2} m_e^{5/2} c^{9/2}$. The radiating volume V can be estimated by assuming a 6′-long cylindrical tail of radius r_0, in which case $V = 1.66 \times 10^{55}$ cm^3. The photon index Γ and luminosity L are measured over the range $\nu_m < \nu < \nu_M$ (0.3–10 keV; see Section 3.2). The boundary frequencies ν_1 and ν_2 are unknown, so we choose arbitrary yet plausible values $h\nu_1 = 3$ eV and $h\nu_2 = 20$ keV. We estimate $B = B_0 = 5.1\sigma^{2/7}$ μG, a reasonable value given the pulsar's offset from the Galactic plane. Extending the range of the boundary frequencies to $h\nu_1 = 3$ eV and $h\nu_2 = 60$ keV and varying Γ within its 1σ uncertainty results in only minor changes, with the resulting estimates of B ranging from 5.0–6.4 μG. We also set $\mathcal{E}_{0,\rm max} = 1600$ erg and $\tau = 114$ kyr, and assume $v = v_0 = 5,000$ km/s. The latter could be fitted when better TeV data become available.

CHAPTER 7

THE PSCT

7.1 CTA & The pSCT

7.1.1 Background

The next generation of IACT telescopes is currently being developed for CTA, in particular the prototype Schwarzchild-Couder telescope (pSCT) which presently in commission. I will describe the work done to enhance and upgrade the camera of the pSCT.

Over the last several years significant effort has gone into planning and constructing the first Schwarzchild-Couder telescope (SCT) for the international Cherenkov Telescope Array (CTA) project. CTA plans to build, at two sites, over one hundred of the 'next generation' of advanced IACTs to probe the VHE universe with sensitivities never before achieved in the field. The SCT is a candidate for the Medium Sized Telescope (MST), along with Small and Large sized telescopes (SSTs,LSTs), that will comprise the telescopes that are designed to be sensitive to different parts of the VHE regime. The SCT, with it's long-ago proposed but innovative, two-mirrored optical design system will have superior angular resolution, off-axis sensitivity and field of view compared to the Davies-Cotton (DC), single reflector, design that all current IACTs are.

Below is an abstract on the characteristics and performance of the pSCT, from https://cta-psct.physics.ucla.edu/

> "The first of its kind in the history of imaging atmospheric Cherenkov telescopes (IACTs), the pSCT uses a secondary mirror to correct comatic aberrations and achieve an aplanatic optical system with 8° wide field of view (FoV). The largest FoV of any IACT currently in operation is $< 5^\circ$ (the FoV of VERITAS is 3.5°). The demagnifying secondary mirror of the SCT improves imag-

ing and significantly reduces the focal plane plate scale compared to the DC telescope. This permits the construction of a high imaging resolution, 0.8m diameter camera of the SCT with 11,328 pixels of 0.067°, while the equivalent DC telescope version of the MST is assembled from 1,570 pixels of 0.18° in a camera of 2.3m in diameter. The small plate scale of the SCT camera is compatible with novel silicon photo-multipliers (SiPMs), which are significantly less expensive than the traditional photomultiplier tubes used in the DC telescope (and VERITAS). It is thus possible to construct the SCT camera at roughly the same or even reduced cost.

The advantages of the SCT for CTA are derived from the superior imaging resolution of its optical system in the wide 8° FoV. The fraction of all detected atmospheric cascades with the shower core inside or near the footprint of the MST array in CTA is significantly larger than for a four-telescope array such as VERITAS. The reconstruction of the arrival direction of the gamma-rays which initiated these cascades is greatly improved when using SCTs, ultimately leading to better angular resolution. Compared to VERITAS, the on-axis angular resolution of the MST array of DC telescopes in CTA is greater by a factor of 1.4, while an SCT-based MST array offers an improvement of up to a factor of 2. This enhancement of gamma-ray angular resolution increases further for off-axis observations of astrophysical sources.

The differential off-axis point source sensitivity benefits dramatically from the improved angular resolution of an SCT-based MST array, which reduces the exposure time required for achieving a given sensitivity for a source at 3.5° off axis by more than factor of 2 (for an on-axis source the exposure reduction is up to 40 %). This enhancement in CTA performance offered by the SCT has direct scientific implications on the detection of large angular-extent sources, sky surveys, as well as follow-up observations triggered by multi-messenger

Table 7.1: Schematics of the FPM module. The SiPM quadrants are shown at the top of the images, along with the foam block for insulation (in yellow), the module housing and heat-sink are also shown.

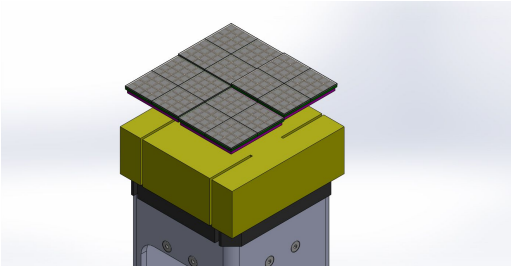

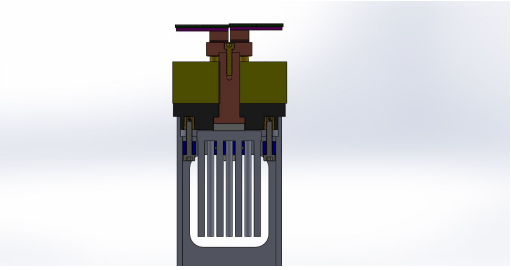

instruments (such as IceCube and LIGO-VIRGO) with relatively poor initial source localization."

Several publications with, contributions from the whole pSCT collaboration, have already been made: further information on the optical system and camera can be found in [293] and [294], respectively.

7.2 pSCT Camera Work

7.2.1 Focal Plane Module Assembly and Testing

The advanced camera of the SCT will comprise of 177 camera modules, each made up of a Front End Electronics (FEE) set of custom electronics boards, with a metal cage housing for protection and to allow easy insertion into the camera housing, and a Focal Plane Module (FPM) that. Each FPM comprises of four PCBs (dubbed 'quadrants') each with a 4x4 array of SiPM imaging pixels mounted on the ASIC, along with a Peltier thermo-electric device to provide cooling to the ASICs, along with a custom heat-sink design, and newly developed 'SMART' amplifier chips. Each quadrant is electrically connected to the FEE with a micro-coaxial ribbon cable that supplies power, allows monitoring of the temperature and also sends the SiPM signals to the FEE.

Due to the SCT requiring a curved focal plane each quadrant is mounted at a specific

Table 7.2: A further schematic of an FPM, note the differing heights of the individual quadrants, is shown on the left. The right image shows the 'dark box' setup with a SiPM module to be tested on the mobile linear stage, with the laser entering through the optic fiber from the side.

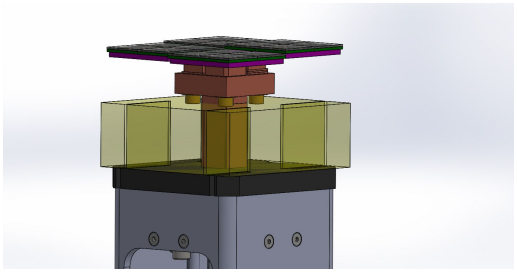

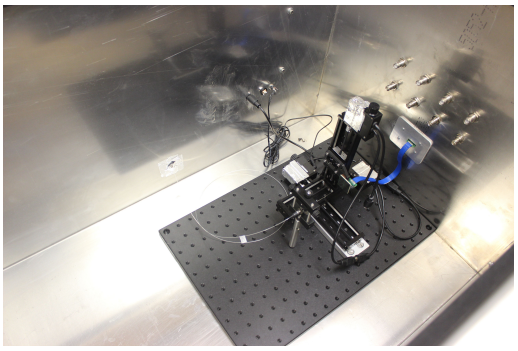

height, through a combination of differing post heights for each FPM and then individually shimming each quadrant to it's desired height to within 100 micrometers. This is an extensive and pain-staking process that needs to be repeated for all camera modules. Currently the central 25 modules have been assembled, adjusted and coarsely tested by myself at GT before being shipped to FLWO to be mounted in the central sector of the camera. We also wrote and implemented firmware, using the Arduino IDE, for the micro-controller that is responsible for controlling various initiation values and PID temperature control using pulse width modulation. Extensive testing and bug fixing was required due to problem communicating via the FPGA mounted on the FEE board.

Before being shipped to the telescope site, testing of each module was performed by scanning each channel with a triggered laser and checking the digitized output was consistent across the quadrants. This allowed for a reasonably quick check that all channels were operational before being installed in the camera.

A subset of the modules were also calibrated for temperature measurements. This was achieved by placing the module to be calibrated into a climate chamber that was ramped from 40°C to 0°C, and reading raw ADC counts from the digitizer connected to the temperature sensor circuit on each quadrant. The ADC values were then fitted with a linear

function, the coefficients of which are stored in the FEE EEPROM and used when a temperature measurement is called. Using the PID temperature control software and the calibration data the FPMs are able to be held to a set temperature with better less than 0.1°C variation. This is important as the SiPM performance can vary with temperature.

7.2.2 Camera Upgrade and Planned work

MRI Consortium funding was secured and an upgrade of the pSCT camera is in progress, although the planned timeline has been severely impacted by the COVID-19 pandemic. This upgrade seeks to fully integrate all of the camera modules, improve various aspects of the camera housing and improve the electronics of the camera. We will be responsible for fabricating and assembling the remaining 150 FPMs along with testing a new amplifier ASIC device called SMART. The aim is to shorten the length of travel before amplification of the photon detector signals, to reduce pickup and noise, by mounting the new amplifier board adjacent to the focal plane quadrants.

The fabrication of the mechanical parts for the remaining FPMs is currently underway at GT, with the Montgomery Machining Mall producing the components from CAD drawings. The involved and precise process of module assembly and alignment is being started up in the early summer 2022, as the parts are fabricated, with plans to continue the assembly and testing pipeline throughout the late summer.

CHAPTER 8

LORENTZ-INVARIANCE VIOLATION WITH H.E.S.S, MAGIC AND VERITAS

In this chapter I detail my contributions to a recently published paper [295], adapting material I authored for said paper. The 'joint task force' consists of members of the three major IACT collaborations. The goal of this project is to develop methods to combine measurements from the separate IACTs to probe possible Lorentz invariance violation (LIV) using gamma-rays.

8.1 Background and Motivation

Quantum Mechanics and Einsteinian General Relativity boast some of the most precise measurements of fundamental physics to date and underpin much of modern physics. However, reconciling the two into a single theory of 'Quantum Gravity' has proved itself, so far, an elusive goal, in the quest to unite the understanding of the minuscule with the cosmological scale that has been ongoing for almost a century.

Several semi-classical analyses were inspired by QG models, in particular; String Theory, Loop Quantum Gravity and Standard Model Extension. Efforts so far have highlighted the fact that it is a difficult to retain Lorentz symmetries when applying quantization to the spacetime geometry of general relativity. Hence, departures from Lorentz invariance has become a key sign we might expect in a QG theory. It follows that Lorentz invariance is an intrinsic property that is applicable at lower energies, but is possibly not adhered to, at higher energies near the Planck scale[1] The common starting point for 'Time of Flight' (ToF) tests is modifying the energy-momentum dispersion relation of free relativistic particles, as

[1] This is thought to be the energy scale when effects from GR and QM are of the same order of importance.

such:

$$E^2 \simeq p^2c^2 \times \left[1 \pm \sum_{n=1}^{\infty} \left(\frac{E}{E_{QG}}\right)^n\right], \tag{8.1}$$

where c is the speed of light[2] and E_{QG} determines the strength of QG effects, with energy. The order of magnitude of E_{QG} is thought to be around the Planck scale ($E_P = \sqrt{\hbar c^5/G} \simeq 10^{19}$ GeV) [295].

This 'in-vacuo' dispersion is a direct result of the 'granular' nature of 'quantum spacetime' interacting differently with photons of different energies as fluctuations of spacetime geometry on the Planck scale leading to a varying refractive index characterizing the metric. Linear or quadratic corrections to the photon group velocity are the focus of current experiments, given the current instrument sensitivity[295].

The difference in arrival time between two photons that are simultaneously produced from a source at redshift z with energies $E_h > E_l$ is:

$$\Delta t_n \simeq \pm \frac{n+1}{2} \frac{E_h^n - E_l^n}{H_0 E_{QG}^n} \kappa_n(z), \tag{8.2}$$

where $\kappa_n(z)$ encodes the effective path-length travelled by the photon from the source, expressed as:

$$\kappa_n(z) \equiv \int_0^z \frac{(1+z')^n}{\sqrt{\Omega_m (1+z')^3 + \Omega_\Lambda}} dz', \tag{8.3}$$

where H_0 is the Hubble parameter.

Due to the minuscule effects of the dispersion the ToF method requires very distant and energetic sources to maximize the potential effect seen, or highly variable sources like PSRs.

Several years ago an inter-collaboration working group was created with members from the three major IACT experiments with the aim of constraining possible LIV effects using

[2]I.e. the 'classical value that is commonly thought of, but here represents the 'true' value, in the limit of low energies

data from the three telescopes. This is the first study of it's kind that uses the combined VHE gamma-ray data to look for possible energy, and redshift, dependent time-lags in the TeV regime. The likelihood approach used allows investigation and validation of the approach to combine limits from different sources and even different experiments.

Highly variable, energetic and distant sources such as Pulsars, flaring Active Galactic Nuclei and Gamma-ray Bursts are the best targets for such studies. However, TeV sources were analyzed only separately so far, preventing a study of LIV effects as a function of redshift. The first paper, of a planned two, has been accepted for publication in May 2022 in The Astrophysical Journal. It details the combination method, based on maximum likelihood analysis, and assess its performance using simulated datasets. It also explores two different scenarios for redshift dependence and a new way to treat statistical and systematic errors in energy-dependant time-lags determination. The second, planned, paper will use published gamma-ray data from the three IACTs to derive combined limits from real observations.

My main contribution to the effort is the simulations of the sources, including modeling the LIV effects that may be present, discussed further in the sections below.

8.2 Source Sample and Simulations

The following section contains details on the simulation implementation I developed for the project and is an adaptation of the sections of the paper [295] that I was responsible for writing.

The non-transient sources used for this work have all been detected by the three experiments H.E.S.S., MAGIC and VERITAS, and have been selected to gather a representative sample. Namely, the three types of source were selected: one GRB, three flaring AGN and one PSR[3], with the following additional criteria:

- the three flaring AGN show different signal to background ratios: negligible back-

[3]The Vela pulsar has since been added as an additional source.

Table 8.1: Simulation settings for the individual sources. The column 'Number of events' gives the number of photons considered when computing the likelihood, *i.e.* excluding the ones used for template determination.

Source	Energy Range (TeV)	Time Range	Spectral index	Lightcurve shape	Energy resolution	Number of events
GRB 190114C	0.3 - 2	60 - 1200	2.5	MWL observations (?)	?	726
PG 1553+113	0.4 - 0.8	0 - 8000 s	4.8	Double Gauss	10%	72
Mrk 501	0.25 - 11	0 - 1531 s	2.2	Simple Gauss	22%	800
PKS 2155-304	0.28 - 4	0 - 4000 s	3.46	5 Asymmetric Gauss	10%	2965
Crab	0.12 - 7	0 - 1 phase	3 (signal), 3.5 (background)	Double Gauss + Baseline	10%	860000
Vela	0.06 - 0.15	0.4 - 0.7 phase	4.0	Asymetric Lorentzian	24%	3956

ground for PKS 2155-304 and Mrk 501 and larger background for PG 1553+113;

- the sources show very different light curve shapes, from a single Gaussian pulse for Mrk 501 flare of 2005 to multiple asymmetric spikes for PKS 2155-304 flare of 2006;
- the sources selected cover a wide range in distance, from 2.2 kpc for the Crab PSR to a redshift of 0.49 for PG 1553+113;
- the two PSR have different distances and were observed on very different time scales;
- in addition, PG 1553+113 has a large uncertainty on the distance which was taken into account in the analysis.

8.2.1 Simulations

The simulated data-sets, used in this work, are modeled on three AGN flares; Mrk501 2005 flare detected by MAGIC, PG1553+113 2012 flare , and PKS 2155-304 2006, flare detected by H.E.S.S– along with Crab Pulsar (PSR B0531+21) observations by VERITAS. The parameterization for each source is summarized in Table 8.1.

The first two terms, linear and quadratic with respect to energy, in equation 8.1, were considered for the simulations and later analysis. For testing of LIV, and hence the corresponding QG models, we generate simulated data sets constructed from parameterizations of published observational data, from the sources mentioned above.

The simulations I developed are written in C++, using the ROOT framework [170] and comprise of the following process: (i) Arrival times are drawn from the parameterized lightcurves, for each source, with the observed number of signal and background events. (ii) The 'true' energy of each event is drawn from a power-law spectrum as appropriate and the LIV dispersion term, of chosen order, is calculated from equation 8.2 (iii) Using the observation-specific Instrument Response Functions (IRFs) the Effective Area for each event is calculated and events are probabilistically 'detected' or rejected. (iv) The reconstructed (measured) energy of each event is drawn from the 'true' energy and IRFs, emulating the energy dependant reconstructed energy 'smearing' systematic . (v) The arrival time, including LIV dispersion, and other metadata of accepted events, are written to the data set. In preparation for further study, and the planned second paper I also implemented absorption of gamma-rays by the extragalactic background light (EBL) using the detailed modeling of Kudoda and Faltenbacher [296]. This is realized in the simulation code with gamma rays being probabilistically attenuated by using the the calculated gamma-ray opacity from the model, that is dependent on the gamma-ray energy and the source redshift.

For each source, 1000 observation data sets are simulated to be used for analysis. The Monte Carlo simulation data is analyzed to show that the spectra and lightcurves are in-agreement with the published data as a baseline check.

8.3 Conclusion

The method has been demonstrated to be successful, producing competitive limits from simulations, and a useful tool to be applied to real data sets in the future publication. The simulation sets produced have proved invaluable for testing the combination procedure and investigating the effects of systematic uncertainties from the different sources and experiments. The simulation code, now used by other members of the working group, will be made publicly available in the future, and can continue to be used as a viable way to quickly

and easily generate data sets for studies, when real data is not a viable option.

CHAPTER 9
FINAL CONCLUSION

This thesis has detailed the study of several long-term projects that have contributed to the field of VHE gamma-ray astronomy in many ways. The main goals that have been achieved in this work are:

1) Performed a novel survey, investigating VERITAS data on six MSPs. Prefacing this study I have provided an extensive review on the fast-evolving and complex current state of pulsar theory and modeling that has undergone rapid development in the last few years. From this analysis, I have provided the results from tests to determine if any significant pulsed emission is detected, and, as no of any hint or detections of pulsed emission in the VHE gamma-ray regime could be claimed, reported upper-limits on the observed VHE pulsed flux and gamma-ray conversion efficiency of these MSPs. Additionally, I have applied the resulting ULs, on various quantities, to carry out a population study to attempt to determine the overall behavior of MSPs, relating their mechanical spin-down properties to their observed VHE gamma-ray luminosity profile. The limits from this work are at competitive levels with other pulsar observations at VHE energies and quantitatively constrain the appearance/possible magnitude of a separate VHE flux element in the VERITAS energy range for the sources studied here. This extends the study of 'regular'/young pulsars done with VERITAS in the past, but, critically, opens up a new chapter for pulsar study by providing the first foray into a more comprehensive study of the fastest-spinning pulsars known. This work represents the first survey of MSPs in the VHE regime and totals over 100hrs of quality IACT gamma-ray data. I have also provided a comparison of the results to the unresolved questions in the modern field, with regard to the most up-to-date pulsar simulation models, in terms of constraining possible theoretical characteristics of VHE production, and the overall behavior of the VHE pulsar population when assessed through

luminosity measurements. The above will form the bases of a planned upcoming publication. As very limited, if any, data have been published in the VHE gamma-ray regime for most pulsars, and many factors in theoreticians models and simulations remain unknown and unconstrained, this represents invaluable data to guide and shape future work by many scientists. Significant advancements in simulation technique has allowed the exploration of hugely advanced pulsar models, only in the past year. This re-invigoration of the field and new predictions of pulsar emission characteristics makes experimental results, such as the limits placed here, even more important as consensus on the exact scenario has not been reached. The additional information gained, by probing the magnetosphere environment that is unique to MSPs, intrinsically explores separate situations than that of the VERITAS young pulsar survey, and so rounds off the arsenal of available data, for theoreticians, nicely. The results of the survey also show that the PSR J0030+0451 could be a promising candidate for observation with CTA as the ULs for J0030 produced here are closest to challenging the scenario of $F = k_{Crab}\ \sqrt{\dot{E}}/d^2$ for the MSP population. The gain in sensitivity will mean that, for the same exposure, the upper limit on pulsed flux, if the pulsar is not detected, from CTA, would likely be placed below the line of proportionality for this flux trend, opposing its universal application to MSPs, and possibly all pulsars, in general.

2) Reported on the search for very-high-energy gamma-ray emission from the regions around three nearby supersonic pulsars that have been seen to posses long tails, in the X-ray regime. Additionally, as no firm detection of these tails was achieved in the VHE domain, I have provided upper limits on the TeV flux and luminosity, and also compared these limits with other pulsar wind nebulae detected in X-rays, along with model predictions for extended pulsar tail emission profiles. The result is that at least one of the three tails is likely to be detected in observations that are a factor of 2-3 more sensitive. The analysis conclusions presented also constrain the parameters for those pulsars whose tail emission might be predicted to be observed in the VHE regime.

3) In addition, I have also made contributions to the wider field and have: Described my

contributions to the building of a novel telescope design for the upcoming the Cherenkov Telescope Array (CTA), that will be the most sensitive IACT instrument ever constructed and used to observe the gamma-ray sky. CTA holds the key to producing more sensitive measurements of undetected targets, such as the MSPs described here, and the measurements of the MSP survey will provide CTA with data that can help guide optimal observation in the future.

Detailed my contribution to a novel study of Lorentz-Invariance Violation and hence, what we can learn about a possible quantum structure of spacetime through VHE gamma-ray observations, via collaboration with the other major IACT groups.

Finally, I have given insight into the large-scale simulation production that I have completed to produce modern IRFs, essential for VERITAS data analysis.

Overall, the fundamentals of VHE pulsar physics remain somewhat elusive, despite the tireless efforts of many scientists. Nevertheless, the possible scenarios *are* being honed in on, often by gradually ruling certain frameworks out. The recent resurgence of interest in the theoretical and experimental aspects of investigating pulsars surely promises an eventful and, hopefully, enlightening near-future.

REFERENCES

[1] C. Venter, A. K. Harding, and I. Grenier, "High-energy Emission Properties of Pulsars," *PoS*, vol. MULTIF2017, p. 038, 2018. arXiv: 1802.00204 [astro-ph.HE].

[2] E. Feenberg and H. Primakoff, "Interaction of cosmic-ray primaries with sunlight and starlight," *Phys. Rev.*, vol. 73, pp. 449–469, 5 1948.

[3] S. Hayakawa, "Propagation of the Cosmic Radiation through Intersteller Space," *Progress of Theoretical Physics*, vol. 8, no. 5, pp. 571–572, Nov. 1952. eprint: https://academic.oup.com/ptp/article-pdf/8/5/571/5221264/8-5-571.pdf.

[4] P. Morrison, "On gamma-ray astronomy," *Il Nuovo Cimento*, vol. 7, no. 6, pp. 858–865, Mar. 1958.

[5] F. K. Ropke and W. Hillebrandt, "The case against the progenitor's carbon-to-oxygen ratio as a source of peak luminosity variations in type Ia supernovae," *aap*, vol. 420, pp. L1–L4, Jun. 2004. arXiv: astro-ph/0403509 [astro-ph].

[6] R. C. Tolman, "Static solutions of einstein's field equations for spheres of fluid," *Phys. Rev.*, vol. 55, pp. 364–373, 4 1939.

[7] J. R. Oppenheimer and G. M. Volkoff, "On Massive Neutron Cores," *Physical Review*, vol. 55, no. 4, pp. 374–381, Feb. 1939.

[8] F. Douchin and P. Haensel, "A unified equation of state of dense matter and neutron star structure," *aap*, vol. 380, pp. 151–167, Dec. 2001. arXiv: astro-ph/0111092 [astro-ph].

[9] V. Kalogera and G. Baym, "The Maximum Mass of a Neutron Star," *apj*, vol. 470, p. L61, Oct. 1996. arXiv: astro-ph/9608059 [astro-ph].

[10] A. Reisenegger, "Origin and evolution of neutron star magnetic fields," *arXiv e-prints*, astro-ph/0307133, astro–ph/0307133, Jul. 2003. arXiv: astro-ph/0307133 [astro-ph].

[11] J. A. Pons, D. Viganò, and N. Rea, "A highly resistive layer within the crust of X-ray pulsars limits their spin periods," *Nature Physics*, vol. 9, no. 7, pp. 431–434, Jul. 2013. arXiv: 1304.6546 [astro-ph.SR].

[12] A. Hewish, S. J. Bell, J. D. H. Pilkington, P. F. Scott, and R. A. Collins, "Observation of a Rapidly Pulsating Radio Source," *nat*, vol. 217, no. 5130, pp. 709–713, Feb. 1968.

[13] F. Pacini, "Energy Emission from a Neutron Star," *nat*, vol. 216, no. 5115, pp. 567–568, Nov. 1967.

[14] T. Gold, "Rotating Neutron Stars as the Origin of the Pulsating Radio Sources," *nat*, vol. 218, no. 5143, pp. 731–732, May 1968.

[15] G. R. BLUMENTHAL and R. J. GOULD, "Bremsstrahlung, synchrotron radiation, and compton scattering of high-energy electrons traversing dilute gases," *Rev. Mod. Phys.*, vol. 42, pp. 237–270, 2 1970.

[16] E. Aliu, T. Arlen, T. Aune, M. Beilicke, W. Benbow, A. Bouvier, S. M. Bradbury, J. H. Buckley, V. Bugaev, K. Byrum, A. Cannon, A. Cesarini, J. L. Christiansen, L. Ciupik, E. Collins-Hughes, M. P. Connolly, W. Cui, R. Dickherber, C. Duke, M. Errando, A. Falcone, J. P. Finley, G. Finnegan, L. Fortson, A. Furniss, N. Galante, D. Gall, K. Gibbs, G. H. Gillanders, S. Godambe, S. Griffin, J. Grube, R. Guenette, G. Gyuk, D. Hanna, J. Holder, H. Huan, G. Hughes, C. M. Hui, T. B. Humensky, A. Imran, P. Kaaret, N. Karlsson, M. Kertzman, D. Kieda, H. Krawczynski, F. Krennrich, M. J. Lang, M. Lyutikov, A. S Madhavan, G. Maier, P. Majumdar, S. McArthur, A. McCann, M. McCutcheon, P. Moriarty, R. Mukherjee, P. Nuñez, R. A. Ong, M. Orr, A. N. Otte, N. Park, J. S. Perkins, F. Pizlo, M. Pohl, H. Prokoph, J. Quinn, K. Ragan, L. C. Reyes, P. T. Reynolds, E. Roache, H. J. Rose, J. Ruppel, D. B. Saxon, M. Schroedter, G. H. Sembroski, G. D. Şenturk, A. W. Smith, D. Staszak, G. Tešić, M. Theiling, S. Thibadeau, K. Tsurusaki, J. Tyler, A. Varlotta, V. V. Vassiliev, S. Vincent, M. Vivier, S. P. Wakely, J. E. Ward, T. C. Weekes, A. Weinstein, T. Weisgarber, D. A. Williams, and B. Zitzer, "Detection of pulsed gamma rays above 100 gev from the crab pulsar," *Science*, vol. 334, no. 6052, pp. 69–72, 2011. eprint: `https://science.sciencemag.org/content/334/6052/69.full.pdf`.

[17] S. Ansoldi, L. A. Antonelli, P. Antoranz, A. Babic, P. Bangale, U. Barres de Almeida, J. A. Barrio, J. Becerra González, W. Bednarek, E. Bernardini, B. Biasuzzi, A. Biland, O. Blanch, S. Bonnefoy, G. Bonnoli, F. Borracci, T. Bretz, E. Carmona, A. Carosi, P. Colin, E. Colombo, J. L. Contreras, J. Cortina, S. Covino, P. Da Vela, F. Dazzi, A. De Angelis, G. De Caneva, B. De Lotto, E. de Oña Wilhelmi, C. Delgado Mendez, F. Di Pierro, D. Dominis Prester, D. Dorner, M. Doro, S. Einecke, D. Eisenacher Glawion, D. Elsaesser, A. Fernández-Barral, D. Fidalgo, M. V. Fonseca, L. Font, K. Frantzen, C. Fruck, D. Galindo, R. J. García López, M. Garczarczyk, D. Garrido Terrats, M. Gaug, N. Godinović, A. González Muñoz, S. R. Gozzini, Y. Hanabata, M. Hayashida, J. Herrera, K. Hirotani, J. Hose, D. Hrupec, G. Hughes, W. Idec, H. Kellermann, M. L. Knoetig, K. Kodani, Y. Konno, J. Krause, H. Kubo, J. Kushida, A. La Barbera, D. Lelas, N. Lewandowska, E.

Lindfors, S. Lombardi, F. Longo, M. López, R. López-Coto, A. López-Oramas, E. Lorenz, M. Makariev, K. Mallot, G. Maneva, K. Mannheim, L. Maraschi, B. Marcote, M. Mariotti, M. Martínez, D. Mazin, U. Menzel, J. M. Miranda, R. Mirzoyan, A. Moralejo, P. Munar-Adrover, D. Nakajima, V. Neustroev, A. Niedzwiecki, M. Nevas Rosillo, K. Nilsson, K. Nishijima, K. Noda, R. Orito, A. Overkemping, S. Paiano, M. Palatiello, D. Paneque, R. Paoletti, J. M. Paredes, X. Paredes-Fortuny, M. Persic, J. Poutanen, P. G. Prada Moroni, E. Prandini, I. Puljak, R. Reinthal, W. Rhode, M. Ribó, J. Rico, J. Rodriguez Garcia, T. Saito, K. Saito, K. Satalecka, V. Scalzotto, V. Scapin, C. Schultz, T. Schweizer, S. N. Shore, A. Sillanpaa, J. Sitarek, I. Snidaric, D. Sobczynska, A. Stamerra, T. Steinbring, M. Strzys, L. Takalo, H. Takami, F. Tavecchio, P. Temnikov, T. Terzić, D. Tescaro, M. Teshima, J. Thaele, D. F. Torres, T. Toyama, A. Treves, J. Ward, M. Will, and R. Zanin, "Teraelectronvolt pulsed emission from the Crab Pulsar detected by MAGIC," *aap*, vol. 585, A133, A133, 2016. arXiv: 1510.07048 [astro-ph.HE].

[18] Aleksi´c, J., Alvarez, E. A., Antonelli, L. A., Antoranz, P., Asensio, M., Backes, M., Barrio, J. A., Bastieri, D., Becerra González, J., Bednarek, W., Berdyugin, A., Berger, K., Bernardini, E., Biland, A., Blanch, O., Bock, R. K., Boller, A., Bonnoli, G., Borla Tridon, D., Braun, I., Bretz, T., Cañellas, A., Carmona, E., Carosi, A., Colin, P., Colombo, E., Contreras, J. L., Cortina, J., Cossio, L., Covino, S., Dazzi, F., De Angelis, A., De Caneva, G., De Cea del Pozo, E., De Lotto, B., Delgado Mendez, C., Diago Ortega, A., Doert, M., Domínguez, A., Dominis Prester, D., Dorner, D., Doro, M., Eisenacher, D., Elsaesser, D., Ferenc, D., Fonseca, M. V., Font, L., Fruck, C., García López, R. J., Garczarczyk, M., Garrido, D., Giavitto, G., Godinovi´c, N., Hadasch, D., Hafner, D., Herrero, A., Hildebrand, D., Hohne-Monch, D., Hose, J., Hrupec, D., Jogler, T., Kellermann, H., Klepser, S., Krahenbuhl, T., Krause, J., Kushida, J., La Barbera, A., Lelas, D., Leonardo, E., Lewandowska, N., Lindfors, E., Lombardi, S., López, M., López-Oramas, A., Lorenz, E., Makariev, M., Maneva, G., Mankuzhiyil, N., Mannheim, K., Maraschi, L., Mariotti, M., Martínez, M., Mazin, D., Meucci, M., Miranda, J. M., Mirzoyan, R., Moldón, J., Moralejo, A., Munar-Adrover, P., Niedzwiecki, A., Nieto, D., Nilsson, K., Nowak, N., Orito, R., Paneque, D., Paoletti, R., Pardo, S., Paredes, J. M., Partini, S., Perez-Torres, M. A., Persic, M., Peruzzo, L., Pilia, M., Pochon, J., Prada, F., Prada Moroni, P. G., Prandini, E., Puerto Gimenez, I., Puljak, I., Reichardt, I., Reinthal, R., Rhode, W., Ribó, M., Rico, J., Rugamer, S., Saggion, A., Saito, K., Saito, T. Y., Salvati, M., Satalecka, K., Scalzotto, V., Scapin, V., Schultz, C., Schweizer, T., Shayduk, M., Shore, S. N., Sillanpaa, A., Sitarek, J., Snidari´c, I., Sobczynska, D., Spanier, F., Spiro, S., Stamatescu, V., Stamerra, A., Steinke, B., Storz, J., Strah, N., Suri´c, T., Takalo, L., Takami, H., Tavecchio, F., Temnikov, P., Terzi´c, T., Tescaro, D., Teshima, M., Tibolla, O., Torres, D. F., Treves, A., Uellenbeck, M., Vankov, H., Vogler, P., Wagner, R. M., Weitzel, Q., Zabalza, V., Zandanel, F., Zanin, R., and Hirotani, K., "Phase-resolved energy spectra of the crab pulsar in the range of 50-400 gev measured with the magic telescopes," *A&A*, vol. 540, A69, 2012.

[19] A. Djannati-Ataï, G. Giavitto, M. Holler, B. Rudak, and C. Venter, "Probing vela pulsar down to 20 gev with h.e.s.s. ii observations," *AIP Conference Proceedings*, vol. 1792, no. 1, p. 040 028, 2017. eprint: https://aip.scitation.org/doi/pdf/10.1063/1.4968932.

[20] G. B. Cook, S. L. Shapiro, and S. A. Teukolsky, "Recycling Pulsars to Millisecond Periods in General Relativity," *apj*, vol. 423, p. L117, Mar. 1994.

[21] S. Kisaka and S. J. Tanaka, "Efficiency of Synchrotron Radiation from Rotation-Powered Pulsars," *Astrophys. J.*, vol. 837, no. 1, p. 76, 2017. arXiv: 1702.03365 [astro-ph.HE].

[22] L. Zhang and K. S. Cheng, "The gamma-ray conversion efficiency of rotation-powered pulsars," *mnras*, vol. 294, p. 177, Feb. 1998.

[23] R. N. Manchester, G. B. Hobbs, A. Teoh, and M. Hobbs, "The Australia Telescope National Facility Pulsar Catalogue," *aj*, vol. 129, no. 4, pp. 1993–2006, Apr. 2005. arXiv: astro-ph/0412641 [astro-ph].

[24] M. Pitkin, "psrqpy: a python interface for querying the ATNF pulsar catalogue," *Journal of Open Source Software*, vol. 3, no. 22, p. 538, Feb. 2018.

[25] K. P. Watters, R. W. Romani, P. Weltevrede, and S. Johnston, "An atlas for interpreting gamma-ray pulsar light curves," *The Astrophysical Journal*, vol. 695, no. 2, pp. 1289–1301, 2009.

[26] R. Zanin, "The Crab pulsar at VHE," in *European Physical Journal Web of Conferences*, ser. European Physical Journal Web of Conferences, vol. 136, 2017, p. 03 003. arXiv: 1701.07364 [astro-ph.HE].

[27] Pierbattista, M., Harding, A. K., Grenier, I. A., Johnson, T. J., Caraveo, P. A., Kerr, M., and Gonthier, P. L., "Light-curve modelling constraints on the obliquities and aspect angles of the young fermi pulsars," *A&A*, vol. 575, A3, 2015.

[28] M. Lyutikov, N. Otte, and A. McCann, "THE VERY HIGH ENERGY EMISSION FROM PULSARS: A CASE FOR INVERSE COMPTON SCATTERING," *The Astrophysical Journal*, vol. 754, no. 1, p. 33, 2012.

[29] A. K. Harding and C. Kalapotharakos, "SYNCHROTRON SELF-COMPTON EMISSION FROM THE CRAB AND OTHER PULSARS," *The Astrophysical Journal*, vol. 811, no. 1, p. 63, 2015.

[30] A. K. Harding and D. Lai, "Physics of strongly magnetized neutron stars," *Reports on Progress in Physics*, vol. 69, no. 9, pp. 2631–2708, Sep. 2006. arXiv: astro-ph/0606674 [astro-ph].

[31] D. Lai, "Physics in Very Strong Magnetic Fields," *ssr*, vol. 191, no. 1-4, pp. 13–25, Oct. 2015. arXiv: 1411.7995 [astro-ph.HE].

[32] A. K. Harding, C. Venter, and C. Kalapotharakos, "Very-high-energy emission from pulsars," *The Astrophysical Journal*, vol. 923, no. 2, p. 194, 2021.

[33] A. McCann, "Discovery of emission above 100 GeV from the crab pulsar with VERITAS," PhD thesis, McGill U., 2012.

[34] J. K. Daugherty and J. Ventura, "Absorption of radiation by electrons in intense magnetic fields," *Phys. Rev. D*, vol. 18, pp. 1053–1067, 4 1978.

[35] Y. E. Lyubarskii and S. A. Petrova, "Synchrotron absorption in pulsar magnetospheres," *aap*, vol. 337, pp. 433–440, Sep. 1998.

[36] G. T. Richards, "A search for very high-energy gamma-ray emission from pulsars with VERITAS," PhD thesis, Georgia Institute of Technology, 2017.

[37] L. D. Landau and E. M. Lifshitz, *The classical theory of fields*. 1975.

[38] A. K. Harding, V. V. Usov, and A. G. Muslimov, "High-Energy Emission from Millisecond Pulsars," *apj*, vol. 622, no. 1, pp. 531–543, Mar. 2005. arXiv: astro-ph/0411805 [astro-ph].

[39] A. K. Harding, M. E. DeCesar, M. C. Miller, C. Kalapotharakos, and I. Contopoulos, "Gamma-Ray Pulsar Light Curves in Vacuum and Force-Free Geometry," *arXiv e-prints*, arXiv:1111.0828, arXiv:1111.0828, Nov. 2011. arXiv: 1111.0828 [astro-ph.HE].

[40] P. Goldreich and W. H. Julian, "Pulsar Electrodynamics," *apj*, vol. 157, p. 869, Aug. 1969.

[41] G. Brambilla, C. Kalapotharakos, A. N. Timokhin, A. K. Harding, and D. Kazanas, "Electron–positron pair flow and current composition in the pulsar magnetosphere," *The Astrophysical Journal*, vol. 858, no. 2, p. 81, 2018.

[42] J. Pétri, "Theory of pulsar magnetosphere and wind," *Journal of Plasma Physics*, vol. 82, no. 5, 635820502, p. 635 820 502, Oct. 2016. arXiv: 1608.04895 [astro-ph.HE].

[43] J. Pétri, "Multipolar electromagnetic fields around neutron stars: exact vacuum solutions and related properties," *mnras*, vol. 450, no. 1, pp. 714–742, Jun. 2015. arXiv: 1503.05307 [astro-ph.HE].

[44] P. M. Bellan, *Fundamentals of plasma physics*. Cambridge university press, 2008.

[45] B. Cerutti, A. A. Philippov, and A. Spitkovsky, "Modelling high-energy pulsar light curves from first principles," *mnras*, vol. 457, no. 3, pp. 2401–2414, Apr. 2016. arXiv: 1511.01785 [astro-ph.HE].

[46] C. Kalapotharakos, D. Kazanas, A. Harding, and I. Contopoulos, "Toward a Realistic Pulsar Magnetosphere," *apj*, vol. 749, no. 1, 2, p. 2, Apr. 2012. arXiv: 1108.2138 [astro-ph.SR].

[47] R. W. Romani and I. A. Yadigaroglu, "Gamma-Ray Pulsars: Emission Zones and Viewing Geometries," *apj*, vol. 438, p. 314, Jan. 1995. arXiv: astro-ph/9401045 [astro-ph].

[48] T. I. Rajib, S. Sultana, and A. A. Mamun, "Solitary waves in rotational pulsar magnetosphere," *apss*, vol. 357, no. 1, 52, p. 52, May 2015.

[49] C. F. Kennel, F. S. Fujimura, and R. Pellat, "Pulsar Magnetospheres," *ssr*, vol. 24, no. 4, pp. 407–436, Dec. 1979.

[50] V. S. Beskin, "Mhd flows in compact astrophysical objects: Accretion, winds and jets," 2009.

[51] H. Herold, T. Ertl, and H. Ruder, "Generation of relativistic particles in pulsar magnetospheres," *Mitteilungen der Astronomischen Gesellschaft Hamburg*, vol. 63, p. 174, Jan. 1985.

[52] A. Gruzinov, "Electrodynamics of Massless Charges with Application to Pulsars," *arXiv e-prints*, arXiv:1205.3367, arXiv:1205.3367, May 2012. arXiv: 1205.3367 [astro-ph.HE].

[53] L. Mestel, "Stellar magnetism.," *Int. Ser. Monogr. Phys*, vol. 99, Jan. 1999.

[54] C. Canuto, M. Hussaini, A. Quarteroni, and T. Zang, *Spectral Methods: Fundamentals in Single Domains*, ser. Scientific Computation. Springer Berlin Heidelberg, 2007, ISBN: 9783540307266.

[55] A. A. Vlasov, "Reviews of Topical Problems: the Vibrational Properties of AN Electron Gas," *Soviet Physics Uspekhi*, vol. 10, no. 6, pp. 721–733, Jun. 1968.

[56] Y. Elskens and M. K. H. Kiessling, "Microscopic Foundations of Kinetic Plasma Theory: The Relativistic Vlasov-Maxwell Equations and Their Radiation-Reaction-Corrected Generalization," *Journal of Statistical Physics*, vol. 180, no. 1-6, pp. 749–772, Mar. 2020. arXiv: 1910.11951 [physics.plasm-ph].

[57] "GAMMA-RAY LIGHT CURVES FROM PULSAR MAGNETOSPHERES WITH FINITE CONDUCTIVITY," *The Astrophysical Journal*, vol. 754, no. 1, p. L1, 2012.

[58] A. Tchekhovskoy, A. Spitkovsky, and J. G. Li, "Time-dependent 3D magneto-hydrodynamic pulsar magnetospheres: oblique rotators," *Monthly Notices of the Royal Astronomical Society: Letters*, vol. 435, no. 1, pp. L1–L5, Aug. 2013. eprint: https://academic.oup.com/mnrasl/article-pdf/435/1/L1/3823710/slt076.pdf.

[59] C. Birdsall and A. Langdon, *Plasma Physics via Computer Simulation*, ser. Series in Plasma Physics and Fluid Dynamics. Taylor & Francis, 2004, ISBN: 9780750310253.

[60] T. Wada and S. Shibata, "A particle simulation for the global pulsar magnetosphere: the pulsar wind linked to the outer gaps," *mnras*, vol. 376, no. 4, pp. 1460–1464, Apr. 2007. arXiv: astro-ph/0701128 [astro-ph].

[61] T. Wada and S. Shibata, "A particle simulation for the global pulsar magnetosphere – II. The case of dipole field," *Monthly Notices of the Royal Astronomical Society*, vol. 418, no. 1, pp. 612–624, Nov. 2011. eprint: https://academic.oup.com/mnras/article-pdf/418/1/612/2914598/mnras0418-0612.pdf.

[62] M. A. Belyaev, "Dissipation, energy transfer, and spin-down luminosity in 2.5D PIC simulations of the pulsar magnetosphere," *Monthly Notices of the Royal Astronomical Society*, vol. 449, no. 3, pp. 2759–2767, Apr. 2015. eprint: https://academic.oup.com/mnras/article-pdf/449/3/2759/9386867/stv468.pdf.

[63] B. Cerutti, A. A. Philippov, and A. Spitkovsky, "Modelling high-energy pulsar light curves from first principles," *Monthly Notices of the Royal Astronomical Society*, vol. 457, no. 3, pp. 2401–2414, Feb. 2016. eprint: https://academic.oup.com/mnras/article-pdf/457/3/2401/8000820/stw124.pdf.

[64] A. K. Harding, "The Emission Physics of Millisecond Pulsars," *arXiv e-prints*, arXiv:2101.05751, arXiv:2101.05751, Jan. 2021. arXiv: 2101.05751 [astro-ph.HE].

[65] C. Guépin, B. Cerutti, and K. Kotera, "Proton acceleration in pulsar magnetospheres," *aap*, vol. 635, A138, A138, Mar. 2020. arXiv: 1910.11387 [astro-ph.HE].

[66] D. A. Uzdensky, "On the axisymmetric force-free pulsar magnetosphere," *The Astrophysical Journal*, vol. 598, no. 1, p. 446, 2003.

[67] C. Kalapotharakos, G. Brambilla, A. Timokhin, A. K. Harding, and D. Kazanas, "Three-dimensional Kinetic Pulsar Magnetosphere Models: Connecting to Gamma-

Ray Observations," *apj*, vol. 857, no. 1, 44, p. 44, Apr. 2018. arXiv: 1710.03170 [astro-ph.HE].

[68] A. A. Philippov and A. Spitkovsky, "Ab-initio Pulsar Magnetosphere: Particle Acceleration in Oblique Rotators and High-energy Emission Modeling," *apj*, vol. 855, no. 2, 94, p. 94, Mar. 2018. arXiv: 1707.04323 [astro-ph.HE].

[69] B. Cerutti, A. Philippov, K. Parfrey, and A. Spitkovsky, "Particle acceleration in axisymmetric pulsar current sheets," *mnras*, vol. 448, no. 1, pp. 606–619, Mar. 2015. arXiv: 1410.3757 [astro-ph.HE].

[70] B. Cerutti and A. M. Beloborodov, "Electrodynamics of Pulsar Magnetospheres," *ssr*, vol. 207, no. 1-4, pp. 111–136, Jul. 2017. arXiv: 1611.04331 [astro-ph.HE].

[71] F. V. Coroniti, "Magnetically Striped Relativistic Magnetohydrodynamic Winds: The Crab Nebula Revisited," *apj*, vol. 349, p. 538, Feb. 1990.

[72] D. A. Uzdensky and A. Spitkovsky, "Physical Conditions in the Reconnection Layer in Pulsar Magnetospheres," *apj*, vol. 780, no. 1, 3, p. 3, Jan. 2014. arXiv: 1210.3346 [astro-ph.HE].

[73] A. Y. Chen and A. M. Beloborodov, "Electrodynamics of Axisymmetric Pulsar Magnetosphere with Electron-Positron Discharge: A Numerical Experiment," *apj*, vol. 795, no. 1, L22, p. L22, Nov. 2014. arXiv: 1406.7834 [astro-ph.HE].

[74] A. A. Philippov, B. Cerutti, A. Tchekhovskoy, and A. Spitkovsky, "Ab Initio Pulsar Magnetosphere: The Role of General Relativity," *apj*, vol. 815, no. 2, L19, p. L19, Dec. 2015. arXiv: 1510.01734 [astro-ph.HE].

[75] I. Mochol and J. Petri, "Very high energy emission as a probe of relativistic magnetic reconnection in pulsar winds.," *mnras*, vol. 449, pp. L51–L55, Apr. 2015. arXiv: 1501.07123 [astro-ph.HE].

[76] J. G. Kirk, O. Skjæraasen, and Y. A. Gallant, "Pulsed radiation from neutron star winds," *aap*, vol. 388, pp. L29–L32, Jun. 2002. arXiv: astro-ph/0204302 [astro-ph].

[77] A. K. Harding, C. Kalapotharakos, M. Barnard, and C. Venter, "Multi-TeV emission from the vela pulsar," *The Astrophysical Journal*, vol. 869, no. 1, p. L18, 2018.

[78] D. B. Melrose and R. Yuen, "Non-corotating models for pulsar magnetospheres," *Monthly Notices of the Royal Astronomical Society*, vol. 437, no. 1, pp. 262–272, 2014.

[79] F. C. Michel, "Vacuum gaps in pulsar magnetospheres.," *apj*, vol. 227, pp. 579–589, Jan. 1979.

[80] J. M. Cohen and E. T. Toton, "Rotating magnetic neutron stars in general relativity," *Annals of Physics*, vol. 87, pp. 244–260, 1974.

[81] J. M. Cohen and M. W. Kearney, "Neutron Star Electrodynamics in Curved Space," *apss*, vol. 70, no. 2, pp. 295–328, Jul. 1980.

[82] V. L. Ginzburg and S. I. Syrovatskii, "Cosmic Magnetobremsstrahlung (synchrotron Radiation)," *araa*, vol. 3, p. 297, Jan. 1965.

[83] J. L. Anderson and J. M. Cohen, "Gravitational Collapse of Magnetic Neutron Stars," *apss*, vol. 9, no. 1, pp. 146–152, Oct. 1970.

[84] M. Lyutikov, "Electromagnetic power of merging and collapsing compact objects," *Phys. Rev. D*, vol. 83, p. 124 035, 12 2011.

[85] A. G. Muslimov and A. I. Tsygan, "General relativistic electric potential drops above pulsar polar caps," *mnras*, vol. 255, pp. 61–70, Mar. 1992.

[86] S. Sengupta, "General Relativistic Effects on the Induced Electric Field Exterior to Pulsars," *apj*, vol. 449, p. 224, Aug. 1995. arXiv: gr-qc/9503031 [gr-qc].

[87] P. L. Gonthier and A. K. Harding, "General Relativistic Corrections in the Gamma-Ray Emission from Pulsars," *apj*, vol. 425, p. 767, Apr. 1994.

[88] M. A. Belyaev and K. Parfrey, "SPATIAL DISTRIBUTION OF PAIR PRODUCTION OVER THE PULSAR POLAR CAP," *The Astrophysical Journal*, vol. 830, no. 2, p. 119, 2016.

[89] J. M. Cohen and A. Rosenblum, "Pulsar Magnetosphere," *apss*, vol. 16, no. 1, pp. 130–136, Apr. 1972.

[90] W. J. Roberts, "Electromagnetic multipole fields of neutron stars.," *apjs*, vol. 41, pp. 75–86, Sep. 1979.

[91] S. E. Gralla, A. Lupsasca, and A. Philippov, "Inclined Pulsar Magnetospheres in General Relativity: Polar Caps for the Dipole, Quadrudipole, and Beyond," *apj*, vol. 851, no. 2, 137, p. 137, Dec. 2017. arXiv: 1704.05062 [astro-ph.HE].

[92] A. K. Harding and A. G. Muslimov, "Pulsar Pair Cascades in a Distorted Magnetic Dipole Field," *apj*, vol. 726, no. 1, L10, p. L10, Jan. 2011. arXiv: 1012.0451 [astro-ph.HE].

[93] C. Kalapotharakos, Z. Wadiasingh, A. K. Harding, and D. Kazanas, "The multipolar magnetic field of the millisecond pulsar PSR j0030+0451," *The Astrophysical Journal*, vol. 907, no. 2, p. 63, 2021.

[94] J. H. Krolik, "Multipolar Magnetic Fields in Neutron Stars," *apj*, vol. 373, p. L69, Jun. 1991.

[95] L. Arzamasskiy, A. Philippov, and A. Tchekhovskoy, "Evolution of non-spherical pulsars with plasma-filled magnetospheres," *mnras*, vol. 453, no. 4, pp. 3540–3553, Nov. 2015. arXiv: 1504.06626 [astro-ph.HE].

[96] B. Zhang, A. K. Harding, and A. G. Muslimov, "Radio Pulsar Death Line Revisited: Is PSR J2144-3933 Anomalous?" *apj*, vol. 531, no. 2, pp. L135–L138, Mar. 2000. arXiv: astro-ph/0001341 [astro-ph].

[97] J. Gil and D. Mitra, "Vacuum Gaps in Pulsars and PSR J2144-3933," *apj*, vol. 550, no. 1, pp. 383–391, Mar. 2001. arXiv: astro-ph/0010603 [astro-ph].

[98] J. A. Gil, G. I. Melikidze, and D. Mitra, "Modelling of the surface magnetic field in neutron stars: Application to radio pulsars," *Astronomy & Astrophysics*, vol. 388, no. 1, pp. 235–245, 2002.

[99] A. K. Harding, "Physics in Ultra-Strong Magnetic Fields," *arXiv e-prints*, arXiv:2202.06845, arXiv:2202.06845, Feb. 2022. arXiv: 2202.06845 [astro-ph.HE].

[100] J. S. Heyl and L. Hernquist, "QED one loop corrections to a macroscopic magnetic dipole," *J. Phys. A*, vol. 30, pp. 6475–6483, 1997. arXiv: hep-ph/9705368.

[101] J Pétri, "Strongly magnetized rotating dipole in general relativity," *arXiv: High Energy Astrophysical Phenomena*, 2016.

[102] M. Freytsis and S. E. Gralla, "QED Plasma and Magnetars," *JCAP*, vol. 05, p. 042, 2016. arXiv: 1503.03867 [astro-ph.HE].

[103] A. J. Deutsch, "The electromagnetic field of an idealized star in rigid rotation in vacuo," *Annales d'Astrophysique*, vol. 18, p. 1, Jan. 1955.

[104] A. Spitkovsky, "Time-dependent Force-free Pulsar Magnetospheres: Axisymmetric and Oblique Rotators," *apj*, vol. 648, no. 1, pp. L51–L54, Sep. 2006. arXiv: astro-ph/0603147 [astro-ph].

[105] F. PACINI, "Rotating neutron stars, pulsars and supernova remnants," *Nature*, vol. 219, no. 5150, pp. 145–146, 1968.

[106] P. Sturrock, "Pulsar radiation mechanisms," *Nature*, vol. 227, no. 5257, pp. 465–470, 1970.

[107] P. A. Sturrock, "A Model of Pulsars," *apj*, vol. 164, p. 529, Mar. 1971.

[108] M. A. Ruderman and P. G. Sutherland, "Theory of pulsars: polar gaps, sparks, and coherent microwave radiation.," *apj*, vol. 196, pp. 51–72, Feb. 1975.

[109] A. N. Timokhin and A. K. Harding, "On the Maximum Pair Multiplicity of Pulsar Cascades," *apj*, vol. 871, no. 1, 12, p. 12, Jan. 2019. arXiv: 1803.08924 [astro-ph.HE].

[110] B. Zhang, G. J. Qiao, and J. L. Han, "Inverse Compton Scattering: Gap Parameters, Energy Loss of the Particles, and Possible Implications for Pulsar Radio Emission," *apj*, vol. 491, no. 2, pp. 891–902, Dec. 1997.

[111] T. ERBER, "High-energy electromagnetic conversion processes in intense magnetic fields," *Rev. Mod. Phys.*, vol. 38, pp. 626–659, 4 1966.

[112] J. Takata, S. Shibata, and K. Hirotani, "A pulsar outer gap model with trans-field structure," *mnras*, vol. 354, no. 4, pp. 1120–1132, Nov. 2004. arXiv: astro-ph/0408044 [astro-ph].

[113] S. Shibata, "Magnetosphere of the Rotation-powered Pulsar: A DC Circuit Model," *apj*, vol. 378, p. 239, Sep. 1991.

[114] ——, "The field-aligned accelerator in the pulsar magnetosphere," *mnras*, vol. 287, no. 2, pp. 262–270, May 1997.

[115] N. J. Holloway, "P-N Junctions in Pulsar Magnetospheres ?" *Nature Physical Science*, vol. 246, no. 149, pp. 6–9, Nov. 1973.

[116] F. C. Michel, "Rotating Magnetosphere: Acceleration of Plasma from the Surface," *apj*, vol. 192, pp. 713–718, Sep. 1974.

[117] J. Arons, "Pair creation above pulsar polar caps - Steady flow in the surface acceleration zone and polar CAP X-ray emission," *apj*, vol. 248, pp. 1099–1116, Sep. 1981.

[118] V. S. Beskin, "General Relativity Effects on Electrodynamic Processes in Radio Pulsars," *Soviet Astronomy Letters*, vol. 16, p. 286, Jul. 1990.

[119] J. Arons, "Pair creation above pulsar polar caps : geometrical structure and energetics of slot gaps.," *apj*, vol. 266, pp. 215–241, Mar. 1983.

[120] J. Dyks and B. Rudak, "Two-Pole Caustic Model for High-Energy Light Curves of Pulsars," *apj*, vol. 598, no. 2, pp. 1201–1206, Dec. 2003. arXiv: astro-ph/0303006 [astro-ph].

[121] A. G. Muslimov and A. K. Harding, "High-altitude particle acceleration and radiation in pulsar slot gaps," *The Astrophysical Journal*, vol. 606, no. 2, pp. 1143–1153, 2004.

[122] K. Hirotani, "Outer-gap versus slot-gap models for pulsar high-energy emissions: The case of the crab pulsar," *The Astrophysical Journal*, vol. 688, no. 1, pp. L25–L28, 2008.

[123] K. S. Cheng, C. Ho, and M. Ruderman, "Energetic Radiation from Rapidly Spinning Pulsars. I. Outer Magnetosphere Gaps," *apj*, vol. 300, p. 500, Jan. 1986.

[124] A. R. Crusius-Watzel, T. Kunzl, and H. Lesch, "Synchrotron Model for the Infrared, Optical, and X-Ray Emission of the Crab Pulsar," *apj*, vol. 546, no. 1, pp. 401–405, Jan. 2001. arXiv: astro-ph/0009324 [astro-ph].

[125] K. Hirotani, "High Energy Emission from Rotation-Powered Pulsars: Outer-gap vs. Slot-gap Models," *arXiv e-prints*, arXiv:0809.1283, arXiv:0809.1283, Sep. 2008. arXiv: 0809.1283 [astro-ph].

[126] B. Rudak and J. Dyks, "Multiwavelength modeling of the Vela pulsar pulses - from Optical light to VHE gamma-rays," in *Proceedings of the 7th International Fermi Symposium*, Oct. 2017, p. 15.

[127] A. A. Abdo, M. Ackermann, W. B. Atwood, R. Bagagli, L. Baldini, J. Ballet, D. L. Band, G. Barbiellini, M. G. Baring, J. Bartelt, D. Bastieri, B. M. Baughman, K. Bechtol, F. Bellardi, R. Bellazzini, B. Berenji, D. Bisello, R. D. Blandford, E. D. Bloom, J. R. Bogart, E. Bonamente, A. W. Borgland, A. Bouvier, J. Bregeon, A. Brez, M. Brigida, P. Bruel, T. H. Burnett, G. A. Caliandro, R. A. Cameron, F. Camilo, P. A. Caraveo, J. M. Casandjian, M. Ceccanti, C. Cecchi, E. Charles, A. Chekhtman, C. C. Cheung, J. Chiang, S. Ciprini, R. Claus, I. Cognard, J. Cohen-Tanugi, L. R. Cominsky, J. Conrad, R. Corbet, L. Corucci, S. Cutini, D. S. Davis, M. DeKlotz, C. D. Dermer, A. de Angelis, F. de Palma, S. W. Digel, M. Dormody, E. d. C. e. Silva, P. S. Drell, R. Dubois, D. Dumora, C. Espinoza, C. Farnier, C. Favuzzi, D. L. Flath, P. Fleury, W. B. Focke, M. Frailis, P. C. C. Freire, Y. Fukazawa, S. Funk, P. Fusco, F. Gargano, D. Gasparrini, N. Gehrels, S. Germani, R. Giannitrapani, B. Giebels, N. Giglietto, F. Giordano, T. Glanzman, G. Godfrey, E. V. Gotthelf, I. A. Grenier, M. H. Grondin, J. E. Grove, L. Guillemot, S. Guiriec, G. Haller, A. K. Harding, P. A. Hart, R. C. Hartman, E. Hays, G. Hobbs, R. E. Hughes, G. Jóhannesson, A. S. Johnson, R. P. Johnson, T. J. Johnson, W. N. Johnson, S. Johnston, T. Kamae, G. Kanbach, V. M. Kaspi, H. Katagiri, J. Kataoka, A. Kavelaars, N. Kawai, H. Kelly, M. Kerr, B. Kiziltan, W. Klamra, J. Knodlseder,

M. Kramer, F. Kuehn, M. Kuss, J. Lande, D. Landriu, L. Latronico, B. Lee, S. H. Lee, M. Lemoine-Goumard, M. Livingstone, F. Longo, F. Loparco, B. Lott, M. N. Lovellette, P. Lubrano, A. G. Lyne, G. M. Madejski, A. Makeev, R. N. Manchester, B. Marangelli, M. Marelli, M. N. Mazziotta, J. E. McEnery, S. McGlynn, M. A. McLaughlin, N. Menon, C. Meurer, P. F. Michelson, T. Mineo, N. Mirizzi, W. Mitthumsiri, T. Mizuno, A. A. Moiseev, M. Mongelli, C. Monte, M. E. Monzani, E. Moretti, A. Morselli, I. V. Moskalenko, S. Murgia, T. Nakamori, P. L. Nolan, A. Noutsos, E. Nuss, T. Ohsugi, N. Omodei, E. Orlando, J. F. Ormes, M. Ozaki, A. Paccagnella, D. Paneque, J. H. Panetta, D. Parent, M. Pearce, M. Pepe, M. Perchiazzi, M. Pesce-Rollins, L. Pieri, M. Pinchera, F. Piron, T. A. Porter, S. Rainò, R. Rando, S. M. Ransom, E. Rapposelli, M. Razzano, A. Reimer, O. Reimer, T. Reposeur, L. C. Reyes, S. Ritz, L. S. Rochester, A. Y. Rodriguez, R. W. Romani, M. Roth, F. Ryde, A. Sacchetti, H. F. W. Sadrozinski, N. Saggini, D. Sanchez, A. Sander, P. M. S. Parkinson, K. N. Segal, A. Sellerholm, C. Sgrò, E. J. Siskind, D. A. Smith, P. D. Smith, G. Spandre, P. Spinelli, M. Stamatikos, J. L. Starck, F. W. Stecker, T. E. Stephens, M. S. Strickman, A. W. Strong, D. J. Suson, H. Tajima, H. Takahashi, T. Takahashi, T. Tanaka, A. Tenze, J. B. Thayer, J. G. Thayer, G. Theureau, D. J. Thompson, S. E. Thorsett, L. Tibaldo, O. Tibolla, D. F. Torres, A. Tramacere, M. Turri, T. L. Usher, L. Vigiani, N. Vilchez, V. Vitale, A. P. Waite, P. Wang, K. Watters, P. Weltevrede, B. L. Winer, K. S. Wood, T. Ylinen, and M. Ziegler, "Fermi Large Area Telescope Observations of the Vela Pulsar," *apj*, vol. 696, no. 2, pp. 1084–1093, May 2009. arXiv: `0812.2960 [astro-ph]`.

[128] N. Chkheidze, G. Machabeli, and Z. Osmanov, "ON THE VERY HIGH ENERGY SPECTRUM OF THE CRAB PULSAR," *The Astrophysical Journal*, vol. 730, no. 2, p. 62, 2011.

[129] F. A. Aharonian, S. V. Bogovalov, and D. Khangulyan, "Abrupt acceleration of a 'cold' ultrarelativistic wind from the Crab pulsar," *nat*, vol. 482, no. 7386, pp. 507–509, Feb. 2012.

[130] G. J. Qiao, K. J. Lee, H. G. Wang, R. X. Xu, and J. L. Han, "The Inner Annular Gap for Pulsar Radiation: γ-Ray and Radio Emission," *apj*, vol. 606, no. 1, pp. L49–L52, May 2004. arXiv: `astro-ph/0403398 [astro-ph]`.

[131] M. Lyutikov, "Inverse Compton model of pulsar high-energy emission," *Monthly Notices of the Royal Astronomical Society*, vol. 431, no. 3, pp. 2580–2589, Mar. 2013. eprint: `https://academic.oup.com/mnras/article-pdf/431/3/2580/4922395/stt351.pdf`.

[132] A. Bhadra and R. K. Dey, "TeV neutrinos and gamma-rays from pulsars," *Monthly Notices of the Royal Astronomical Society*, vol. 395, no. 3, pp. 1371–1375, May 2009. eprint: `https://academic.oup.com/mnras/article-pdf/395/3/1371/18234216/mnras0395-1371.pdf`.

[133] T. Lin, "Measurement of the bethe-heitler cross section in the tev regime and search for lorentz invariance violation with veritas," PhD thesis, McGill U, 2020.

[134] C. Kalapotharakos, A. K. Harding, D. Kazanas, and Z. Wadiasingh, "A Fundamental Plane for Gamma-Ray Pulsars," *apj*, vol. 883, no. 1, L4, p. L4, Sep. 2019. arXiv: 1904.01765 [astro-ph.HE].

[135] H. Ploeg, C. Gordon, R. Crocker, and O. Macias, "Comparing the galactic bulge and galactic disk millisecond pulsars," *jcap*, vol. 2020, no. 12, 035, p. 035, Dec. 2020. arXiv: 2008.10821 [astro-ph.HE].

[136] J. Rayimbaev, B. Ahmedov, N. Juraeva, and A. Rakhmatov, "Plasma magnetosphere of deformed magnetized neutron star," *Astrophysics and Space Science*, vol. 356, Dec. 2014.

[137] J. Takata, S. Shibata, K. Hirotani, and H. K. Chang, "A two-dimensional electrodynamical outer gap model for γ-ray pulsars: γ-ray spectrum," *mnras*, vol. 366, no. 4, pp. 1310–1328, Mar. 2006. arXiv: astro-ph/0511690 [astro-ph].

[138] A. Zangwill, *Modern Electrodynamics*, ser. Modern Electrodynamics. Cambridge University Press, 2013, ISBN: 9780521896979.

[139] H. J. Völk and K. Bernlöhr, "Imaging very high energy gamma-ray telescopes," *Experimental Astronomy*, vol. 25, no. 1-3, 173–191, 2009.

[140] T. C. Weekes *et al.*, "VERITAS: The Very energetic radiation imaging telescope array system," *Astropart. Phys.*, vol. 17, pp. 221–243, 2002. arXiv: astro-ph/0108478 [astro-ph].

[141] J. Holder *et al.*, "The first VERITAS telescope," *Astropart. Phys.*, vol. 25, pp. 391–401, 2006. arXiv: astro-ph/0604119 [astro-ph].

[142] N. Park and VERITAS Collaboration, "Performance of the VERITAS experiment," in *34th International Cosmic Ray Conference (ICRC2015)*, vol. 34, 2015, p. 771. arXiv: 1508.07070 [astro-ph.IM].

[143] J. S. Perkins, G. Maier, and The VERITAS Collaboration, "VERITAS Telescope 1 Relocation: Details and Improvements," *arXiv e-prints*, arXiv:0912.3841, arXiv:0912.3841, Dec. 2009. arXiv: 0912.3841 [astro-ph.IM].

[144] J. M. Davies and E. S. Cotton, "Design of the quartermaster solar furnace," *Solar Energy*, vol. 1, no. 2, pp. 16–22, 1957.

[145] E. Roache, R. Irvin, J. S. Perkins, K. Harris, A. Falcone, J. Finley, and T. Weeks, "Mirror Facets for the VERITAS Telescopes," in *International Cosmic Ray Con-*

ference, ser. International Cosmic Ray Conference, vol. 3, Jan. 2008, pp. 1397–1400.

[146] J. M. Davies and E. S. Cotton, "Design of the quartermaster solar furnace," *Solar Energy*, vol. 1, no. 2-3, pp. 16–22, Apr. 1957.

[147] B. Zitzer and VERITAS Collaboration, "The VERITAS Upgraded Telescope-Level Trigger Systems: Technical Details and Performance Characterization," in *International Cosmic Ray Conference*, ser. International Cosmic Ray Conference, vol. 33, Jan. 2013, p. 3076. arXiv: 1307.8360 [astro-ph.IM].

[148] J. Prescott, "A statistical model for photomultiplier single-electron statistics," *Nuclear Instruments and Methods*, vol. 39, no. 1, pp. 173–179, 1966.

[149] P. B. Coates, "The edge effect in electron multiplier statistics," *Journal of Physics D Applied Physics*, vol. 3, no. 8, pp. 1290–1296, Aug. 1970.

[150] B. López Paredes, H. Araújo, F. Froborg, N. Marangou, I. Olcina, T. Sumner, R. Taylor, A. Tomás, and A. Vacheret, "Response of photomultiplier tubes to xenon scintillation light," *Astroparticle Physics*, vol. 102, 56–66, 2018.

[151] F. Neves, V. Chepel, D. Akimov, H. Araújo, E. Barnes, V. Belov, A. Burenkov, A. Currie, B. Edwards, C. Ghag, M. Horn, A. Hughes, G. Kalmus, A. Kobyakin, A. Kovalenko, V. Lebedenko, A. Lindote, M. Lopes, R. Lüscher, K. Lyons, P. Majewski, A. Murphy, J. Pinto da Cunha, R. Preece, J. Quenby, P. Scovell, C. Silva, V. Solovov, N. Smith, P. Smith, V. Stekhanov, T. Sumner, C. Thorne, and R. Walker, "Calibration of photomultiplier arrays," *Astroparticle Physics*, vol. 33, no. 1, pp. 13–18, 2010.

[152] P. A. Amaudruz *et al.*, "In-situ characterization of the Hamamatsu R5912-HQE photomultiplier tubes used in the DEAP-3600 experiment," *Nucl. Instrum. Meth. A*, vol. 922, pp. 373–384, 2019. arXiv: 1705.10183 [physics.ins-det].

[153] M. Nievas Rosillo, C. Adams, A. Archer, W. Benbow, A. Brill, J. H. Buckley, M. Capasso, J. Christiansen, A. J. Chromey, M. Errando, A. Falcone, K. A. Farrell, Q. Feng, G. M. Foote, L. Fortson, A. Furniss, A. Gent, G. H. Gillanders, C. Giuri, O. Gueta, D. Hanna, O. Hervet, J. Holder, B. Hona, T. B. Humensky, W. Jin, P. Kaaret, M. Kertzman, D. Kieda, T. K. Kleiner, S. Kumar, M. Lang, M. Lundy, G. Maier, C. E. McGrath, P. Moriarty, R. Mukherjee, D. Nieto, S. O'Brien, R. A. Ong, A. Otte, S. R. Patel, S. R. Patel, K. Pfrang, M. Pohl, R. Prado, E. Pueschel, J. Quinn, K. Ragan, P. T. Reynolds, D. Ribeiro, E. Roache, J. A. Ryan, I. Sadeh, M. Santander, G. H. Sembroski, R. Shang, D. Tak, V. Vassiliev, A. Weinstein, D. A. Williams, and T. J. Williamson, "The throughput calibration of the VERITAS telescopes," *PoS*, vol. ICRC2021, p. 721, 2021.

[154] S. Abdollahi, F. Acero, M. Ackermann, M. Ajello, W. B. Atwood, M. Axelsson, L. Baldini, J. Ballet, G. Barbiellini, D. Bastieri, J. B. Gonzalez, R. Bellazzini, A. Berretta, E. Bissaldi, R. D. Blandford, E. D. Bloom, R. Bonino, E. Bottacini, T. J. Brandt, J. Bregeon, P. Bruel, R. Buehler, T. H. Burnett, S. Buson, R. A. Cameron, R. Caputo, P. A. Caraveo, J. M. Casandjian, D. Castro, E. Cavazzuti, E. Charles, S. Chaty, S. Chen, C. C. Cheung, G. Chiaro, S. Ciprini, J. Cohen-Tanugi, L. R. Cominsky, J. Coronado-Blázquez, D. Costantin, A. Cuoco, S. Cutini, F. D'Ammando, M. DeKlotz, P. de la Torre Luque, F. de Palma, A. Desai, S. W. Digel, N. D. Lalla, M. D. Mauro, L. D. Venere, A. Domínguez, D. Dumora, F. F. Dirirsa, S. J. Fegan, E. C. Ferrara, A. Franckowiak, Y. Fukazawa, S. Funk, P. Fusco, F. Gargano, D. Gasparrini, N. Giglietto, P. Giommi, F. Giordano, M. Giroletti, T. Glanzman, D. Green, I. A. Grenier, S. Griffin, M.-H. Grondin, J. E. Grove, S. Guiriec, A. K. Harding, K. Hayashi, E. Hays, J. W. Hewitt, D. Horan, G. Jóhannesson, T. J. Johnson, T. Kamae, M. Kerr, D. Kocevski, M. Kovac'evic', M. Kuss, D. Landriu, S. Larsson, L. Latronico, M. Lemoine-Goumard, J. Li, I. Liodakis, F. Longo, F. Loparco, B. Lott, M. N. Lovellette, P. Lubrano, G. M. Madejski, S. Maldera, D. Malyshev, A. Manfreda, E. J. Marchesini, L. Marcotulli, G. Martí-Devesa, P. Martin, F. Massaro, M. N. Mazziotta, J. E. McEnery, I. Mereu, M. Meyer, P. F. Michelson, N. Mirabal, T. Mizuno, M. E. Monzani, A. Morselli, I. V. Moskalenko, M. Negro, E. Nuss, R. Ojha, N. Omodei, M. Orienti, E. Orlando, J. F. Ormes, M. Palatiello, V. S. Paliya, D. Paneque, Z. Pei, H. Peña-Herazo, J. S. Perkins, M. Persic, M. Pesce-Rollins, V. Petrosian, L. Petrov, F. Piron, H. Poon, T. A. Porter, G. Principe, S. Rainò, R. Rando, M. Razzano, S. Razzaque, A. Reimer, O. Reimer, Q. Remy, T. Reposeur, R. W. Romani, P. M. S. Parkinson, F. K. Schinzel, D. Serini, C. Sgrò, E. J. Siskind, D. A. Smith, G. Spandre, P. Spinelli, A. W. Strong, D. J. Suson, H. Tajima, M. N. Takahashi, D. Tak, J. B. Thayer, D. J. Thompson, L. Tibaldo, D. F. Torres, E. Torresi, J. Valverde, B. V. Klaveren, P. van Zyl, K. Wood, M. Yassine, and G. Zaharijas, "Fermi large area telescope fourth source catalog," *The Astrophysical Journal Supplement Series*, vol. 247, no. 1, p. 33, 2020.

[155] M. Ackermann, M. Ajello, W. B. Atwood, L. Baldini, J. Ballet, G. Barbiellini, D. Bastieri, J. B. Gonzalez, R. Bellazzini, E. Bissaldi, R. D. Blandford, E. D. Bloom, R. Bonino, E. Bottacini, T. J. Brandt, J. Bregeon, P. Bruel, R. Buehler, S. Buson, G. A. Caliandro, R. A. Cameron, R. Caputo, M. Caragiulo, P. A. Caraveo, E. Cavazzuti, C. Cecchi, E. Charles, A. Chekhtman, C. C. Cheung, J. Chiang, G. Chiaro, S. Ciprini, J. M. Cohen, J. Cohen-Tanugi, L. R. Cominsky, J. Conrad, A. Cuoco, S. Cutini, F. D'Ammando, A. de Angelis, F. de Palma, R. Desiante, M. D. Mauro, L. D. Venere, A. Dominguez, P. S. Drell, C. Favuzzi, S. J. Fegan, E. C. Ferrara, W. B. Focke, P. Fortin, A. Franckowiak, Y. Fukazawa, S. Funk, A. K. Furniss, P. Fusco, F. Gargano, D. Gasparrini, N. Giglietto, P. Giommi, F. Giordano, M. Giroletti, T. Glanzman, G. Godfrey, I. A. Grenier, M.-H. Grondin, L. Guillemot, S. Guiriec, A. K. Harding, E. Hays, J. W. Hewitt, A. B. Hill, D. Horan, G. Iafrate, D. Hartmann, T. Jogler, G. Jóhannesson, A. S. Johnson, T. Kamae, J. Kataoka, J. Knödlseder, M. Kuss, G. L. Mura, S. Larsson, L. Latronico, M. Lemoine-Goumard, J. Li, L. Li, F. Longo, F. Loparco, B. Lott, M. N. Lovellette, P. Lubrano, G. M.

Madejski, S. Maldera, A. Manfreda, M. Mayer, M. N. Mazziotta, P. F. Michelson, N. Mirabal, W. Mitthumsiri, T. Mizuno, A. A. Moiseev, M. E. Monzani, A. Morselli, I. V. Moskalenko, S. Murgia, E. Nuss, T. Ohsugi, N. Omodei, M. Orienti, E. Orlando, J. F. Ormes, D. Paneque, J. S. Perkins, M. Pesce-Rollins, V. Petrosian, F. Piron, G. Pivato, T. A. Porter, S. Rainò, R. Rando, M. Razzano, S. Razzaque, A. Reimer, O. Reimer, T. Reposeur, R. W. Romani, M. Sánchez-Conde, P. M. S. Parkinson, J. Schmid, A. Schulz, C. Sgrò, E. J. Siskind, F. Spada, G. Spandre, P. Spinelli, D. J. Suson, H. Tajima, H. Takahashi, M. Takahashi, T. Takahashi, J. B. Thayer, D. J. Thompson, L. Tibaldo, D. F. Torres, G. Tosti, E. Troja, G. Vianello, K. S. Wood, M. Wood, M. Yassine, G. Zaharijas, and S. Zimmer, "2fhl: THE SECOND CATALOG OF HARDFERMI-LAT SOURCES," *The Astrophysical Journal Supplement Series*, vol. 222, no. 1, p. 5, 2016.

[156] W. B. Atwood, A. A. Abdo, M. Ackermann, W. Althouse, B. Anderson, M. Axelsson, L. Baldini, J. Ballet, D. L. Band, G. Barbiellini, J. Bartelt, D. Bastieri, B. M. Baughman, K. Bechtol, D. Bédérède, F. Bellardi, R. Bellazzini, B. Berenji, G. F. Bignami, D. Bisello, E. Bissaldi, R. D. Blandford, E. D. Bloom, J. R. Bogart, E. Bonamente, J. Bonnell, A. W. Borgland, A. Bouvier, J. Bregeon, A. Brez, M. Brigida, P. Bruel, T. H. Burnett, G. Busetto, G. A. Caliandro, R. A. Cameron, P. A. Caraveo, S. Carius, P. Carlson, J. M. Casandjian, E. Cavazzuti, M. Ceccanti, C. Cecchi, E. Charles, A. Chekhtman, C. C. Cheung, J. Chiang, R. Chipaux, A. N. Cillis, S. Ciprini, R. Claus, J. Cohen-Tanugi, S. Condamoor, J. Conrad, R. Corbet, L. Corucci, L. Costamante, S. Cutini, D. S. Davis, D. Decotigny, M. DeKlotz, C. D. Dermer, A. de Angelis, S. W. Digel, E. do Couto e Silva, P. S. Drell, R. Dubois, D. Dumora, Y. Edmonds, D. Fabiani, C. Farnier, C. Favuzzi, D. L. Flath, P. Fleury, W. B. Focke, S. Funk, P. Fusco, F. Gargano, D. Gasparrini, N. Gehrels, F.-X. Gentit, S. Germani, B. Giebels, N. Giglietto, P. Giommi, F. Giordano, T. Glanzman, G. Godfrey, I. A. Grenier, M.-H. Grondin, J. E. Grove, L. Guillemot, S. Guiriec, G. Haller, A. K. Harding, P. A. Hart, E. Hays, S. E. Healey, M. Hirayama, L. Hjalmarsdotter, R. Horn, R. E. Hughes, G. Jóhannesson, G. Johansson, A. S. Johnson, R. P. Johnson, T. J. Johnson, W. N. Johnson, T. Kamae, H. Katagiri, J. Kataoka, A. Kavelaars, N. Kawai, H. Kelly, M. Kerr, W. Klamra, J. Knödlseder, M. L. Kocian, N. Komin, F. Kuehn, M. Kuss, D. Landriu, L. Latronico, B. Lee, S.-H. Lee, M. Lemoine-Goumard, A. M. Lionetto, F. Longo, F. Loparco, B. Lott, M. N. Lovellette, P. Lubrano, G. M. Madejski, A. Makeev, B. Marangelli, M. M. Massai, M. N. Mazziotta, J. E. McEnery, N. Menon, C. Meurer, P. F. Michelson, M. Minuti, N. Mirizzi, W. Mitthumsiri, T. Mizuno, A. A. Moiseev, C. Monte, M. E. Monzani, E. Moretti, A. Morselli, I. V. Moskalenko, S. Murgia, T. Nakamori, S. Nishino, P. L. Nolan, J. P. Norris, E. Nuss, M. Ohno, T. Ohsugi, N. Omodei, E. Orlando, J. F. Ormes, A. Paccagnella, D. Paneque, J. H. Panetta, D. Parent, M. Pearce, M. Pepe, A. Perazzo, M. Pesce-Rollins, P. Picozza, L. Pieri, M. Pinchera, F. Piron, T. A. Porter, L. Poupard, S. Rainò, R. Rando, E. Rapposelli, M. Razzano, A. Reimer, O. Reimer, T. Reposeur, L. C. Reyes, S. Ritz, L. S. Rochester, A. Y. Rodriguez, R. W. Romani, M. Roth, J. J. Russell, F. Ryde, S. Sabatini, H. F.-W. Sadrozinski, D. Sanchez, A. Sander, L. Sapozhnikov, P. M. S. Parkinson, J. D. Scargle, T. L.

Schalk, G. Scolieri, C. Sgrò, G. H. Share, M. Shaw, T. Shimokawabe, C. Shrader, A. Sierpowska-Bartosik, E. J. Siskind, D. A. Smith, P. D. Smith, G. Spandre, P. Spinelli, J.-L. Starck, T. E. Stephens, M. S. Strickman, A. W. Strong, D. J. Suson, H. Tajima, H. Takahashi, T. Takahashi, T. Tanaka, A. Tenze, S. Tether, J. B. Thayer, J. G. Thayer, D. J. Thompson, L. Tibaldo, O. Tibolla, D. F. Torres, G. Tosti, A. Tramacere, M. Turri, T. L. Usher, N. Vilchez, V. Vitale, P. Wang, K. Watters, B. L. Winer, K. S. Wood, T. Ylinen, and M. Ziegler, "THE LARGE AREA TELESCOPE ON THEFERMI GAMMA-RAY SPACE TELESCOPEMISSION," *The Astrophysical Journal*, vol. 697, no. 2, pp. 1071–1102, 2009.

[157] M. Ackermann, M. Ajello, A. Albert, A. Allafort, W. B. Atwood, M. Axelsson, L. Baldini, J. Ballet, G. Barbiellini, D. Bastieri, K. Bechtol, R. Bellazzini, E. Bissaldi, R. D. Blandford, E. D. Bloom, J. R. Bogart, E. Bonamente, A. W. Borgland, E. Bottacini, A. Bouvier, T. J. Brandt, J. Bregeon, M. Brigida, P. Bruel, R. Buehler, T. H. Burnett, S. Buson, G. A. Caliandro, R. A. Cameron, P. A. Caraveo, J. M. Casandjian, E. Cavazzuti, C. Cecchi, Çelik, E. Charles, R. C. G. Chaves, A. Chekhtman, C. C. Cheung, J. Chiang, S. Ciprini, R. Claus, J. Cohen-Tanugi, J. Conrad, R. Corbet, S. Cutini, F. D'Ammando, D. S. Davis, A. de Angelis, M. DeKlotz, F. de Palma, C. D. Dermer, S. W. Digel, E. do Couto e Silva, P. S. Drell, A. Drlica-Wagner, R. Dubois, C. Favuzzi, S. J. Fegan, E. C. Ferrara, W. B. Focke, P. Fortin, Y. Fukazawa, S. Funk, P. Fusco, F. Gargano, D. Gasparrini, N. Gehrels, B. Giebels, N. Giglietto, F. Giordano, M. Giroletti, T. Glanzman, G. Godfrey, I. A. Grenier, J. E. Grove, S. Guiriec, D. Hadasch, M. Hayashida, E. Hays, D. Horan, X. Hou, R. E. Hughes, M. S. Jackson, T. Jogler, G. Jóhannesson, R. P. Johnson, T. J. Johnson, W. N. Johnson, T. Kamae, H. Katagiri, J. Kataoka, M. Kerr, J. Knödlseder, M. Kuss, J. Lande, S. Larsson, L. Latronico, C. Lavalley, M. Lemoine-Goumard, F. Longo, F. Loparco, B. Lott, M. N. Lovellette, P. Lubrano, M. N. Mazziotta, W. McConville, J. E. McEnery, J. Mehault, P. F. Michelson, W. Mitthumsiri, T. Mizuno, A. A. Moiseev, C. Monte, M. E. Monzani, A. Morselli, I. V. Moskalenko, S. Murgia, M. Naumann-Godo, R. Nemmen, S. Nishino, J. P. Norris, E. Nuss, M. Ohno, T. Ohsugi, A. Okumura, N. Omodei, M. Orienti, E. Orlando, J. F. Ormes, D. Paneque, J. H. Panetta, J. S. Perkins, M. Pesce-Rollins, M. Pierbattista, F. Piron, G. Pivato, T. A. Porter, J. L. Racusin, S. Rainò, R. Rando, M. Razzano, S. Razzaque, A. Reimer, O. Reimer, T. Reposeur, L. C. Reyes, S. Ritz, L. S. Rochester, C. Romoli, M. Roth, H. F.-W. Sadrozinski, D. A. Sanchez, P. M. S. Parkinson, C. Sbarra, J. D. Scargle, C. Sgrò, J. Siegal-Gaskins, E. J. Siskind, G. Spandre, P. Spinelli, T. E. Stephens, D. J. Suson, H. Tajima, H. Takahashi, T. Tanaka, J. G. Thayer, J. B. Thayer, D. J. Thompson, L. Tibaldo, M. Tinivella, G. Tosti, E. Troja, T. L. Usher, J. Vandenbroucke, B. V. Klaveren, V. Vasileiou, G. Vianello, V. Vitale, A. P. Waite, E. Wallace, B. L. Winer, D. L. Wood, K. S. Wood, M. Wood, Z. Yang, and S. Zimmer, "THEFERMILARGE AREA TELESCOPE ON ORBIT: EVENT CLASSIFICATION, INSTRUMENT RESPONSE FUNCTIONS, AND CALIBRATION," *The Astrophysical Journal Supplement Series*, vol. 203, no. 1, p. 4, 2012.

[158] R. N. Manchester, R. T. Edwards, and G. B. Hobbs, "tempo2, a new pulsar-timing package – I. An overview," *Monthly Notices of the Royal Astronomical Society*, vol. 369, no. 2, pp. 655–672, May 2006. eprint: http://oup.prod.sis.lan/mnras/article-pdf/369/2/655/11178603/mnras0369-0655.pdf.

[159] P. L. Nolan, A. A. Abdo, M. Ackermann, M. Ajello, A. Allafort, E. Antolini, W. B. Atwood, M. Axelsson, L. Baldini, J. Ballet, G. Barbiellini, D. Bastieri, K. Bechtol, A. Belfiore, R. Bellazzini, B. Berenji, G. F. Bignami, R. D. Blandford, E. D. Bloom, E. Bonamente, J. Bonnell, A. W. Borgland, E. Bottacini, A. Bouvier, T. J. Brandt, J. Bregeon, M. Brigida, P. Bruel, R. Buehler, T. H. Burnett, S. Buson, G. A. Caliandro, R. A. Cameron, R. Campana, B. Cañadas, A. Cannon, P. A. Caraveo, J. M. Casandjian, E. Cavazzuti, M. Ceccanti, C. Cecchi, Çelik, E. Charles, A. Chekhtman, C. C. Cheung, J. Chiang, R. Chipaux, S. Ciprini, R. Claus, J. Cohen-Tanugi, L. R. Cominsky, J. Conrad, R. Corbet, S. Cutini, F. DAmmando, D. S. Davis, A. de Angelis, M. E. DeCesar, M. DeKlotz, A. D. Luca, P. R. den Hartog, F. de Palma, C. D. Dermer, S. W. Digel, E. do Couto e Silva, P. S. Drell, A. Drlica-Wagner, R. Dubois, D. Dumora, T. Enoto, L. Escande, D. Fabiani, L. Falletti, C. Favuzzi, S. J. Fegan, E. C. Ferrara, W. B. Focke, P. Fortin, M. Frailis, Y. Fukazawa, S. Funk, P. Fusco, F. Gargano, D. Gasparrini, N. Gehrels, S. Germani, B. Giebels, N. Giglietto, P. Giommi, F. Giordano, M. Giroletti, T. Glanzman, G. Godfrey, I. A. Grenier, M.-H. Grondin, J. E. Grove, L. Guillemot, S. Guiriec, M. Gustafsson, D. Hadasch, Y. Hanabata, A. K. Harding, M. Hayashida, E. Hays, A. B. Hill, D. Horan, X. Hou, R. E. Hughes, G. Iafrate, R. Itoh, G. Jóhannesson, R. P. Johnson, T. E. Johnson, A. S. Johnson, T. J. Johnson, T. Kamae, H. Katagiri, J. Kataoka, J. Katsuta, N. Kawai, M. Kerr, J. Knödlseder, D. Kocevski, M. Kuss, J. Lande, D. Landriu, L. Latronico, M. Lemoine-Goumard, A. M. Lionetto, M. L. Garde, F. Longo, F. Loparco, B. Lott, M. N. Lovellette, P. Lubrano, G. M. Madejski, M. Marelli, E. Massaro, M. N. Mazziotta, W. McConville, J. E. McEnery, J. Mehault, P. F. Michelson, M. Minuti, W. Mitthumsiri, T. Mizuno, A. A. Moiseev, M. Mongelli, C. Monte, M. E. Monzani, A. Morselli, I. V. Moskalenko, S. Murgia, T. Nakamori, M. Naumann-Godo, J. P. Norris, E. Nuss, T. Nymark, M. Ohno, T. Ohsugi, A. Okumura, N. Omodei, E. Orlando, J. F. Ormes, M. Ozaki, D. Paneque, J. H. Panetta, D. Parent, J. S. Perkins, M. Pesce-Rollins, M. Pierbattista, M. Pinchera, F. Piron, G. Pivato, T. A. Porter, J. L. Racusin, S. Rainò, R. Rando, M. Razzano, S. Razzaque, A. Reimer, O. Reimer, T. Reposeur, S. Ritz, L. S. Rochester, R. W. Romani, M. Roth, R. Rousseau, F. Ryde, H. F.-W. Sadrozinski, D. Salvetti, D. A. Sanchez, P. M. S. Parkinson, C. Sbarra, J. D. Scargle, T. L. Schalk, C. Sgrò, M. S. Shaw, C. Shrader, E. J. Siskind, D. A. Smith, G. Spandre, P. Spinelli, T. E. Stephens, M. S. Strickman, D. J. Suson, H. Tajima, H. Takahashi, T. Takahashi, T. Tanaka, J. G. Thayer, J. B. Thayer, D. J. Thompson, L. Tibaldo, O. Tibolla, F. Tinebra, M. Tinivella, D. F. Torres, G. Tosti, E. Troja, Y. Uchiyama, J. Vandenbroucke, A. V. Etten, B. V. Klaveren, V. Vasileiou, G. Vianello, V. Vitale, A. P. Waite, E. Wallace, P. Wang, M. Werner, B. L. Winer, D. L. Wood, K. S. Wood, M. Wood, Z. Yang, and S. Zim-

mer, "FERMILARGE AREA TELESCOPE SECOND SOURCE CATALOG," *The Astrophysical Journal Supplement Series*, vol. 199, no. 2, p. 31, 2012.

[160] P. S. Ray, M. Kerr, D. Parent, A. A. Abdo, L. Guillemot, S. M. Ransom, N. Rea, M. T. Wolff, A. Makeev, M. S. E. Roberts, F. Camilo, M. Dormody, P. C. C. Freire, J. E. Grove, C. Gwon, A. K. Harding, S. Johnston, M. Keith, M. Kramer, P. F. Michelson, R. W. Romani, P. M. Saz Parkinson, D. J. Thompson, P. Weltevrede, K. S. Wood, and M. Ziegler, "Precise γ-ray Timing and Radio Observations of 17 Fermi γ-ray Pulsars," *The Astrophysical Journal Supplement Series*, vol. 194, no. 2, 17, p. 17, 2011. arXiv: 1011.2468 [astro-ph.HE].

[161] A. Archer and for the VERITAS Collaboration, "Search for Pulsed Emission in Archival VERITAS Data," *arXiv e-prints*, arXiv:1509.01201, arXiv:1509.01201, 2015. arXiv: 1509.01201 [astro-ph.HE].

[162] A. Archer, W. Benbow, R. Bird, R. Brose, M. Buchovecky, J. H. Buckley, A. J. Chromey, W. Cui, A. Falcone, Q. Feng, J. P. Finley, L. Fortson, A. Furniss, A. Gent, O. Gueta, D. Hanna, T. Hassan, O. Hervet, J. Holder, G. Hughes, T. B. Humensky, C. A. Johnson, P. Kaaret, P. Kar, N. Kelley-Hoskins, M. Kertzman, D. Kieda, F. Krennrich, S. Kumar, M. J. Lang, T. T. Y. Lin, A. McCann, P. Moriarty, R. Mukherjee, S. O'Brien, R. A. Ong, A. N. Otte, D. Pandel, N. Park, A. Petrashyk, M. Pohl, E. Pueschel, J. Quinn, K. Ragan, G. T. Richards, E. Roache, I. Sadeh, M. Santander, S. S. Scott, G. H. Sembroski, K. Shahinyan, I. Sushch, J. Tyler, S. P. Wakely, A. Weinstein, R. M. Wells, P. Wilcox, A. Wilhelm, D. A. Williams, T. J Williamson, and B. Zitzer, "A Search for Pulsed Very High-Energy Gamma Rays from Thirteen Young Pulsars in Archival VERITAS Data," *arXiv e-prints*, arXiv:1904.09329, arXiv:1904.09329, 2019. arXiv: 1904.09329 [astro-ph.HE].

[163] A. A. Abdo, M. Ajello, A. Allafort, L. Baldini, J. Ballet, G. Barbiellini, M. G. Baring, D. Bastieri, A. Belfiore, R. Bellazzini, B. Bhattacharyya, E. Bissaldi, E. D. Bloom, E. Bonamente, E. Bottacini, T. J. Brandt, J. Bregeon, M. Brigida, P. Bruel, R. Buehler, M. Burgay, T. H. Burnett, G. Busetto, S. Buson, G. A. Caliandro, R. A. Cameron, F. Camilo, P. A. Caraveo, J. M. Casandjian, C. Cecchi, O. Çelik, E. Charles, S. Chaty, R. C. G. Chaves, A. Chekhtman, A. W. Chen, J. Chiang, G. Chiaro, S. Ciprini, R. Claus, I. Cognard, J. Cohen-Tanugi, L. R. Cominsky, J. Conrad, S. Cutini, F. D'Ammando, A. de Angelis, M. E. DeCesar, A. De Luca, P. R. den Hartog, F. de Palma, C. D. Dermer, G. Desvignes, S. W. Digel, L. Di Venere, P. S. Drell, A. Drlica-Wagner, R. Dubois, D. Dumora, C. M. Espinoza, L. Falletti, C. Favuzzi, E. C. Ferrara, W. B. Focke, A. Franckowiak, P. C. C. Freire, S. Funk, P. Fusco, F. Gargano, D. Gasparrini, S. Germani, N. Giglietto, P. Giommi, F. Giordano, M. Giroletti, T. Glanzman, G. Godfrey, E. V. Gotthelf, I. A. Grenier, M. H. Grondin, J. E. Grove, L. Guillemot, S. Guiriec, D. Hadasch, Y. Hanabata, A. K. Harding, M. Hayashida, E. Hays, J. Hessels, J. Hewitt, A. B. Hill, D. Horan, X. Hou, R. E. Hughes, M. S. Jackson, G. H. Janssen, T. Jogler, G. Jóhannesson, R. P. Johnson, A. S. Johnson, T. J. Johnson, W. N. Johnson, S. Johnston, T. Kamae, J.

Kataoka, M. Keith, M. Kerr, J. Knodlseder, M. Kramer, M. Kuss, J. Lande, S. Larsson, L. Latronico, M. Lemoine-Goumard, F. Longo, F. Loparco, M. N. Lovellette, P. Lubrano, A. G. Lyne, R. N. Manchester, M. Marelli, F. Massaro, M. Mayer, M. N. Mazziotta, J. E. McEnery, M. A. McLaughlin, J. Mehault, P. F. Michelson, R. P. Mignani, W. Mitthumsiri, T. Mizuno, A. A. Moiseev, M. E. Monzani, A. Morselli, I. V. Moskalenko, S. Murgia, T. Nakamori, R. Nemmen, E. Nuss, M. Ohno, T. Ohsugi, M. Orienti, E. Orlando, J. F. Ormes, D. Paneque, J. H. Panetta, D. Parent, J. S. Perkins, M. Pesce-Rollins, M. Pierbattista, F. Piron, G. Pivato, H. J. Pletsch, T. A. Porter, A. Possenti, S. Rainò, R. Rando, S. M. Ransom, P. S. Ray, M. Razzano, N. Rea, A. Reimer, O. Reimer, N. Renault, T. Reposeur, S. Ritz, R. W. Romani, M. Roth, R. Rousseau, J. Roy, J. Ruan, A. Sartori, P. M. Saz Parkinson, J. D. Scargle, A. Schulz, C. Sgrò, R. Shannon, E. J. Siskind, D. A. Smith, G. Spandre, P. Spinelli, B. W. Stappers, A. W. Strong, D. J. Suson, H. Takahashi, J. G. Thayer, J. B. Thayer, G. Theureau, D. J. Thompson, S. E. Thorsett, L. Tibaldo, O. Tibolla, M. Tinivella, D. F. Torres, G. Tosti, E. Troja, Y. Uchiyama, T. L. Usher, J. Vandenbroucke, V. Vasileiou, C. Venter, G. Vianello, V. Vitale, N. Wang, P. Weltevrede, B. L. Winer, M. T. Wolff, D. L. Wood, K. S. Wood, M. Wood, and Z. Yang, "The Second Fermi Large Area Telescope Catalog of Gamma-Ray Pulsars," *The Astrophysical Journal Supplement Series*, vol. 208, no. 2, 17, p. 17, 2013. arXiv: 1305.4385 [astro-ph.HE].

[164] M. Kerr, "Improving Sensitivity to Weak Pulsations with Photon Probability Weighting," *apj*, vol. 732, no. 1, 38, p. 38, 2011. arXiv: 1103.2128 [astro-ph.IM].

[165] Aharonian, F., Akhperjanian, A., Barrio, J., Bernlohr, K., Borst, H., Bojahr, H., Bolz, O., Contreras, J., Cortina, J., Denninghoff, S., Fonseca, V., Gonzalez, J., Gotting, N., Heinzelmann, G., Hermann, G., Heusler, A., Hofmann, W., Horns, D., Ibarra, A., Iserlohe, C., Jung, I., Kankanyan, R., Kestel, M., Kettler, J., Kohnle, A., Konopelko, A., Kornmeyer, H., Kranich, D., Krawczynski, H., Lampeitl, H., Lopez, M., Lorenz, E., Lucarelli, F., Magnussen, N., Mang, O., Meyer, H., Mirzoyan, R., Moralejo, A., Ona, E., Padilla, L., Panter, M., Plaga, R., Plyasheshnikov, A., Prahl, J., Puhlhofer, G., Rauterberg, G., Rohring, A., Rhode, W., Rowell, G. P., Sahakian, V., Samorski, M., Schilling, M., Schroder, F., Siems, M., Stamm, W., Tluczykont, M., Volk, H. J., Wiedner, C. A., and Wittek, W., "Evidence for tev gamma ray emission from cassiopeia a," *A&A*, vol. 370, no. 1, pp. 112–120, 2001.

[166] M. K. Daniel, "The VERITAS standard data analysis," *International Cosmic Ray Conference*, vol. 3, pp. 1325–1328, 2008. arXiv: 0709.4006.

[167] P. Cogan, "VEGAS, the VERITAS Gamma-ray Analysis Suite," vol. 3, p. 1385, 2007. arXiv: 0709.4233 [astro-ph].

[168] V. A. Acciari *et al.*, "VERITAS Observations of the gamma-Ray Binary LS I +61 303," *Astrophys. J.*, vol. 679, p. 1427, 2008. arXiv: 0802.2363 [astro-ph].

[169] G. Maier and J. Holder, "Eventdisplay: An Analysis and Reconstruction Package for Ground-based Gamma-ray Astronomy," *PoS*, vol. ICRC2017, p. 747, 2018, [35,747(2017)]. arXiv: 1708.04048 [astro-ph.IM].

[170] R. Brun, F. Rademakers, P. Canal, A. Naumann, O. Couet, L. Moneta, V. Vassilev, S. Linev, D. Piparo, G. GANIS, B. Bellenot, E. Guiraud, G. Amadio, wverkerke, P. Mato, TimurP, M. Tadel, wlav, E. Tejedor, J. Blomer, A. Gheata, S. Hageboeck, S. Roiser, marsupial, S. Wunsch, O. Shadura, A. Bose, CristinaCristescu, X. Valls, and R. Isemann, *Root-project/root: V6.18/02*, version v6-18-02, Aug. 2019.

[171] A. M. Hillas, "Cerenkov Light Images of EAS Produced by Primary Gamma Rays and by Nuclei," in *19th International Cosmic Ray Conference (ICRC19), Volume 3*, ser. International Cosmic Ray Conference, vol. 3, Aug. 1985, p. 445.

[172] H. Krawczynski, D. A. Carter-Lewis, C. Duke, J. Holder, G. Maier, S. Le Bohec, and G. Sembroski, "Gamma hadron separation methods for the VERITAS array of four imaging atmospheric Cherenkov telescopes," *Astroparticle Physics*, vol. 25, pp. 380–390, Jul. 2006. eprint: astro-ph/0604508.

[173] T.-P. Li and Y.-Q. Ma, "Analysis methods for results in gamma-ray astronomy," *apj*, vol. 272, pp. 317–324, Sep. 1983.

[174] O. C. de Jager, B. C. Raubenheimer, and J. W. H. Swanepoel, "A poweful test for weak periodic signals with unknown light curve shape in sparse data," *aap*, vol. 221, pp. 180–190, Aug. 1989.

[175] M. Shayduk, T. Hengstebeck, O. Kalekin, N Pavel, and T. Schweizer, "A new image cleaning method for the magic telescope," vol. 00, pp. 101–104, Jan. 2005.

[176] M. Shayduk and C. Consortium, "Optimized Next-neighbour Image Cleaning Method for Cherenkov Telescopes," in *International Cosmic Ray Conference*, ser. International Cosmic Ray Conference, vol. 33, Jan. 2013, p. 3000. arXiv: 1307.4939 [astro-ph.IM].

[177] T. C. Weekes, M. F. Cawley, D. J. Fegan, K. G. Gibbs, A. M. Hillas, P. W. Kowk, R. C. Lamb, D. A. Lewis, D. Macomb, N. A. Porter, P. T. Reynolds, and G. Vacanti, "Observation of TeV Gamma Rays from the Crab Nebula Using the Atmospheric Cerenkov Imaging Technique," *apj*, vol. 342, p. 379, Jul. 1989.

[178] S. LeBohec, C. Duke, and P. Jordan, "Minimal stereoscopic analysis for imaging atmospheric cherenkov telescope arrays," *Astroparticle Physics*, vol. 24, no. 1, pp. 26–31, 2005.

[179] D. Berge, S. Funk, and J. Hinton, "Background modelling in very-high-energy γ-ray astronomy," *aap*, vol. 466, no. 3, pp. 1219–1229, May 2007. arXiv: astro-ph/0610959 [astro-ph].

[180] S Wilks, *Mathematical Statistics*. J. Wiley and Sons, 1962.

[181] W. A. Rolke and A. M. Lopez, "Confidence intervals and upper bounds for small signals in the presence of background noise," *Nucl. Instrum. Meth.*, vol. A458, pp. 745–758, 2001. arXiv: hep-ph/0005187 [hep-ph].

[182] R. Pordes, D. Petravick, B. Kramer, D. Olson, M. Livny, A. Roy, P. Avery, K. Blackburn, T. Wenaus, F. Würthwein, I. Foster, R. Gardner, M. Wilde, A. Blatecky, J. McGee, and R. Quick, "The open science grid," in *J. Phys. Conf. Ser.*, ser. 78, vol. 78, 2007, p. 012 057.

[183] I. Sfiligoi, D. C. Bradley, B. Holzman, P. Mhashilkar, S. Padhi, and F. Wurthwein, "The pilot way to grid resources using glideinwms," in *2009 WRI World Congress on Computer Science and Information Engineering*, ser. 2, vol. 2, 2009, pp. 428–432.

[184] PACE, *Partnership for an Advanced Computing Environment (PACE)*, 2017.

[185] D. Heck, J. Knapp, J. N. Capdevielle, G. Schatz, and T. Thouw, "CORSIKA: A Monte Carlo code to simulate extensive air showers," Feb. 1998.

[186] K. Bernlöhr, "Simulation of imaging atmospheric Cherenkov telescopes with CORSIKA and sim_telarray," *Astroparticle Physics*, vol. 30, no. 3, pp. 149–158, Oct. 2008. arXiv: 0808.2253 [astro-ph].

[187] E. Deelman, K. Vahi, G. Juve, M. Rynge, S. Callaghan, P. J. Maechling, R. Mayani, W. Chen, R. Ferreira da Silva, M. Livny, and K. Wenger, "Pegasus, a workflow management system for science automation," *Future Generation Computer Systems*, vol. 46, pp. 17–35, 2015.

[188] P. Paschos, B. Riedel, J. Stephen, R. Gardner, E. Fajardo, J. Hicks, F. Wuerthwein, and J. Clark, *Distributed computing software and data access patterns in osg mid-scale collaborations*, Apr. 2020.

[189] H. E. S. S. Collaboration, H. Abdalla, F. Aharonian, F. Ait Benkhali, E. O. Anguner, M. Arakawa, C. Arcaro, C. Armand, M. Arrieta, M. Backes, M. Barnard, Y. Becherini, J. Becker Tjus, D. Berge, S. Bernhard, K. Bernlohr, R. Blackwell, M. Bottcher, C. Boisson, J. Bolmont, S. Bonnefoy, P. Bordas, J. Bregeon, F. Brun, P. Brun, M. Bryan, M. Buchele, T. Bulik, T. Bylund, M. Capasso, S. Caroff, A. Carosi, S. Casanova, M. Cerruti, N. Chakraborty, S. Chandra, R. C. G. Chaves, A. Chen, S. Colafrancesco, B. Condon, I. D. Davids, C. Deil, J. Devin, P. deWilt, L.

Dirson, A. Djannati-Ataı, A. Dmytriiev, A. Donath, V. Doroshenko, L. O. C. Drury, J. Dyks, K. Egberts, G. Emery, J. P. Ernenwein, S. Eschbach, S. Fegan, A. Fiasson, G. Fontaine, S. Funk, M. Fußling, S. Gabici, Y. A. Gallant, F. Gaté, G. Giavitto, D. Glawion, J. F. Glicenstein, D. Gottschall, M. H. Grondin, J. Hahn, M. Haupt, G. Heinzelmann, G. Henri, G. Hermann, J. A. Hinton, W. Hofmann, C. Hoischen, T. L. Holch, M. Holler, D. Horns, D. Huber, H. Iwasaki, A. Jacholkowska, M. Jamrozy, D. Jankowsky, F. Jankowsky, L. Jouvin, I. Jung-Richardt, M. A. Kastendieck, K. Katarzyński, M. Katsuragawa, U. Katz, D. Kerszberg, D. Khangulyan, B. Khélifi, J. King, S. Klepser, W. Kluźniak, N. Komin, K. Kosack, S. Krakau, M. Kraus, P. P. Kruger, G. Lamanna, J. Lau, J. Lefaucheur, A. Lemière, M. Lemoine-Goumard, J. P. Lenain, E. Leser, T. Lohse, M. Lorentz, R. López-Coto, I. Lypova, D. Malyshev, V. Marandon, A. Marcowith, C. Mariaud, G. Martí-Devesa, R. Marx, G. Maurin, P. J. Meintjes, A. M. W. Mitchell, R. Moderski, M. Mohamed, L. Mohrmann, E. Moulin, T. Murach, S. Nakashima, M. de Naurois, H. Ndiyavala, F. Niederwanger, J. Niemiec, L. Oakes, P. O'Brien, H. Odaka, S. Ohm, M. Ostrowski, I. Oya, M. Padovani, M. Panter, R. D. Parsons, C. Perennes, P. O. Petrucci, B. Peyaud, Q. Piel, S. Pita, V. Poireau, A. Priyana Noel, D. A. Prokhorov, H. Prokoph, G. Puhlhofer, M. Punch, A. Quirrenbach, S. Raab, R. Rauth, A. Reimer, O. Reimer, M. Renaud, F. Rieger, L. Rinchiuso, C. Romoli, G. Rowell, B. Rudak, E. Ruiz-Velasco, V. Sahakian, S. Saito, D. A. Sanchez, A. Santangelo, M. Sasaki, R. Schlickeiser, F. Schussler, A. Schulz, U. Schwanke, S. Schwemmer, M. Seglar-Arroyo, M. Senniappan, A. S. Seyffert, N. Shafi, I. Shilon, K. Shiningayamwe, R. Simoni, A. Sinha, H. Sol, F. Spanier, A. Specovius, M. Spir-Jacob, Ł. Stawarz, R. Steenkamp, C. Stegmann, C. Steppa, T. Takahashi, J. P. Tavernet, T. Tavernier, A. M. Taylor, R. Terrier, L. Tibaldo, D. Tiziani, M. Tluczykont, C. Trichard, M. Tsirou, N. Tsuji, R. Tuffs, Y. Uchiyama, D. J. van der Walt, C. van Eldik, C. van Rensburg, B. van Soelen, G. Vasileiadis, J. Veh, C. Venter, P. Vincent, J. Vink, F. Voisin, H. J. Volk, T. Vuillaume, Z. Wadiasingh, S. J. Wagner, R. M. Wagner, R. White, A. Wierzcholska, R. Yang, D. Zaborov, M. Zacharias, R. Zanin, A. A. Zdziarski, A. Zech, F. Zefi, A. Ziegler, J. Zorn, N. Żywucka, M. Kerr, S. Johnston, and R. M. Shannon, "First ground-based measurement of sub-20 GeV to 100 GeV γ-Rays from the Vela pulsar with H.E.S.S. II," *aap*, vol. 620, A66, A66, Dec. 2018. arXiv: 1807.01302 [astro-ph.HE].

[190] M. Spir-Jacob, A. Djannati-Ataı, L. Mohrmann, G. Giavitto, B. Khélifi, B. Rudak, C. Venter, and R. Zanin, "Detection of sub-100 GeV gamma-ray pulsations from PSR B1706-44 with H.E.S.S," *arXiv e-prints*, arXiv:1908.06464, arXiv:1908.06464, Aug. 2019. arXiv: 1908.06464 [astro-ph.HE].

[191] MAGIC Collaboration, V. A. Acciari, S. Ansoldi, L. A. Antonelli, A. Arbet Engels, K. Asano, D. Baack, A. Babić, A. Baquero, U. Barres de Almeida, J. A. Barrio, J. Becerra González, W. Bednarek, L. Bellizzi, E. Bernardini, M. Bernardos, A. Berti, J. Besenrieder, W. Bhattacharyya, C. Bigongiari, A. Biland, O. Blanch, G. Bonnoli, Ž. Bošnjak, G. Busetto, R. Carosi, G. Ceribella, M. Cerruti, Y. Chai, A. Chilingarian, S. Cikota, S. M. Colak, E. Colombo, J. L. Contreras, J. Cortina, S.

Covino, G. D'Amico, V. D'Elia, P. da Vela, F. Dazzi, A. de Angelis, B. de Lotto, M. Delfino, J. Delgado, C. Delgado Mendez, D. Depaoli, T. di Girolamo, F. di Pierro, L. di Venere, E. Do Souto Espiñeira, D. Dominis Prester, A. Donini, D. Dorner, M. Doro, D. Elsaesser, V. Fallah Ramazani, A. Fattorini, G. Ferrara, L. Foffano, M. V. Fonseca, L. Font, C. Fruck, S. Fukami, R. J. García López, M. Garczarczyk, S. Gasparyan, M. Gaug, N. Giglietto, F. Giordano, P. Gliwny, N. Godinović, J. G. Green, D. Green, D. Hadasch, A. Hahn, L. Heckmann, J. Herrera, J. Hoang, D. Hrupec, M. Hutten, T. Inada, S. Inoue, K. Ishio, Y. Iwamura, J. Jormanainen, L. Jouvin, Y. Kajiwara, M. Karjalainen, D. Kerszberg, Y. Kobayashi, H. Kubo, J. Kushida, A. Lamastra, D. Lelas, F. Leone, E. Lindfors, S. Lombardi, F. Longo, R. López-Coto, M. López-Moya, A. López-Oramas, S. Loporchio, B. Machado de Oliveira Fraga, C. Maggio, P. Majumdar, M. Makariev, M. Mallamaci, G. Maneva, M. Manganaro, K. Mannheim, L. Maraschi, M. Mariotti, M. Martínez, D. Mazin, S. Mender, S. Mićanović, D. Miceli, T. Miener, M. Minev, J. M. Miranda, R. Mirzoyan, E. Molina, A. Moralejo, D. Morcuende, V. Moreno, E. Moretti, P. Munar-Adrover, V. Neustroev, C. Nigro, K. Nilsson, D. Ninci, K. Nishijima, K. Noda, S. Nozaki, Y. Ohtani, T. Oka, J. Otero-Santos, M. Palatiello, D. Paneque, R. Paoletti, J. M. Paredes, L. Pavletić, P. Peñil, C. Perennes, M. Persic, P. G. Prada Moroni, E. Prandini, C. Priyadarshi, I. Puljak, W. Rhode, M. Ribó, J. Rico, C. Righi, A. Rugliancich, L. Saha, N. Sahakyan, T. Saito, S. Sakurai, K. Satalecka, F. G. Saturni, B. Schleicher, K. Schmidt, T. Schweizer, J. Sitarek, I. Šnidarić, D. Sobczynska, A. Spolon, A. Stamerra, D. Strom, M. Strzys, Y. Suda, T. Surić, M. Takahashi, F. Tavecchio, P. Temnikov, T. Terzić, M. Teshima, N. Torres-Albà, L. Tosti, S. Truzzi, A. Tutone, J. van Scherpenberg, G. Vanzo, M. Vazquez Acosta, S. Ventura, V. Verguilov, C. F. Vigorito, V. Vitale, I. Vovk, M. Will, D. Zarić, K. Hirotani, and P. M. Saz Parkinson, "Detection of the Geminga pulsar with MAGIC hints at a power-law tail emission beyond 15 GeV," *aap*, vol. 643, L14, p. L14, Nov. 2020. arXiv: 2011.10412 [astro-ph.HE].

[192] M. Breed, C. Venter, and A. K. Harding, "Very-high energy emission from pulsars," *arXiv e-prints*, arXiv:1607.06480, arXiv:1607.06480, Jul. 2016. arXiv: 1607.06480 [astro-ph.HE].

[193] A. K. Harding, "Gamma-ray pulsar light curves as probes of magnetospheric structure," *Journal of Plasma Physics*, vol. 82, no. 3, p. 635 820 306, 2016.

[194] S. V. Bogovalov, "Magnetocentrifugal acceleration of bulk motion of plasma in pulsar magnetosphere," *Monthly Notices of the Royal Astronomical Society*, vol. 443, no. 3, pp. 2197–2203, Jul. 2014. eprint: https://academic.oup.com/mnras/article-pdf/443/3/2197/4915288/stu1283.pdf.

[195] W. Bednarek, "On the origin of sub-TeV gamma-ray pulsed emission from rotating neutron stars," *Monthly Notices of the Royal Astronomical Society*, vol. 424, no. 3, pp. 2079–2085, Aug. 2012. eprint: https://academic.oup.com/mnras/article-pdf/424/3/2079/2996716/424-3-2079.pdf.

[196] A. Philippov, D. A. Uzdensky, A. Spitkovsky, and B. Cerutti, "Pulsar Radio Emission Mechanism: Radio Nanoshots as a Low-frequency Afterglow of Relativistic Magnetic Reconnection," *apj*, vol. 876, no. 1, L6, p. L6, May 2019. arXiv: 1902.07730 [astro-ph.HE].

[197] T. J. Johnson, C. Venter, A. K. Harding, L. Guillemot, D. A. Smith, M. Kramer, O. Çelik, P. R. den Hartog, E. C. Ferrara, X. Hou, J. Lande, and P. S. Ray, "Constraints on the Emission Geometries and Spin Evolution of Gamma-Ray Millisecond Pulsars," *apjs*, vol. 213, no. 1, 6, p. 6, Jul. 2014. arXiv: 1404.2264 [astro-ph.HE].

[198] V. A. Acciari, S. Ansoldi, L. A. Antonelli, A. Arbet Engels, M. Artero, K. Asano, D. Baack, A. Babić, A. Baquero, U. Barres de Almeida, J. A. Barrio, I. Batković, J. Becerra González, W. Bednarek, L. Bellizzi, E. Bernardini, M. Bernardos, A. Berti, J. Besenrieder, W. Bhattacharyya, C. Bigongiari, A. Biland, O. Blanch, G. Bonnoli, Ž. Bošnjak, G. Busetto, R. Carosi, G. Ceribella, M. Cerruti, Y. Chai, A. Chilingarian, S. Cikota, S. M. Colak, E. Colombo, J. L. Contreras, J. Cortina, S. Covino, G. D'Amico, V. D'Elia, P. Da Vela, F. Dazzi, A. De Angelis, B. De Lotto, M. Delfino, J. Delgado, C. Delgado Mendez, D. Depaoli, F. Di Pierro, L. Di Venere, E. Do Souto Espiñeira, D. Dominis Prester, A. Donini, D. Dorner, M. Doro, D. Elsaesser, V. Fallah Ramazani, A. Fattorini, G. Ferrara, M. V. Fonseca, L. Font, C. Fruck, S. Fukami, R. J. García López, M. Garczarczyk, S. Gasparyan, M. Gaug, N. Giglietto, F. Giordano, P. Gliwny, N. Godinović, J. G. Green, D. Green, D. Hadasch, A. Hahn, L. Heckmann, J. Herrera, J. Hoang, D. Hrupec, M. Hutten, T. Inada, S. Inoue, K. Ishio, Y. Iwamura, I. Jiménez, J. Jormanainen, L. Jouvin, Y. Kajiwara, M. Karjalainen, D. Kerszberg, Y. Kobayashi, H. Kubo, J. Kushida, A. Lamastra, D. Lelas, F. Leone, E. Lindfors, S. Lombardi, F. Longo, R. López-Coto, M. López-Moya, A. López-Oramas, S. Loporchio, B. Machado de Oliveira Fraga, C. Maggio, P. Majumdar, M. Makariev, M. Mallamaci, G. Maneva, M. Manganaro, K. Mannheim, L. Maraschi, M. Mariotti, M. Martínez, D. Mazin, S. Menchiari, S. Mender, S. Mićanović, D. Miceli, T. Miener, M. Minev, J. M. Miranda, R. Mirzoyan, E. Molina, A. Moralejo, D. Morcuende, V. Moreno, E. Moretti, V. Neustroev, C. Nigro, K. Nilsson, K. Nishijima, K. Noda, S. Nozaki, Y. Ohtani, T. Oka, J. Otero-Santos, S. Paiano, M. Palatiello, D. Paneque, R. Paoletti, J. M. Paredes, L. Pavletić, P. Peñil, C. Perennes, M. Persic, P. G. Prada Moroni, E. Prandini, C. Priyadarshi, I. Puljak, W. Rhode, M. Ribó, J. Rico, C. Righi, A. Rugliancich, L. Saha, N. Sahakyan, T. Saito, S. Sakurai, K. Satalecka, F. G. Saturni, B. Schleicher, K. Schmidt, T. Schweizer, J. Sitarek, I. Šnidarić, D. Sobczynska, A. Spolon, A. Stamerra, D. Strom, M. Strzys, Y. Suda, T. Surić, M. Takahashi, F. Tavecchio, P. Temnikov, T. Terzić, M. Teshima, L. Tosti, S. Truzzi, A. Tutone, S. Ubach, J. van Scherpenberg, G. Vanzo, M. Vazquez Acosta, S. Ventura, V. Verguilov, C. F. Vigorito, V. Vitale, I. Vovk, M. Will, C. Wunderlich, D. Zarić, D. Zarić, P. A. Caraveo, I. Cognard, L. Guillemot, A. K. Harding, J. Li, B. Limyansky, C. Y. Ng, D. F. Torres, and P. M. Saz Parkinson, "Search for Very High-energy Emission from the Millisecond Pulsar PSR J0218+4232," *apj*, vol. 922, no. 2, 251, p. 251, Dec. 2021. arXiv: 2108.11373 [astro-ph.HE].

[199] A. V. Bilous, A. L. Watts, A. K. Harding, T. E. Riley, Z. Arzoumanian, S. Bogdanov, K. C. Gendreau, P. S. Ray, S. Guillot, W. C. G. Ho, and D. Chakrabarty, "A NICER View of PSR J0030+0451: Evidence for a Global-scale Multipolar Magnetic Field," *apj*, vol. 887, no. 1, L23, p. L23, Dec. 2019. arXiv: 1912.05704 [astro-ph.HE].

[200] D. J. Thompson, Z. Arzoumanian, D. L. Bertsch, K. T. S. Brazier, J. Chiang, N. D'Amico, B. L. Dingus, J. A. Esposito, J. M. Fierro, C. E. Fichtel, R. C. Hartman, S. D. Hunter, S. Johnston, G. Kanbach, V. M. Kaspi, D. A. Kniffen, Y. C. Lin, A. G. Lyne, R. N. Manchester, J. R. Mattox, H. A. Mayer-Hasselwander, P. F. Michelson, C. von Montigny, H. I. Nel, D. J. Nice, P. L. Nolan, P. V. Ramanamurthy, S. L. Shemar, E. J. Schneid, P. Sreekumar, and J. H. Taylor, "EGRET High-Energy Gamma-Ray Pulsar Studies. I. Young Spin-powered Pulsars," *apj*, vol. 436, p. 229, Nov. 1994.

[201] H. I. Nel, Z. Arzoumanian, M. Bailes, K. T. S. Brazier, N. D'Amico, J. A. Esposito, C. E. Fichtel, J. M. Fierro, S. D. Hunter, S. Johnston, G. Kanbach, V. M. Kaspi, D. A. Kniffen, Y. C. Lin, A. G. Lyne, R. N. Manchester, J. R. Mattox, H. A. Mayer-Hasselwander, M. Merck, P. F. Michelson, D. J. Nice, P. L. Nolan, P. V. Ramanamurthy, J. H. Taylor, D. J. Thompson, and C. Westbrook, "EGRET High-Energy Gamma-Ray Pulsar Studies. III. A Survey," *apj*, vol. 465, p. 898, Jul. 1996.

[202] A. Somer, "New Pulsars from Arecibo Drift Scan Search," in *IAU Colloq. 177: Pulsar Astronomy - 2000 and Beyond*, M. Kramer, N. Wex, and R. Wielebinski, Eds., ser. Astronomical Society of the Pacific Conference Series, vol. 202, 2000, p. 17. arXiv: astro-ph/9911222 [astro-ph].

[203] Z. Arzoumanian, A. Brazier, S. Burke-Spolaor, S. Chamberlin, S. Chatterjee, B. Christy, J. M. Cordes, N. J. Cornish, F. Crawford, H. T. Cromartie, K. Crowter, M. E. DeCesar, P. B. Demorest, T. Dolch, J. A. Ellis, R. D. Ferdman, E. C. Ferrara, E. Fonseca, N. Garver-Daniels, P. A. Gentile, D. Halmrast, E. A. Huerta, F. A. Jenet, C. Jessup, G. Jones, M. L. Jones, D. L. Kaplan, M. T. Lam, T. J. W. Lazio, L. Levin, A. Lommen, D. R. Lorimer, J. Luo, R. S. Lynch, D. Madison, A. M. Matthews, M. A. McLaughlin, S. T. McWilliams, C. Mingarelli, C. Ng, D. J. Nice, T. T. Pennucci, S. M. Ransom, P. S. Ray, X. Siemens, J. Simon, R. Spiewak, I. H. Stairs, D. R. Stinebring, K. Stovall, J. K. Swiggum, S. R. Taylor, M. Vallisneri, R. van Haasteren, S. J. Vigeland, and W. Z. and, "The NANOGrav 11-year data set: High-precision timing of 45 millisecond pulsars," *The Astrophysical Journal Supplement Series*, vol. 235, no. 2, p. 37, 2018.

[204] J. M. Yao, R. N. Manchester, and N. Wang, "A New Electron-density Model for Estimation of Pulsar and FRB Distances," *apj*, vol. 835, 29, p. 29, Jan. 2017. arXiv: 1610.09448.

[205] A. N. Lommen, R. A. Kipphorn, D. J. Nice, E. M. Splaver, I. H. Stairs, and D. C. Backer, "The Parallax and Proper Motion of PSR J0030+0451," *apj*, vol. 642, pp. 1012–1017, 2006. arXiv: astro-ph/0601521 [astro-ph].

[206] M. Ruderman, J. Shaham, and M. Tavani, "Accretion turnoff and rapid evaporation of very light secondaries in low-mass X-ray binaries," *apj*, vol. 336, pp. 507–518, Jan. 1989.

[207] G. Desvignes, R. N. Caballero, L. Lentati, J. P. W. Verbiest, D. J. Champion, B. W. Stappers, G. H. Janssen, P. Lazarus, S. Osłowski, S. Babak, C. G. Bassa, P. Brem, M. Burgay, I. Cognard, J. R. Gair, E. Graikou, L. Guillemot, J. W. T. Hessels, A. Jessner, C. Jordan, R. Karuppusamy, M. Kramer, A. Lassus, K. Lazaridis, K. J. Lee, K. Liu, A. G. Lyne, J. McKee, C. M. F. Mingarelli, D. Perrodin, A. Petiteau, A. Possenti, M. B. Purver, P. A. Rosado, S. Sanidas, A. Sesana, G. Shaifullah, R. Smits, S. R. Taylor, G. Theureau, C. Tiburzi, R. van Haasteren, and A. Vecchio, "High-precision timing of 42 millisecond pulsars with the European Pulsar Timing Array," *mnras*, vol. 458, pp. 3341–3380, May 2016. arXiv: 1602.08511 [astro-ph.HE].

[208] S. C. Lundgren, A. F. Zepka, and J. M. Cordes, "A Millisecond Pulsar in a 6 Hour Orbit: PSR J0751+1807," *apj*, vol. 453, p. 419, Nov. 1995.

[209] D. J. Nice, E. M. Splaver, I. H. Stairs, O. Loehmer, A. Jessner, M. Kramer, and J. M. Cordes, "A 2.1 solar mass pulsar measured by relativistic orbital decay," *Astrophys. J.*, vol. 634, pp. 1242–1249, 2005. arXiv: astro-ph/0508050 [astro-ph].

[210] L. Guillemot, D. A. Smith, H. Laffon, G. H. Janssen, I. Cognard, G. Theureau, G. Desvignes, E. C. Ferrara, and P. S. Ray, "The gamma-ray millisecond pulsar deathline, revisited. New velocity and distance measurements," *aap*, vol. 587, A109, A109, 2016. arXiv: 1601.05987 [astro-ph.HE].

[211] M. Bailes, S. Johnston, J. F. Bell, D. R. Lorimer, B. W. Stappers, R. N. Manchester, A. G. Lyne, L. Nicastro, and B. M. Gaensler, "Discovery of Four Isolated Millisecond Pulsars," *apj*, vol. 481, pp. 386–391, May 1997.

[212] W. Becker and J. Trumper, "The X-ray emission properties of millisecond pulsars," *Astron. Astrophys.*, vol. 341, p. 803, 1999. arXiv: astro-ph/9806381 [astro-ph].

[213] M. Toscano, J. S. Sandhu, M. Bailes, R. N. Manchester, M. C. Britton, S. R. Kulkarni, S. B. Anderson, and B. W. Stappers, "Millisecond pulsar velocities," *Mon. Not. Roy. Astron. Soc.*, vol. 307, p. 925, 1999. arXiv: astro-ph/9811398 [astro-ph].

[214] C. G. Bassa *et al.*, "A millisecond pulsar in an extremely wide binary system," *Mon. Not. Roy. Astron. Soc.*, vol. 460, no. 2, pp. 2207–2222, 2016. arXiv: 1604.00129 [astro-ph.HE].

[215] T. E. Lutz and D. H. Kelker, "On the Use of Trigonometric Parallaxes for the Calibration of Luminosity Systems: Theory," *pasp*, vol. 85, p. 573, Oct. 1973.

[216] J. P. W. Verbiest, D. R. Lorimer, and M. A. McLaughlin, "Lutz-Kelker bias in pulsar parallax measurements," *mnras*, vol. 405, pp. 564–572, Jun. 2010. arXiv: 1002.1213 [astro-ph.GA].

[217] J. L. Han, R. N. Manchester, W. van Straten, and P. Demorest, "Pulsar rotation measures and large-scale magnetic field reversals in the galactic disk," *The Astrophysical Journal Supplement Series*, vol. 234, no. 1, p. 11, 2018.

[218] P. C. C. Freire, C. G. Bassa, N. Wex, I. H. Stairs, D. J. Champion, S. M. Ransom, P. Lazarus, V. M. Kaspi, J. W. T. Hessels, M. Kramer, J. M. Cordes, J. P. W. Verbiest, P. Podsiadlowski, D. J. Nice, J. S. Deneva, D. R. Lorimer, B. W. Stappers, M. A. McLaughlin, and F. Camilo, "On the nature and evolution of the unique binary pulsar J1903+0327," *mnras*, vol. 412, pp. 2763–2780, Apr. 2011. arXiv: 1011.5809.

[219] S. Portegies Zwart, E. P. J. van den Heuvel, J. van Leeuwen, and G. Nelemans, "The Formation of the Eccentric-orbit Millisecond Pulsar J1903+0327 and the Origin of Single Millisecond Pulsars," *apj*, vol. 734, 55, p. 55, Jun. 2011. arXiv: 1103.2375 [astro-ph.SR].

[220] H.-L. Chen, X. Chen, T. M. Tauris, and Z. Han, "FORMATION OF BLACK WIDOWS AND REDBACKS—TWO DISTINCT POPULATIONS OF ECLIPSING BINARY MILLISECOND PULSARS," *The Astrophysical Journal*, vol. 775, no. 1, p. 27, 2013.

[221] K. Stovall, R. S. Lynch, S. M. Ransom, A. M. Archibald, S. Banaszak, C. M. Biwer, J. Boyles, L. P. Dartez, D. Day, A. J. Ford, J. Flanigan, A. Garcia, J. W. T. Hessels, J. Hinojosa, F. A. Jenet, D. L. Kaplan, C. Karako-Argaman, V. M. Kaspi, V. I. Kondratiev, S. Leake, D. R. Lorimer, G. Lunsford, J. G. Martinez, A. Mata, M. A. McLaughlin, M. S. E. Roberts, M. D. Rohr, X. Siemens, I. H. Stairs, J. van Leeuwen, A. N. Walker, and B. L. Wells, "The Green Bank Northern Celestial Cap Pulsar Survey. I. Survey Description, Data Analysis, and Initial Results," *apj*, vol. 791, 67, p. 67, Aug. 2014. arXiv: 1406.5214 [astro-ph.HE].

[222] D. L. Kaplan, K. Stovall, S. M. Ransom, M. S. E. Roberts, R. Kotulla, A. M. Archibald, C. M. Biwer, J. Boyles, L. Dartez, D. F. Day, A. J. Ford, A. Garcia, J. W. T. Hessels, F. A. Jenet, C. Karako, V. M. Kaspi, V. I. Kondratiev, D. R. Lorimer, R. S. Lynch, M. A. McLaughlin, M. D. W. Rohr, X. Siemens, I. H. Stairs,

and J. van Leeuwen, "Discovery of the Optical/Ultraviolet/Gamma-Ray Counterpart to the Eclipsing Millisecond Pulsar J1816+4510," *apj*, vol. 753, 174, p. 174, Jul. 2012. arXiv: 1205.3699 [astro-ph.HE].

[223] D. L. Kaplan, V. B. Bhalerao, M. H. van Kerkwijk, D. Koester, S. R. Kulkarni, and K. Stovall, "A Metal-Rich Low-Gravity Companion to a Massive Millisecond Pulsar," *Astrophys. J.*, vol. 765, p. 158, 2013. arXiv: 1302.2492 [astro-ph.SR].

[224] J. Strader *et al.*, "Optical spectroscopy and demographics of redback millisecond pulsar binaries," *Astrophys. J.*, vol. 872, no. 1, p. 42, 2019. arXiv: 1812.04626 [astro-ph.HE].

[225] D. C. Backer, S. R. Kulkarni, C. Heiles, M. Davis, and W. Goss, "A millisecond pulsar," *Nature*, vol. 300, no. 5893, p. 615, 1982.

[226] L. Nicastro, G. Cusumano, O. Lohmer, M. Kramer, L. Kuiper, W. Hermsen, T. Mineo, and W. Becker, "BeppoSAX observation of PSR B1937+21," *Astron. Astrophys.*, vol. 413, pp. 1065–1072, 2004. arXiv: astro-ph/0310299 [astro-ph].

[227] A. S. Fruchter, D. R. Stinebring, and J. H. Taylor, "A millisecond pulsar in an eclipsing binary," *nat*, vol. 333, pp. 237–239, May 1988.

[228] Z. Arzoumanian, A. S. Fruchter, and J. H. Taylor, "Orbital variability in the eclipsing pulsar binary PSR B1957+20," *apj*, vol. 426, pp. 85–88, May 1994. eprint: astro-ph/9312032.

[229] M. H. van Kerkwijk, R. P. Breton, and S. R. Kulkarni, "Evidence for a Massive Neutron Star from a Radial-velocity Study of the Companion to the Black-widow Pulsar PSR B1957+20," *apj*, vol. 728, 95, p. 95, Feb. 2011. arXiv: 1009.5427 [astro-ph.HE].

[230] M. Kerr, "Improving pulsar timing precision with single pulses," *mnras*, vol. 452, no. 1, pp. 607–615, Sep. 2015. arXiv: 1506.03527 [astro-ph.IM].

[231] A. Lyne and F. Graham-Smith, *Pulsar Astronomy*. 2012.

[232] Z. J. Jiang, S. B. Chen, X. Li, and L. Zhang, "Phase-averaged gamma-ray spectra from rotation-powered millisecond pulsars," *Monthly Notices of the Royal Astronomical Society*, vol. 437, no. 3, pp. 2957–2965, Nov. 2013. eprint: https://academic.oup.com/mnras/article-pdf/437/3/2957/18468064/stt2120.pdf.

[233] W. Benbow, A. Brill, J. H. Buckley, M. Capasso, A. J. Chromey, M. Errando, A. Falcone, K. A Farrell, Q. Feng, J. P. Finley, G. M. Foote, L. Fortson, A. Furniss, A. Gent, C. Giuri, D. Hanna, T. Hassan, O. Hervet, J. Holder, G. Hughes, T. B.

Humensky, W. Jin, P. Kaaret, O. Kargaltsev, M. Kertzman, D. Kieda, N. Klingler, S. Kumar, M. J. Lang, M. Lundy, G. Maier, C. E McGrath, P. Moriarty, R. Mukherjee, D. Nieto, M. Nievas-Rosillo, S. O'Brien, R. A. Ong, A. N. Otte, S. Patel, K. Pfrang, M. Pohl, R. R. Prado, J. Quinn, K. Ragan, P. T. Reynolds, D. Ribeiro, G. T. Richards, E. Roache, J. L. Ryan, M. Santander, G. H. Sembroski, R. Shang, I. Volkov, S. P. Wakely, A. Weinstein, P. Wilcox, and D. A. Williams, "A search for TeV gamma-ray emission from pulsar tails by VERITAS," *The Astrophysical Journal*, vol. 916, no. 2, p. 117, 2021.

[234] F. Verbunt, A. Igoshev, and E. Cator, "The observed velocity distribution of young pulsars," *aap*, vol. 608, A57, A57, Dec. 2017. arXiv: 1708.08281 [astro-ph.HE].

[235] O. Kargaltsev, N. Klingler, S. Chastain, and G. G. Pavlov, "Toward understanding the physical underpinnings of spatial and spectral morphologies of pulsar wind nebulae," in *Journal of Physics Conference Series*, ser. Journal of Physics Conference Series, vol. 932, Dec. 2017, p. 012 050. arXiv: 1711.02656 [astro-ph.HE].

[236] A. Bykov, E. Amato, A. Petrov, A. Krassilchtchikov, and K. Levenfish, "Pulsar wind nebulae with bow shocks: Non-thermal radiation and cosmic ray leptons," *Space Science Reviews*, vol. 207, no. 1, pp. 235–290, 2017.

[237] N. Klingler, O. Kargaltsev, G. G. Pavlov, C. Y. Ng, P. Beniamini, and I. Volkov, "The Mouse Pulsar Wind Nebula," *apj*, vol. 861, no. 1, 5, p. 5, Jul. 2018. arXiv: 1803.10294 [astro-ph.HE].

[238] C. Y. Ng, N. Bucciantini, B. M. Gaensler, F. Camilo, S. Chatterjee, and A. Bouchard, "An Extreme Pulsar Tail Protruding from the Frying Pan Supernova Remnant," *apj*, vol. 746, no. 1, 105, p. 105, Feb. 2012. arXiv: 1109.2233 [astro-ph.HE].

[239] R. A. Chevalier and S. P. Reynolds, "PULSAR WIND NEBULAE WITH THICK TOROIDAL STRUCTURE," *The Astrophysical Journal*, vol. 740, no. 1, p. L26, 2011.

[240] Aharonian, F., Akhperjanian, A. G., Bazer-Bachi, A. R., Beilicke, M., Benbow, W., Berge, D., Bernlohr, K., Boisson, C., Bolz, O., Borrel, V., Braun, I., Breitling, F., Brown, A. M., Buhler, R., Busching, I., Carrigan, S., Chadwick, P. M., Chounet, L.-M., Cornils, R., Costamante, L., Degrange, B., Dickinson, H. J., Djannati-Ataı, A., Drury, L. O'C., Dubus, G., Egberts, K., Emmanoulopoulos, D., Epinat, B., Espigat, P., Feinstein, F., Ferrero, E., Fontaine, G., Funk, Seb., Funk, S., Gallant, Y. A., Giebels, B., Glicenstein, J. F., Goret, P., Hadjichristidis, C., Hauser, D., Hauser, M., Heinzelmann, G., Henri, G., Hermann, G., Hinton, J. A., Hofmann, W., Holleran, M., Horns, D., Jacholkowska, A., de Jager, O. C., Khélifi, B., Komin, Nu., Konopelko, A., Latham, I. J., Le Gallou, R., Lemière, A., Lemoine-Goumard, M., Lohse, T., Martin, J. M., Martineau-Huynh, O., Marcowith, A., Masterson, C., McComb, T. J. L., de Naurois, M., Nedbal, D., Nolan, S. J., Noutsos, A., Orford,

K. J., Osborne, J. L., Ouchrif, M., Panter, M., Pelletier, G., Pita, S., Puhlhofer, G., Punch, M., Raubenheimer, B. C., Raue, M., Rayner, S. M., Reimer, A., Reimer, O., Ripken, J., Rob, L., Rolland, L., Rowell, G., Sahakian, V., Saugé, L., Schlenker, S., Schlickeiser, R., Schwanke, U., Sol, H., Spangler, D., Spanier, F., Steenkamp, R., Stegmann, C., Superina, G., Tavernet, J.-P., Terrier, R., Théoret, C. G., Tluczykont, M., van Eldik, C., Vasileiadis, G., Venter, C., Vincent, P., Volk, H. J., Wagner, S. J., and Ward, M., "First detection of a vhe gamma-ray spectral maximum from a cosmic source: Hesscovery of the vela x nebula," *A&A*, vol. 448, no. 2, pp. L43–L47, 2006.

[241] A. Abramowski, F. Acero, F. Aharonian, A. G. Akhperjanian, G. Anton, S. Balenderan, A. Balzer, A. Barnacka, Y. Becherini, J. Becker Tjus, K. Bernlohr, E. Birsin, J. Biteau, A. Bochow, C. Boisson, J. Bolmont, P. Bordas, J. Brucker, F. Brun, P. Brun, T. Bulik, S. Carrigan, S. Casanova, M. Cerruti, P. M. Chadwick, A. Charbonnier, R. C. G. Chaves, A. Cheesebrough, G. Cologna, J. Conrad, C. Couturier, M. Dalton, M. K. Daniel, I. D. Davids, B. Degrange, C. Deil, P. deWilt, H. J. Dickinson, A. Djannati-Ataı, W. Domainko, L. O. C. Drury, F. Dubois, G. Dubus, K. Dutson, J. Dyks, M. Dyrda, K. Egberts, P. Eger, P. Espigat, L. Fallon, C. Farnier, S. Fegan, F. Feinstein, M. V. Fernandes, D. Fernandez, A. Fiasson, G. Fontaine, A. Forster, M. Fußling, M. Gajdus, Y. A. Gallant, T. Garrigoux, H. Gast, B. Giebels, J. F. Glicenstein, B. Gluck, D. Goring, M. H. Grondin, S. Haffner, J. D. Hague, J. Hahn, D. Hampf, J. Harris, S. Heinz, G. Heinzelmann, G. Henri, G. Hermann, A. Hillert, J. A. Hinton, W. Hofmann, P. Hofverberg, M. Holler, D. Horns, A. Jacholkowska, C. Jahn, M. Jamrozy, I. Jung, M. A. Kastendieck, K. Katarzyński, U. Katz, S. Kaufmann, B. Khélifi, D. Klochkov, W. Kluźniak, T. Kneiske, N. Komin, K. Kosack, R. Kossakowski, F. Krayzel, P. P. Kruger, H. Laffon, G. Lamanna, J. P. Lenain, D. Lennarz, T. Lohse, A. Lopatin, C. C. Lu, V. Marandon, A. Marcowith, J. Masbou, G. Maurin, N. Maxted, M. Mayer, T. J. L. McComb, M. C. Medina, J. Méhault, U. Menzler, R. Moderski, M. Mohamed, E. Moulin, C. L. Naumann, M. Naumann-Godo, M. de Naurois, D. Nedbal, N. Nguyen, J. Niemiec, S. J. Nolan, S. Ohm, E. de Oña Wilhelmi, B. Opitz, M. Ostrowski, I. Oya, M. Panter, D. Parsons, M. Paz Arribas, N. W. Pekeur, G. Pelletier, J. Perez, P. O. Petrucci, B. Peyaud, S. Pita, G. Puhlhofer, M. Punch, A. Quirrenbach, M. Raue, A. Reimer, O. Reimer, M. Renaud, R. de los Reyes, F. Rieger, J. Ripken, L. Rob, S. Rosier-Lees, G. Rowell, B. Rudak, C. B. Rulten, V. Sahakian, D. A. Sanchez, A. Santangelo, R. Schlickeiser, A. Schulz, U. Schwanke, S. Schwarzburg, S. Schwemmer, F. Sheidaei, J. L. Skilton, H. Sol, G. Spengler, Ł. Stawarz, R. Steenkamp, C. Stegmann, F. Stinzing, K. Stycz, I. Sushch, A. Szostek, J. P. Tavernet, R. Terrier, M. Tluczykont, C. Trichard, K. Valerius, C. van Eldik, G. Vasileiadis, C. Venter, A. Viana, P. Vincent, H. J. Volk, F. Volpe, S. Vorobiov, M. Vorster, S. J. Wagner, M. Ward, R. White, A. Wierzcholska, D. Wouters, M. Zacharias, A. Zajczyk, A. A. Zdziarski, A. Zech, and H. S. Zechlin, "Probing the extent of the non-thermal emission from the Vela X region at TeV energies with H.E.S.S.," *aap*, vol. 548, A38, A38, Dec. 2012. arXiv: 1210.1359 [astro-ph.HE].

[242] P. Slane, I. Lovchinsky, C. Kolb, S. L. Snowden, T. Temim, J. Blondin, F. Bocchino, M. Miceli, R. A. Chevalier, J. P. Hughes, D. J. Patnaude, and T. Gaetz, "Investigating the structure of vela x," *The Astrophysical Journal*, vol. 865, no. 2, p. 86, 2018.

[243] O. Kargaltsev, B. Rangelov, and G. G. Pavlov, "Gamma-ray and X-ray Properties of Pulsar Wind Nebulae and Unidentified Galactic TeV Sources," *arXiv e-prints*, arXiv:1305.2552, arXiv:1305.2552, May 2013. arXiv: 1305.2552 [astro-ph.HE].

[244] C. M. Hui and H. Zhou, "HAWC Observation of Supernova Remnants and Pulsar Wind Nebulae," in *34th International Cosmic Ray Conference (ICRC2015)*, ser. International Cosmic Ray Conference, vol. 34, Jul. 2015, p. 739. arXiv: 1508.07391 [astro-ph.HE].

[245] H. E. S. S. Collaboration, H. Abdalla, A. Abramowski, F. Aharonian, F. Ait Benkhali, A. G. Akhperjanian, T. Andersson, E. O. Anguner, M. Arrieta, P. Aubert, M. Backes, A. Balzer, M. Barnard, Y. Becherini, J. Becker Tjus, D. Berge, S. Bernhard, K. Bernlohr, R. Blackwell, M. Bottcher, C. Boisson, J. Bolmont, P. Bordas, J. Bregeon, F. Brun, P. Brun, M. Bryan, T. Bulik, M. Capasso, J. Carr, S. Carrigan, S. Casanova, M. Cerruti, N. Chakraborty, R. Chalme-Calvet, R. C. G. Chaves, A. Chen, J. Chevalier, M. Chrétien, S. Colafrancesco, G. Cologna, B. Condon, J. Conrad, C. Couturier, Y. Cui, I. D. Davids, B. Degrange, C. Deil, J. Devin, P. deWilt, L. Dirson, A. Djannati-Ataı, W. Domainko, A. Donath, L. O. C. Drury, G. Dubus, K. Dutson, J. Dyks, T. Edwards, K. Egberts, P. Eger, J. P. Ernenwein, S. Eschbach, C. Farnier, S. Fegan, M. V. Fernandes, A. Fiasson, G. Fontaine, A. Forster, S. Funk, M. Fußling, S. Gabici, M. Gajdus, Y. A. Gallant, T. Garrigoux, G. Giavitto, B. Giebels, J. F. Glicenstein, D. Gottschall, A. Goyal, M. H. Grondin, D. Hadasch, J. Hahn, M. Haupt, J. Hawkes, G. Heinzelmann, G. Henri, G. Hermann, O. Hervet, A. Hillert, J. A. Hinton, W. Hofmann, C. Hoischen, M. Holler, D. Horns, A. Ivascenko, A. Jacholkowska, M. Jamrozy, M. Janiak, D. Jankowsky, F. Jankowsky, M. Jingo, T. Jogler, L. Jouvin, I. Jung-Richardt, M. A. Kastendieck, K. Katarzyński, U. Katz, D. Kerszberg, B. Khélifi, M. Kieffer, J. King, S. Klepser, D. Klochkov, W. Kluźniak, D. Kolitzus, N. Komin, K. Kosack, S. Krakau, M. Kraus, F. Krayzel, P. P. Kruger, H. Laffon, G. Lamanna, J. Lau, J. P. Lees, J. Lefaucheur, V. Lefranc, A. Lemière, M. Lemoine-Goumard, J. P. Lenain, E. Leser, T. Lohse, M. Lorentz, R. Liu, R. López-Coto, I. Lypova, V. Marandon, A. Marcowith, C. Mariaud, R. Marx, G. Maurin, N. Maxted, M. Mayer, P. J. Meintjes, M. Meyer, A. M. W. Mitchell, R. Moderski, M. Mohamed, L. Mohrmann, K. Morå, E. Moulin, T. Murach, M. de Naurois, F. Niederwanger, J. Niemiec, L. Oakes, P. O'Brien, H. Odaka, S. Ottl, S. Ohm, E. de Oña Wilhelmi, M. Ostrowski, I. Oya, M. Padovani, M. Panter, R. D. Parsons, M. Paz Arribas, N. W. Pekeur, G. Pelletier, C. Perennes, P. O. Petrucci, B. Peyaud, S. Pita, H. Poon, D. Prokhorov, H. Prokoph, G. Puhlhofer, M. Punch, A. Quirrenbach, S. Raab, A. Reimer, O. Reimer, M. Renaud, R. de los Reyes, F. Rieger, C. Romoli, S. Rosier-Lees, G. Rowell, B. Rudak, C. B. Rulten, V. Sahakian, D. Salek, D. A. Sanchez, A. Santangelo, M. Sasaki, R. Schlickeiser, F. Schussler, A. Schulz, U. Schwanke, S. Schwemmer, M. Settimo, A. S. Seyffert, N.

Shafi, I. Shilon, R. Simoni, H. Sol, F. Spanier, G. Spengler, F. Spies, Ł. Stawarz, R. Steenkamp, C. Stegmann, F. Stinzing, K. Stycz, I. Sushch, J. P. Tavernet, T. Tavernier, A. M. Taylor, R. Terrier, L. Tibaldo, D. Tiziani, M. Tluczykont, C. Trichard, R. Tuffs, Y. Uchiyama, K. Valerius, D. J. van der Walt, C. van Eldik, B. van Soelen, G. Vasileiadis, J. Veh, C. Venter, A. Viana, P. Vincent, J. Vink, F. Voisin, H. J. Volk, T. Vuillaume, Z. Wadiasingh, S. J. Wagner, P. Wagner, R. M. Wagner, R. White, A. Wierzcholska, P. Willmann, A. Wornlein, D. Wouters, R. Yang, V. Zabalza, D. Zaborov, M. Zacharias, A. A. Zdziarski, A. Zech, F. Zefi, A. Ziegler, and N. Żywucka, "The population of TeV pulsar wind nebulae in the H.E.S.S. Galactic Plane Survey," *aap*, vol. 612, A2, A2, Apr. 2018. arXiv: 1702.08280 [astro-ph.HE].

[246] B. Posselt, G. G. Pavlov, P. O. Slane, R. Romani, N. Bucciantini, A. M. Bykov, O. Kargaltsev, M. C. Weisskopf, and C. Y. Ng, "Geminga's Puzzling Pulsar Wind Nebula," *apj*, vol. 835, no. 1, 66, p. 66, Jan. 2017. arXiv: 1611.03496 [astro-ph.HE].

[247] A. U. Abeysekara, A. Albert, R. Alfaro, C. Alvarez, J. D. Álvarez, R. Arceo, J. C. Arteaga-Velázquez, H. A. Ayala Solares, A. S. Barber, B. Baughman, N. Bautista-Elivar, J. Becerra Gonzalez, A. Becerril, E. Belmont-Moreno, S. Y. BenZvi, D. Berley, A. Bernal, J. Braun, C. Brisbois, K. S. Caballero-Mora, T. Capistrán, A. Carramiñana, S. Casanova, M. Castillo, U. Cotti, J. Cotzomi, S. Coutiño de León, E. de la Fuente, C. De León, R. Diaz Hernandez, B. L. Dingus, M. A. DuVernois, J. C. Díaz-Vélez, R. W. Ellsworth, K. Engel, D. W. Fiorino, N. Fraija, J. A. García-González, F. Garfias, M. Gerhardt, A. González Muñoz, M. M. González, J. A. Goodman, Z. Hampel-Arias, J. P. Harding, S. Hernandez, A. Hernandez-Almada, J. Hinton, C. M. Hui, P. Huntemeyer, A. Iriarte, A. Jardin-Blicq, V. Joshi, S. Kaufmann, D. Kieda, A. Lara, R. J. Lauer, W. H. Lee, D. Lennarz, H. León Vargas, J. T. Linnemann, A. L. Longinotti, G. L. Raya, R. Luna-García, R. López-Coto, K. Malone, S. S. Marinelli, O. Martinez, I. Martinez-Castellanos, J. Martínez-Castro, H. Martínez-Huerta, J. A. Matthews, P. Miranda-Romagnoli, E. Moreno, M. Mostafá, L. Nellen, M. Newbold, M. U. Nisa, R. Noriega-Papaqui, R. Pelayo, J. Pretz, E. G. Pérez-Pérez, Z. Ren, C. D. Rho, C. Rivière, D. Rosa-González, M. Rosenberg, E. Ruiz-Velasco, H. Salazar, F. Salesa Greus, A. Sandoval, M. Schneider, H. Schoorlemmer, G. Sinnis, A. J. Smith, R. W. Springer, P. Surajbali, I. Taboada, O. Tibolla, K. Tollefson, I. Torres, T. N. Ukwatta, G. Vianello, L. Villaseñor, T. Weisgarber, S. Westerhoff, I. G. Wisher, J. Wood, T. Yapici, P. W. Younk, A. Zepeda, and H. Zhou, "The 2HWC HAWC Observatory Gamma-Ray Catalog," *apj*, vol. 843, no. 1, 40, p. 40, Jul. 2017. arXiv: 1702.02992 [astro-ph.HE].

[248] T. Linden, K. Auchettl, J. Bramante, I. Cholis, K. Fang, D. Hooper, T. Karwal, and S. W. Li, "Using HAWC to discover invisible pulsars," *prd*, vol. 96, no. 10, 103016, p. 103 016, Nov. 2017. arXiv: 1703.09704 [astro-ph.HE].

[249] A. A. Abdo, M. Ackermann, M. Ajello, B. Anderson, W. B. Atwood, M. Axelsson, L. Baldini, J. Ballet, G. Barbiellini, M. G. Baring, D. Bastieri, B. M. Baughman, K.

Bechtol, R. Bellazzini, B. Berenji, G. F. Bignami, R. D. Blandford, E. D. Bloom, E. Bonamente, A. W. Borgland, J. Bregeon, A. Brez, M. Brigida, P. Bruel, T. H. Burnett, G. A. Caliandro, R. A. Cameron, P. A. Caraveo, J. M. Casandjian, C. Cecchi, O. Çelik, A. Chekhtman, C. C. Cheung, J. Chiang, S. Ciprini, R. Claus, J. Cohen-Tanugi, J. Conrad, S. Cutini, C. D. Dermer, A. de Angelis, A. de Luca, F. de Palma, S. W. Digel, M. Dormody, E. do Couto e Silva, P. S. Drell, R. Dubois, D. Dumora, C. Farnier, C. Favuzzi, S. J. Fegan, Y. Fukazawa, S. Funk, P. Fusco, F. Gargano, D. Gasparrini, N. Gehrels, S. Germani, B. Giebels, N. Giglietto, P. Giommi, F. Giordano, T. Glanzman, G. Godfrey, I. A. Grenier, M. H. Grondin, J. E. Grove, L. Guillemot, S. Guiriec, C. Gwon, Y. Hanabata, A. K. Harding, M. Hayashida, E. Hays, R. E. Hughes, G. Jóhannesson, R. P. Johnson, T. J. Johnson, W. N. Johnson, T. Kamae, H. Katagiri, J. Kataoka, N. Kawai, M. Kerr, J. Knodlseder, M. L. Kocian, M. Kuss, J. Lande, L. Latronico, M. Lemoine-Goumard, F. Longo, F. Loparco, B. Lott, M. N. Lovellette, P. Lubrano, G. M. Madejski, A. Makeev, M. Marelli, M. N. Mazziotta, W. McConville, J. E. McEnery, C. Meurer, P. F. Michelson, W. Mitthumsiri, T. Mizuno, C. Monte, M. E. Monzani, A. Morselli, I. V. Moskalenko, S. Murgia, P. L. Nolan, J. P. Norris, E. Nuss, T. Ohsugi, N. Omodei, E. Orlando, J. F. Ormes, D. Paneque, D. Parent, V. Pelassa, M. Pepe, M. Pesce-Rollins, M. Pierbattista, F. Piron, T. A. Porter, J. R. Primack, S. Rainò, R. Rando, P. S. Ray, M. Razzano, N. Rea, A. Reimer, O. Reimer, T. Reposeur, S. Ritz, L. S. Rochester, A. Y. Rodriguez, R. W. Romani, F. Ryde, H. F. W. Sadrozinski, D. Sanchez, A. Sander, P. M. S. Parkinson, J. D. Scargle, C. Sgrò, E. J. Siskind, D. A. Smith, P. D. Smith, G. Spandre, P. Spinelli, J. L. Starck, M. S. Strickman, D. J. Suson, H. Tajima, H. Takahashi, T. Takahashi, T. Tanaka, J. G. Thayer, D. J. Thompson, L. Tibaldo, O. Tibolla, D. F. Torres, G. Tosti, A. Tramacere, Y. Uchiyama, T. L. Usher, A. Van Etten, V. Vasileiou, N. Vilchez, V. Vitale, A. P. Waite, P. Wang, K. Watters, B. L. Winer, M. T. Wolff, K. S. Wood, T. Ylinen, M. Ziegler, and Fermi LAT Collaboration, "Detection of 16 Gamma-Ray Pulsars Through Blind Frequency Searches Using the Fermi LAT," *Science*, vol. 325, no. 5942, p. 840, Aug. 2009. arXiv: `1009.0748 [astro-ph.GA]`.

[250] A. De Luca, M. Marelli, R. P. Mignani, P. A. Caraveo, W. Hummel, S. Collins, A. Shearer, P. M. Saz Parkinson, A. Belfiore, and G. F. Bignami, "Discovery of a Faint X-Ray Counterpart and a Parsec-long X-Ray Tail for the Middle-aged, γ-Ray-only Pulsar PSR J0357+3205," *apj*, vol. 733, no. 2, 104, p. 104, Jun. 2011. arXiv: `1102.3278 [astro-ph.HE]`.

[251] P. M. Saz Parkinson, M. Dormody, M. Ziegler, P. S. Ray, A. A. Abdo, J. Ballet, M. G. Baring, A. Belfiore, T. H. Burnett, G. A. Caliandro, F. Camilo, P. A. Caraveo, A. de Luca, E. C. Ferrara, P. C. C. Freire, J. E. Grove, C. Gwon, A. K. Harding, R. P. Johnson, T. J. Johnson, S. Johnston, M. Keith, M. Kerr, J. Knodlseder, A. Makeev, M. Marelli, P. F. Michelson, D. Parent, S. M. Ransom, O. Reimer, R. W. Romani, D. A. Smith, D. J. Thompson, K. Watters, P. Weltevrede, M. T. Wolff, and K. S. Wood, "Eight γ-ray Pulsars Discovered in Blind Frequency Searches of Fermi

LAT Data," *apj*, vol. 725, no. 1, pp. 571–584, Dec. 2010. arXiv: 1006.2134 [astro-ph.HE].

[252] A. De Luca, R. P. Mignani, M. Marelli, D. Salvetti, N. Sartore, A. Belfiore, P. Saz Parkinson, P. A. Caraveo, and G. F. Bignami, "PSR J0357+3205: A Fast-moving Pulsar with a Very Unusual X-Ray Trail," *apj*, vol. 765, no. 1, L19, p. L19, Mar. 2013. arXiv: 1212.6532 [astro-ph.HE].

[253] S. Chatterjee, J. Cordes, W. Vlemmings, Z Arzoumanian, W. Goss, and T. Lazio, "Pulsar parallaxes at 5 ghz with the very long baseline array," *The Astrophysical Journal*, vol. 604, no. 1, p. 339, 2004.

[254] J. P. W. Verbiest, J. M. Weisberg, A. A. Chael, K. J. Lee, and D. R. Lorimer, "On Pulsar Distance Measurements and Their Uncertainties," *apj*, vol. 755, no. 1, 39, p. 39, Aug. 2012. arXiv: 1206.0428 [astro-ph.GA].

[255] K. E. McGowan, W. T. Vestrand, J. A. Kennea, S. Zane, M. Cropper, and F. A. Córdova, "Probing the Pulsar Wind Nebula of PSR B0355+54," *apj*, vol. 647, no. 2, pp. 1300–1308, Aug. 2006. arXiv: astro-ph/0605087 [astro-ph].

[256] N. Klingler, B. Rangelov, O. Kargaltsev, G. G. Pavlov, R. W. Romani, B. Posselt, P. Slane, T. Temim, C.-Y. Ng, N. Bucciantini, A. Bykov, D. A. Swartz, and R. Buehler, "DEEPCHANDRAOBSERVATIONS OF THE PULSAR WIND NEBULA CREATED BY PSR b0355+54," *The Astrophysical Journal*, vol. 833, no. 2, p. 253, 2016.

[257] F. Acero, M. Ackermann, M. Ajello, A. Albert, W. B. Atwood, M. Axelsson, L. Baldini, J. Ballet, G. Barbiellini, D. Bastieri, A. Belfiore, R. Bellazzini, E. Bissaldi, R. D. Blandford, E. D. Bloom, J. R. Bogart, R. Bonino, E. Bottacini, J. Bregeon, R. J. Britto, P. Bruel, R. Buehler, T. H. Burnett, S. Buson, G. A. Caliandro, R. A. Cameron, R. Caputo, M. Caragiulo, P. A. Caraveo, J. M. Casandjian, E. Cavazzuti, E. Charles, R. C. G. Chaves, A. Chekhtman, C. C. Cheung, J. Chiang, G. Chiaro, S. Ciprini, R. Claus, J. Cohen-Tanugi, L. R. Cominsky, J. Conrad, S. Cutini, F. D'Ammando, A. de Angelis, M. DeKlotz, F. de Palma, R. Desiante, S. W. Digel, L. Di Venere, P. S. Drell, R. Dubois, D. Dumora, C. Favuzzi, S. J. Fegan, E. C. Ferrara, J. Finke, A. Franckowiak, Y. Fukazawa, S. Funk, P. Fusco, F. Gargano, D. Gasparrini, B. Giebels, N. Giglietto, P. Giommi, F. Giordano, M. Giroletti, T. Glanzman, G. Godfrey, I. A. Grenier, M. H. Grondin, J. E. Grove, L. Guillemot, S. Guiriec, D. Hadasch, A. K. Harding, E. Hays, J. W. Hewitt, A. B. Hill, D. Horan, G. Iafrate, T. Jogler, G. Jóhannesson, R. P. Johnson, A. S. Johnson, T. J. Johnson, W. N. Johnson, T. Kamae, J. Kataoka, J. Katsuta, M. Kuss, G. La Mura, D. Landriu, S. Larsson, L. Latronico, M. Lemoine-Goumard, J. Li, L. Li, F. Longo, F. Loparco, B. Lott, M. N. Lovellette, P. Lubrano, G. M. Madejski, F. Massaro, M. Mayer, M. N. Mazziotta, J. E. McEnery, P. F. Michelson, N. Mirabal, T. Mizuno, A. A. Moiseev, M. Mongelli, M. E. Monzani, A. Morselli, I. V. Moskalenko, S. Murgia,

E. Nuss, M. Ohno, T. Ohsugi, N. Omodei, M. Orienti, E. Orlando, J. F. Ormes, D. Paneque, J. H. Panetta, J. S. Perkins, M. Pesce-Rollins, F. Piron, G. Pivato, T. A. Porter, J. L. Racusin, R. Rando, M. Razzano, S. Razzaque, A. Reimer, O. Reimer, T. Reposeur, L. S. Rochester, R. W. Romani, D. Salvetti, M. Sánchez-Conde, P. M. Saz Parkinson, A. Schulz, E. J. Siskind, D. A. Smith, F. Spada, G. Spandre, P. Spinelli, T. E. Stephens, A. W. Strong, D. J. Suson, H. Takahashi, T. Takahashi, Y. Tanaka, J. G. Thayer, J. B. Thayer, D. J. Thompson, L. Tibaldo, O. Tibolla, D. F. Torres, E. Torresi, G. Tosti, E. Troja, B. Van Klaveren, G. Vianello, B. L. Winer, K. S. Wood, M. Wood, S. Zimmer, and Fermi-LAT Collaboration, "Fermi Large Area Telescope Third Source Catalog," *apjs*, vol. 218, no. 2, 23, p. 23, Jun. 2015. arXiv: 1501.02003 [astro-ph.HE].

[258] C. J. Clark, J. Wu, H. J. Pletsch, L. Guillemot, B. Allen, C. Aulbert, C. Beer, O. Bock, A. Cuéllar, H. B. Eggenstein, H. Fehrmann, M. Kramer, B. Machenschalk, and L. Nieder, "The Einstein@Home Gamma-ray Pulsar Survey. I. Search Methods, Sensitivity, and Discovery of New Young Gamma-Ray Pulsars," *apj*, vol. 834, no. 2, 106, p. 106, Jan. 2017. arXiv: 1611.01015 [astro-ph.HE].

[259] M. McLaughlin, J. M. Cordes, and Z. Arzoumanian, "Searching for FAST Pulsars," in *IAU Colloq. 177: Pulsar Astronomy - 2000 and Beyond*, M. Kramer, N. Wex, and R. Wielebinski, Eds., ser. Astronomical Society of the Pacific Conference Series, vol. 202, Jan. 2000, p. 41.

[260] M. A. McLaughlin, Z. Arzoumanian, J. M. Cordes, D. C. Backer, A. N. Lommen, D. R. Lorimer, and A. F. Zepka, "PSR J1740+1000: A Young Pulsar Well Out of the Galactic Plane," *apj*, vol. 564, no. 1, pp. 333–342, Jan. 2002. arXiv: astro-ph/0106371 [astro-ph].

[261] G. Hobbs, D. R. Lorimer, A. G. Lyne, and M. Kramer, "A statistical study of 233 pulsar proper motions," *mnras*, vol. 360, no. 3, pp. 974–992, Jul. 2005. arXiv: astro-ph/0504584 [astro-ph].

[262] A. T. Deller, W. M. Goss, W. F. Brisken, S. Chatterjee, J. M. Cordes, G. H. Janssen, Y. Y. Kovalev, T. J. W. Lazio, L. Petrov, B. W. Stappers, and A. Lyne, "Microarcsecond VLBI Pulsar Astrometry with PSRπ II. Parallax Distances for 57 Pulsars," *apj*, vol. 875, no. 2, 100, p. 100, Apr. 2019. arXiv: 1808.09046 [astro-ph.IM].

[263] L. Pavan, P. Bordas, G. Pühlhofer, M. Filipović, A. Horta, A. O'Brien, E. Crawford, M. Balbo, R. Walter, E. Bozzo, C. Ferrigno, and L. Stella, "The puzzling jet and pulsar wind nebula of igr j11014-6103," *International Journal of Modern Physics: Conference Series*, vol. 28, Sep. 2014.

[264] J. P. Halpern, S. Bogdanov, and E. V. Gotthelf, "X-RAY MEASUREMENT OF THE SPIN-DOWN OF CALVERA: A RADIO- AND GAMMA-RAY-QUIET PULSAR," *The Astrophysical Journal*, vol. 778, no. 2, p. 120, 2013.

[265] O. Kargaltsev, Z. Misanovic, G. G. Pavlov, J. A. Wong, and G. P. Garmire, "X-Ray Observations of Parsec-scale Tails behind Two Middle-Aged Pulsars," *apj*, vol. 684, no. 1, pp. 542–557, Sep. 2008. arXiv: 0802.2963 [astro-ph].

[266] O. Kargaltsev and G. G. Pavlov, "Pulsar-wind nebulae in X-rays and TeV γ-rays," in *X-ray Astronomy 2009; Present Status, Multi-Wavelength Approach and Future Perspectives*, A. Comastri, L. Angelini, and M. Cappi, Eds., ser. American Institute of Physics Conference Series, vol. 1248, Jul. 2010, pp. 25–28. arXiv: 1002.0885 [astro-ph.HE].

[267] G. Maier and J. Holder, "Eventdisplay: An Analysis and Reconstruction Package for Ground-based Gamma-ray Astronomy," *PoS*, vol. ICRC2017, p. 747, 2017.

[268] W. Hofmann, I Jung, A Konopelko, H Krawczynski, H Lampeitl, and G Puhlhofer, "Comparison of techniques to reconstruct vhe gamma-ray showers from multiple stereoscopic cherenkov images," *Astroparticle Physics*, vol. 12, no. 3, pp. 135–143, 1999.

[269] F. Aharonian, W. Hofmann, A. Konopelko, and H. Völk, "The potential of ground based arrays of imaging atmospheric cherenkov telescopes. i. determination of shower parameters," *Astroparticle Physics*, vol. 6, no. 3, pp. 343–368, 1997.

[270] H. Krawczynski, D. Carter-Lewis, C Duke, J Holder, G Maier, S Le Bohec, and G Sembroski, "Gamma–hadron separation methods for the veritas array of four imaging atmospheric cherenkov telescopes," *Astroparticle Physics*, vol. 25, no. 6, pp. 380–390, 2006.

[271] J. Wilms, A. Allen, and R. McCray, "On the Absorption of X-Rays in the Interstellar Medium," *apj*, vol. 542, no. 2, pp. 914–924, Oct. 2000. arXiv: astro-ph/0008425 [astro-ph].

[272] W. A. Rolke, A. M. López, and J. Conrad, "Limits and confidence intervals in the presence of nuisance parameters," *Nuclear Instruments and Methods in Physics Research A*, vol. 551, no. 2-3, pp. 493–503, Oct. 2005. arXiv: physics/0403059 [physics.data-an].

[273] M. Marelli, A. D. Luca, D. Salvetti, N. Sartore, A. Sartori, P. Caraveo, F. Pizzolato, P. M. S. Parkinson, and A. Belfiore, "PSR j0357+3205: THE TAIL OF THE TURTLE," *The Astrophysical Journal*, vol. 765, no. 1, p. 36, 2013.

[274] N. Klingler, O. Kargaltsev, B. Rangelov, G. G. Pavlov, B. Posselt, and C.-Y. Ng, "CHANDRAOBSERVATIONS OF OUTFLOWS FROM PSR j1509–5850," *The Astrophysical Journal*, vol. 828, no. 2, p. 70, 2016.

[275] D. A. Zyuzin, A. V. Karpova, and Y. A. Shibanov, "X-ray counterpart candidates for six new gamma-ray pulsars," *Monthly Notices of the Royal Astronomical Society*, vol. 476, no. 2, pp. 2177–2185, Feb. 2018. eprint: https://academic.oup.com/mnras/article-pdf/476/2/2177/24353143/sty359.pdf.

[276] K. Auchettl, P. Slane, R. W. Romani, B. Posselt, G. G. Pavlov, O. Kargaltsev, C.-Y. Ng, T. Temim, M. C. Weisskopf, A. Bykov, and D. A. Swartz, "X-RAY ANALYSIS OF THE PROPER MOTION AND PULSAR WIND NEBULA FOR PSR j1741-2054," *The Astrophysical Journal*, vol. 802, no. 1, p. 68, 2015.

[277] C. He, C. Y. Ng, and V. M. Kaspi, "The Correlation between Dispersion Measure and X-Ray Column Density from Radio Pulsars," *apj*, vol. 768, no. 1, 64, p. 64, May 2013. arXiv: 1303.5170 [astro-ph.HE].

[278] A. U. Abeysekara, A. Albert, R. Alfaro, C. Alvarez, J. D. Álvarez, R. Arceo, J. C. Arteaga-Velázquez, D. Avila Rojas, H. A. Ayala Solares, A. S. Barber, N. Bautista-Elivar, A. Becerril, E. Belmont-Moreno, S. Y. BenZvi, D. Berley, A. Bernal, J. Braun, C. Brisbois, K. S. Caballero-Mora, T. Capistrán, A. Carramiñana, S. Casanova, M. Castillo, U. Cotti, J. Cotzomi, S. Coutiño de León, C. De León, E. De la Fuente, B. L. Dingus, M. A. DuVernois, J. C. Díaz-Vélez, R. W. Ellsworth, K. Engel, O. Enríquez-Rivera, D. W. Fiorino, N. Fraija, J. A. García-González, F. Garfias, M. Gerhardt, A. González Muñoz, M. M. González, J. A. Goodman, Z. Hampel-Arias, J. P. Harding, S. Hernández, A. Hernández-Almada, J. Hinton, B. Hona, C. M. Hui, P. Huntemeyer, A. Iriarte, A. Jardin-Blicq, V. Joshi, S. Kaufmann, D. Kieda, A. Lara, R. J. Lauer, W. H. Lee, D. Lennarz, H. L. Vargas, J. T. Linnemann, A. L. Longinotti, G. Luis Raya, R. Luna-García, R. López-Coto, K. Malone, S. S. Marinelli, O. Martinez, I. Martinez-Castellanos, J. Martínez-Castro, H. Martínez-Huerta, J. A. Matthews, P. Miranda-Romagnoli, E. Moreno, M. Mostafá, L. Nellen, M. Newbold, M. U. Nisa, R. Noriega-Papaqui, R. Pelayo, J. Pretz, E. G. Pérez-Pérez, Z. Ren, C. D. Rho, C. Rivière, D. Rosa-González, M. Rosenberg, E. Ruiz-Velasco, H. Salazar, F. Salesa Greus, A. Sandoval, M. Schneider, H. Schoorlemmer, G. Sinnis, A. J. Smith, R. W. Springer, P. Surajbali, I. Taboada, O. Tibolla, K. Tollefson, I. Torres, T. N. Ukwatta, G. Vianello, T. Weisgarber, S. Westerhoff, I. G. Wisher, J. Wood, T. Yapici, G. Yodh, P. W. Younk, A. Zepeda, H. Zhou, F. Guo, J. Hahn, H. Li, and H. Zhang, "Extended gamma-ray sources around pulsars constrain the origin of the positron flux at Earth," *Science*, vol. 358, no. 6365, pp. 911–914, Nov. 2017. arXiv: 1711.06223 [astro-ph.HE].

[279] B. M. Baughman and J. Wood, "TeV Gamma-Ray Emission Observed from Geminga with HAWC," *arXiv e-prints*, arXiv:1508.03497, arXiv:1508.03497, Aug. 2015. arXiv: 1508.03497 [astro-ph.HE].

[280] A. Flinders, "VERITAS Observations of the Geminga Supernova Remnant," *arXiv e-prints*, arXiv:1509.04224, arXiv:1509.04224, Sep. 2015. arXiv: 1509.04224 [astro-ph.HE].

[281] A. Abeysekara, "Search for very high energy (E ¿ 100 GeV) Emission from Geminga supernova by VERITAS," in *36th International Cosmic Ray Conference (ICRC2019)*, ser. International Cosmic Ray Conference, vol. 36, Jul. 2019, p. 616. arXiv: 1908.05369 [astro-ph.HE].

[282] G. Morlino, M. Lyutikov, and M. Vorster, "Mass loading of bow shock pulsar wind nebulae," *mnras*, vol. 454, no. 4, pp. 3886–3901, Dec. 2015. arXiv: 1505.01712 [astro-ph.HE].

[283] M. V. Barkov, M. Lyutikov, and D. Khangulyan, "3D dynamics and morphology of bow-shock pulsar wind nebulae," *Monthly Notices of the Royal Astronomical Society*, vol. 484, no. 4, pp. 4760–4784, Jan. 2019. eprint: https://academic.oup.com/mnras/article-pdf/484/4/4760/27781891/stz213.pdf.

[284] S. Xu, N. Klingler, O. Kargaltsev, and B. Zhang, "On the broadband synchrotron spectra of pulsar wind nebulae," *The Astrophysical Journal*, vol. 872, no. 1, p. 10, 2019.

[285] C. Y. Ng, B. M. Gaensler, S. Chatterjee, and S. Johnston, "Radio Polarization Observations of G319.9-0.7: A Bow-Shock Nebula with an Azimuthal Magnetic Field Powered by Pulsar J1509-5850," *apj*, vol. 712, no. 1, pp. 596–603, Mar. 2010. arXiv: 1002.1815 [astro-ph.HE].

[286] F. Yusef-Zadeh and B. M. Gaensler, "A radio study of the mouse, G359.23 - 0.82," *Advances in Space Research*, vol. 35, no. 6, pp. 1129–1136, Jan. 2005. arXiv: astro-ph/0503031 [astro-ph].

[287] Y. Chen, Q. D. Wang, E. V. Gotthelf, B. Jiang, Y.-H. Chu, and R. Gruendl, "ChandraACIS spectroscopy of n157b: A young composite supernova remnant in a superbubble," *The Astrophysical Journal*, vol. 651, no. 1, pp. 237–249, 2006.

[288] V. Zabalza, "Naima: a Python package for inference of particle distribution properties from nonthermal spectra," in *34th International Cosmic Ray Conference (ICRC2015)*, ser. International Cosmic Ray Conference, vol. 34, Jul. 2015, p. 922. arXiv: 1509.03319 [astro-ph.HE].

[289] O. Kargaltsev and G. G. Pavlov, "Pulsar Wind Nebulae in the Chandra Era," in *40 Years of Pulsars: Millisecond Pulsars, Magnetars and More*, C. Bassa, Z. Wang, A. Cumming, and V. M. Kaspi, Eds., ser. American Institute of Physics Conference Series, vol. 983, Feb. 2008, pp. 171–185. arXiv: 0801.2602 [astro-ph].

[290] A. Albert, R. Alfaro, C. Alvarez, J. R. A. Camacho, J. C. Arteaga-Velázquez, K. P. Arunbabu, D. Avila Rojas, H. A. Ayala Solares, V. Baghmanyan, E. Belmont-Moreno, S. Y. BenZvi, C. Brisbois, K. S. Caballero-Mora, T. Capistrán, A. Car-

ramiñana, S. Casanova, U. Cotti, S. Coutiño de León, E. De la Fuente, R. Diaz Hernandez, L. Diaz-Cruz, B. L. Dingus, M. A. DuVernois, M. Durocher, J. C. Díaz-Vélez, R. W. Ellsworth, K. Engel, C. Espinoza, K. L. Fan, K. Fang, M. F. Alonso, H. Fleischhack, N. Fraija, A. Galván-Gámez, D. Garcia, J. A. García-González, F. Garfias, G. Giacinti, M. M. González, J. A. Goodman, J. P. Harding, S. Hernandez, J. Hinton, B. Hona, D. Huang, F. Hueyotl-Zahuantitla, P. Huntemeyer, A. Iriarte, A. Jardin-Blicq, V. Joshi, D. Kieda, A. Lara, W. H. Lee, H. León Vargas, J. T. Linnemann, A. L. Longinotti, G. Luis-Raya, J. Lundeen, R. López-Coto, K. Malone, V. Marandon, O. Martinez, I. Martinez-Castellanos, J. Martínez-Castro, J. A. Matthews, P. Miranda-Romagnoli, J. A. Morales-Soto, E. Moreno, M. Mostafá, A. Nayerhoda, L. Nellen, M. Newbold, M. U. Nisa, R. Noriega-Papaqui, L. Olivera-Nieto, N. Omodei, A. Peisker, Y. Pérez Araujo, E. G. Pérez-Pérez, Z. Ren, C. D. Rho, C. Rivière, D. Rosa-González, E. Ruiz-Velasco, H. Salazar, F. Salesa Greus, A. Sandoval, M. Schneider, H. Schoorlemmer, F. Serna, G. Sinnis, A. J. Smith, R. W. Springer, P. Surajbali, K. Tollefson, I. Torres, R. Torres-Escobedo, T. N. Ukwatta, F. Ureña-Mena, T. Weisgarber, F. Werner, E. Willox, A. Zepeda, H. Zhou, C. de León, J. D. Álvarez, and HAWC Collaboration, "3HWC: The Third HAWC Catalog of Very-high-energy Gamma-Ray Sources," *apj*, vol. 905, no. 1, 76, p. 76, Dec. 2020. arXiv: 2007.08582 [astro-ph.HE].

[291] J. Arons, "Pulsar Wind Nebulae as Cosmic Pevatrons: A Current Sheet's Tale," *ssr*, vol. 173, no. 1-4, pp. 341–367, Nov. 2012. arXiv: 1208.5787 [astro-ph.HE].

[292] A. G. Pacholczyk, *Radio astrophysics. Nonthermal processes in galactic and extragalactic sources*. 1970.

[293] C. B. Adams, G. Ambrosi, M. Ambrosio, C. Aramo, P. I. Batista, W. Benbow, B. Bertucci, E. Bissaldi, M. Bitossi, A. Boiano, C. Bonavolontà, R. Bose, A. Brill, J. H. Buckley, R. A. Cameron, R. Canestrari, M. Capasso, M. Caprai, C. E. Covault, D. Depaoli, L. Di Venere, M. Errando, S. Fegan, Q. Feng, E. Fiandrini, A. Furniss, A. Gent, N. Giglietto, F. Giordano, E. Giro, R. Halliday, O. Hervet, T. B. Humensky, S. Incardona, M. Ionica, W. Jin, D. Kieda, F. Licciulli, S. Loporchio, G. Marsella, V. Masone, K. Meagher, T. Meures, B. A. W. Mode, S. A. I. Mognet, R. Mukherjee, D. Nieto, A. Okumura, N. Otte, F. R. Pantaleo, R. Paoletti, G. Pareschi, F. Di Pierro, E. Pueschel, D. Ribeiro, L. Riitano, E. Roache, J. Rousselle, A. Rugliancich, M. Santander, R. Shang, L. Stiaccini, L. P. Taylor, L. Tosti, G. Tovmassian, G. Tripodo, V. Vagelli, M. Valentino, J. Vandenbroucke, V. V. Vassiliev, D. A. Williams, and P. Yu, "Prototype Schwarzschild-Couder Telescope for the Cherenkov Telescope Array: Commissioning the Optical System," *arXiv e-prints*, arXiv:2110.07463, arXiv:2110.07463, Oct. 2021. arXiv: 2110.07463 [astro-ph.IM].

[294] C. B. Adams, G. Ambrosi, M. Ambrosio, C. Aramo, P. I. Batista, W. Benbow, B. Bertucci, E. Bissaldi, M. Bitossi, A. Boiano, C. Bonavolonta, R. Bose, A. Brill, A. M. Brown, J. H. Buckley, R. A. Cameron, M. Capasso, M. Caprai, C. E. Covault,

D. Depaoli, L. Di Venere, M. Errando, S. Fegan, Q. Feng, E. Fiandrini, A. Furniss, A. Gent, N. Giglietto, F. Giordano, R. Halliday, O. Hervet, T. B. Humensky, S. Incardona, M. Ionica, W. Jin, D. Kieda, F. Licciulli, S. Loporchio, G. Marsella, V. Masone, K. Meagher, T. Meures, B. A. W. Mode, S. A. I. Mognet, R. Mukherjee, A. Okumura, N. Otte, F. R. Pantaleo, R. Paoletti, G. Pareschi, F. Di Pierro, E. Pueschel, D. Ribeiro, L. Riitano, E. Roache, D. Ross, J. Rousselle, A. Rugliancich, M. Santander, R. Shang, L. Stiaccini, H. Tajima, L. P. Taylor, L. Tosti, G. Tovmassian, G. Tripodo, V. Vagelli, M. Valentino, J. Vandenbroucke, V. V. Vassiliev, J. J. Watson, R. White, D. A. Williams, and A. Zink, "Design and performance of the prototype Schwarzschild-Couder Telescope camera," *arXiv e-prints*, arXiv:2109.05127, arXiv:2109.05127, Sep. 2021. arXiv: 2109.05127 [astro-ph.IM].

[295] J. Bolmont, S. Caroff, M. Gaug, A. Gent, A. Jacholkowska, D. Kerszberg, C. Levy, T. Lin, M. Martinez, L. Nogués, A. N. Otte, C. Perennes, M. Ronco, and T. Terzić, "First Combined Study on Lorentz Invariance Violation from Observations of Energy-dependent Time Delays from Multiple-type Gamma-Ray Sources. I. Motivation, Method Description, and Validation through Simulations of H.E.S.S., MAGIC, and VERITAS Data Sets,", vol. 930, no. 1, 75, p. 75, May 2022. arXiv: 2201.02087 [astro-ph.HE].

[296] A. M. Kudoda and A. Faltenbacher, "Detailed modelling of the EBL along VHE γ-ray paths,", vol. 481, no. 1, pp. 405–413, Nov. 2018. arXiv: 1808.06205 [astro-ph.GA].